THE SMOKING GUN: SEARCH FOR A CP-ODD HIGGS BOSON DECAYING TO A HEAVY CP-EVEN HIGGS BOSON AND A Z BOSON IN THE $\ell\ell t\bar{t}$ AND $\nu\bar{\nu}b\bar{b}$ FINAL STATES WITH THE ATLAS EXPERIMENT AND UPGRADE OF THE ATLAS INNER TRACKER FOR THE HIGH LUMINOSITY LHC

by

Punit Sharma

A thesis submitted in partial fulfillment of the
requirements for the Doctor of Philosophy
degree in Physics
in the Graduate College of
The University of Iowa

August 2024

Thesis Committee: Usha Mallik, Thesis Supervisor
Yannick Meurice
Frederick Skiff
Alessandro Tricoli
David Lynn

ACKNOWLEDGEMENTS

I want to express my deepest gratitude to those who have supported me throughout my thesis journey. This work was only possible with the guidance, encouragement, and assistance of many individuals and institutions. First, I sincerely thank my advisor, Dr. Usha Mallik, for providing me the platform and resources to work and learn from some of the best in their fields throughout the thesis. I am grateful for your guidance and support over the past five years in physics and beyond. Your experience and expertise in the field of physics and your patience as an advisor have helped me grow as a physicist and a person.

I am also grateful to my committee members, Dr. Yannick Meurice, Dr. Frederick N. Skiff, Dr. David Lynn, and Dr. Alessandro Tricoli, for their time and interest and for being on my PhD thesis committee. Your diverse perspectives and input on my writing have been precious. I thank The University Of Iowa Department of Physics and Astronomy for allowing me to be a Hawkeye and for all the interactions and discussions throughout the years.

I am grateful to Dr. Weitao Wang, who has been like a second supervisor to me. Thank you for all your help with the physics discussions and debugging sessions during our time at CERN. I thank Dr. Spyridon Argyropoulos, Dr. Tetiana Moskalets, Dr. Anindya Ghosh, the AZH analysis team, and the VH analysis team; working with them has been a pleasure.

I want to thank the BNL ITk group, which taught me invaluable lessons about building

and testing a detector. Dr. David Lynn has always inspired me with his knowledge and experience on detectors. Thank you for all the lessons and discussions. Thanks to my nonna, Dr. Stefania Stucci, for all her detector guidance, ITSDAQ sessions, and pizza lessons. I want to thank the other members of the ITk team: Dr. Olivier Arnaez, Dr. George Iakovidis, Dr. Geoffrey Mullier, Dr. Dominique Trischuk, and Dr. Masahiro Morii for all the support and discussions during my time at CERN.

My friends and colleagues have been a constant support over the years. Thanks to OPG, Apurv, Divyat, Sagar, Kirti, Francesca, Elise, Stuti, Neha, Diksha, Todd, Zenny, Kees, Ayushi, Monideepa and others. I am thankful for your friendship.

Finally, thanks to my family, your constant support and motivation have meant the world to me.

ABSTRACT

The Standard Model (SM) of particle physics is considered one of the most outstanding achievements of modern physics. It has successfully explained the existence of elementary particles and their interactions. Numerous experiments have been conducted to confirm the SM's predictions. So far, the experimental observations agree with the SM predictions. One of the most significant confirmations came in 2012 with the discovery of the Higgs Boson at the LHC. However, the SM alone cannot address many outstanding questions in modern physics, such as the existence of baryon-antibaryon asymmetry, dark matter, and dark energy (DE) in our universe. Electroweak Baryogenesis (EWB) is one of the most straightforward mechanisms explaining baryon-antibaryon asymmetry. EWB generates the observed asymmetry via the dynamics of the Electroweak symmetry breaking, hence making it tightly related to the properties of the Higgs boson. Since the Standard Model does not satisfy the conditions for baryogenesis, the simplest extension, "The Two Higgs Doublet Model" (2HDM), which predicts the existence of 5 Higgs-like particles, could potentially explain the matter-antimatter asymmetry when $300 \leq m_A \leq 700$ GeV and $m_A - m_H \geq 250$ GeV where A is the CP-Odd Higgs and H is the heavy neutral Higgs. The analysis presented in the thesis uses the full Run 2 ATLAS dataset of 140 fb^{-1} to search for a CP-odd Higgs boson A that decays to a Z boson and heavy neutral Higgs H with two final states where the Z decays into leptons or neutrinos and H decays into two beauty quark or two top quarks, $A \to ZH \to lltt/vvbb$. The ATLAS experiment is preparing to upgrade the inner tracking (ITk) detector for High-luminosity

LHC operation starting in 2029. One of the major components of the ITk upgrade is quality assurance and control (QA/QC), which requires testing and characterizing the micro-strip sensors and front-end electronics for noise. Studies and results of the QA/QC of the silicon microstrip sensor and development/ validation of the front-end calibration scans for the ITk microstrip sensors are presented.

PUBLIC ABSTRACT

The world around us is filled with mysteries and puzzles, like why there are more baryons than anti-baryons, what dark matter and dark energy are, and why neutrinos have such small masses. The most accepted theory among physicists is the Standard Model (SM) of particle physics, which has successfully explained the existence of elementary particles and their interactions. Numerous experiments have been conducted to confirm the SM's predictions. One of the most significant confirmations came in 2012 when the Higgs Boson was discovered at the LHC. However, the SM alone cannot address many outstanding questions in modern physics, such as the existence of baryon-antibaryon asymmetry, as observed in astrophysics. One of the ways to check why the baryon-antibaryon asymmetry exists is by looking at the signatures of the early universe at particle colliders like the Large Hadron Collider (LHC) at CERN. Protons(p) are made to collide at high energies, and the products of their collisions are recorded using the ATLAS detector. This thesis describes a search for beyond SM particle decays in the proton-proton collision data recorded by the ATLAS experiment between 2015 and 2018. The LHC plans to increase the luminosity from 2029, requiring upgrading the ATLAS detector recording the pp collisions. Studies and results of the silicon microstrip sensor being constructed are presented in this thesis.

TABLE OF CONTENTS

LIST OF TABLES

LIST OF FIGURES

CHAPTER 1

INTRODUCTION

In 2012, the discovery of the Higgs boson (mass=125 GeV) by the ATLAS and CMS collaboration at the Large Hadron Collider (LHC) marked a significant milestone in particle physics, completing the puzzle of the Standard Model (SM) [30, 72]. However, despite its success, the SM fails to address fundamental questions such as Dark Matter, Dark Energy, and Baryogenesis. This thesis explores Baryogenesis, a phenomenon where the universe has an excess of matter over antimatter despite the Dirac equation predicting a balance. A class of Beyond Standard Model (BSM) theories explains the baryon-antibaryon asymmetry in the early universe via the mechanism called "Electroweak Baryogenesis" (EWB), which relates it to the properties of the Higgs-boson. One of the most straightforward extensions of the SM with an additional Higgs doublet, the Two-Higgs Doublet Model (2HDM) satisfies the condition for EWB only in a range of the parameter space, i.e., $300 \leq m_A \leq 700$ GeV and $m_A - m_H \geq 250$ GeV where A is the CP-Odd Higgs and H is the Heavy neutral Higgs. A search for the CP-odd Higgs boson decaying into a heavy CP-even Higgs boson and a Z boson in the final stages of $\ell\ell t\bar{t}$ and $\nu\bar{\nu}b\bar{b}$ is done using the complete Run-2 dataset of pp collisions at $\sqrt{s} = 13$ TeV corresponding to an integrated luminosity of 140.1 fb^{-1} as recorded by the ATLAS experiment. The thesis is organized to give a comprehensive overview of the theoretical framework in Chapter 2, the ATLAS experiment at the LHC in Chapter 3, the reconstruction and identification strategies used for physics objects in the ATLAS experiment in Chapter 4 and the anal-

ysis in Chapter 5. Once the SM Higgs boson was discovered, it was important to study its properties, like production and decay modes. A brief overview of the measurement of $VH(\rightarrow b\bar{b}, c\bar{c})$ where $V = W/Z$ boson is presented in Appendix A focusing on the different measurement strategies.

Along with analyzing the data already taken by the ATLAS detector, future upgrades are also in progress. A planned LHC upgrade starting at 2029 will increase the luminosity of the machine up to a peak instantaneous luminosity of 7.5×10^{34} s^{-1} cm^{-2}, corresponding to a maximum of 200 inelastic proton-proton collisions per bunch crossing and the hadron fluence of approximately 2×10^{16} $\mathrm{n_{eq}}$ $\mathrm{cm}^{-}2$ [21]. To withstand this high radiation environment of 3000 fb^{-1} total accumulated luminosity, detector upgrades for the High Luminosity-LHC (HL-LHC) have already started. One of the major upgrades for the ATLAS experiment is the ATLAS inner tracker (ITk) upgrade. A comprehensive overview of the ATLAS inner tracker upgrade has been provided in Chapter 6.

CHAPTER 2

FRAMEWORKS IN THEORY AND ANALYTICS

The theoretical framework that best describes our current understanding of the universe is the Standard Model of particle physics (SM). It explains three of the four fundamental forces of nature, Strong, Weak, and Electromagnetic interactions, and classifies elementary particles into fermions and bosons. It was developed in the latter half of the 20^{th} century and came to its current form in the 1970s; since then, it has been tested thoroughly, with the latest example being the discovery of the "Higgs boson" of mass 125 GeV in 2012.

This chapter lays the theoretical foundation of SM and its extensions, giving a context to the work presented in the thesis. Section 2.1 introduces SM as a quantum field theory, mainly focusing on the Higgs boson and spontaneous symmetry breaking. In section 2.1.3, we briefly discuss the limitations of the standard model, mainly focusing on the baryogenesis in 2.1.3. Section 2.2 discusses the basics of simulating proton-proton collisions, section 2.3 gives an overview of the analysis strategy, and section 2.3.1 briefly introduces the statistical analysis and the likelihood functions, highlighting strategies used in the physics analysis.

2.1 Standard Model of Particle Physics

The SM is a Lorentz-invariant relativistic quantum field theory. It is also a renormalizable gauge theory invariant under the local gauge transformation of the non-Abelian

symmetry group

$$SU(3)_{\mathcal{C}} \otimes SU(2)_L \otimes U(1)_Y, \tag{2.1}$$

where the $SU(3)_c$ covers the Quantum ChromoDynamics (QCD) with color charge $\mathcal{C}$; the $SU(2)_L \otimes U(1)_Y$ covers the electroweak theory (EW) describing the weak and electromagnetic sectors. In addition, another $SU(2)$ doublet corresponds to the scalar Higgs field.

2.1.1 World of particles

The universe's building blocks are classified into matter particles $fermions$ with half-integer spin and force carriers *bosons* with integral spin-mediating the interactions between the matter particles. Figure 2.1 gives an overview of the particle/fields content in the SM.

Fermions The matter components include spin 1/2 particles, known as *leptons* and $quarks$. These fermions are arranged into three generations of doublets, each successive generation with a higher mass than the previous one. The *leptons* carry an electric charge of -1 (e^-, μ^-, τ^-) and the corresponding neutral neutrinos $(\nu_e, \nu_\mu, \nu_\tau)$ with zero charges. The Up type (u, c, t) and the down type (d, s, b) doublets of $quark$ carry an electromagnetic charge of $+2/3$ or $-1/3$ respectively, along with a color charge $\mathcal{C}$.

Gauge Bosons The gauge bosons mediate the three fundamental forces described by the SM. The photon γ mediates the electromagnetic interactions, the $W^{\pm}$ and Z mediate the weak interactions, and the gluons mediate the strong interactions. Mathematically, they are explained by the gauge fields introduced to make the Lagrangian invariant under a particular group's symmetry transformation.

Higgs Boson The spin 0 particle Higgs boson H[1] is the only scalar in theory. It is not connected to the SM symmetry groups but arises from the need to generate mass without violating the local gauge invariance. The interaction with the Higgs boson gives masses to the quark and fermion fields.

Composite Particles Along with the particles described above, many composite particles arise from combinations of quarks known as $Hadrons$. These particles can be classified into $Baryons$ ($anti-Baryons$) or $Mesons$. $Baryons$ have a half-integer spin and consist of three quarks (anti-quarks). These include the proton (uud), neutrons (udd), Ω (sss), λ (uds) etc. $Mesons$, on the other hand, have integer spin and consist of a pair of quarks and an anti-quark. Some of the examples include pions (π^+, π^-, π^0), kaons (k^+, k^-, k^0), etc. Even though composite particles play an important role in physics, they are mostly observed as Jets following strong interactions at the detector level.

[1]Here we are talking about the SM Higgs boson. The SM Higgs and the 2HDM CP-Even Higgs boson are generally called H in the thesis. The distinction can be made from the context.

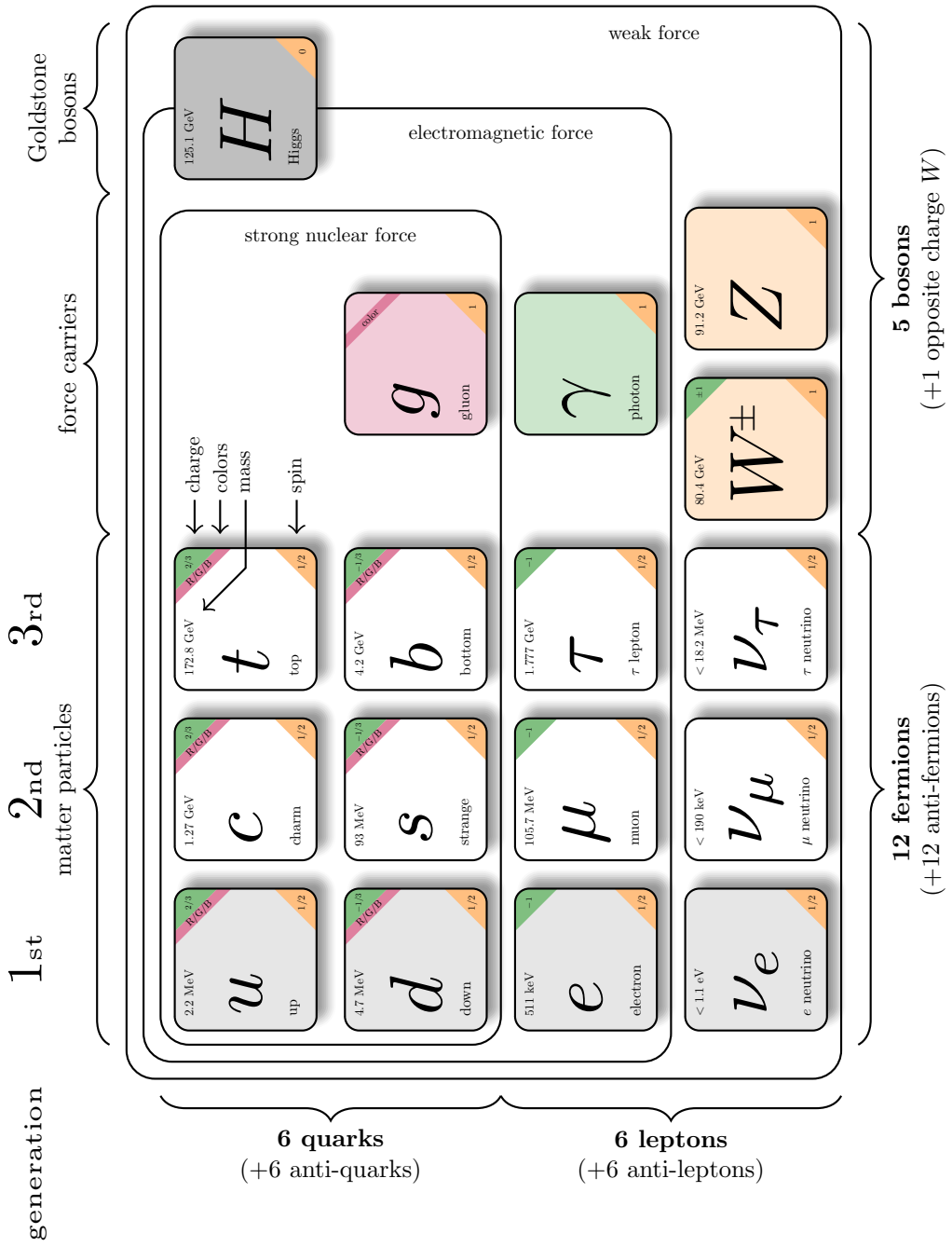

Figure 2.1. Info-graphic showing the particles and the anti-particles (in brackets where needed) in the SM of particle physics. Figure adapted from [61]

2.1.2 The Standard Model as a Quantum Field Theory

The following subsections will build towards the complete SM Lagrangian, starting from the first principles: the action (S), the Lagrangian (L), the Euler-Lagrange equations, and Noether's theorem.

The action is the scalar value accumulated by the energy function, aka Lagrangian, between two states. The variational principles of mechanics is defined with:

$$S = \int L \, dt$$

where the Lagrangian represents the system and dt is the small change in time. One of the key concepts used in theoretical physics is the principle of least action, which explains that the actual path taken by a system between two states is the one for which the S is stationary. The Lagrangian encapsulates its dynamics and is generally expressed as the difference between kinetic and potential energies:

$$L = T - V$$

where T is the kinetic energy and V is the potential energy. The Lagrangian formulation allows for the derivation of the equations of motion, i.e., the Euler-Lagrange equations, providing a straightforward approach to understanding the system dynamics. For a system defined by generalized coordinates q_i and their time derivatives $\dot{q}_i$, the Euler-Lagrange equations are given by:

$$\frac{d}{dt}\left(\frac{\partial L}{\partial \dot{q}_i}\right) - \frac{\partial L}{\partial q_i} = 0$$

Noether's theorem, named after the mathematician Emmy Noether, links sym-

metries in physical laws with conservation principles. The theorem states that each differentiable symmetry of the action of a physical system corresponds to a particular conservation law. For instance:

- Conservation of energy results from time symmetry.
- Conservation of linear momentum results from continuous translational symmetry.
- Conservation of angular momentum results from continuous rotational symmetry.

These foundational principles are used towards the complete SM Lagrangian, explained in the following section.

2.1.2.1 Quantum Electrodynamics

The theory of Quantum Electrodynamics (QED) is invariant under local symmetry transformation $U(1)$ and describes electromagnetic interactions. According to group theory, $U(1)$ has only one generator, which is realized as the electric charge in the following calculations.

The Lagrangian of QED ($\mathcal{L}_{QED}$) is expressed as the sum of the free electron Lagrangian or the Dirac Lagrangian $\mathcal{L}_D$, the free photon Lagrangian $\mathcal{L}_\gamma$, and the interaction between the electrons and photons $\mathcal{L}_{int}$. The Dirac Lagrangian (2.2) describes the free propagation of massive fermions of mass m in a vacuum

$$\mathcal{L}_D = \bar{\psi}(i\gamma_\mu \partial^\mu - m)\psi \tag{2.2}$$

where ψ represents the fermionic spinor, γ^μ the Dirac matrices, $\bar{\psi} = \psi^\dagger \gamma^\mu$ where $\psi^\dagger$ is the Hermitian adjoint of ψ.

Given that the electromagnetism has the underlying local $U(1)$ symmetry, the fields ψ with a $U(1)$ charge q transform as follows

$$\psi(x) \to e^{-i\alpha q}\psi(x) \tag{2.3}$$

where α is the phase. In the transformation of the derivative

$$\partial_\mu\psi(x) \to \psi'(x) = e^{i\alpha(x)}[\partial_\mu\psi(x) + i(\partial_\mu\alpha(x))\psi(x)] \tag{2.4}$$

the last term $e^{i\alpha(x)}[i(\partial_\mu\alpha(x))\psi(x)]$, however, breaks the invariance of the Lagrangian under local phase transformation.

This is fixed by promoting the derivative to be gauge covariant, i.e.

$$\partial_\mu \to D_\mu = \partial_\mu + iqA_\mu \tag{2.5}$$

Here q is the particle's charge described by the field ψ. We also introduce a gauge field A_μ that transforms as

$$A_\mu \to A'_\mu = A_\mu - \frac{1}{q}\partial_\mu\alpha(x) \tag{2.6}$$

Replacing the normal derivative in (2.2) with the gauge covariant derivative from (2.5)

$$\mathcal{L}_D \to \mathcal{L}_D - q\bar{\psi}\gamma^\mu A_\mu\psi \tag{2.7}$$

The second term in (2.7) $q\bar{\psi}\gamma^\mu A_\mu\psi$ is the interaction term between the gauge field A_μ and the fermion field ψ.

The last piece of the kinematic term $\mathcal{L}_\gamma$ is

$$\mathcal{L}_\gamma = -\frac{1}{4} F_{\mu\nu} F^{\mu\nu} \tag{2.8}$$

Where $F_{\mu\nu} = \partial_\mu A_\nu - \partial_\nu A_\mu$ is the field strength tensor, invariant under the gauge transformation of A_μ

The Full QED Lagrangian is

$$\mathcal{L}_{QED} = \mathcal{L}_D + \mathcal{L}_\gamma + \mathcal{L}_{int} = \bar{\psi}(i\gamma^\mu \partial^\mu - m)\psi - \frac{1}{4} F_{\mu\nu} F^{\mu\nu} - q\bar{\psi}\gamma^\mu \psi A_\mu \tag{2.9}$$

QED has been one of the most precise theories, with accurate predictions and subsequent experimental confirmations. The fine structure constant or the coupling strength of electromagnetic particles, predicted by QED as $\sim \frac{1}{137}$ has been verified by experiments with very high precision.

2.1.2.2 Quantum Chromodynamics

Quantum chromodynamics (QCD) describes the interactions between the quarks and gluons, also known as the strong interactions. The gauge group for QCD is $SU(3)_{\mathcal{C}}$, which comes with eight generators realized in the eight different gluon fields. The quantum number associated with the $SU(3)_{\mathcal{C}}$ is the color charge $\mathcal{C}$, which could be either red (r), blue (b), or green (g), along with their anti-color counterparts. Any bound state of quarks and anti-quarks must be color-neutral, which can be achieved by combining color (anti-color).

The fermion field transforms as a triplet, and the group's generators are expressed in terms of eight Gell-Mann matrices (λ) with a generator algebra:

$$[T^a, T^b] = if^{abc}T^c \tag{2.10}$$

where $T^a = \lambda^a/2; a \in \{1, ..., 8\}$ and f^{abc} is the structure constant of the $SU(3)$ group.

The QCD covariant derivative is written in terms of the gluon fields G^a_μ as

$$D_\mu = \partial_\mu - ig_s\frac{\lambda^a}{2}G^a_\mu \tag{2.11}$$

Using the covariant derivative, the kinematic term of QCD in terms of field strength tensors is:

$$G^a_{\mu\nu} = \partial_\mu G^a_\nu - \partial_\nu G^a_\mu + g_s f^{abc} G^b_\mu G^c_\nu \tag{2.12}$$

and the kinematic term is:

$$\mathcal{L}_g = -\frac{1}{4}G^a_{\mu\nu}G^{a,\mu\nu} \tag{2.13}$$

The last term in (2.12) comes from the non-abelian nature of QCD representing gluon self-interactions. This self-interaction leads to rich hadron spectroscopy, showering, various types of jet formations, etc.

Following the same prescription as for QED, the QCD Lagrangian can be written in terms of the free fermion Dirac Lagrangian, kinematic term, and the interaction term as

$$\mathcal{L}_{QCD} = \sum_f \bar{\psi}_f(i\gamma^\mu\partial_\mu - m_f)\psi_f - g_s\sum_f(\bar{\psi}_f\gamma^\mu\frac{\lambda}{2}\psi_f)G^a_\mu - \frac{1}{4}G^a_{\mu\nu}G^{\mu\nu}_a \tag{2.14}$$

Here, the sum runs over different quarks f and Einstein summation is assumed.

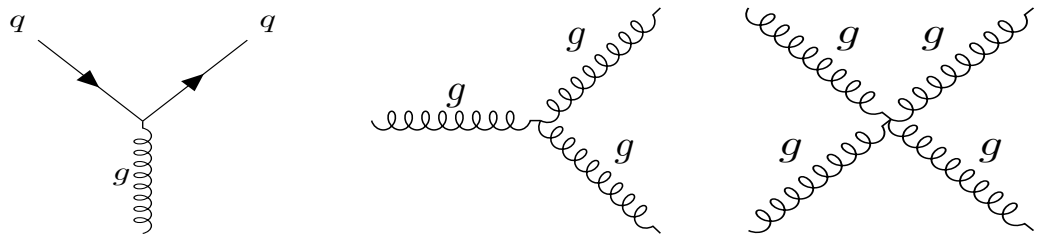

Figure 2.2. QCD interactions.

The evolution of the couplings with energy scale is pivotal for understanding the observed physics at the LHC energies. One of the key concepts is the Renormalization Group (RG) equation, which describes how the coupling constants evolve with the energy scale:

$$\frac{d\alpha(q)}{d\log q} = \beta(\alpha(q)) \tag{2.15}$$

where $\alpha(q)$ is a coupling constant dependent on energy scale q, and β is the renormalization beta function. Equation 2.15 reveals how physical properties morph as the scale of observation changes, allowing the evolution of the system at various energy scales. For QCD, it can be used to explain the strength of the interactions, like the strong force, which is not fixed but varies with the energy scale q. As displayed in Figure 2.3b, the coupling constant of QCD decreases as the energy scale increases, a phenomenon known as *asymptotic freedom*. This behavior is mathematically expressed through the dependence of the coupling constant $\alpha_s(q)$ on the energy scale:

$$\alpha_s(q) = \frac{\alpha_s(q_0)}{1 + \frac{\beta_0 \alpha_s(q_0)}{2\pi} \log\left(\frac{q^2}{q_0^2}\right)}$$

where q_0 is a reference scale, $\alpha_s(q_0)$ is the coupling strength at this scale, and β_0 is a constant derived from a one loop correction [121, 163]. One direct consequence is in the

simulation of the QCD process, as the higher-order corrections can be non-negligible. In those cases, contributions from diagrams from higher-order corrections make the predictions more precise.

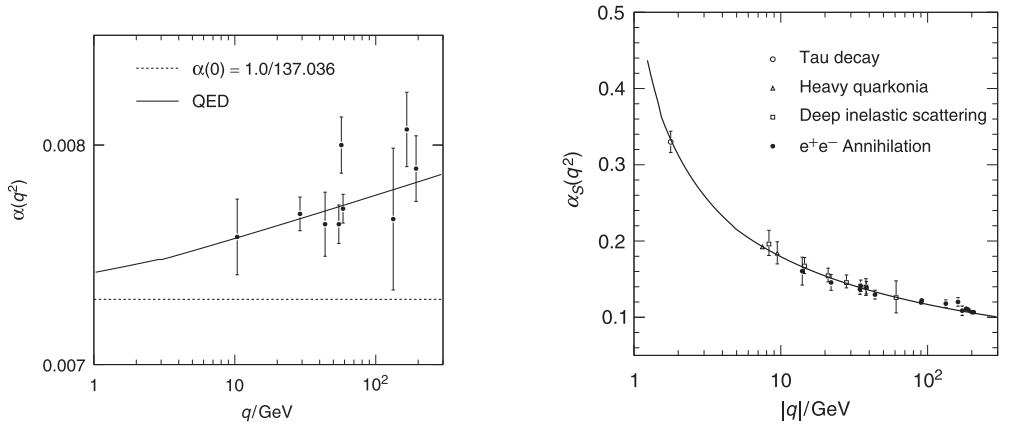

(a) α at different energy ($|q|$) scales (b) α_s at different energy ($|q|$) scales

Figure 2.3. Coupling constants for QED (left) and QCD (right) at different energy scales. Figure from [184]

Another critical property of QCD is *confinement*, which says that the color-charged particles (such as quarks) cannot be isolated and must instead form color-neutral bound states known as hadrons or masons. Confinement relates to the running coupling constant at low energy scales. As the energy scale decreases, the coupling constant $\alpha_s(q)$ increases, leading to a stronger interaction. The precise mathematical description of confinement remains a challenge in theoretical physics, but one direct consequence of these properties is the formation of jets in particle detectors. When high-energy protons collide in LHC, the quarks and gluons can be violently ejected from the hadrons. Due to confinement,

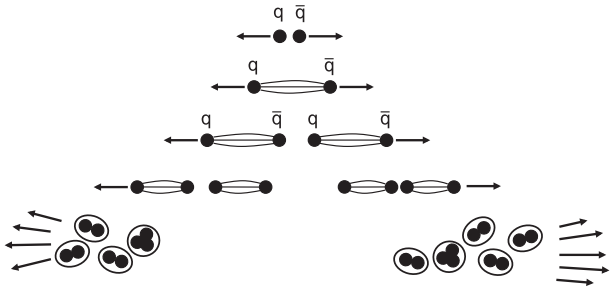

Figure 2.4. Formation of hadrons from quarks. Figure adapted from [184]

as these quarks and gluons begin to separate, the strong force between them does not diminish, unlike electromagnetic or gravitational forces. As the separation increases, the energy in the gluon field between two color charges increases, eventually creating new quark-antiquark pairs when the energy is sufficient. This process, known as hadronization, results in a cascade of hadron formation, which typically occurs along the original direction of the quark or gluon. This cascade manifests as a jet, a highly collimated stream of hadrons, as shown in Figure 2.4 and 4.8.

2.1.2.3 Weak interactions and Electroweak unification

The weak interaction (WI) is one of the four fundamental forces of nature observed in processes like the β decay ($n \rightarrow p + e^- + \bar{\nu_e}$). It is extremely short-range and can transform one type of quark into another (e.g., $u \rightarrow d$). Observations of parity violation in the β decay of ^{60}Co showed these interactions to be described by a $V - A$ structure where the charged current interactions are observed to involve only the LH fermions (and RH anti-fermions); however, the neutral current involves both LH and RH fermions.

Electroweak unification, realized by the Glashow-Weinberg-Salam model, combines

the electromagnetic and weak forces into a single framework in the gauge group

$$SU(2)_L \times U(1)_Y \tag{2.16}$$

encompassing weak isospin (I) and hypercharge (Y). The L in $SU(2)_L$ stands for "Left", indicating that this symmetry group acts only on left-handed fermions and is associated with a quantum number known as weak isospin, I. The $U(1)_Y$ is added to incorporate the electromagnetic interactions with the generator Y, the hypercharge.

The generators of $U(1)_{EM}$ and $U(1)_Y$ are related by the Gell-Mann-Nishijima relation

$$Q = I_3 + \frac{Y}{2} \tag{2.17}$$

The electroweak Lagrangian, $\mathcal{L}_{\text{EW}}$ is formed as:

$$\mathcal{L}_{\text{EW}} = \mathcal{L}_{\text{gauge}} + \mathcal{L}_{\text{fermion}} + \mathcal{L}_{\text{Higgs}} + \mathcal{L}_{\text{Yukawa}}$$

- **Gauge Term:**

$$\mathcal{L}_{\text{gauge}} = -\frac{1}{4} W^a_{\mu\nu} W^{a\mu\nu} - \frac{1}{4} B_{\mu\nu} B^{\mu\nu}$$

where $W^a_{\mu\nu}$ and $B_{\mu\nu}$ are the field strength tensors for $SU(2)_L$ and $U(1)_Y$, respectively:

$$\begin{aligned} B_{\mu\nu} &= \partial_\mu B_\nu - \partial_\nu B_\mu \\ W^i_{\mu\nu} &= \partial_\mu W^i_\nu - \partial_\nu W^i_\mu + g_W \varepsilon^{abc} W^j_\mu W^k_\nu \quad \text{where } a = 1, 2, 3 \end{aligned} \tag{2.18}$$

- **Fermion Term:**

$$\mathcal{L}_{\text{fermion}} = \overline{\psi}_L i\gamma^\mu D_{\mu,L} \psi_L + \overline{\psi}_R i\gamma^\mu D_{\mu,R} \psi_R$$

where ψ_L and ψ_R are left-handed and right-handed fermion fields, and $D_{\mu,L}$, $D_{\mu,L}$ are the covariant derivatives:

$$\begin{aligned} D_{\mu,L} = &\quad \left[\partial_\mu - ig_W \frac{\sigma_i}{2} W^i_\mu(x) - ig_Y \frac{Y}{2} B_\mu(x)\right] \\ D_{\mu,R} = &\quad \left[\partial_\mu - ig_Y \frac{Y}{2} B_\mu(x)\right]. \end{aligned} \tag{2.19}$$

The electroweak symmetry breaking, facilitated by the Higgs field acquiring a nonzero vacuum expectation value, differentiates the electromagnetic from weak forces. Mass terms for the fermions and the massive weak bosons cannot be directly added to preserve the local gauge invariance of the SM Lagrangian. Instead, masses for these particles are dynamically generated via the Higgs mechanism.

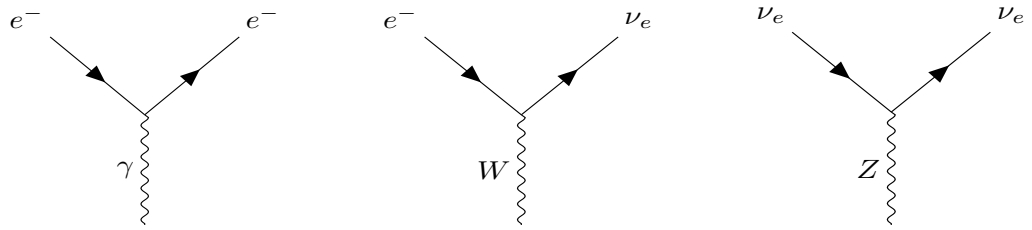

(a) Electron photon vertex (b) W boson vertex (c) Z boson vertex

Figure 2.5. Feynman diagrams for electromagnetic and weak interactions.

Spontaneous Symmetry Breaking and The Higgs boson

The Brout-Englert-Higgs mechanism introduces a complex scalar field that transforms as a doublet under the $SU(2)_L$ gauge transformation and has a hypercharge $Y = +1$.

- **Higgs Term:** The Lagrangian for the scalar Higgs field is

$$\mathcal{L}_{\text{Higgs}} = (D_\mu\phi)^\dagger(D^\mu\phi) - V(\phi) = (D_\mu\phi)^\dagger(D^\mu\phi) - \mu^2(\phi^\dagger\phi) - \lambda(\phi^\dagger\phi)^2 \tag{2.20}$$

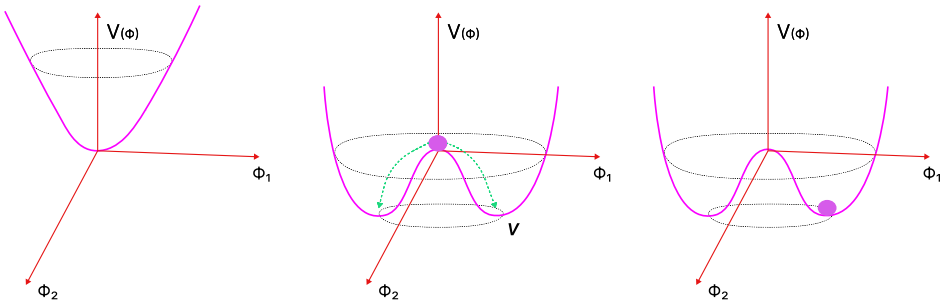

Figure 2.6. Left: Scalar potential with $\mu^2 > 0$ which has a stable minimum. Middle: Scalar potential with $\mu^2 < 0$, degenerate vacuum states, and unbroken state symmetry. Right: Scalar potential with $\mu^2 < 0$, degenerate vacuum states and broken state symmetry

The Higgs field, Φ, is a complex doublet representing two complex fields, given by:

$$\phi = \begin{pmatrix} \phi^+ \\ \phi^0 \end{pmatrix} = \frac{1}{\sqrt{2}} \begin{pmatrix} \phi_1 + i\phi_2 \\ \phi_3 + i\phi_4 \end{pmatrix} \quad . \tag{2.21}$$

where ϕ^+ is a charged component and ϕ^0 is neutral. The Higgs potential $V(\Phi)$ has the form of a Mexican hat:

$$V(\Phi) = \mu^2 \Phi^\dagger \Phi + \lambda (\Phi^\dagger \Phi)^2$$

with $\mu^2 < 0$ and $\lambda > 0$ to ensure the stability of the potential with the value of the field at the minimum given by

$$\phi^\dagger \phi = \frac{\mu^2}{2\lambda} = \frac{v^2}{2}, \tag{2.22}$$

where v is the radius of the circle of the minima of the potential $V(\phi)$. Spontaneous Symmetry breaking (SSB) occurs when the Higgs field acquires a non-zero vacuum expectation value (VEV), Figure 2.6. There are many possible solutions for ϕ that would satisfy the minimum, and without any loss of generality, we can choose $\phi_1 = \phi_2 = \phi_3 = 0$, leading to

$$\langle \Phi \rangle = \frac{1}{\sqrt{2}} \begin{pmatrix} 0 \\ v \end{pmatrix}$$

with $v = \sqrt{-\mu^2/\lambda} \approx 246$ GeV, which minimizes the potential. The selection of a particular minimum breaks the symmetry of the state, and since it breaks the electroweak symmetry, this is known as the electroweak symmetry breaking (EWSB). Understanding the consequences of EWSB involves the study of the Higgs field under small perturbations $(h(x))$ around its minimum as

$$\Phi(x) = \frac{1}{\sqrt{2}} \begin{pmatrix} 0 \\ v + h(x) \end{pmatrix},$$

Here, $h(x)$ represents excitations of the Higgs field, which represents the physical Higgs boson with mass, and the masses for the W and Z bosons are generated via the kinetic term of the $\mathcal{L}_{\text{Higgs}}$ where the covariant derivatives couple the Higgs field to the gauge bosons.

$$\begin{aligned} \mathscr{L}_{\text{Higgs}} =& \frac{g_W^2 v^2}{4} W_\mu^+ W^{-,\mu} + \frac{g_W^2 v}{2} h W_\mu^+ W^{-,\mu} + \frac{g_W^2}{4} h h W_\mu^+ W^{-,\mu} \\ & \frac{(g_W^2 + g_Y^2) v^2}{8} Z_\mu Z^\mu + \frac{(g_W^2 + g_Y^2) v}{4} h Z_\mu Z^\mu + \frac{(g_W^2 + g_Y^2)}{8} h h Z_\mu Z^\mu. \end{aligned} \tag{2.23}$$

The first terms in both lines of the R.H.S. of Equation 2.23, with the fields $W_\mu^+ W^{-,\mu}$ and $Z_\mu Z^\mu$ are identified as the mass terms

$$m_W^2 = \frac{g_W^2 v^2}{4} \text{ and } m_Z^2 = \frac{(g_W^2 + g_Y^2) v^2}{4}. \tag{2.24}$$

The terms like $h W_\mu^+ W^{-,\mu}$, $h Z_\mu Z^\mu$ and in the R.H.S. of Equation 2.23 are the coupling between a pair of either W or Z with the Higgs boson results in generating the masses

of the vector bosons. The last terms $hhW_\mu^+W^{-,\mu}$ and $hhZ_\mu Z^\mu$ in the R.H.S. represents the coupling between two Higgs bosons and two vector bosons. One important point in Equation 2.23 has no photon-related mass term exists. The physical observable states of the gauge bosons, masses of the bosons, and the weak mixing angle θ_w are given as:

$$\begin{aligned} Z_\mu = &\quad cos\theta_w W_\mu^3 - sin\theta_w B_\mu \quad \text{with} \quad m_Z = \frac{1}{2}\nu\sqrt{g_W^2 + g_Y^2} \\ W_\mu^\pm = &\quad \frac{1}{\sqrt{2}}(W_\mu^1 \pm iW_\mu^2) \quad \text{with} \quad m_{W^\pm} = \frac{1}{2}\nu g_W \\ A_\mu = &\quad sin\theta_w W_\mu^3 + cos\theta_w B_\mu \quad \text{with} \quad m_A = 0 \\ m_h = &\quad \sqrt{2}\mu \quad \text{and} \quad cos\theta_w = \frac{g_W}{\sqrt{g_W^2 + g_Y^2}} = \frac{m_W}{m_Z}. \end{aligned} \tag{2.25}$$

- **Yukawa Term:** In addition to providing masses to the heavy bosons in the SM, the Higgs mechanism also gives rise to the masses of the fermions via the Yukawa coupling y_f as:

$$\mathcal{L}_{\text{Yukawa}} = \sum_f -\frac{y_f v}{\sqrt{2}}\bar{\psi}_f\psi_f - \frac{y_f}{\sqrt{2}}\bar{\psi}_f\psi_f h. \tag{2.26}$$

  These couplings can be parameterized with the observed masses of the fermions as

$$y_f = \sqrt{2}\frac{m_f}{v}$$

Quark Mixing/CKM matrix

An additional matrix in the quark sector is needed to account for the differences between the flavor-eigenstate and the mass-eigenstate bases. The transformation from mass eigenstate basis is achieved using the *Cabbibo-Kobayashi-Maskawa (CKM) matrix.*

$$V_{CKM} = \begin{pmatrix} V_{ud} & V_{cd} & V_{td} \\ V_{us} & V_{cs} & V_{ts} \\ V_{ub} & V_{cb} & V_{tb} \end{pmatrix} \approx \begin{pmatrix} 0.974 & 0.225 & 0.003 \\ 0.225 & 0.973 & 0.041 \\ 0.009 & 0.040 & 0.999 \end{pmatrix} \tag{2.27}$$

here V_{ij} represents the probability of quark i to transform into j via weak interactions. The CKM matrix is almost diagonal, meaning the transition between quarks of the same generations is preferred in charged current interactions, e.g., $u \to d$, but $u \to s$ is possible at lower rates; mixing between first and third generations being very small.

The Higgs mechanism completes the current formulation of the SM of particle physics, though it still has several free parameters that are not predicted and require measurements. Precision measurement of these free parameters is currently one of the main goals of particle physics. These free parameters are:

- The masses of the quarks and leptons (9).
- The coupling strengths (3).
- The CKM matrix can be parameterized in terms of 3 mixing angles and 1 complex phase (4).
- The Higgs boson's mass and the Higgs field's vacuum expectation value (2).
- The CP violating terms of QCD Lagrangian a.k.a, θ-vaccua (1).
- Masses of the Weakly interacting bosons, W and Z (3).

2.1.3 Limitations of the SM

The Standard Model (SM) has been a highly successful theory, as evidenced by various measurements of SM; Figure 2.7 shows the total production cross-sections pre-

dicted and measured. However, despite its many successes, the SM still needs to address several unanswered questions summarized in this section.

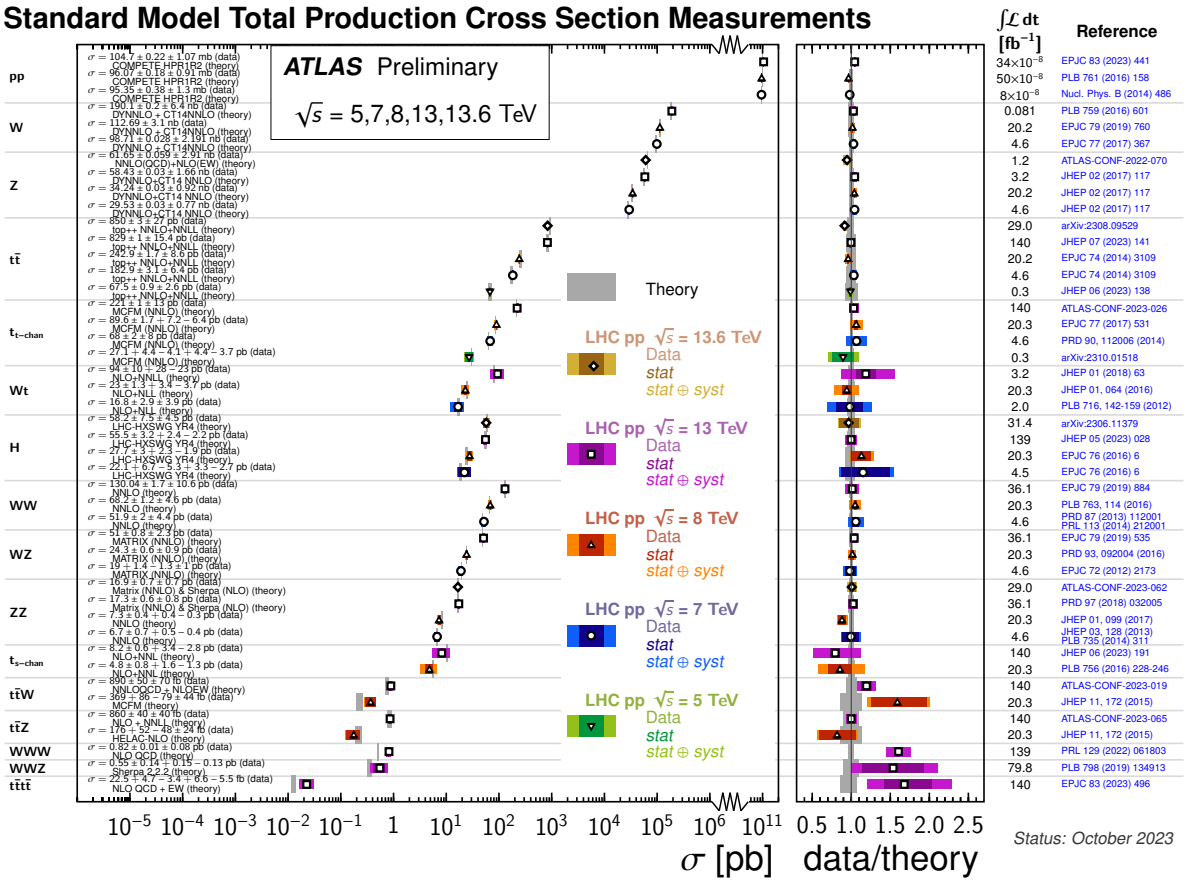

Figure 2.7. Summary of several SM total production cross-section measurements showing no significant deviation from the SM predictions. [178]

Vacuum stability / Higgs potential

In SM, the value of μ can be arbitrary, and the value of $\lambda > 0$ is restricted by the requirements of vacuum stability. It does not fix the shape of the scalar potential, as any even polynomial in $\phi^\dagger\phi$ fulfills the symmetry requirements. This raises the question of

whether the vacuum state we observe is a local minimum or a global minimum. Efforts are being made to better understand the Higgs potential by analyzing the quadratic and trilinear Higgs coupling.

Quantum theory of gravity

While a powerful tool for understanding the universe, the SM does not provide an Ultraviolet (UV) complete description of gravitation at the quantum level. The space-time structure of the macroscopic theory of general relativity suggests that its force carrier, the graviton, must be a spin-two particle. However, attempts to quantize the theory lead to issues with renormalisability since an infinite number of counterterms would be needed to renormalize the theory to all orders. While only becoming relevant at very high energies, this limitation underscores the need for further experimental research and exploration of new theoretical frameworks.

Charge quantization

SM does not explain why the charges only appear as a multiple of 1/3. Charge quantization follows the anomaly cancellation requirements and the representation structure of the gauge groups. However, it does not provide a fundamental reason why the charges should be quantized in the first place, nor does it predict the pattern of these charges.

SM flavor structure

While the CKM matrix describes the quark mixing, the SM does not explain the origin of the flavor structure, including why there are three generations of fermions or

what determines their mass hierarchies and mixing patterns.

Strong CP problem

QCD allows for a term in the Lagrangian, which violates CP symmetry, related to the QCD vacuum topology and is proportional to the theta (θ) parameter as

$$\mathcal{L}_{\text{QCD}} = \mathcal{L}^0_{\text{QCD}} + \theta \frac{g_s^2}{32\pi^2} G^a_{\mu\nu} \tilde{G}^{a\mu\nu}, \tag{2.28}$$

where g_s is the strong coupling constant, $G_{\mu\nu}$ is gluon field strength tensor with $\tilde{G}^{\mu\nu}$ as it's dual tensor. The term involving θ can induce CP-violating effects, such as an electric dipole moment for the neutron. However, experiments have shown that if the neutron has an EDM, it is below the current detection threshold, suggesting that any CP violation in the strong force is extremely small. Although a solution to the strong CP problem exists in the Peccei-Quinn theory [158], the Axion particle predicted by this theory has not been observed.

Neutrino masses

Right-handed neutrinos are not part of the SM; they, therefore, have no mechanism to generate neutrino masses. However, it is known from experimental observations of neutrino oscillations that neutrinos have small masses. Direct measurements constrain the absolute mass scale of neutrinos to be < 1.1 eV at 90% CL. Mass terms for neutrinos can be added if the SM is treated as an effective field theory. However, since it is still being determined whether neutrinos are Majorana or Dirac particles, it is unclear which terms to add.

Dark matter

Various experiments have shown that only about 5% of the universe's energy density comprises ordinary matter, while approximately 27% is "Dark Matter (DM)". Although the nature of DM is still unknown, one of the leading hypotheses suggests that DM candidates could be Weakly Interacting Massive Particles (WIMPs). However, the particle nature of the DM candidates has not yet been experimentally verified, and the Standard Model (SM) does not predict any likely DM candidates.

Dark Energy

Cosmological and astrophysical observations have shown that the universe's expansion is accelerating. One possible explanation for this phenomenon is the presence of a mysterious energy called dark energy (DE), which counteracts the gravitational pull. However, the Standard Model (SM) does not explain the universe's accelerating expansion.

Matter-antimatter asymmetry

The Standard Model (SM) of particle physics puts matter and anti-matter on nearly the same footing. This questions whether there is a balance between the amount of matter and anti-matter in the universe. Absence of very large γ-ray bursts, observations from the astrophysical and cosmic ray measurements [52] show more matter flux

$$\frac{\bar{p}}{p} \sim 10^{-4}$$

Big-Bang nucleosynthesis calculations and the study of Cosmic-Microwave-Background show that regular matter makes up about 5% of the total energy density of the universe

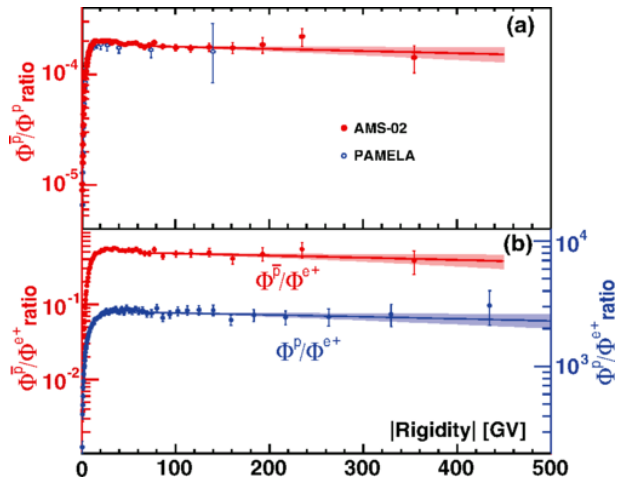

Figure 2.8. The top part of the figure shows the measured proton anti-proton flux ratio as a function of the absolute value of the rigidity from 1 to 450 GV, as measured by the AMS-02 and PAMELA detector [7]

[174], and consists nearly entirely of matter. Baryons dominate this excess of matter; thus, the excess of matter over anti-matter is often called Baryon Asymmetry of the Universe (BAU).

Baryogenesis refers to the process by which the excess of matter over anti-matter was generated during the early stages of the universe's evolution. Sakharov [168] postulated three conditions that could explain the significant excess of baryons in the early universe.

- Violation of Baryon Number (B-Violation)
- Violation of Charge and Charge-Parity (C, CP Violation)
- Loss of thermal equilibrium

Electroweak Baryogenesis (EWBG) is a mechanism to create baryon asym-

metry during electroweak phase transition [147]. If the phase transition is strongly first order, it proceeds through the nucleation of bubbles with a broken phase within a surrounding symmetric phase. These bubbles merge, expand, and collide until they cover the entire universe.

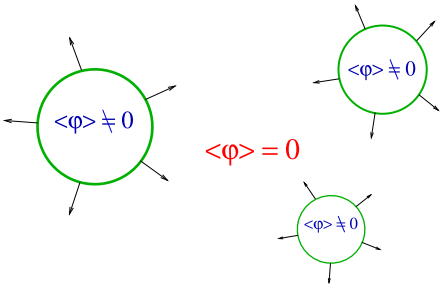

(a) A schematic showing how the bubbles with a broken phase expand in the medium of an unbroken phase.

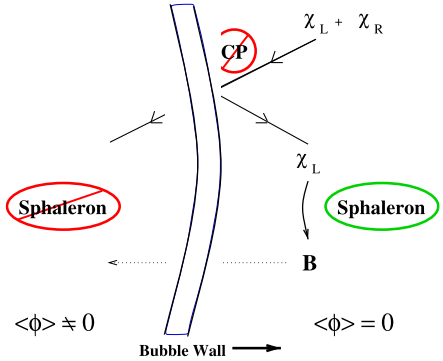

(b) The bubble wall moving from left to right separates the broken(left, $< \phi > \neq 0$) and unbroken phase(right,$< \phi >= 0$). Fermions scatter off the walls with CP violation biasing the sphaleron transitions

Figure 2.9. A schematic diagram for EWB. [155]

The first-order phase transition also provides a significant departure from the thermal equilibrium. Baryon creation in EWBG happens in the vicinity of the bubble walls. Particles scattering off the bubble walls with C and CP Violation generate a net chiral asymmetry, which biases the sphaleron[2] transitions to create more baryons than anti-baryons outside the bubble. These baryons are then engulfed in the interior of the ex-

[2]Sphalerons are the static solutions to the electroweak field equations.

panding bubble, where they are stable. Figure 2.9 gives a visualization of the process.

The nature of electroweak phase transition in SM for a 125 GeV Higgs boson does not have a departure from thermal equilibrium. However, models like 2HDM provide tools for making the phase transition first order while allowing for the possibilities of CP Violation and sphaleron processes. In the 2HDM models, the scenario $m_A \neq m_H$ is particularly compelling, with $m_A > m_H$ being favored for a strong first-order phase transition in the early universe [102].

2.1.4 Two-Higgs doublet model

Multiple extensions of the SM have been developed to provide solutions to the incompleteness of the SM, generally focusing on the BSM theories. One of the simplest extensions is the Two-Higgs doublet model (2HDM), with two Higgs doublets instead of one, which does not change the relative strength of charged and neutral couplings. This parameter, ρ, can also be calculated generally for the $SU(2) \times U(1)$ gauge theory, if there are n scalar multiplets ϕ_i, with weak isospin I_i, weak hypercharge Y_i, and vacuum expectation value (VEV) of the neutral components v_i, then the parameter ρ is, at tree level

$$\rho = \frac{\sum_{i=1}^{n} \left[I_i \left(I_i + 1 \right) - \frac{1}{4} Y_i^2 \right] v_i}{\sum_{i=1}^{n} \frac{1}{2} Y_i^2 v_i} = \frac{M_W^2}{M_Z^2 cos^2 \theta_w}. \tag{2.29}$$

both SU(2) singlets with $Y = 0$ and SU(2) doublets with $Y = \pm 1$ give $\rho = 1$, since they both have $I \left(I + 1 \right) = \frac{3}{4} Y^2$.

With the additional doublet, the scalar potential becomes more complex and has

more free parameters. The most general scalar potential for two doublets Φ_1 and Φ_2 is written as

$$V = m_{11}^2\,\Phi_1^\dagger\Phi_1 + m_{22}^2\,\Phi_2^\dagger\Phi_2 - m_{12}^2\,\left(\Phi_1^\dagger\Phi_2 + \Phi_2^\dagger\Phi_1\right) + \frac{\lambda_1}{2}\left(\Phi_1^\dagger\Phi_1\right)^2 + \frac{\lambda_2}{2}\left(\Phi_2^\dagger\Phi_2\right)^2$$
$$+$$
$$\lambda_3\,\Phi_1^\dagger\Phi_1\,\Phi_2^\dagger\Phi_2 + \lambda_4\,\Phi_1^\dagger\Phi_2\,\Phi_2^\dagger\Phi_1 + \frac{\lambda_5}{2}\left[\left(\Phi_1^\dagger\Phi_2\right)^2 + \left(\Phi_2^\dagger\Phi_1\right)^2\right], \quad (2.30)$$

where all the parameters are real, and

$$\langle\Phi_1\rangle_0 = \begin{pmatrix} 0 \\ \frac{v_1}{\sqrt{2}} \end{pmatrix}, \quad \langle\Phi_2\rangle_0 = \begin{pmatrix} 0 \\ \frac{v_2}{\sqrt{2}} \end{pmatrix}.$$

With two complex scalar SU(2) doublets, there are eight fields:

$$\Phi_a = \begin{pmatrix} \phi_a^+ \\ \left(v_a + \rho_a + i\eta_a\right)/\sqrt{2} \end{pmatrix}, \quad a = 1, 2.$$

Following the same process as in the SM, we end up with five Higgs. Two CP even (h,H)[3], two Charged ($H^\pm$), and a CP odd Higgs A, with

$$\tan\beta \equiv \frac{v_2}{v_1}.$$

the angle β is the rotation angle that diagonalizes the mass-squared matrices of the charged and pseudoscalar Higgs; The angle α does the same for the neutral scalars. The parameter space includes $\alpha, \beta, v = \sqrt{v_1^2 + v_2^2}, M_H, M_h, M_A, M_{H^\pm}$ and λ_5, which are mainly

[3]Here h is the light (low mass) CP-even neutral Higgs and H is the heavy CP-even neutral Higgs. In the alignment limit the light CP-even neutral higgs corresponds to the SM Higgs of mass 125 GeV.

the masses and the mixing angles. The **alignment limit** corresponds to recovering a CP-even scalar mass eigenstate with the same gauge, Yukawa and self-couplings are at tree level, as those of the SM Higgs bosons.

$$H^{\mathrm{SM}} = h\sin(\alpha-\beta) - H\cos(\alpha-\beta)$$

i.e. $\sin(\alpha-\beta)=1$ In the standard model, diagonalizing the mass matrix simultaneously diagonalizes the Yukawa interactions, resulting in no tree-level FCNCs. However, this is impossible in 2HDMs and is achieved by assuming discrete or continuous symmetry [120, 173]. Based on how the scalar fields (Φ_1, Φ_2) and fermions (u_R^i, d_R^i and e_R^i) couple, there are four types of models as shown in Table 2.1 [54]. The Yukawa couplings of the fermions and the neutral Higgs bosons are shown in Table 2.2.

Model	u_R^i	d_R^i	e_R^i
Type I	Φ_2	Φ_2	Φ_2
Type II	Φ_2	Φ_1	Φ_1
Lepton-specific	Φ_2	Φ_2	Φ_1
Flipped	Φ_2	Φ_1	Φ_2

Table 2.1. Models which lead to natural flavor conservation. The superscript i is a generation index. By convention, the u_R^i always couples to Φ_2.

	Type I	Type II
ξ_h^u	$\cos\alpha/\sin\beta$	$\cos\alpha/\sin\beta$
ξ_h^d	$\cos\alpha/\sin\beta$	$-\sin\alpha/\cos\beta$
ξ_h^ℓ	$\cos\alpha/\sin\beta$	$-\sin\alpha/\cos\beta$
ξ_H^u	$\sin\alpha/\sin\beta$	$\sin\alpha/\sin\beta$
ξ_H^d	$\sin\alpha/\sin\beta$	$\cos\alpha/\cos\beta$
ξ_H^ℓ	$\sin\alpha/\sin\beta$	$\cos\alpha/\cos\beta$
ξ_A^u	$\cot\beta$	$\cot\beta$
ξ_A^d	$-\cot\beta$	$\tan\beta$
ξ_A^ℓ	$-\cot\beta$	$\tan\beta$

Table 2.2. Yukawa couplings of u, d, ℓ to the neutral Higgs bosons h, H, A in the two different models.

2.2 Simulation of physics processes in pp-collision events

This section will discuss the different components used to simulate the proton-proton collisions. Section 2.2.1 describes the fundamentals of hard scattering cross-section calculations, including Matrix element and Parton shower, etc, while Section 2.2.2 goes over the different parts of the numerical software used in the simulation.

2.2.1 Hard scattering cross-section calculation

According to the factorization theorem [91], collisions occur between various proton constituents, known as partons. These can be quarks, gluons, photons, or leptons, although the latter occur much less frequently. The cross-section for a process $pp \to hX$ where h is a hadron and X is any arbitrary particle is given as

$$d\sigma_{pp\to hX} = \sum_{i,j,k} \int_0^1 dx_i \int_0^1 dx_j \int dz_k f_{i/p_1}(x_i, \mu_{\mathrm{F}}^2) f_{j/p_2}(x_j, \mu_{\mathrm{F}}^2) F_k(z_k, \mu_{\mathrm{F}}^2) d\hat{\sigma}_{ij\to hX}(\hat{s}, \mu_F^2, \mu_R^2). \tag{2.31}$$

In equation 2.31, the sum runs over i and j, representing all the partons in the two incoming colliding protons. The $f_{i/p1}(x_i, \mu_F^2)$ and $f_{j/p2}(x_j, \mu_F^2)$ are the *parton distribution functions* (PDF) which quantify the probability of finding a parton inside the proton with momentum fraction $x_{i/j}$ of the protons total z-momentum when probed at an energy scale μ_F, known as the *factorization scale*. The factorization scale μ_F is introduced to regularize the infrared (IR) divergences, which appear in partonic cross-section calculation beyond the leading order (LO). PDFs are non-perturbative functions of energy scale Q extracted from measurements, mostly from deep inelastic scattering, and the DGLAP equation [184] gives their evolution at different energy scales. Example PDFs are shown in Figure 2.10. The $F_k(z_k, \mu_{\mathrm{F}}^2)$ is the parton fragmentation function, which represents the probability that a parton k will hadronize into a particle h carrying a fraction z_k of the parton momentum.

The second part, $d\hat{\sigma}_{ij\to hX}(\hat{s}, \mu_F^2, \mu_R^2)$, is the partonic cross-section obtained from the perturbation theory and is calculated using Feynman diagrams. It depends on the partonic center of mass energy given as $\sqrt{\hat{s}} = \sqrt{sx_1x_2}$, the *renormalization scale* μ_R and the factorization scale μ_F.

2.2.2 Monte Carlo Simulation

The outcome of a collision between the two incoming particles or of the isolated decay of a particle is called an "event" [51]. With the fundamental conservation laws in

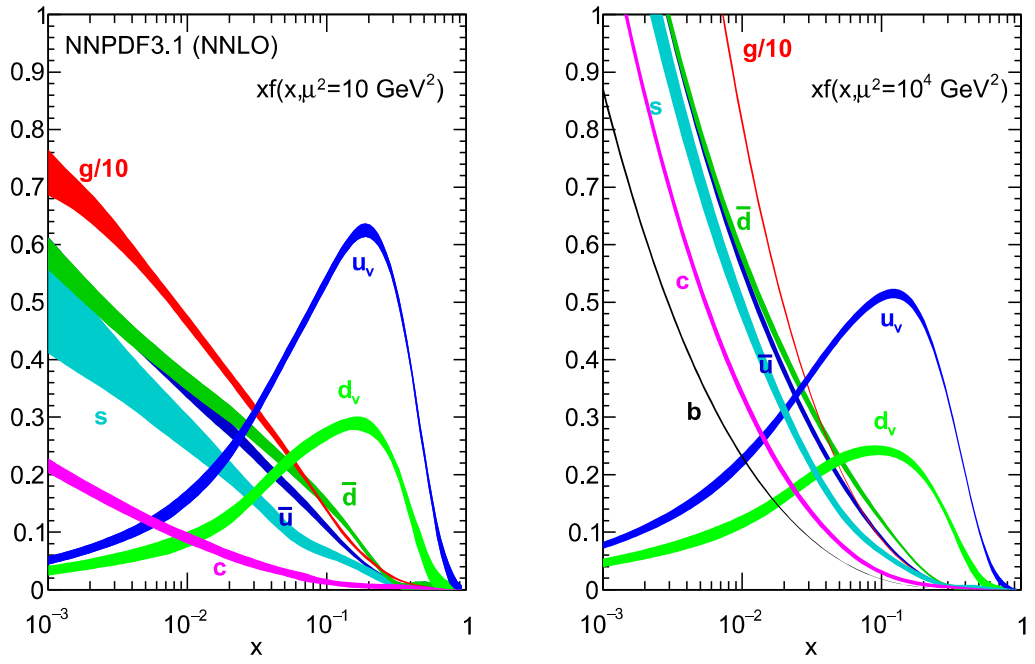

T

Figure 2.10. The parton distribution function from the NNPDF collaboration for two different energy scales μ^2 as a function of x. [42]

place, an event in a p-p collision consists of two incoming particles and several outgoing particles that can be detected via their signatures in the detectors (described in detail in the Chapters 3, 4 and 6). The different kinds of events include *signal events*, representing the specific process or new physics phenomenon being searched for or studied. *Background events* involve the known SM processes that can mimic the signal. Background events are essential for understanding and subtracting the contributions of processes that can produce similar experimental signatures to the signal. *Underlying events* include Initial state radiation (ISR), Final state radiation (FSR), and multi-parton interactions (MPI) that contaminate the primary events of interest. *Pile-up* events are the proton-proton col-

lisions occurring in the same bunch crossing. The final simulations simulate and consider all these relevant event processes that may occur during a p-p collision in the detector.

Given the stochastic nature of the quantum processes, the number of outgoing particles and their properties vary from event to event, giving us probability distributions to be inferred by studying an ensemble of events in data. A theoretically modeled probability distribution that follows SM predictions can be validated by comparing it with data. *Event generators* are numerical packages that generate random sequences of simulated events based on known (SM) or hypothetical laws of nature (BSM hypothesis), making it possible to validate existing physics, conduct sensitivity studies of observables, and explore new physics. Figure 2.11 shows the different components in a simulated $pp \to A \to ZH \to \nu\bar{\nu}b\bar{b}$ process.

The following sections briefly overview the different components of 2.31.

2.2.2.1 Matrix Element

For a fixed-order calculation, the Matrix Element (ME) of a process $ij \to n$ can be expressed using the *Fermi's golden rule* as

$$\hat{\sigma}_{ij\to n}(\mu_F) = \int \mathrm{d}\Phi_n \frac{1}{2\hat{s}} |\mathcal{M}_{ij\to n}(\Phi_n; \mu_F)|^2, \tag{2.32}$$

where $\mathcal{M}_{ij\to n}$ is the matrix element describing the transition $ij \to n$ and Φ_n is the phase-space element of the final state n. The contributions to the matrix element are calculated perturbatively using Feynman diagrams where the dependence on the μ_R and μ_F is introduced to deal with the UV and IR divergences. Since μ_R and μ_F are spurious parameters, the dependence of the observables on the choice of scales reduces as higher

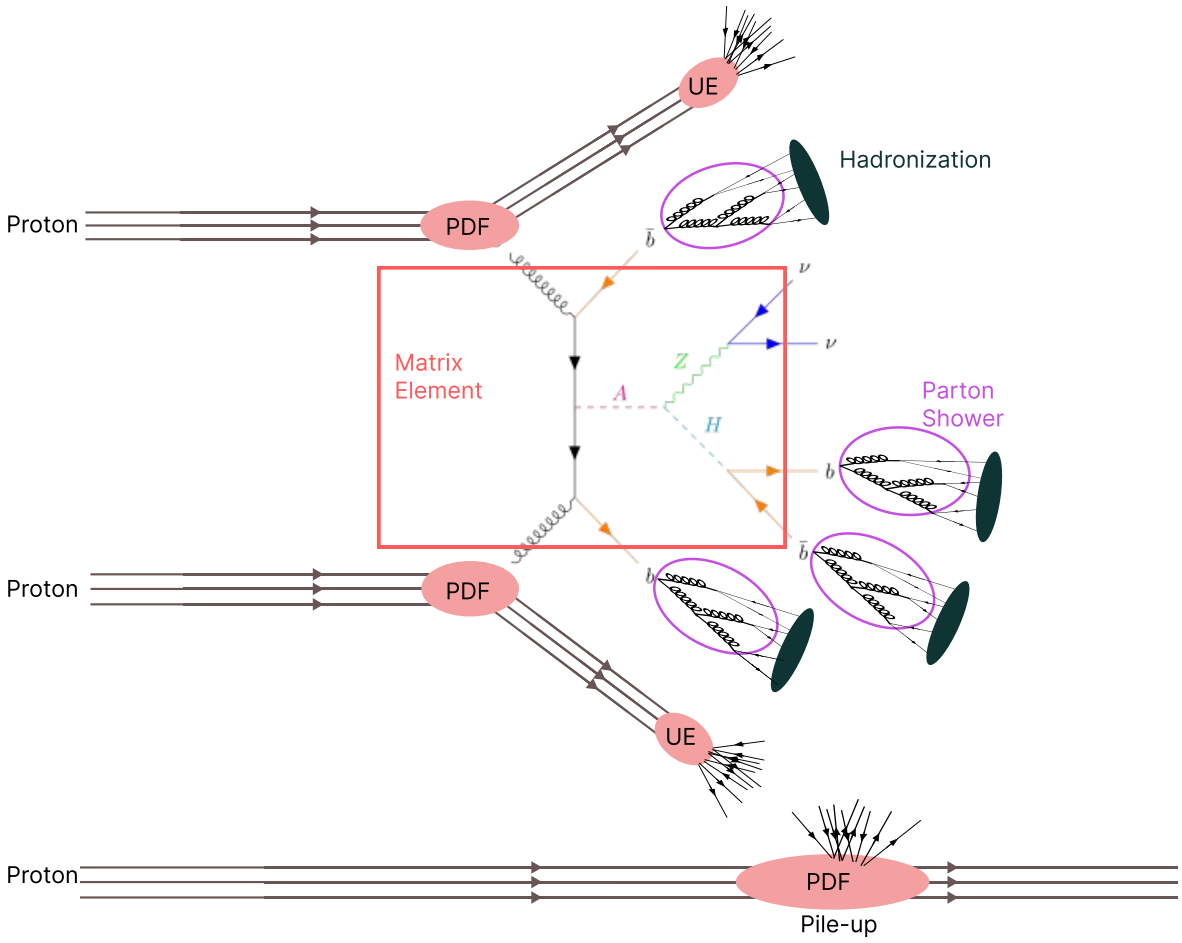

Figure 2.11. Different components of a p-p collision for an $pp \to AZH \to \nu\bar{\nu}b\bar{b}$ event.

orders of the perturbative series are considered. A common choice for the scales is to use $\mu_F^2 = \mu_R^2 = Q^2$ with Q being the energy scale of the process. The impact of the choice of μ_R and μ_F is usually studied where the nominal choice is compared against the double or half of the scale used in simulations and is considered a source of modeling uncertainty.

Multipurpose event generators like Pythia [51], Sherpa [171], Herwig++ [41] can be used for LO calculations of matrix elements. Dedicated matrix element generators like MadGraph5_aMC@NLO [11] can be used for full tree-level calculations for a fixed

number of partons.

2.2.2.2 Parton Shower

The divergences limit the fixed-order calculations where the final states are infrared and collinear-safe. Given that the physics we measure by the detectors in the experiments are not limited to fixed orders, an all-order approach is used in simulation using *parton shower* algorithms. The details of the algorithm are given in [59]. The shower produces detector-stable particles by hadronization, which are used for studies in physics analyses.

Some of the commonly used parton showering generators are Pythia [51], Sherpa [171], Herwig++ [41]. Comparing different generators for parton showering can be used to evaluate uncertainties in the observables from the showering algorithms. A complete event simulation includes combining the generation of matrix elements and showering. Several strategies have been developed to remove the overlapping phase space, which can be roughly classified into two groups: matching and merging approaches.

2.2.2.3 Detector Simulation

The detector effects on the MC samples are included to produce a detector response to the simulated events. This includes particle interactions with the materials as they traverse the magnetic field. The commonly used detector simulation by the ATLAS collaboration are GEANT4 toolkit [6] or a comparatively faster simulation called ATLFAST-II [87].

These simulation techniques set up the basics of the MC samples used in the thesis, with further details provided in Chapter 5.

2.3 Statistical analysis

The MC samples and the real data from the ATLAS experiment undergo identical reconstruction chains (discussed in detail in the following chapters). These can be used for statistical analysis and hypothesis testing to empirically verify the new physics and develop a qualitative and quantitative measure of discovery or rejection. The following section will give a short overview of hypothesis testing and some of the methods used in particle physics. This lays the premise of later analysis results, which give an overview of the likelihood function and the need for different kinematic regions in physics analysis. In the case of the 2HDM model, the events from the process $A \to ZH$ to $\ell\ell t\bar{t}$ or $\nu\bar{\nu}b\bar{b}$ are called signal events, all the remaining events known to have originated from processes other than these two are background events. Theoretically, the expected signal and background events (typically from the SM process) are calculated using the corresponding cross-sections (σ), the observed luminosity ($\mathscr{L}$), and the detector efficiency (ϵ) and geometrical acceptance (A)[4] as:

$$n = \mathscr{L} \cdot \sigma \cdot \epsilon \cdot A. \tag{2.33}$$

In a simple case of a single bin experiment with the expected signal s, background b, the total number of observed events n_{obs} after the measurement can be represented as

$$n_{obs} = \mu \times s + b, \tag{2.34}$$

[4]Geometric acceptance refers to the region of space within the detector where particles can be detected and reconstructed.

where the parameter of interest μ normalizes the s and describes the strength of the signal, further discussed in the Appendix section A.2.1. This helps build two hypotheses: the background only (b) and the $\mu \times s + b$ hypothesis, i.e., a signal strength μ on top of the background. The reliability of the measurement can be tested using the statistical methods of hypothesis testing, explained in the following section.

2.3.1 Hypothesis testing

In hypothesis testing, one starts by constructing hypotheses that could describe the observation from the detector. The null hypothesis, H_0, typically represents a known model for the observation. In particle physics searches, the null hypothesis only represents the known physics or standard model background (b) hypothesis. The second would be the alternative hypothesis H_1, representing a model to be tested against the known one. This would be the standard model with the new signal ($\mu \times s + b$ with $\mu = 1$) in particle physics searches.

2.3.1.1 Test statistic and p-value

The observed data is then tested for compatibility with the two hypotheses using a *test statistic* $q_\mu(x)$, which is a function of a measured quantity (x) in the analysis. One of the most common choices for building test statistics is using a binned Likelihood function. A predefined cut on the test statistic, $q_\mu(x)\prime$, is used to conclude the hypothesis test, as shown in Figure 2.12.

Given the probabilistic nature of the test, there is a possibility of errors in accepting and rejecting a hypothesis based on which side of the $q_\mu(x)\prime$ the value of the test statistics

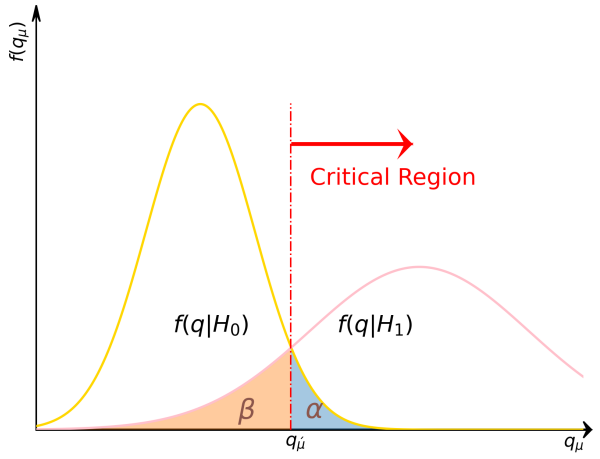

Figure 2.12. A plot showing the test statistic distribution for the two hypotheses.

falls. There are two cases, as given below,

- Accepting alternative hypothesis given the null is true, type-I error. The rate of type-I error is defined as $\alpha = \int_{q_{\mu}\prime}^{\infty} f(q_\mu|H_0)dq$ where $f(q_\mu|H_0)$ is the probability density function of q_μ under the null hypothesis H_0.

- Accepting the null hypothesis given the alternative hypothesis is a true, type-II error. The rate of type-II error is defined as $\beta = \int_{\infty}^{q_{\mu}\prime} f(q_\mu|H_1)dq$ where $f(q_\mu|H_1)$ is the probability density function of q_μ under alternative hypothesis H_1.

To quantify the probability of finding data of greater or equal incompatibility with the prediction of the hypothesis, the p-value parameter is defined as

$$p_\mu = \int_{q_{\mu,obs}}^{\infty} f(q_\mu|\mu)dq_\mu \tag{2.35}$$

where μ represents the signal strength, $q_{\mu,obs}$ is the observed test statistic, and $f(q_\mu|\mu)$

represents the probability density function under the assumed signal strength. The smaller the p-value, the more significant the evidence against H_u, and if the p-value falls below the predefined threshold, H_μ is rejected. A popular term for particle physicists is *significance*, defined as

$$Z = \phi^{-1}(1 - p) \tag{2.36}$$

where ϕ^{-1} is known as the quantile, it represents the inverse of the cumulative distribution of a standard Gaussian (Fig 2.13). This interprets as if the Gaussian distributed variable is Z standard deviations away from the mean; then, the p-value is the upper tail of the distribution. The null hypothesis ($\mu = 0$) is rejected in particle physics (now considered a standard) if the significance level is at least $Z = 5$, corresponding to $p = 2.87 \times 10^{-7}$. The exclusion of a signal hypothesis requires a significance level of at least $Z = 1.64$ equivalent to $p_0 = 0.05$ or a 95% confidence level (also known as CL_b). It is important to note that the signal model will not be studied further once a signal hypothesis is excluded.

2.3.1.2 CL_s construction

In many cases of LHC physics analysis, the H_0 and H_1 are almost indistinguishable in specific kinematic ranges, meaning that the expected signal is shallow. It may also happen that the number of data events is incompatible (lower than expected) with either of the two hypotheses. This would lead to a low p_1 value; hence, the H_1 would be rejected. Regarding physics analysis, which is not sensitive to the signal model, excluding the H_1 based on its $p - value$ may not be accurate enough. To get a better handle on cases like

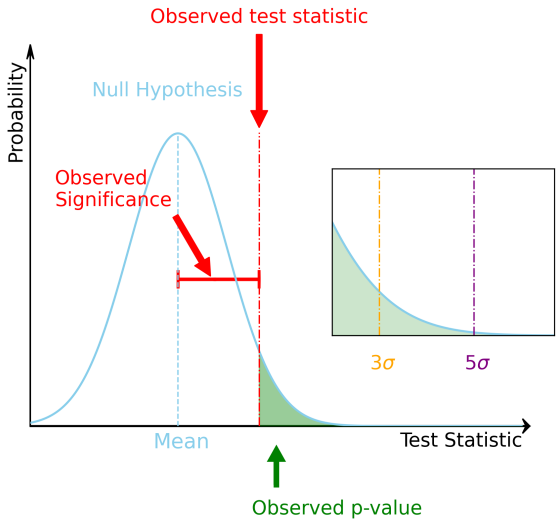

Figure 2.13. A plot showing the significance with a Gaussian.

this it is better to use CL_s or confidence limits defined as

$$CL_s = \frac{p_1}{1 - p_0} \tag{2.37}$$

where p_0 and p_1 are the p-values for the null ($\mu = 0$) and alternative hypothesis ($\mu = 1$) respectively. A downward data fluctuation would lead to higher p_0, resulting in a larger CL_s. A larger value of p_1 means p_0 would be small, leading to a $CL_s \approx p_1$ and $CL_s \approx CL_b$, meaning one cannot reject the alternative hypothesis. At the LHC experiments, for a signal hypothesis to be rejected, the predefined significance level is set at 0.05, also interpreted as 95% CL_s

2.3.1.3 Upper limits

Physics analysis, which searches for a new process or measures the existing SM process, defines parameters of interest (POI), e.g., μ for the $\nu\bar{\nu}b\bar{b}$ process. In those cases,

upper limits are put on the values of the POIs with a predefined CL of a significance level (0.05). This upper limit would represent the largest value of cross-section satisfying the criteria of $CL_s \geq 0.05$ that cannot be excluded.

2.3.1.4 Likelihood function

The likelihood function, which contains all the analysis details in a single equation, is at the core of statistical analysis. Continuing the simple single bin example for understanding purposes with expected signal s, background b, and the total number of observed events n_{obs} and the total number of expected events as n_{exp} where the parameter of interest μ normalizes the s and describes the strength of the signal. The Likelihood ($\mathcal{L}$) is the Poisson probability of the observed and expected event in the region known as *Signal Region* (SR), where high signal purity is expected by design for signal isolation and is given as follows

$$\mathcal{L}(\mu) \equiv \mathbf{P}(n_{obs}|n_{exp}) \equiv \mathbf{P}(n_{obs}|\mu s + b) \tag{2.38}$$

where the symbol $\mathbf{P}$ is used for probability. In reality, the signal and background counting have uncertainties that should be incorporated into the likelihood as:

$$\mathcal{L}(\mu, \boldsymbol{\theta}) \equiv \mathbf{P}(n_{obs}|\mu s(\theta_s) + b(\theta_b)) \tag{2.39}$$

Where $\boldsymbol{\theta} = (\theta_s, \theta_b, b_{total})$ represents the nuisance parameters (NP) corresponding to the uncertainties on signal and backgrounds.

Subsidiary measurements constrain the NPs ($\boldsymbol{\theta}$). One may select a control sample where one expects mainly background events known as **Control Region** (CR), which is included

in the likelihood as:

$$\mathcal{L}(\mu, \boldsymbol{\theta}) \equiv \mathbf{P}(n_{obs}|\mu s(\theta_s) + b(\theta_b))\mathbf{P}(n_{obs;CR}|b(\theta_b)) \tag{2.40}$$

Here $n_{obs;CR}$ represents the observed number of events in the CR. For a multi-bin counting experiment with N bins in SR and M bins in CR with u_k events in the k_{th} bin, the $\mathcal{L}(\mu, \boldsymbol{\theta})$ would be

$$\mathcal{L}(\mu, \boldsymbol{\theta}) = \prod_{i=1}^{N} \frac{(\mu s_i(\theta) + b_i(\theta))^{n_i}}{n_i!} e^{-(\mu s_i(\theta)+b_i(\theta))} \prod_{k=1}^{M} \frac{u_k(\theta)^{m_k}}{m_k!} e^{-u_k(\theta)} \prod_{\theta\in\vec{\theta}} \frac{1}{\sqrt{2\pi}} e^{-\theta^2/2} \tag{2.41}$$

The last term in the product is the Gaussian prior, which is used to constrain the effect of the NPs. These nuisance parameters include the uncertainties from the reconstruction of physics objects, the renormalization scale, algorithm efficiencies, etc.

An additional Poissonian probability term constrains the parameters (γ) corresponding to the statistical uncertainty on the expected background yield in each bin and constrains the statistical uncertainties. An additional term ($\mathcal{L}_{\text{Stat}}$) is multiplied with (2.41)

$$\mathcal{L}_{\text{Stat}}(\vec{\gamma}) = \prod_{i\in\text{bins}} \mathbf{P}\left(\beta_i|\gamma_i\beta_i\right), \quad \beta_i = \frac{1}{\sigma_i^2}, \tag{2.42}$$

here σ_i is the relative MC statistical uncertainty on the total background yield in bin i.

To test the hypothesized value of μ, a profile likelihood ratio is considered

$$\lambda(\mu) = \frac{\mathcal{L}(\mu, \hat{\hat{\boldsymbol{\theta}}})}{\mathcal{L}(\hat{\mu}, \hat{\boldsymbol{\theta}})} \tag{2.43}$$

where $\hat{\hat{\boldsymbol{\theta}}}$ in the numerator represents the value of $\boldsymbol{\theta}$ that maximizes $\mathcal{L}$ for a given

μ. It is also called the conditional Maximum Likelihood Estimator (MLE) of $\boldsymbol{\theta}$. The denominator represents the unconditionally maximized likelihood.

The test statistic associated with the MLE is given as

$$q_\mu = -2 \ln \lambda(\mu). \tag{2.44}$$

A higher test statistic value represents a more outstanding incompatibility between the data and the test hypothesis.

CHAPTER 3

ATLAS EXPERIMENT AT THE LARGE HADRON COLLIDER

The Large Hadron Collider (LHC) [58] at CERN, the European Organisation of Nuclear Research, is the world's largest accelerator located in Geneva at the border of France and Switzerland. The protons (p), or heavy ions, accelerated to unprecedented high energies from the LHC that are made to collide in the complex detectors, making it feasible to study the interactions taking place by studying their decay products from the head-on collisions. The "**A** **T**oroidal **L**HC **A**pparatu**S**" ATLAS experiment is one of the two general-purpose detectors designed to detect a wide range of physics signatures coming from these particle collisions at the LHC. The data analyzed in this thesis was collected from the ATLAS experiment during the p-p collisions at $\sqrt{13}$ TeV in 2015-2016, also known as the Run 2.

3.1 The Large Hadron Collider

The **Large Hadron Collider** (LHC) is a particle accelerator and collider located in a 26.7 kilometer-long tunnel of the former Large Electron-Positron Collider, situated at depths ranging from 45 to 170 meters underground. The LHC was designed to serve two primary objectives. First, it aims to operate at the highest possible energy level, generating particles with masses up to the TeV scale. Accelerating electrons at such high energies is extremely difficult without significant losses. Hence, protons were chosen over electrons because they lose less energy due to their high mass and synchrotron radiation

during circulation.

Secondly, the LHC aims to operate at an instantaneous luminosity sufficient to observe rare processes within an affordable run-time. Hence, protons collide with protons rather than anti-protons due to the difficulty of creating the latter.

It resembles the LEP and comprises eight arc sectors and eight straight sections. The arc sector houses approximately 1232 dipole magnets with a magnetic field of 8.3 T and is made of niobium-titanium coils. Their primary function is to bend the proton beams of 7 TeV in the closed path. These magnets are cooled to 1.9 K using superfluid helium to achieve superconductivity. Additional magnets, 858 quadrupoles, and around 600 correctors are located along the ring that act on beam characteristics like focusing and corrections of aberrations.

Four of the eight straight sections have beam interaction points where the protons collide. The other four sections comprise utilities for the beam dump, beam cleaning, and superconducting **radio-frequency** (RF) cavities for accelerating the beams. The RF cavities are metallic chambers containing oscillating electric fields at a frequency. At the LHC, the RF cavities are tuned to oscillate at 400 MHz; the ideally timed proton with precisely the right energy will see zero accelerating voltage. Protons with slightly different energies are accelerated or decelerated to stay close to the energy of the ideal energy particle. Before entering the LHC, the beams undergo a series of pre-acceleration processes. The injector chain employed is illustrated in the displayed diagram 3.1.

The initial step to obtaining a continuous proton beam involves ionizing hydrogen gas using the Duoplasmotron. Subsequently, an RF quadrupole focuses and accelerates

the protons to an energy level of 50 MeV before they enter the **linear accelerator** (LINAC 2, which was replaced by LINAC 4 in 2020). The protons are then subjected to a sequence of synchrotrons, each one larger than the previous one, namely the **Proton Synchrotron Booster** (PBS), the **proton synchrotron** (PS), the **Super Proton Synchrotron** (SPS), and finally, the LHC.

The PBS, which comprises four stacked synchrotron rings, accelerates the protons to 1.4 GeV, shapes the beam into batches (also referred to as bunches), and injects it into the PS. The PS increases the beam energy to 25 GeV, after which it is injected into the SPS. Upon exiting the SPS, the proton beam has an energy level of 450 GeV.

At its maximum luminosity of 10^{34} $s^{-1}cm^{-2}$, each proton beam consists of up to 2808 bunches containing approximately 10^{11} protons. These protons circulate in the LHC rings nearly at the speed of light and collide every 25 ns at four interaction points (IP) with a *bunch crossing frequency* of 40 MHz. There is also a non-negligible probability of having multiple proton-proton interactions, called *pile-up*, which occur in a single bunch crossing.

At each collision point, a particle detector records the debris generated. Two general-purpose detectors, **ATLAS** and **CMS**, record the collisions on the opposite sides of the LHC ring. They are designed independently, allowing cross-confirmation of the measurements between the two detectors. The **LHCb** is a forward spectrometer with excellent vertex resolution to measure heavy flavor hadron decay chains. The asymmetric shape is designed to study the B-mesons primarily produced in the forward direction. Optimized to study heavy ion physics, the **ALICE** detector explores very high-density

states, particularly the quark-gluon plasma. In addition to these four main detectors, many smaller experiments are installed around the LHC, such as FASER, which is designed to search for light and extremely weakly interacting particles.

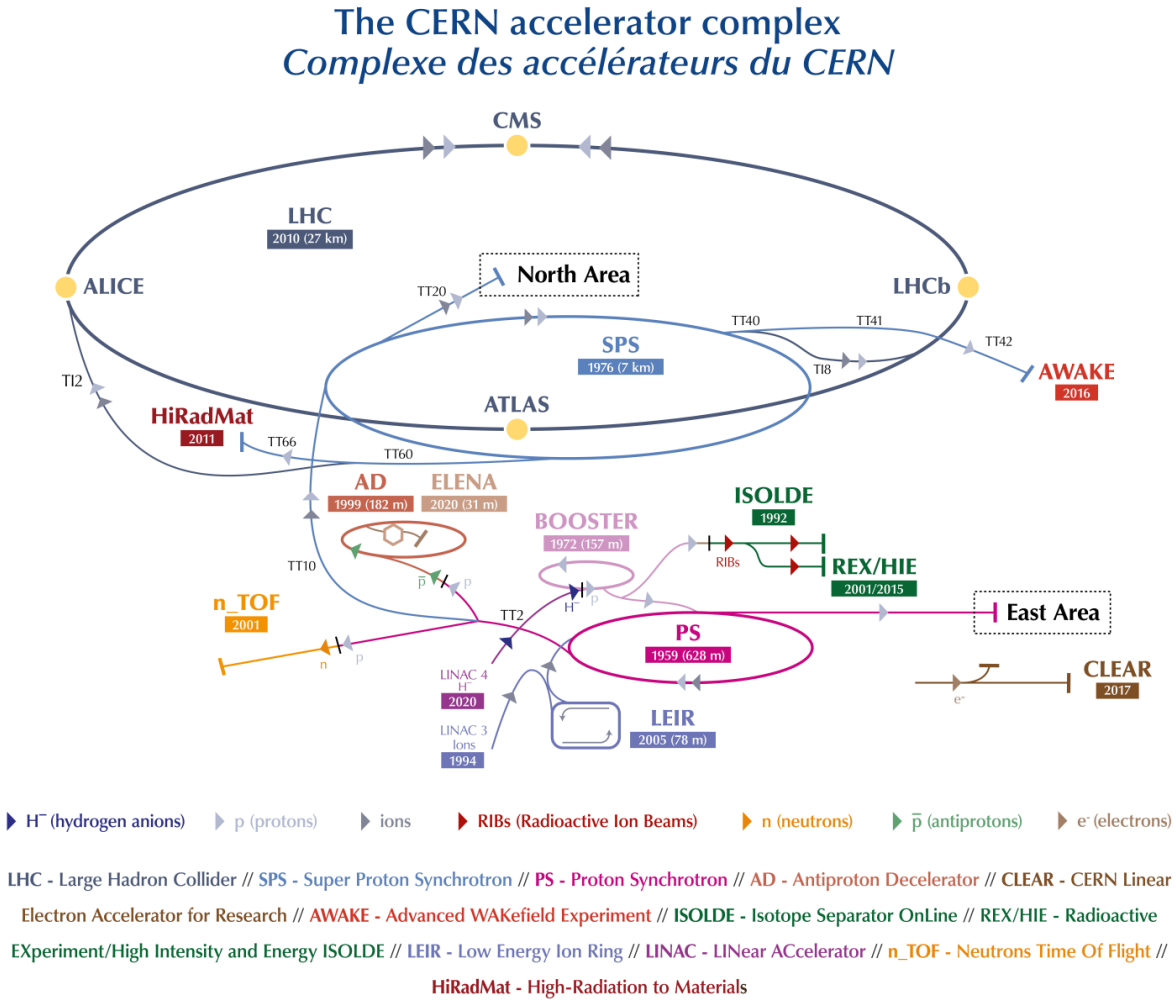

Figure 3.1. LHC accelerator complex [153]

Operation of the LHC is staged into the Runs and Long Shutdown (LS) periods.

Run 1 of LHC went from the spring of 2010 until the end of 2012, recording p-p collisions at the center of mass energies(s) of 7 to 8 TeV. Run 1 followed a long shutdown (LS1) period from 2013 to 2015. Run 2 of LHC occurred between 2015 and 2018, recording the $p-p$ collisions at the same center of mass energy as Run 1. Long Shutdown (LS2) from the end of 2018 to 2022, followed by Run 3, which is currently underway.

3.2 The ATLAS Experiment

The ATLAS (**A** **T**oroidal **L**HC **A**pparatu**S**) detector is a cylindrically symmetrical general-purpose detector built at the IP1 to record the LHC collisions. It comprises barrels and end-caps that cover the entire 4π solid angle, maximizing the detector's acceptance and enabling nearly complete reconstruction of the final state particles. The ATLAS detector, shown in Figure 3.2, has dimensions of 44 m in length and 24 m in height and weighs 7000 tonnes.

3.2.1 Coordinate system used in ATLAS

The ATLAS experiment uses a right-handed Cartesian coordinate system with the Z-axis points along the beam direction, the X-axis points from the interaction point to the center of LHC, and the Y-axis points upward as shown in Figure 3.3. Benefiting from the detector's cylindrical symmetry, we define the azimuthal angle ϕ and radius r in the plane perpendicular to the beam axis.

Another useful quantity used in place of the polar angles is the rapidity y.It is defined using the energy of the particle E and the longitudinal projection of the momentum p_z along the beam axis. Differences in rapidity are a Lorentz boost invariant quantity,

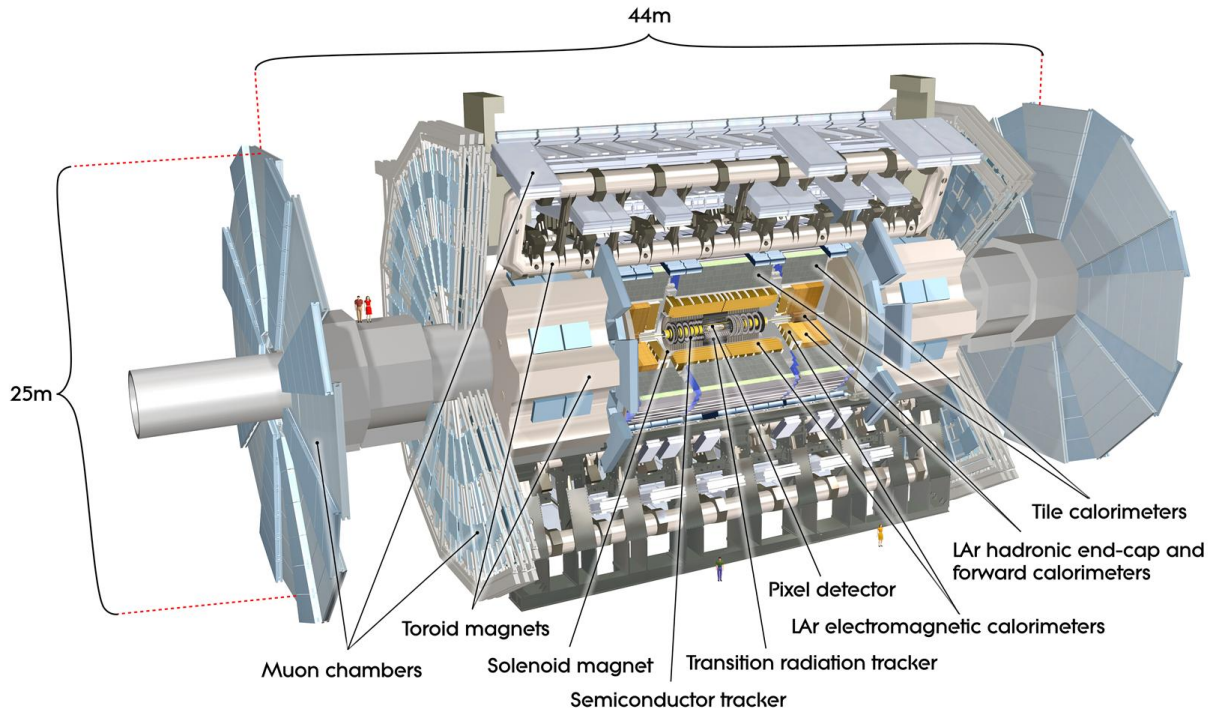

Figure 3.2. The ATLAS Experiment [37]

which can be a crucial handle on the colliding partons with unknown momentum fractions and boost along the beam axis.

$$y = \frac{1}{2} \ln \left(\frac{E + p_z}{E - p_z} \right) \tag{3.1}$$

For ultra-relativistic particles, $p >> m$, pseudorapidity η is an approximate quantity defined by the polar angle θ is generally used.

$$\eta = -\ln \left(\tan \frac{\theta}{2} \right) \tag{3.2}$$

A Lorentz invariant geometric distance ΔR is defined using the azimuthal angle ϕ

and η.

$$\Delta R = \sqrt{\Delta\eta^2 + \Delta\phi^2} \tag{3.3}$$

In the following sections and chapters, quantities like $\eta, \Delta R$, and p_T will appear when describing the detector coverage or event selections[1].

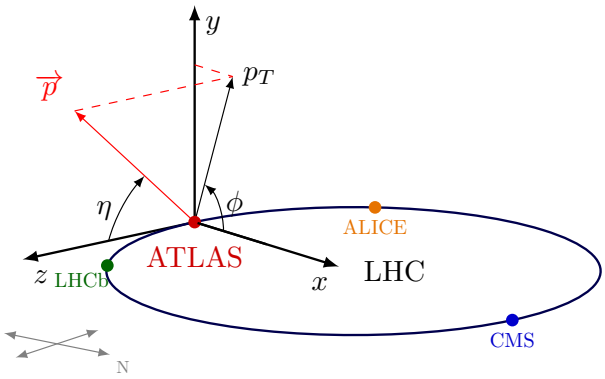

Figure 3.3. Coordinate system used in ATLAS [179]

3.2.2 Magnet system

A combination of magnet systems, as shown in Figure 3.4, is used in the ATLAS experiment to bend the charged particles for momentum measurements. The central

[1]Transverse quantities are often used in ATLAS and will be marked with a subscript T in this thesis as the projection of three vectors on the transverse plane. Transverse momentum p_T is one of particle collisions' most frequently measured values. This quantity is expected to be zero before the particles collide, as resolution effects usually account for the small crossing angle of the beams at the collision point. As a result, the net transverse momentum after the collision is expected to be very close to zero.

solenoid provides a 2 T magnetic field along the z-axis to deflect the charged particles in the ϕ-direction. The toroid magnets bend the particle trajectories in the η-directions. The longer barrel toroid provides a magnetic field of 0.5 T, and the smaller length end-cap toroid generates a resulting field of 1 T.

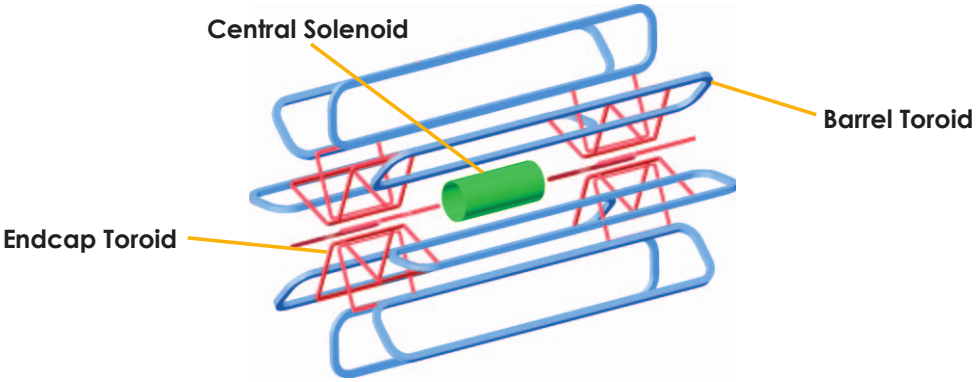

Figure 3.4. A schematic of the magnet system used in ATLAS detector. [37]

Particle Identification in the ATLAS Experiment

The scatter products from the $p-p$ collisions in the ATLAS detector are identified and tracked in the different subdetectors of the ATLAS Experiment. Information from the different subdetectors provides the needed scatters' energy and momentum to reconstruct the physics processes. The inner detector is the innermost part close to the beam pipe and is responsible for tracking and charge identification. Calorimeters are further radially outside the inner detector and are used for particles' energy. In the following subsections, we go through the different sub-detectors of the ATLAS experiment.

3.2.3 Inner Detector

The innermost part of the ATLAS detector closest to the beam pipe is the Inner Detector (ID). The ID covers a region of $|\eta| < 2.5$ and a 3 cm to 1 m radius. Immersed in the superconducting magnets' 2 T axial magnetic field, it aims to track charged particles using information from the subdetector.

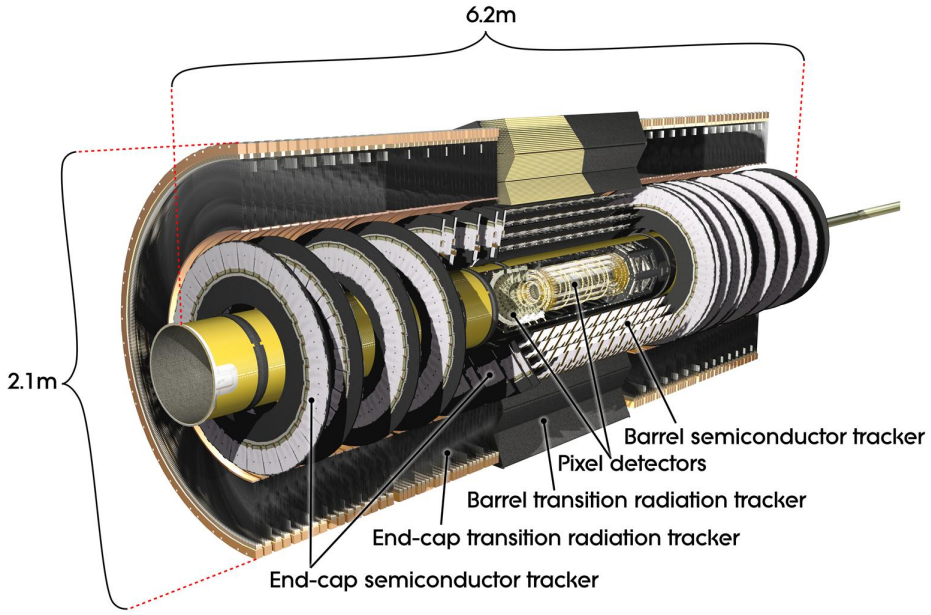

Figure 3.5. A schematic of the ATLAS inner detector and it's different components. Figure adapted from [37].

It comprises three subdetectors: The *Pixel Detector*, the *SemiConductor Tracker* (SCT), and the *Transition Radiation Tracker* (TRT). Particles passing through the Inner detector leave localized energy deposits called hits. These hits are then subsequently used

to trace the path of flight the particle takes, referred to as tracks, explained in more detail in the following chapter. The simplest algebraic formulation of a particle of charge q, mass m, and velocity v in a magnetic field B is:

$$\frac{mv^2}{R} = q(v \times B) \tag{3.4}$$

The knowledge of R from the tracks can be used to infer the particle momentum and the charge. These reconstructed tracks can then form the primary or secondary interaction vertices from the primary interaction, e.g., hadronic decay chains, or secondary/long-lived decays, e.g., K^o. The momentum resolution σ_{p_T} of the ATLAS ID is measured as:

$$\frac{\sigma_{p_T}}{p_T} = 0.05\%\ p_T\ [GeV] \oplus 1\%$$

Figure 3.6 shows a cutaway image of the cylindrically shaped inner detector. A combination of all three subdetectors, the cylinder length of ID is 6.2 m and an outer radius of 2.1 m. The barrel part of the detector is made up of concentric cylinders around the beam axis, and the wheel-shaped endcap part is perpendicular to the beam axis.

Pixel Detector with Insertable B-Layer

The ATLAS ID's innermost part is the silicon pixel detector, which includes four barrel layers and three end-cap disks and comprises 1744 pixel modules with 80 million pixels. The pixel modules contain planer sensors with a pitch of 50×400 μm^2 and a sensor thickness of 250 μm. The innermost layer of the barrel, known as the Insertable B-Layer (IBL) introduced during the long shutdown 1 (LS1), is placed at a distance of 33 mm from the center of the beam pipe and consists of 12 million pixels with a pixel pitch

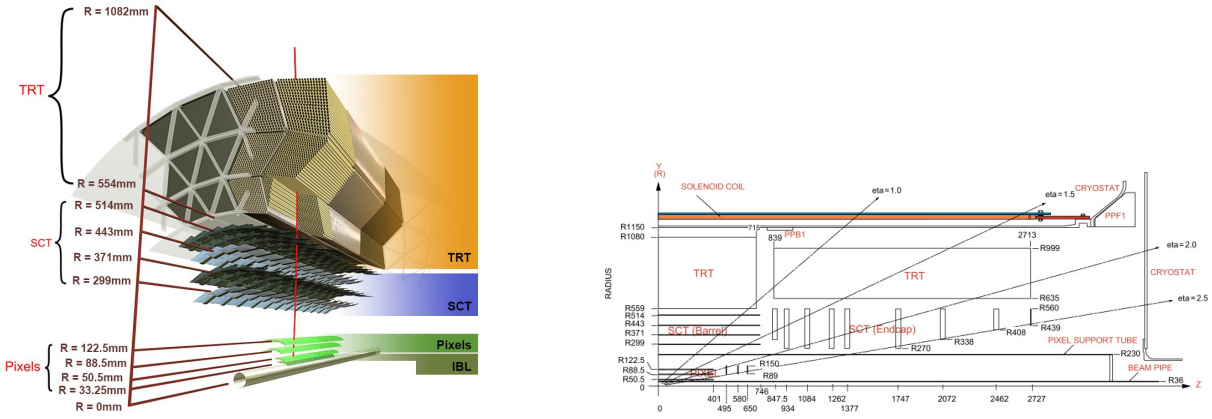

(a) A Sketch of the ATLAS ID components and their radial placements. [37]

(b) A Sketch of the ATLAS ID components and their placements along the z-axis.

Figure 3.6. ATLAS Tracker

of 50×250 μm. Adding IBL provides an extra hit that improves the impact parameter resolution for the low p_{T} particles. It improves the performance of the tracking, secondary vertex reconstruction, and flavor tagging algorithm. On average, a charged particle leaves four hits in the pixel detector, leading to a spatial resolution of 10 μm in the $r - \phi$ plane and 67 μm along the Z-direction.

The Semiconductor Tracker

The semiconductor tracker (SCT) is the radially next layer in the ID system. It consists of silicon micro-strip modules with four concentric barrel layers and two end caps with nine discs. The pitch of the strips on the modules is 80 micrometers, and the thickness is 285 μm. Each module has two back-to-back micro-strip layers rotated by 40 mrad to allow 2D reconstruction. On average, a charged particle leaves eight hits in the pixel detector, giving an intrinsic SCT resolution of 17 μm in the $r - \phi$ plane and 580 μm^2 for the z-direction.

The Transition Radiation Tracker

The Transition Radiation tracker is the outermost part of the ATLAS ID. It is a straw tube tracker with 300 thousand cylindrical drift tubes with a diameter of 4 mm. Each straw was initially planned to be filled with a mixture of Xenon-Co2-O2 in $70\% - 27\% - 3\%$ and has a gold-plated anode wire in the center. It also consists of the barrel region with 72 layers of straw tubes of length 144 running parallel to the beam pipe and the end-cap with 160 layers of 37 cm long straw tubes. The straw tubes are embedded in a matrix of polypropylene fibers, which creates *transition radiation* when a relativistic particle traverses between the interface of two materials. This transition radiation depends on the Lorentz boost $\gamma \simeq E/m$ and can distinguish particles with the same momentum but different masses, e.g., pions from electrons. In Run 2, due to irreplaceable gas leaks, the ATLAS collaboration moved from the xenon-based mixture to a cost-effective Argon-based solution. On average, TRT sees 36 hits from charged particles with an accuracy of 130 μm in the $r - \phi$ ($z - \phi$) planes in the barrel (end-cap).

3.2.4 Calorimeters

After determining the momentum and charge of the particles using trackers, the calorimeters are utilized to measure the energy of the particles by reconstructing the electromagnetic or hadronic showers. As shown in Figure 3.7, ATLAS calorimeters are located outside the superconducting solenoids and consist of an electromagnetic calorimeter (ECAL) and a Hadronic Calorimeter (HCAL). The calorimeters are cylindrically symmetric and cover a range of $|\eta| < 4.9$. ECAL and HCAL are sampling calorimeters containing

multiple alternating active detection layers and passive high-density absorption materials. The particle's total energy is then extrapolated from the signal detected in the active layers during each sampling. The calorimeters are constructed to fully contain the showers, allowing them to identify the particles' energy and prevent particle leakage into the muon spectrometer, the next subdetector system. The calorimeter system consists of the electromagnetic and the hadronic calorimeter.

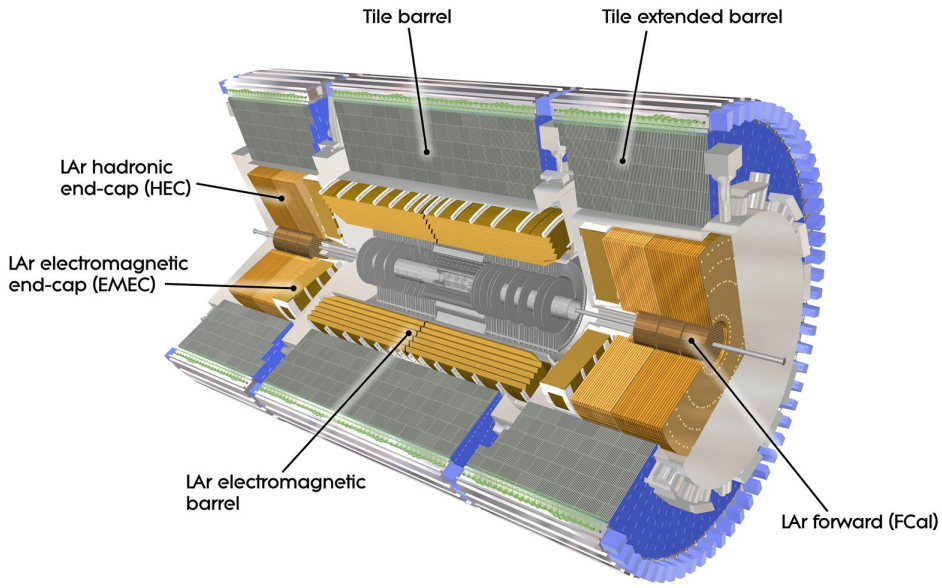

Figure 3.7. A cut-away sketch of the ATLAS calorimeter system. Figure adapted from [159]

3.2.5 The Electromagnetic calorimeter

The Electromagnetic calorimeter (ECAL) measures the energy deposited mainly by electrons, photons, and jet constituents. The two primary processes responsible for

creating showers in the ECAL are the Bremsstrahlung (by the e^+ and e^-) and pair creation (by photons), where the electron, positron, or photons are the sole components of the showers in the ECAL with rare probabilities for the hadrons. The ATLAS ECAL is an accordion-shaped sampling calorimeter using liquid Argon (cooled at 88.5K) with Kapton electrodes as active material and lead plates as absorbers, see Figure 3.9. It is symmetric around the Interaction point and comprises a barrel region covering η up to 1.475 and two end-cap regions covering $1.375 \leq \eta \leq 2.5$. The eta range of 1.37 to 1.52 due to a large amount of inactive material is called the crack region and is removed from the reconstruction of electrons or photons.

The barrel region is behind the superconducting solenoid and consists of two coaxial cylinders separated by a small gap. Each cylinder is about 3.2 meters long and has an inner radius of 1.4 m and an outer radius of 2 m. Together, they cover the region up to an ETA of less than 1.475. The high voltage is applied between the electrodes to collect the ionization charge from interacting particles with liquid Argon. The barrel region readout is separated into three radial layers with varying depths, each segmented in ϕ and η to provide shape information about the particle shower.

The energy resolution of the ECAL was measured in test beams with electrons before installation in the ATLAS experiment. Equation (3.5) shows the fractional energy resolution measured as a function of the energy.

$$\frac{\sigma(E)}{E} = \frac{10.1\%}{\sqrt{E(\text{GeV})}} \oplus 0.17\% \tag{3.5}$$

Here, the first term is the stochastic response, and the second is related to the non-uniformity of the detector response.

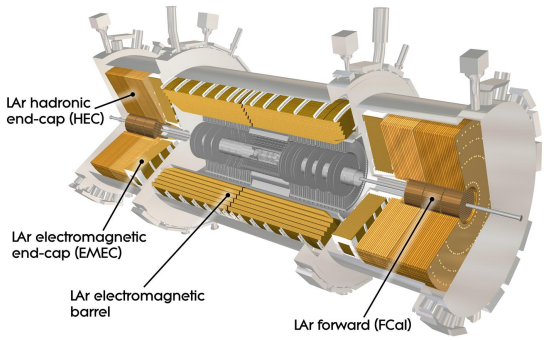

Figure 3.8. A sketch for the different components of the liquid Argon calorimeter. Figure adapted from [160]

3.2.6 The Hadronic calorimeter

The ATLAS Hadronic Calorimeter (HCAL) is located behind the ECAL and measures the energy of particles producing hadronic showers from their strong interaction in the HCAL. The HCAL consists of three sampling calorimeters with different active and passive materials depending on the performance requirements and radiation.

Tile calorimeter

The Tile calorimeter consists of a 5.8 m long barrel covering $|\eta| < 1$ and two extensions, each 2.6m long covering $0.8 < |\eta| < 1.7$. The inner radius of the barrels is $\simeq 2.3$ m, and the outer radius is $\simeq 4.3$ m. It uses steel as the absorber and scintillating plastic tiles as the active material. Like ECAL, the tile calorimeter is segmented radially

into three layers of different thicknesses. In the barrel region, the individual layers have nuclear interaction lengths of 1.5, 4.1, and 1.8 λ, while in the extended barrel region, they have 1.5, 2.6, and 3.3 λ. The tile calorimeter has a reduced granularity compared to the ECAL because of the typical shower difference between the EM and HCAL and has a typical cell size of $\Delta\phi \times \Delta\eta \approx 0.1 \times 0.1$.

Hadronic End Cap

The Hadronic End Cap (HEC), the LAr hadronic end cap calorimeter, is directly behind the ECAL end caps and uses Liquid Argon as the active medium and Copper as the absorber. The HEC consists of two wheels, the front HEC1, and the rear HEC2, covering a pseudorapidity range of 1.5 to 3.2. Like the tile calorimeter, the readout cells of size $\Delta\phi \times \Delta\eta \approx 0.1 \times 0.1$ are used in the central region. The granularity reduces as we go further away from the IP. The HEC shares the same cryostat as the ECAL endcaps and the Forward Calorimeter.

Forward calorimeter

The LAr Forward calorimeter FCal is the third component of the HCAL, covering the forward region of $3.1 \leq \eta \leq 4.9$. It consists of three modules on each side made of metal bases with holes parallel to the beam pipe. Metal rods with diameters smaller than the holes are placed, and liquid Argon fills the space left. The first module uses Copper as a passive material, while the next two use tungsten.

The Energy resolution of the HCal is given by the convolution of the stochastic term, the readout noise term, and a constant to account for unknown effects.

$$\frac{\sigma(E)}{E} = \frac{52\%}{\sqrt{E(GeV)}} \oplus \frac{1.6GeV}{E} \oplus 3\% \tag{3.6}$$

At $\eta = 0$, the HCAL material corresponding to 7.4λ and the ECAL with 1.5λ provide enough material to ensure hermetic closure. The ECal and HCal shield the Muon spectrometer from punch-through particles other than Muons and Neutrinos.

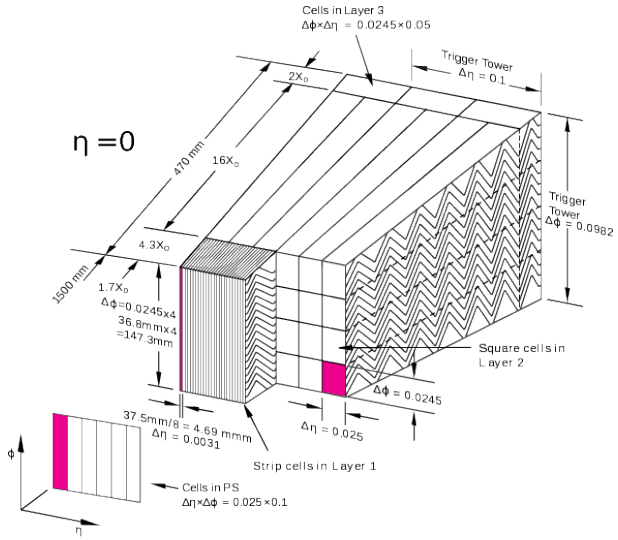

Figure 3.9. A sketch of the barrel module of the ATLAS EM calorimeter with accordion-shaped layers. Figure adapted from [37]

3.2.7 Muon Spectrometer

The ATLAS experiment houses the Muon Spectrometer(MS) in its outermost region. It provides precise tracking information of muons in the interval of pseudorapidity less than 2.7 with momentum up to 3 GeV. On average, muons produced in the p-p collisions have a lifespan of approximately 2.2 microseconds. Almost all muons leave the

ATLAS detector before they decay, as they lose very little energy through ionization and are, therefore, not stopped in the calorimeters. Any isolated track in the muon spectrometer (MS) indicates a muon since all standard model particles except neutrinos do not pass through the calorimeters (except for non-interacting charged pions).

A toroid magnet system creates the magnetic field that bends the muons. In the barrel region, eight superconducting coils generate a 4T magnetic field, which deflects the muons in the eta direction for eta values less than 1.4. In the end caps, two smaller toroid magnets produce a 4T magnetic field for the region where $1.6 < \eta < 2.7$. Installation of these separate magnetic fields maximizes the bending volume and increases the momentum resolution. Tracking chambers are placed in the air volume around the toroids to record the trajectories of muons. The barrel detectors are placed at three separate stations from the beam pipe, while the end-cap detectors are mounted on wheels. The innermost one is called the small wheel, and the two outside are called the big wheels. A cutaway sketch of the MS is shown in Figure 3.10

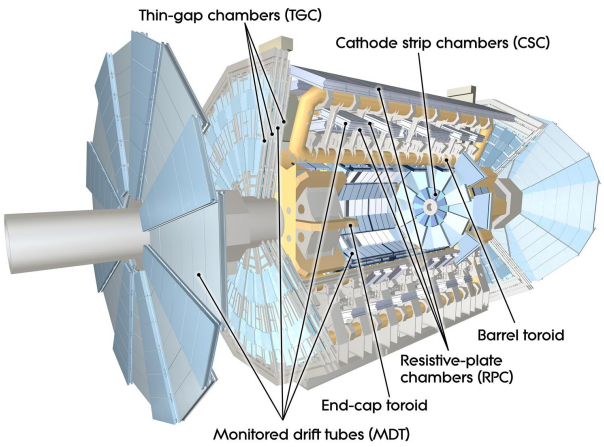

Figure 3.10. A cut-away sketch showing different components of the muon spectrometer. Figure adapted from [37]

Tracking Chambers

The tracking chambers consist of the Monitoring Drift Tubes (MDT), which precisely track the muons. These aluminum tubes, which have a diameter of 3 cm, have an anode wire at the center and are filled with a mixture of Argon and Co2 (93:7). A laser monitoring system installed to control the chamber's alignment is the largest source of uncertainty for muons of high p_T. The low p_T muon energy deposited between the IP and MS is the primary source of uncertainty. MDT chambers are installed on all MS stations except for the small wheel, where cathode strip chambers are installed in regions $|\eta| > 2$ to cope with the high particle rate.

Trigger Chambers

Since muons can be produced in W, Z, or Higgs decays and indicate an interesting event, MS is used to fire the trigger system. Special triggering chambers are installed around the precision tracking chambers to provide a fast signal for triggering and com-

pleting the MDT position measurement. Resistive Plate Chambers (RPC) are installed around the middle MDT layer and behind the third layer in the barrel region. They consist of two electrode plates with a thin gas-filled gap between them and high voltage applied. Both electrodes are orthogonally segmented to provide coarse spatial information with a resolution of 10mm in both directions. In the forward region, thin gap chambers (TGCs), multi-wire proportion chambers with a small distance between the wire and the cathode provide fast signals for triggering and spatial measurements with mm precision. Both the technologies combined achieve a nanosecond time resolution.

The MS alone is designed to provide a relative momentum resolution of $\sigma_{p_T}/p_T =$ 10% for 1 TeV muons within $|\eta| < 2.7$. Combining the information from ID and the information from MS improves the momentum resolution of low p_T muons.

3.2.8 Trigger and Data Acquisition

During a physics run at a beam luminosity of 10^{34} cm^{-2} s^{-1}, there are about ~ 20 hard scatters per bunch crossing. There are $\sim$ billion collisions per second at a frequency of 40 MHz i.e. 40 million bunch crossings per second. This amounts to a huge amount of data that cannot be stored in tapes; therefore, a multi-level trigger and Data Acquisition (DAQ) system is designed to select and store events of particular physics interest. The trigger is a dedicated hardware and software system that makes real-time decisions about which events to record for further analysis and which to discard. An overview of the amount of data generated from collisions and stored is depicted in figure 3.11.

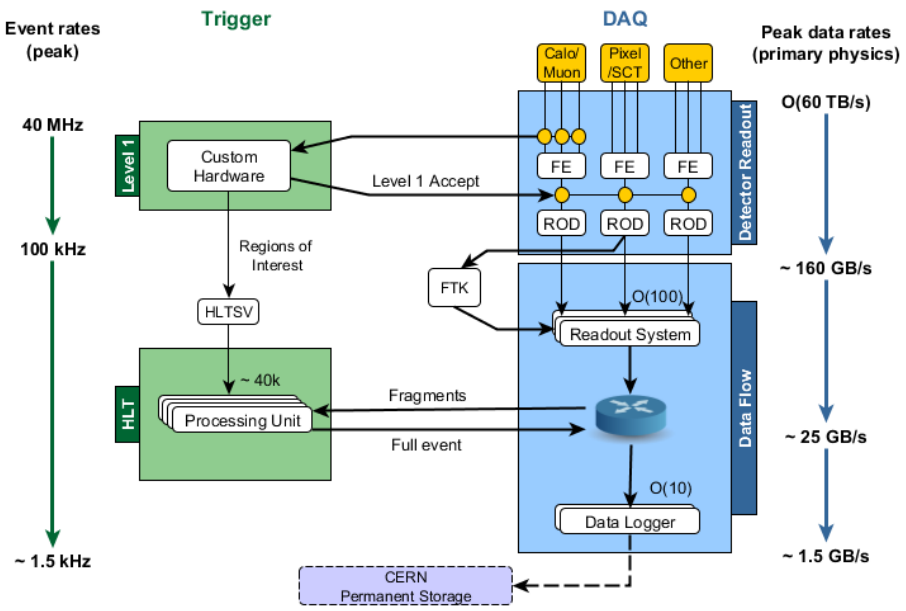

Figure 3.11. Amount of data generated and stored by the ATLAS TDAQ system. Figure adapted from [86]

During Run 2, the ATLAS trigger system was based on two levels. The main components of the trigger system are the Level-1 trigger (L1) and the high-level trigger (HLT); see Figure 3.12.

Level-1 Trigger

Event signatures with potential interest are identified by either the Level-1 Calo (L1Calo) or the Level-1 Muon (L1Muon) systems, both hardware-based. L1Calo gathers information from the calorimeters at a reduced granularity level, performs an analog-digital conversion, and sends the information to the Cluster Processor (CP) and Jet/Energy-sum Processor. The Cluster Processor identifies electrons, photons, or tau leptons, while

the Jet/Energy sum processor identifies the jet candidates and calculates the missing transverse momentum. L1Muon takes the input from the MS and the calorimeters, signals from RPC in the barrel region, and the endcap region, TGC, and tile calorimeters. Information from the L1Calo and L1 Muon is sent to the central trigger processor (CTP) via the L1 Topo and muon CTP. The CTP decides whether to accept or reject the event based on the information according to a pre-set condition. The L1 trigger event selection can be based on the number of muons above a certain p_{T} threshold, leptons, photons, the energy measured in the calorimeters, or the missing transverse energy. L1 algorithms have a latency of about 2.5 microseconds, reducing the event rates to about 100 kHz and defining a crude region of interest for the detector, which then is passed on to the HLT.

High level Trigger

After an event is accepted by the L1 trigger, regions of interest (ROI) are identified, and the data is transmitted from the front-end (FE) boards to the readout system (ROS) through the readout drivers (ROD). The HLT, which is software-based, operates on dedicated computing farms interfaced with ROS and has access to all detector information and the particular area of interest from the L1 Trigger. The HLT then further reduces the event rate to 1.5 kHz (at peak times), which is then permanently stored and sent to the CERN T0 computing site for offline reconstruction.

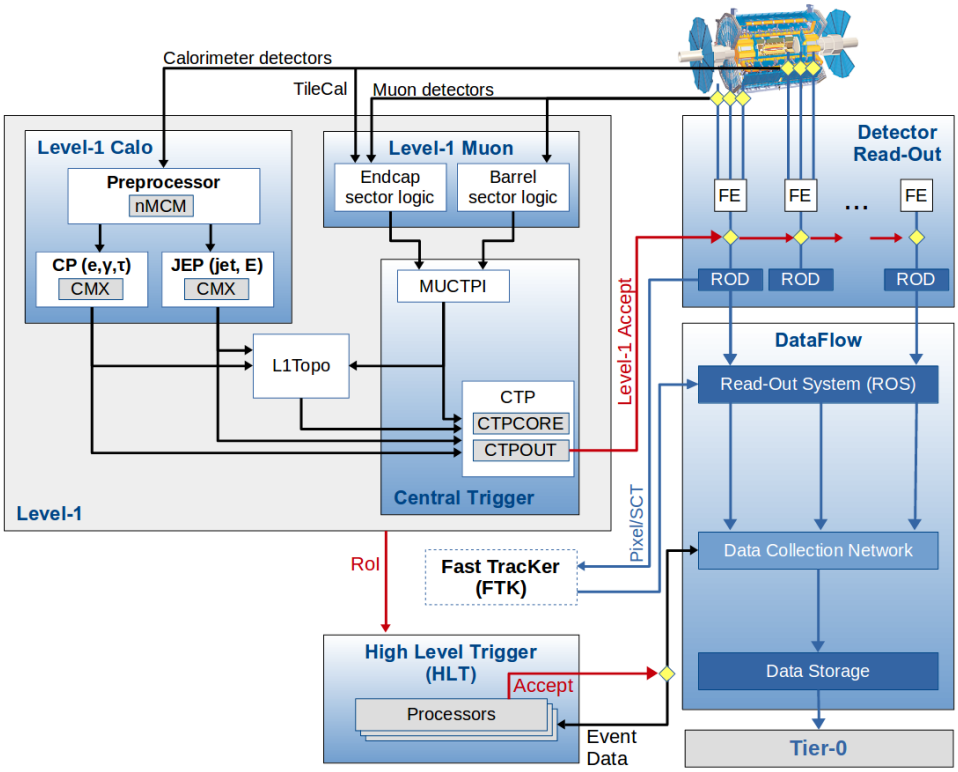

Figure 3.12. A schematic of the different components of the ATLAS Trigger and DAQ system. Figure adapted from [16]

3.3 Luminosity and Data taking in Run 2

Dedicated detectors in the front arms (forward directions) of the ATLAS experiment monitor the instantaneous luminosity, with the primary measurement provided by the LUCID2 Cherenkov detector. The detector system comprises 16 Photo Multiplier Tubes (PMTs) at $z = \pm 17$ m from the Interaction Point (IP). It can provide the number of particles detected in N out of the 16 PMTs for each colliding bunched. The counts are averaged over one minute when the experimental conditions are stable, referred to as Luminosity Blocks (LB). LB multiplied by the instantaneous luminosity gives the integrated

luminosity, assuming constant instantaneous luminosity.

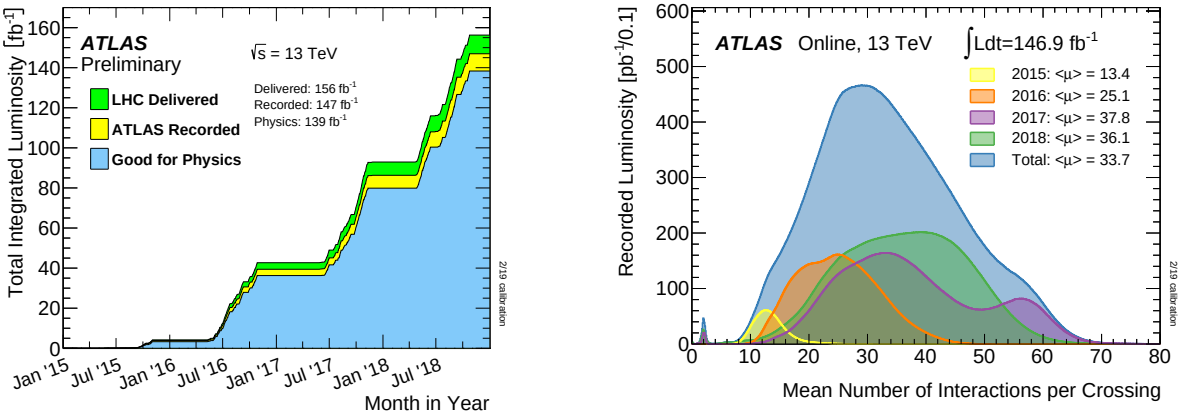

(a) Cumulative Luminosity vs time delivered by LHC (green), recorded by ATLAS (Yellow) and Good for physics (blue) [19]

(b) Luminosity weighted distributions for the mean number of interactions per bunch crossing in the different years. [19]

Figure 3.13. ATLAS Luminosity measurement for Run 2

At the beginning of each year of data taking, special runs of LHC take place; during these runs, *Van der Meer* [151] scans are performed to provide algorithm-specific absolute luminosity calibration constants σ_{vis}. Using σ_{vis} and the μ_{vis} (number of visible hits) derived from the PMTs, one can calculate the Instantaneous Luminosity.

$$\mathscr{L} = \frac{\mu_{vis} f_r}{\sigma_{vis}} \tag{3.7}$$

Here f_r is the LHC revolution frequency (40 MHz / 3564 LHC total bunch slots). A *good run list* consists of the dataset's physics-ready portion, obtained when LBs with a malfunctioning detector are excluded from the recorded dataset.

Figure 3.13a shows the total integrated luminosity delivered by the LHC, recorded by the ATLAS experiment, and good for physics. Figure 3.13a shows the Luminosity weighted distribution for the mean number of interactions per bunch crossing in the different years.

3.4 ATLAS Upgrade projects

The Large Hadron Collider (LHC) is the world's most advanced facility for investigating the structure of matter at the smallest scales. Significant progress has already been made in addressing these questions, the discovery of the Higgs boson being the most famous. Since its start in 2008, there has been a constant drive to push the boundaries of the LHC machine and the detectors. However, we are seeking extremely rare, low-probability events to be observed in a statistically significant way. One way to proceed is to increase the available statistics, i.e., the interaction rate. LHC was designed initially for proton-proton collisions at the center of mass energy of $\sqrt{s} = 14$ TeV and to deliver an instantaneous luminosity of 10^{34} cm^{2}s^{-1} but exceeded the peak luminosity target in 2016 by delivering 2.1×10^{34} cm^{2}s^{-1} at the center of mass energy $\sqrt{s} = 13$ TeV. Significant changes have been planned for the High-Luminosity LHC (HL-LHC) starting in 2029 to increase the instantaneous luminosity to 7.5×10^{34} cm^{2}s^{-1} generating about 3000 fb^{-1} of data for the experiments corresponding to approximately 200 inelastic proton-proton collisions per beam crossing and the hadron fluence of approximately 2×10^{16} neq/cm^2[2].

[2]Hadron fluence is defined as the time integral of the hadron flux density, expressed as the number of particles (neutrons) per cm^2

Figure 3.14 highlights the timeline for the LHC and the transition to HL-LHC.

Figure 3.14. LHC Timeline with the plan for HL-LHC

To withstand and properly use it, significant detector upgrades, known as HL-LHC detector upgrades, have already started.

3.4.1 Trigger and Data Acquisition

An upgraded trigger system is necessary to fully exploit the potential of HL-LHC's physics. The new trigger system will benefit from the increased granularity provided by the calorimeters and improve efficiency for muon-based triggers. It will also perform hardware-based tracking with the extended coverage of the planned Inner Tracker (ITk). To perform the physics program in Run 4, a factor of 10 higher trigger rates than the

ones expected in Run 3 is needed to retain the events.

3.4.2 The Inner Tracker (ITk)

The silicon strip and pixel detectors will reach the end of their life by the end of Run 3 as they were not designed to withstand the harsh conditions of the HL-LHC. Under HL-LHC conditions, TRT's occupancy will reach 100%, and the Pixels and SCT performance will suffer from saturation of the readout bandwidth. The Inner Tracker (ITk) project is to build an all-silicon detector that will completely replace the current tracker to provide similar or better tracking performance compared to the present ID, posing severe technical challenges in the design of the detector. Details about ITk have been discussed in chapter 6.

3.4.3 High Granularity Timing Detector

A High Granularity Timing Detector (HGTD) based on the new Low Gain Avalanche Diode (LGAD) technology will be installed in the forward region of the ATLAS detector to provide precise timing measurement ($\sim$ 30 ps) of charged tracks.

3.4.4 Calorimeters and Muon System

The LAr Calorimeter and the Tile Calorimeter require significant changes in the electronics to ensure compatibility with the new level-0 trigger's higher trigger rates and longer latencies. A significant portion of the frontend, on-detector, and off-detector read-out and trigger electronics for the Resistive Plate Chambers (RPC), Thin Gap Chambers (TGC), and Monitored Drift Tube (MDT) chambers will undergo replacement.

CHAPTER 4

RECONSTRUCTION AND IDENTIFICATION

Particles produced in the proton-proton collisions in the ATLAS experiment are detected by their interactions with the sub-detectors as they leave different signatures traversing the various sub-detector layers, as illustrated in Figure 4.1. The raw detector information is translated into an event is eventually reconstructed into specific physics objects like jets, electrons, muons, or missing transverse energy to be used for analysis. The ATLAS experiment uses dedicated reconstruction and identification algorithms centrally implemented in the ATHENA framework [18].

The reconstruction process is divided into several steps. Initially, objects at the detector level, such as *tracks*, *vertices*, or *calorimeter clusters*, are formed. These objects are then combined to create high-level objects corresponding to different types of particles. The physics objects are then reconstructed and subjected to additional identification and isolation criteria. Finally, the physics objects are calibrated to adjust for any differences between data and simulation in the detector effects. This chapter overviews the detector-level and high-level objects and the methods used in their reconstruction.

4.1 Tracks, Vertices and Calorimeter Clusters

This section overviews the *detector-level* objects reconstructed with the ATLAS detector.

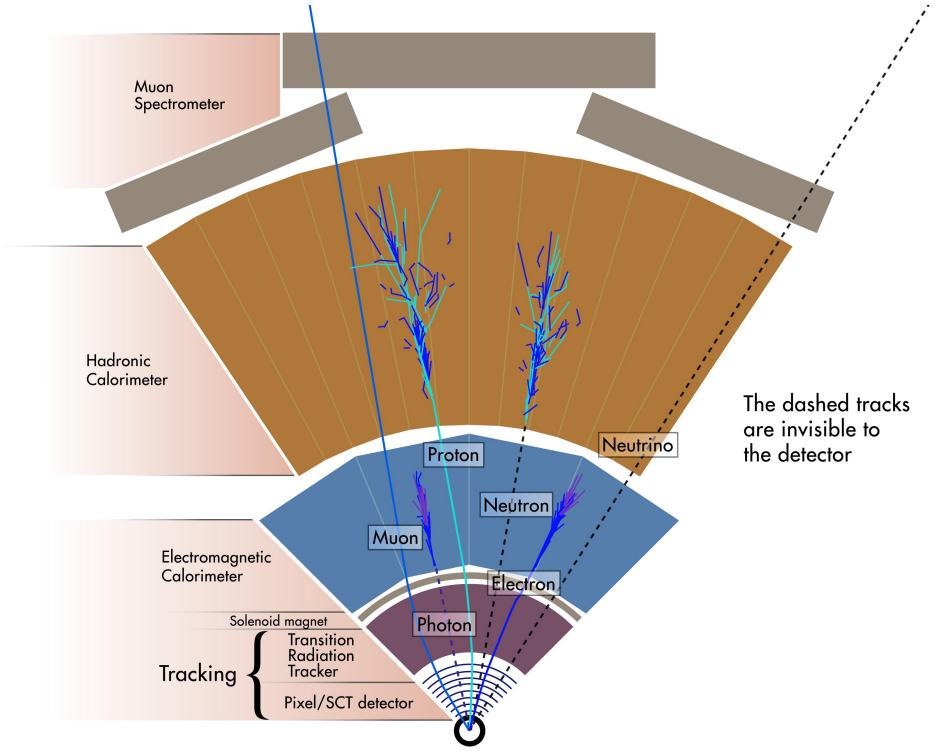

Figure 4.1. Particle paths and signatures in the ATLAS detector as viewed from the transverse plane. Figure adapted from [161]

Tracks

The "track" or trajectory of a charged particle can be reconstructed from the energy it deposits in the ATLAS ID and MS. Around 600 charged particles were produced in each bunch crossing during the Run 2 data-taking period. Proper reconstruction tracks are essential for accurately reconstructing physics objects. These tracks are inputs for lepton reconstruction, primary vertex finding, and flavor tagging.

A helicoidal charge particle track can be described by five parameters as shown in figure 4.2. These parameters include the magnitude of the transverse momentum, the

polar angle, the azimuthal angle, the transverse impact parameter to the beam direction, and the longitudinal impact parameter to the nominal interaction point.

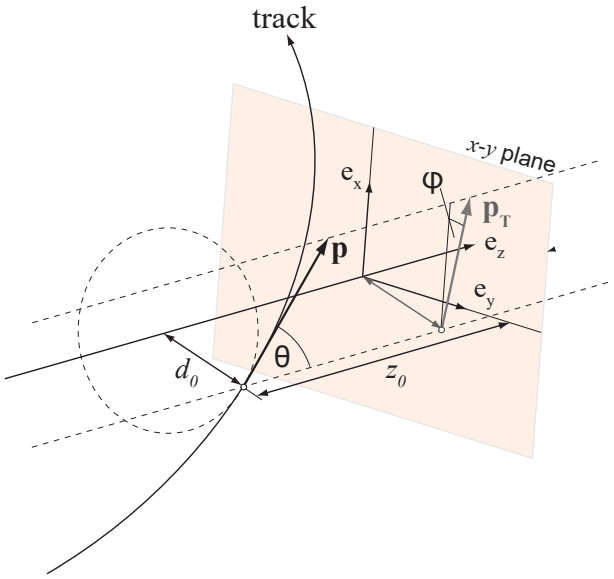

Figure 4.2. A schematic view of the parameters used to describe tracks in the ATLAS detector.

Figure 4.3 showcases the two algorithms used to convert hit information into tracks. The first is the inside-out algorithm, which begins from the pixel layer and builds tracks outwards. This algorithm utilizes a triplet of hits in the Pixel and SCT detectors to seed the track. Once the seed is set, the track is extrapolated from the seed to the end of SCT using a combinatorial Kalman filter [139]. If there is any ambiguity, multiple track candidates are considered. To resolve the ambiguity, an ambiguity solver applies quality requirements to the track candidates and ranks them based on quality standards, eliminating candidates failing the required quality criteria. After ambiguity resolution, the

high-precision track parameter estimate is obtained by re-fitting the refined and purified track candidates using a global χ^2 method. The final step extends the remaining tracks to the TRT for combinations.

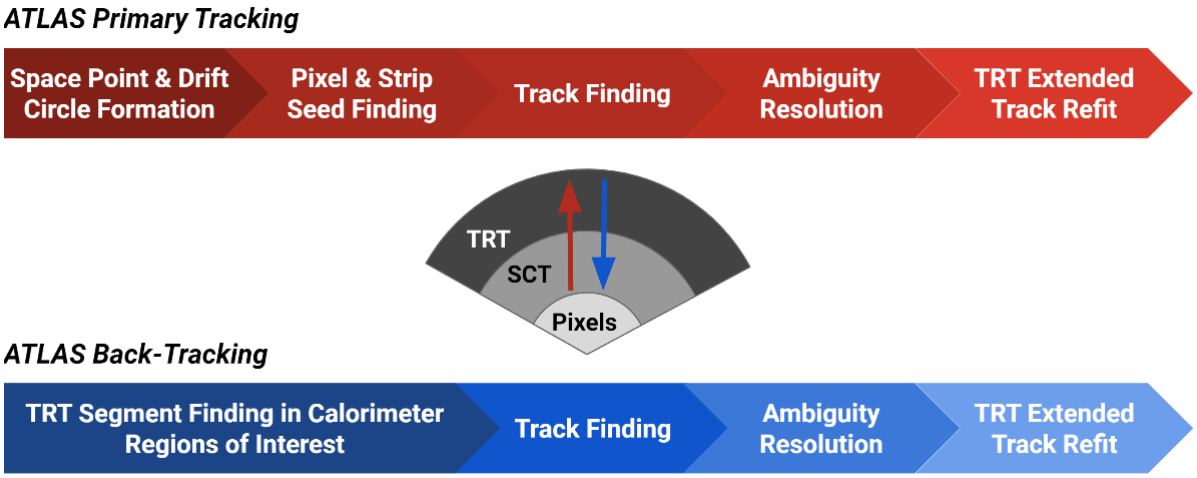

Figure 4.3. The two complimentary algorithms used in the ATLAS tracking. The Inside-out algorithm is in red, and the outside algorithm is in blue. Figure adapted from [39]

A complimentary outside-in algorithm tracks particles produced at a greater distance from the beamline, e.g., electrons from photon conversion in the detector material. This secondary back-tracking is performed using detector hits not already assigned to tracks in the inside-out algorithm. In this case, the track reconstruction is only attempted in regions of interest (ROI) determined by the energy deposits in the EM calorimeters. This algorithm starts with segments of hits in the TRT compatible with the ROI and goes inside the SCT and pixel hits. Additionally, all tracks need to pass additional criteria given

Requirements
7 clusters in pixels and SCT detector
≤ 2 holes in the pixel or SCT detector
< 2 holes in the pixel detector
$\lvert d_0 \rvert < 2$mm with respect to the beam-line
$z_0 sin\theta < 3$ mm with respect to the beam-line
$\lvert \eta \rvert < 2.5$
$p_T > 500$ MeV

Table 4.1. Requirements for track characterization

in the table 4.1.

Vertices

Vertices are identified in an iterative process, starting with a seed vertex identified from all good-quality tracks. The next step is to remove all tracks incompatible with the computed vertex and recalculate the vertex position. This iterative process repeats until the reconstructed vertex passes specific quality requirements. The tracks previously rejected are then utilized to identify more vertices. All the vertices created are ranked based on the sum of squared track transverse momentum (Σp_{T}^2), and the one with the largest Σp_{T}^2 is called the primary vertex.

Topological calorimeter clusters

Particles interacting electromagnetically or hadronically deposit their energy in the calorimeters. These deposits are generally in the form of groups called *clusters*. ATLAS experiment uses two algorithms to identify these clusters: the *sliding window* and the *topological clustering* algorithm. The sliding window clustering algorithm builds clusters with a fixed size in $\eta \times \phi$. The window's position is adjusted to maximize the transverse

energy. The fixed window allows for a very precise cluster energy calibration; therefore, it is used to reconstruct electrons, photons, and tau-lepton decays.

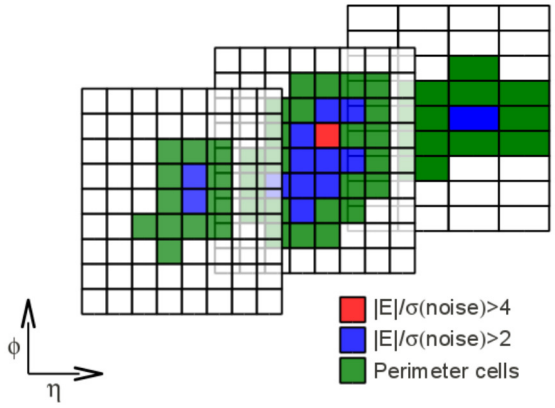

Figure 4.4. A grid representing calorimeter cells and showing topo-cluster formation in the hadronic layers in the barrel.

Topological energy deposit clusters are created using a spatial significance-based approach in the topological clustering algorithm. These clusters called *topo-clusters*, group energy deposits in calorimeter cells from a single particle shower. The algorithm generates these topo-clusters by selecting the cell with the highest energy deposit and grouping adjacent calorimeter cells based on signal significance.

The signal significance used for clustering is calculated as

$$Z = |\frac{E^{EM}_{\text{cell}}}{\sigma^{EM}_{\text{noise, cell}}}|, \tag{4.1}$$

where E^{EM}_{cell} is the cell energy and $\sigma^{EM}_{\text{noise, cell}}$ is the expected cell noise. Seeds are formed by considering cells starting from the second calorimeter layer outwards that have

$Z \geq 4$. Adjacent cells with $Z \geq 2$ are merged into one cluster, and finally, $Z \geq 0$ are also merged sequentially. This algorithm is primarily used for reconstructing jets and E_T^{miss}, as it has the advantage of suppressing noise in clusters with a large number of cells.

Calibration constants derived during test beams calibrate each cell to the *EM scale* or the electromagnetic scale, which correctly measures the energy in the calorimeter deposited by particles produced in an electromagnetic shower. To measure the energy deposited by particles produced in hadronic showers, these calorimeter cells are recalibrated to account for the difference between the electromagnetic and hadronic showers. This is achieved by the *local cell weighting* (LCW) calibration scheme. The LCW calibration scheme first classifies topo-clusters into electromagnetic or hadronic depending on the longitudinal shower depth and the measured energy density. Energy corrections are later derived for the topo-clusters using single-charged and neutral pion MC simulations.

4.2 Leptons and Photons

Leptons are detected by three sub-detectors: ID, ECAL, and MS. The ID and MS detectors help determine the curvature and momentum of the leptons in the magnetic field, while the ECAL measures the energy. Leptons are categorized into two types, *prompt* and *non-prompt*, based on their origin. Prompt leptons originate from the primary vertex, and the non-prompt from the secondary decays. This section provides an overview of the different steps involved in reconstructing leptons.

4.2.1 Electrons

Electrons produced in the ATLAS experiment leave tracks in the ID and deposit energy in the ECAL. Dedicated algorithms use a combination of tracks from the ID and energy deposits in the ECAL to identify electrons in the detector's central region ($\eta < 2.47$). The ID does not cover the forward region, so only calorimeter information, i.e., the shape of the showers, can be used for electron identification. In this thesis, only electrons in the central region are considered.

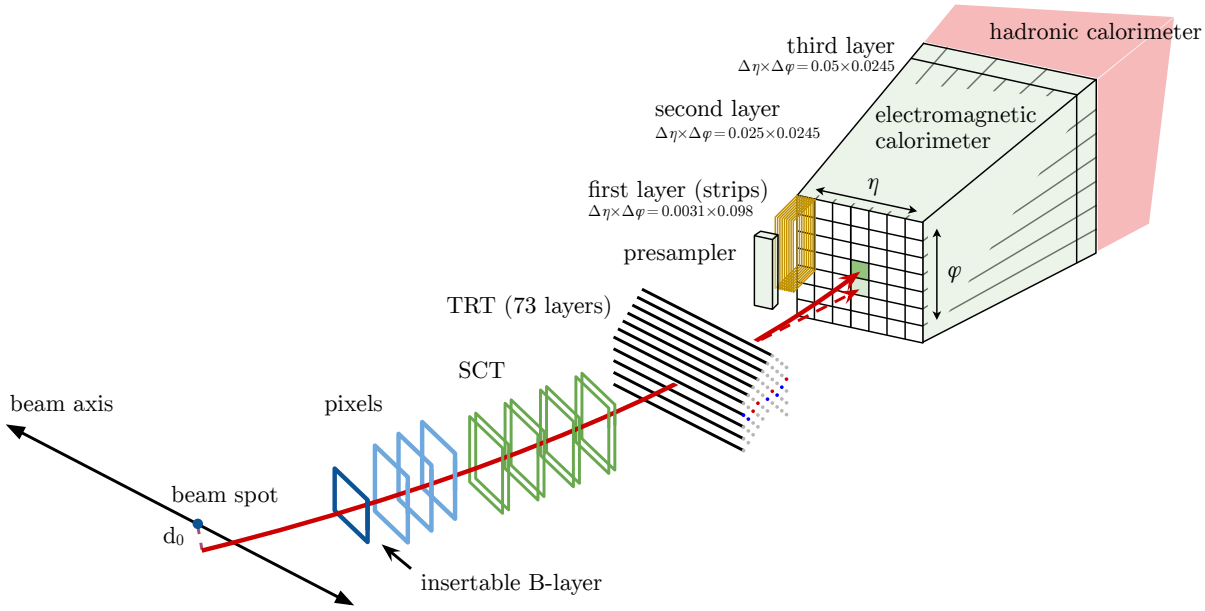

Figure 4.5. A visualization of the electron passing through the sub-systems of the ATLAS detector. The solid red line shows the electron, and the dashed red line shows the Bremsstrahlung radiation photon depositing energy in the adjacent cell in the ECAL. Figure adapted from [105]

Reconstruction

The electron reconstruction process begins with calibrating topo-clusters using the EM scale. Tracks loosely matched to a topo-cluster are then refitted with a Gaussian Sum Fitter optimized for electron track-fitting to account for non-linear Bremsstrahlung effects. An electron candidate is identified when at least one track is matched to a calorimeter cluster. The track closest to the cluster's center is selected if multiple tracks exist. Any electron candidate without a proper track hits is removed and is considered a photon. Finally, a prompt electron candidate must meet the primary vertex criterion and additional impact parameter requirements.

Identification

Jets with a high electromagnetic (EM) fraction, electrons from photon conversion, and electrons from semi-leptonic heavy-flavor hadron decays may interfere with electron reconstruction and are considered potential backgrounds. Although conversion electrons and electrons from heavy-flavor hadron decays are real electrons, they can still be considered backgrounds because they are not created in the hard scatter. An electron identification algorithm distinguishes prompt electrons and reduces the background from photon conversion and non-prompt electrons. This algorithm uses a likelihood-based approach that combines several parameters into a multivariate analysis (MVA), including the number of hits in each layer, transverse and longitudinal impact parameters, momentum lost in the ID, and information about the calorimeter cluster. The algorithm uses $Z \to ee$ and $J/\psi \to ee$ as signals and dijet events as background to create a likelihood

discriminant. The algorithm establishes several working points (WP) using fixed values of the likelihood discriminant: *Loose*, *Medium*, and *Tight*, corresponding to the levels of reduced signal efficiency versus increased background rejection. Each operating point has different reconstruction efficiency and background rejection, depending on p_T and η, as shown in Figure 4.6.

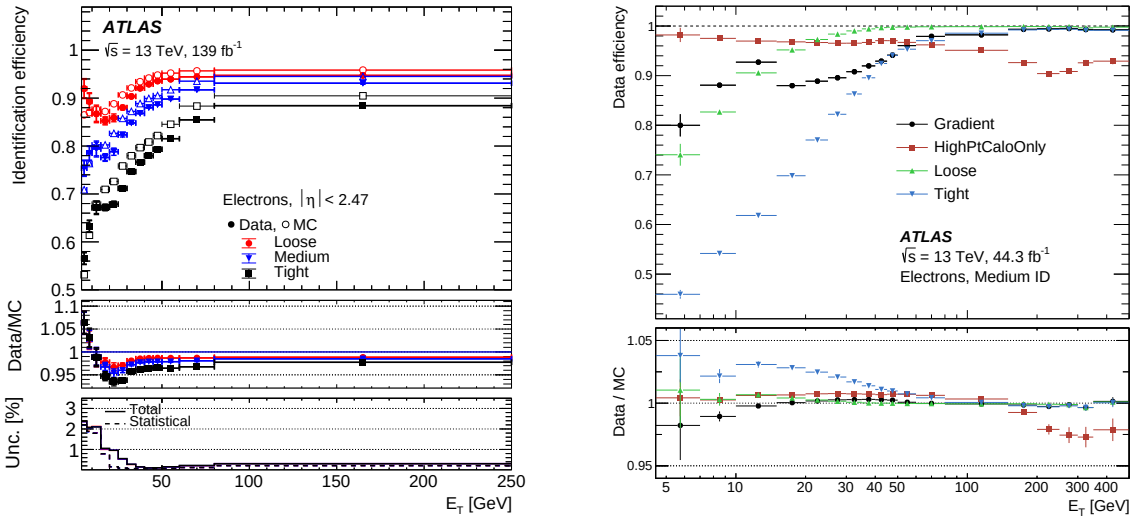

Figure 4.6. The figure on the left shows the identification efficiencies of electrons from $Z \rightarrow ee$ decays as a function of the electron's transverse energy (E_T). The figure on the right shows the isolation efficiency of different working points as a function of the electron's transverse energy (E_T). Figures from [76]

Isolation

The isolation criterion is applied to further reduce the backgrounds for the prompt electrons coming from W, Z, or H decays. Two variables are defined to evaluate the electron candidate's isolation using calorimeter-based and track-based isolation variables.

The former is more sensitive to pileup and uses topo-clusters to compute energy in a cone of size ΔR around the electron candidate. $E_{\mathrm{T,\,cone}}^{\mathrm{isol}}$, defined as the energy in the cone after the candidate electron energy is subtracted, is used to construct isolation WP. The sum of transverse momenta of tracks with $p_T > 1$ GeV excluding the electron candidate in a given ΔR cone, $P_{\mathrm{T,\,var}}^{\mathrm{isol}}$, is calculated for the track-based isolation criterion.

Calibration

The total efficiency $\varepsilon_{\mathrm{total}}$ of correctly identifying the electron is a combination of the different components as

$$\varepsilon_{\mathrm{total}} = \varepsilon_{\mathrm{cluster}} \times \varepsilon_{\mathrm{reco}} \times \varepsilon_{\mathrm{id}} \times \varepsilon_{\mathrm{iso}} \times \varepsilon_{\mathrm{trigger}} , \tag{4.2}$$

We evaluate each efficiency term in data and MC using the dedicated measurements of $Z \to ee$ and $J/\psi \to ee$ events, except for the clustering efficiency ($\varepsilon_{\mathrm{cluster}}$). To ensure the simulation matches the actual data, scale factors (SF) are derived. These factors are obtained by calculating the ratio of the efficiency measured in data to that measured with MC. The SFs are usually very close to 1 and are used to correct the simulation. To determine the uncertainties in these SFs, each component's efficiency estimation method is systematically varied.

4.2.2 Photons

Simultaneously reconstructing electrons and photons is possible because their energy deposits in the ECAL are similar, even though photons do not leave hits or have an associated track in the ID. The reconstruction process of photons and electrons begins con-

currently with the electromagnetic clusters. The candidates are either electrons/positrons (converted photons) or unconverted photons. The distinction between converted and unconverted photons is made using an ambiguity resolver that uses the tracks in the ID and the conversion vertex. It is vital to differentiate between prompt photons and hadronic jets for which the shower characteristics are used. Prompt photons have a narrow shower and less impact in the hadronic calorimeter. Optimization of cuts applied to discriminant distributions in different η bins defines three WP: Loose, Medium, and Tight. The efficiency of identifying particles is measured in data and compared to MC simulation in $Z \to l^+l^-\gamma$ and $Z \to ee$ events. Isolation criteria defined for photons are similar to those for electrons.

4.2.3 Muons

At the LHC energy levels, muons generated in the hard scatter are minimum ionizing particles (MIP) and leave the ATLAS experiment above. Unlike other particles, muons leave tracks in the ID and the MS while depositing only a small amount of energy typical to an MIP in the calorimeter.

Reconstruction

Given the variety of signatures in the ATLAS subdetectors, multiple ways of reconstructing muons exist. Section 4.1 explains how to reconstruct muon tracks in ID. The initial formation of tracks in the MS happens per station in a straight line. The MDT hits are responsible for the bending plane alignment, while the RPC and TGC hit provide information on the coordinate orthogonal to the bending plane. These segments

act as seeds in the fitting process, starting from the middle layer of the MS and moving successively toward the inner and outer layers. Each segment is evaluated based on the track quality criterion. To create a track, at least two matching segments are required for each η region of the MS, except for the transition region between the barrel and end-cap, where only one high-quality segment is adequate. Overlap removal is done to improve track quality, and a global χ^2 fit is performed with loose constraints from the IP location.

The reconstructed muons can be classified into five different categories based on the reconstruction strategy:

- *Combined (CB):* The reconstruction of tracks in the MS and ID takes place independently at first. However, if two tracks from ID and MS are found to match, their combined hits are refitted as a single track, taking the energy loss in the calorimeter into account. A global fit is then performed from the MS to the ID, which usually results in commonly used good-quality reconstructed muons. For $|\eta| > 2.5$, MS tracks can be combined with short track segments reconstructed from the hits in the pixel and the SCT detector. Muons reconstructed with this method are a subset of CB muons referred to as Silicon-Associated Forward (SiF) muons.

- *Inside-out (IO):* A complementary algorithm extrapolates ID tracks to the MS, searching for loosely aligned MS hits. This algorithm does not depend on an independently reconstructed MS track and recovers efficiency for regions with limited MS coverage and low p_T muons.

- *Muon Spectrometer extrapolated (ME):* When an MS track cannot be matched with

an ID track, the parameters of the MS tracks are extrapolated to the beamline, extending the acceptance outside of the ID and fully exploiting the full MS coverage.

- *Segment tagged (ST):* The ST muons are identified based on a tight angular matching requirement between the ID track and at least one reconstructed MS segment. If a candidate ID track successfully matches an MS segment, it is considered a muon candidate, and the muon's parameters are obtained directly from the ID track fit.

- *Calorimeter tagged (CT):* ID tracks are extrapolated through calorimeters to identify CT muons and search for energy deposits matching the characteristics of an MIP. These energy deposits are then used to tag the ID tracks as muons, and the muon parameters are directly taken from the ID track fit. The CT muons have large background contamination at low p_T; hence, a threshold of 5 GeV is used.

Identification

Following the reconstruction process, we select high-quality muon candidates for physics analyses by using criteria depending on the number of hits in the various ID subdetectors and MS stations, track fit properties, and compatibility between the MS and ID tracks. Analyses have varying prerequisites concerning the efficiency of prompt-muon identification, momentum measurement resolution, and elimination of background caused by non-prompt muons. Non-prompt muons are categorized as muon candidates resulting from the semileptonic in-flight decay of light hadrons and those originating from heavy-flavor hadronic decays.

Three standard WPs, *Loose*, *Medium*, and *Tight*, are designed to meet the require-

ments of physics analyses. The Medium WP is generally used since it provides an optimal balance between efficiency and purity for a wide range of analyses while minimizing the uncertainties in the prompt-muon efficiency and background rejection. Figure 4.7 shows the efficiency of the three working points.

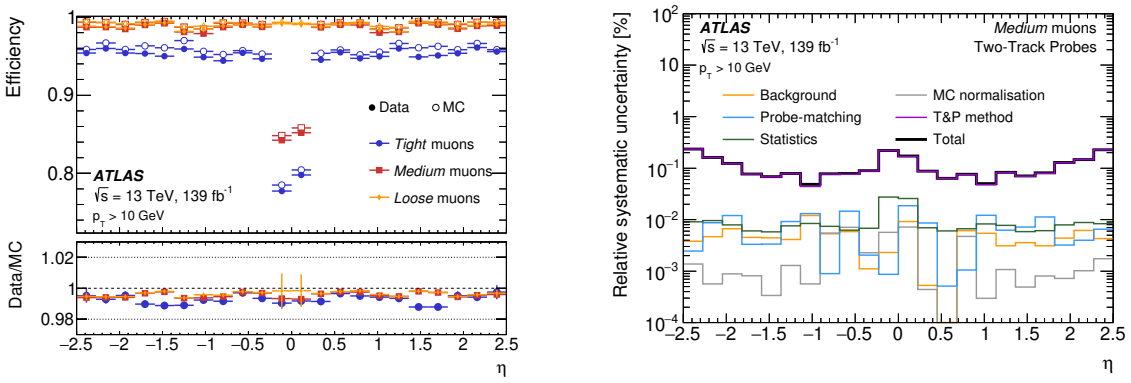

Figure 4.7. The figure on the left shows the identification efficiencies of muons from $Z \to \mu\mu$ decays as a function of pseudorapidity (η). The figure on the right shows the breakdown of systematic uncertainties affecting scale factors as a function of pseudorapidity (η) for the *medium* working point. Figures from [77]

Isolation

To distinguish between the prompt and non-prompt muons, further isolation criteria are constructed using the track and calorimeter information, like that of electrons. The track-based isolation variable is the scalar sum of the transverse momentum of particles with tracks in a ΔR cone around the muon candidate, excluding the muon track. The ΔR can be chosen to be fixed 0.2 or variable $\min(10\text{ GeV}/p_T^{\mu}, 0.3)$. The variable ΔR is optimized for topologies where jets or other leptons are expected to be close to an ener-

getic muon. The calorimeter-based isolation variable is the sum of the transverse energy of topological cell clusters in a cone of $\Delta R = 0.2$ around the muon candidate, subtracting the muon contribution itself after correcting for pile-up. Although the calorimeter-based isolation technique corrects for the effects of pile-up on average, it results in poor energy resolution because of the large pile-up correction relative to the average calorimeter isolation values.

Calibration

The identification and isolation efficiencies are measured using a tag and probe method in the $Z \rightarrow \mu\mu$ and $J/\psi \rightarrow \mu\mu$ events similar to the electron identification efficiencies. Scale factors account for the differences in the efficiencies measured in the data and MC. Figure 4.7 (right) shows the uncertainty contributions affecting scale factors as a function of the pseudorapidity (η).

4.3 Jets

The quarks and gluons produced in the p-p collisions undergo fragmentation and hadronization to generate a collimated stream of color-neutral hadrons like kaons, pions, etc. This so-called collimated stream of particles called a jet, is visible in the ATLAS detector through tracks in the ID and energy deposits in the calorimeter. We can also define a jet as a group of 4-vectors representing either a calorimeter cluster (calorimeter jet) or tracks in the ID (track jet). To optimize this correspondence, one must use an infrared and collinear-safe jet algorithm, meaning that the algorithm should not alter the jet definition for either very low energy or collinear radiation off the initial parton. Figure

4.8 shows the length scales and the corresponding detector signatures.

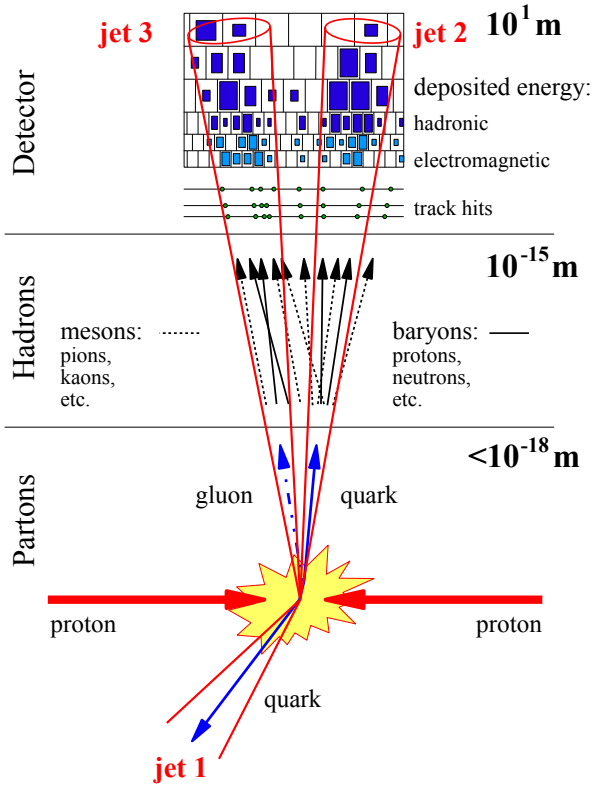

Figure 4.8. A sketch displaying the Jets evolution at different length scales, the corresponding particle content, and the detector signatures. Figure adapted from [69]

4.3.1 Jet Algorithms

Different jet algorithms define jets by giving prescriptions for grouping particles. In general, jet algorithms involve a distance measure and a recombination scheme. The jets used in this thesis are all reconstructed using a sequential recombination algorithm called the *anti-k_t* algorithm [66], an UV and IR safe algorithm which defines a distance measure d_{ij} between two particles i and j and a minimum distance d_{min} as

$$d_{ij} = \min\left(p_{\mathrm{T}i}^{2n}, p_{\mathrm{T}i}^{2n}\right)\frac{\Delta R_{ij}^2}{R^2}, \tag{4.3}$$

$$d_{\min} = \min\left(d_{iB}, d_{ij}\right) \quad \text{with} \quad d_{iB} = p_{\mathrm{T}i}^{2n}. \tag{4.4}$$

where, $n = -1$, $p_{\mathrm{T}i}$ is the transverse momentum, d_{iB} is the distance between the particle i and the beam B, ΔR(equation 3.3) and R are the radius of the jet. The algorithm starts with calculating the distance measures (d_{ij} and $d_{\min}$) for the hard (high p_{T}) objects. If the smallest distance is d_{ij}, we combine the two objects i and j to find the next smallest until the smallest distance is d_{iB}. Once the smallest distance is d_{iB}, the combined particles are removed from the list and called a jet. This process goes on until all the particles are clustered into jets. The parameter R, the radius of the jet, scales the d_{ij} such that any pair of final jets is at least separated by $\Delta R_{ij}^2 = R^2$. The benefits of using *anti-k_t* algorithm are that it starts with hard objects, and the jets are cone-shaped, which can be inferred from Figures 4.8 and 4.9. Another algorithm commonly used to reconstruct jets from the soft (low momentum) particles is the k_t-algorithm. This can be obtained by setting $n = 1$ in Equation 4.3 and 4.4. It follows the singularity structure of QCD but is highly susceptible to noise from soft processes.

Other sets of algorithms not commonly used are the cone-type algorithms, e.g., iterative cone, ATLAS cone, midpoint cone, and SISCone. As the name suggests, these algorithms look for a cone-like object in the p-p collisions. However, the major drawback of these algorithms is they are usually not infrared or collinear safe except for SISCone [169].

The commonly used values of R in the ATLAS analyses are 0.4 and 1.0. Jets with

$R = 1.0$ are called *large-R* jets, and jets with $R = 0.4$ are called *small-R* jets. The small-R jets represent quarks and gluons, whereas the large-R jets represent the hadronically decaying massive particles, often with overlapping small-R jets.

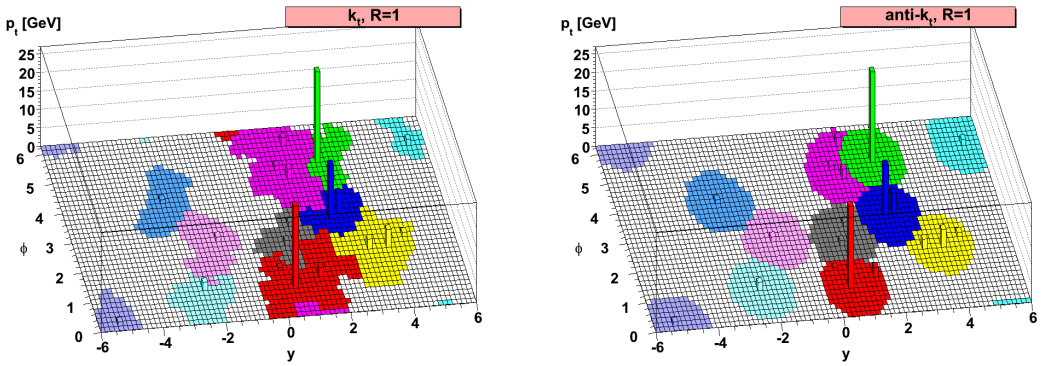

Figure 4.9. Illustration of the two jet clustering algorithms, k_t (left) and anti-k_t (right). The figure shows the different jets with different colored sections in the $y-\phi$ plane. Figure from [66].

4.3.2 Jet Calibration

The reconstructed jets are adjusted to compensate for various detector effects such as calorimeter non-compensation, dead material, jets with leaks outside the calorimeter, pile-ups, and reconstruction efficiency, including energy deposited outside the jet cone. Figure 4.10 depicts the calibration process for both large-R and small-R jets.

Jet origin correction

During the initial jet reconstruction (small-R jets) from the EM-scale topo-clusters, the jet axis points to the detector center instead of the primary vertex (PV). A correction is applied to fix the jet origin, rectifying the jet 4-momentum vector to point towards the

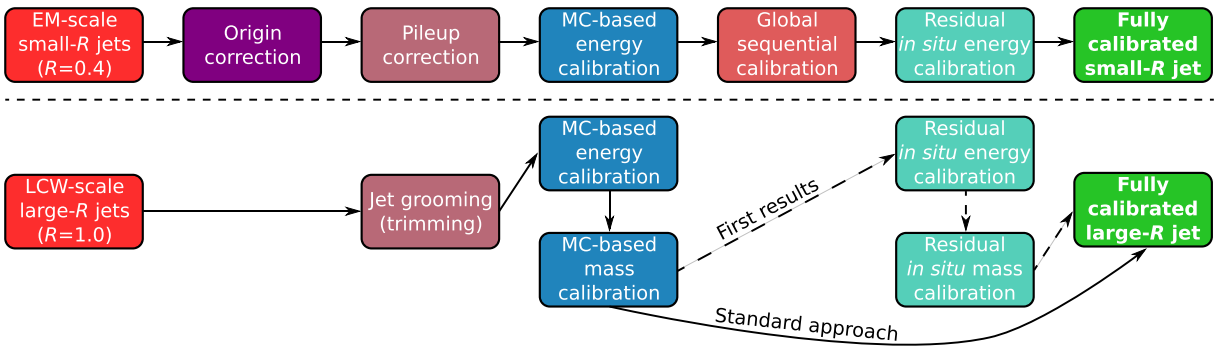

Figure 4.10. Calibration sequence for $R = 0.4$ jets and $R = 1.0$ jets [170]

PV while keeping the jet energy constant.

Pile-up correction

To adjust for pile-up in an event, the energy of the jet candidate is subtracted based on the average energy density (ρ) and the actual jet area (A) [64]. The ρ value is determined by analyzing jets within $|\eta| < 2$ clustered using the k_t algorithm, which evaluates the value in the (y, ϕ) plane. This algorithm clusters soft radiation and considers the soft background while defining the jet, resulting in some dependence on pile-up due to the evaluation of rho in the calorimeter's low-occupancy region and the detector's limited range. A second correction is obtained through the MC simulation using truth particle-level jets, i.e., by running the kt algorithm on charged and neutral truth collider stable particles ($c\tau_0 > 10$ mm) excluding neutrinos and muons.

$$p_{\mathrm{T}}^{\mathrm{corr}} = p_{\mathrm{reco}} - \rho \times A - \alpha(N_{\mathrm{PV}} - 1) - \beta\mu, \tag{4.5}$$

The parameters $\alpha = \frac{\partial p_{\mathrm{T}}}{\partial N_{\mathrm{PV}}}$ (in-time) and $\beta = \frac{\partial p_{\mathrm{T}}}{\partial \mu}$ (out-of-time) are determined by fitting the data in the bins of truth p_T and $|\eta_{\mathrm{det}}|$. In this context, η_{det} is the pseudo-

rapidity evaluated, assuming the jet originates from the geometric center of the detector. The uncertainties associated with the modeling of these parameters are taken into account through systematic uncertainties.

Jet grooming

Due to their large jet area, large-R jets are more vulnerable to pile-ups, which obscure the jet's angular structure; consequently, the hadronic particle decays inside the jet cone are not fully reconstructed. The large-R jets used here are groomed using a trimming algorithm explained in [146].

MC-based calibration

After removing the contribution from the pile-up, the next step is calibrating the jets' energy using information from the MC simulations. This calibration is necessary because the detector does not detect a significant amount of the energy in a hadronic shower. For instance, some of the hadronic shower energy gets absorbed in the inactive areas of the detector, like the cracks. Moreover, hadronic showers rely on the strong force to initiate electromagnetic cascades via the creation of π^0 and $\pi^{\pm}$, which results in a considerable amount of energy being used to split the nuclei by overcoming the binding energy. This energy is not observed and must be accounted for to accurately measure the Jet Energy Scale (JES). This can be achieved in MC simulation by comparing reconstructed jets with jets built from simulated particles, commonly known as "truth jets." Correcting for lost energy and calibrating the average reconstructed jet to the truth scale is achieved by using the response $X_{\text{reco}}/X_{\text{truth}}$. The response is used in fine bins of

η and energy to properly account for the detector structure and hadronic interactions. Figure 4.11 shows the Jet energy response as a function of η_{det} and E^{reco}. The large R jets ideally have a well-defined mass because they represent hadronic decays of massive particles. It is thus useful for the reconstructed large-R jets to have a mass corresponding to the parent massive particle to help with their identification and interpretation. A matching procedure known as the Jet Mass Scale (JMS) calibration is used to match truth to reconstructed jets with the mass response parametrized in p_{T}, mass, and η.

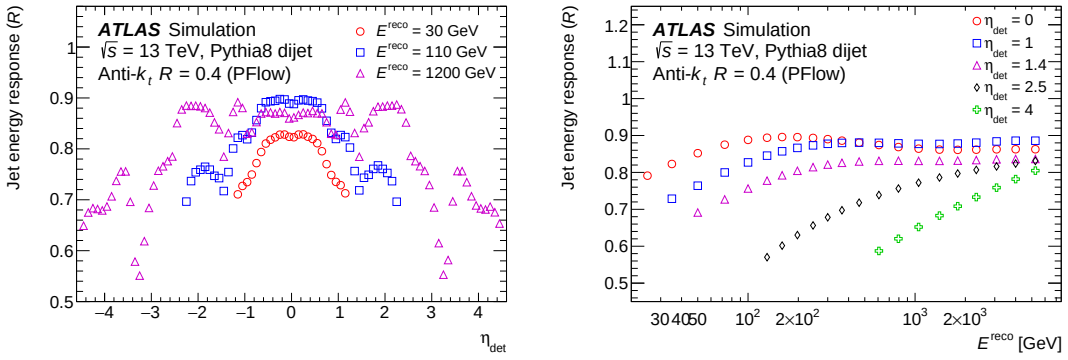

Figure 4.11. The average energy response as a function of reconstructed jet η_{det} and energy E^{reco}. Figure from [85].

Global sequential calibration

The response of a detector to a jet is influenced by various factors such as energy distributions, flavor compositions, punch-throughs, and whether a quark or gluon initiated the jet. To further improve the Jet Energy Scale (JES) of small R jets, a Global Sequential Calibration (GSC) is applied to consider the jets' properties. The GSC is a series of

multiplicative corrections that only affect the resolution of the jet response function, not its central value, ending up with a better Jet Energy Resolution (JER) and resulting in a narrower distribution of jet energy. Applying GSC improves jet p_{T} resolution by almost 30% in the 20 GeV to 2 TeV range.

In-situ calibration

After correcting the jets to their particle level using MC, JES, and GSC, the final step is calibrating them to address any differences between the jet response observed in the data and the MC simulations [85]. Such differences arise due to imperfect simulation of the detector materials and the physics processes involved, such as the hard scatter, underlying event, jet formation, pile-up, and particle interactions with the detector. The *in situ* calibration measures the jet response separately in data and MC simulation and applies the ratio as an additional correction in data. The small-R jets correction process depends on measuring the average jet response by comparing the jet p_{T} to that of a well-reconstructed and calibrated object in Z+jets, γ+jets, and multi-jet events in both data and MC simulation. The response ratio, described in equation 4.6, is used to minimize the effect of extra jets in the event from any error in the reconstruction.

$$\mathcal{R}_{in\ situ} = \left\langle \frac{\text{jet } p_{\mathrm{T}}}{\text{reference object } p_{\mathrm{T}}} \right\rangle, \tag{4.6}$$

The first set of corrections for the small R jets is the $|\eta|$ inter-calibration accounting for the differences in the technologies used in the different η regions. In this correction, the well-understood central jets $|\eta| < 0.8$ are used as a reference to calibrate the forward jets in the range $0.8 < |\eta| < 4.5$. The leading source of uncertainty for this correction comes from

the choice of MC sample used for the correction. The second round of corrections is carried out based on the jet's transverse momentum (p_{T}) and aims to rectify the calorimeter's response to hadrons; it relies on the missing momentum projection fraction technique. At the particle level in a γ+jets event, the sum of the transverse momenta of the photon and the hadrons recoiling against it is zero, i.e., $p_{\mathrm{T}}^{\gamma} + p_{\mathrm{T}}^{\mathrm{Recoil}} = 0$. At the reconstruction level, this can be expressed as

$$p_{\mathrm{T}}^{y} + \mathcal{R}_{MPF} \times p_{\mathrm{T}}^{\mathrm{Recoil}} = -\mathrm{E}_{\mathrm{T}}^{\mathrm{miss}}. \tag{4.7}$$

Here, $\mathcal{R}_{MPF}$ is the calorimeter's response to the hadrons, and $\mathrm{E}_{\mathrm{T}}^{\mathrm{miss}}$ is obtained from the topo-clusters. It is then possible to rectify the measured jet's response using the derived value of $\mathcal{R}_{MPF}$. The calibration for corrections is assessed in events involving $Z \to ee/\mu\mu$+jets for low momentum ($20 < p_{\mathrm{T}} < 500$ GeV) and γ+jets for intermediate momentum ($30 < p_{\mathrm{T}} < 900$ GeV). For higher p_{T}, QCD multi-jet events are used. A calibration factor can be calculated using another lower-energy jet recoiling against a single jet. Above 1 TeV calibration factors are derived using other lower energy jets recoiling against a single jet in Multi-Jet balancing methods to extend the calibration up to 2 TeV of jet p_{T}. A weighted combination of the three methods, as shown in Figure 4.12 (left), is used to obtain a smooth correction function to correct the data.

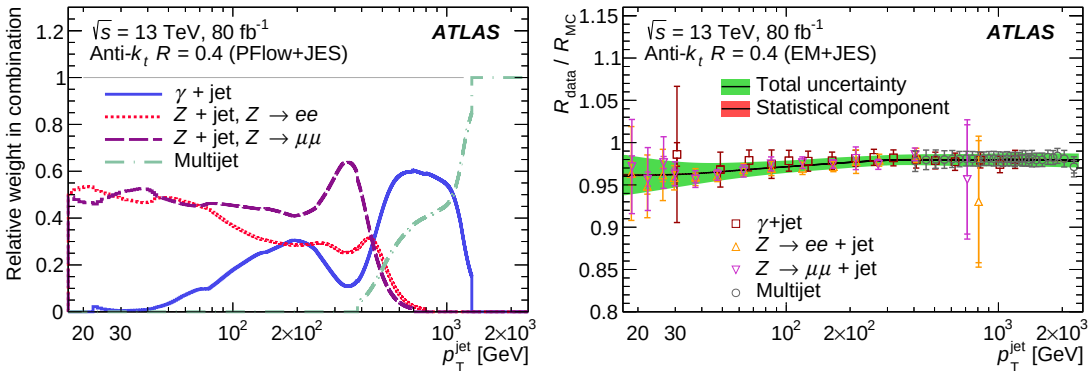

Figure 4.12. The figure on the left shows the relative weight assigned to different techniques in the evaluation of *in-situ* calibration as a function of jet p_{T}. The figure on the right shows the *in-situ* response factor as a function of jet p_{T} evaluated from the 2015, 2016, and 2017 ATLAS data set. Figures from [85].

An in-situ calibration method is also used to calibrate the large R jets. For the large-R jets, it involves the R_{trk} parameter, which is defined as

$$R_{trk} = \frac{(X_{calo})/X_{track})_{data}}{(X_{calo})/X_{track})_{MC}}. \tag{4.8}$$

The R_{trk} parameter helps estimate the differences between the calorimeter and tracker jet representations by assigning uncertainties to X, as shown in figure 4.12 (right). The forward-folding procedure is then applied to constrain the JMS for both data and MC. Finally, the large-R jet in-situ calibration process combines forward-folding and R_{trk} methods.

The Jet energy resolution is parameterized as a function of p_{T} in equation 4.9

$$\frac{\sigma(p_{\mathrm{T}})}{p_{\mathrm{T}}} = \frac{N}{p_{\mathrm{T}}} \oplus \frac{S}{\sqrt{p_{\mathrm{T}}}} \oplus C. \tag{4.9}$$

The first term on the right is the noise term with a constant N, the second term

is a stochastic term with a constant S, and the third term is a constant to parameterize the fluctuations due to the jet formation position and its interaction with the detector. Figure 4.13 (left) shows the different components of the JER as a function of jet p_{T}.

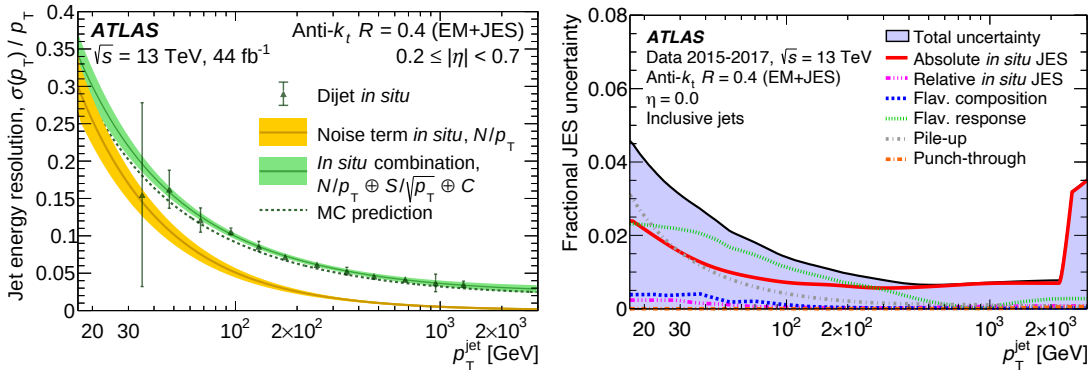

Figure 4.13. The figure on the left shows the relative jet energy resolution as a function of jet p_{T}. The figure on the right shows the total uncertainty and its components as a function of jet p_{T}. Figure from [85].

The JES (Jet Energy Scale) and JER (Jet Energy Resolution) are evaluated through calibration stages involving many systematic uncertainties. These uncertainties are mainly associated with the data-driven calibration stages and depend on factors such as the available statistics, the assumptions made on the simulated samples, the mismodeling of pile-up, the jet flavor composition in MC, and uncertainties on the energy scales of other objects. The systematic uncertainties are assessed by varying parameters of the object selection and using alternative simulated samples. The total uncertainty on the JES calibration is 4.5% at 20 GeV and reduces to a few percent above 200 GeV in di-jet events. On the other hand, the uncertainties in the JER calibration vary between

3% at 20 GeV and less than 1% above 40 GeV in a di-jet sample. Figure 4.13 (right) shows the components of the JES uncertainties as a function of jet p_{T}.

4.3.3 Jet Flavor Tagging

In physics analysis, it is important to identify the flavor of a heavy quark from which a jet originated to fully reconstruct the hard scatter process. Flavor tagging, which identifies the flavor of jets, has been specially developed in ATLAS to identify b-quark jets. This technique is vital for many analyses, including observing $VH(H \to bb)$ decays and searches like $VH(H \to bb)$, $A \to ZH \to \ell\ell tt/\nu\nu bb$ and many others. Different methodologies are used to distinguish b-jets, c-jets, and light jets, which include jets from u, d, s-quarks, and gluons. Jets from hadronic decays of τ-leptons are also considered. The algorithms used for flavor tagging require an understanding of the characteristics of different jets, schematically shown in Figure 4.14. This section outlines the principles of the flavor tagging methodologies used in the ATLAS experiment, focusing on the methods developed for b-jet identification.

- **b-jets** are produced when a b-quark hadronizes into a B-hadron. These B-hadrons have a relatively long lifetime of ~ 1.6 ps ($c\tau \sim 450$ μm), which allows them to travel around 5 mm inside the detector before decaying. This results in a secondary vertex (Figure 4.14). B-hadrons have a mass of 5 GeV and carry $\approx 75\%$ of the jet energy, resulting in hard objects inside the jet and a large diversity of decay compared to other jet flavors. The b-hadron typically decays into a c-quark about 90% of the time, forming a c-hadron, which then decays after traveling a few millimeters inside the

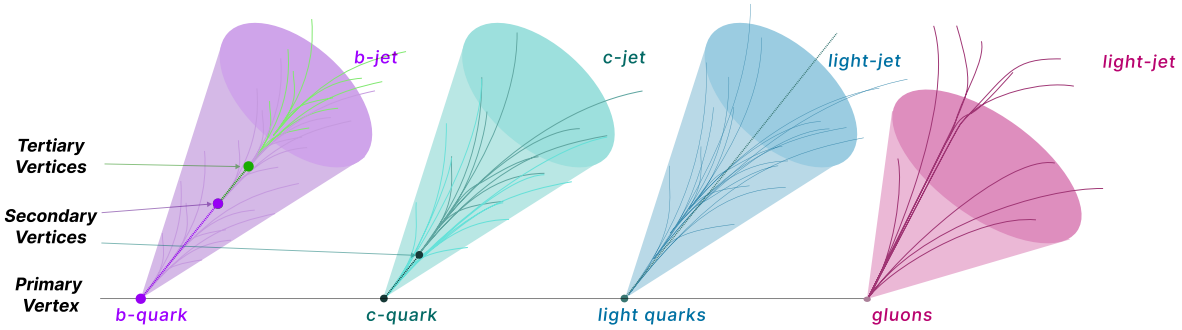

Figure 4.14. A figure depicting the different flavors of Jets and their unique characteristics.

detector, creating a tertiary vertex. It is important to note that the BR ($t \to Wb$) is $\approx 100\%$; hence, identifying b-jets is an important aspect of the $A \to ZH \to \ell\ell tt$ analysis.

- **c-jets** originate from the hadronization of a c-quark, usually forming a D or D^*-meson (or a Λ_c baryon) with a lifetime between 0.2 and 1 ps which decays to a kaon via $c \to s$ transition. The D-meson (mass $\sim$ 2 GeV) has a shorter decay length and carries around 55% of the jet energy, leading to a low multiplicity of decay products and softer jets compared to the b-jets.

- **light-jets** originate from the hadronization of u, d, s-quark or gluons. The light quarks hadronize into light hadrons instantaneously, combining hadrons with different lifetimes that share the jet's energy. Due to the different lifetimes, the reconstruction of a secondary vertex is not possible within the ID. Jets originated from the hadronization of gluons share the same characteristics except that the jets are

wider.

The ATLAS experiment utilizes Different flavor tagging algorithms to identify and classify jets. The tagging strategy comprises two levels of taggers. The first level of taggers extracts low-level features such as the track's impact parameters, location of vertices, and other pertinent information. The output from the low-level taggers is then input into the high-level taggers, which utilize machine-learning techniques to classify the jets into different flavors by treating the problem as a multi-class classification problem. The high-level taggers output the probability of the jet being of a particular flavor.

Low level taggers

- **Impact Parameter Based Algorithms** These algorithms utilize the impact parameters of the tracks in the ID. IP2D and IP3D are impact parameter-based algorithms [25]. A log-likelihood ratio (LLR) discriminant is created based on the signed impact parameter significances, $d_0/\sigma(d_0)$ for the transverse and $z_0 \sin\theta/\sigma(z_0)$ for the longitudinal. Due to their longer lifetime, the b and c hadron tracks are expected to have larger impact parameters than those originating from the PV, leading to an asymmetric LLR. The IP2D algorithm uses only the transverse impact parameter, and the IP3D algorithm uses both transverse and longitudinal parameters. The output of these algorithms is fed forward to the high-level taggers. Figure 4.15 shows the LRR for the IP2D and the IP3D algorithm for b, c and light flavor jets.

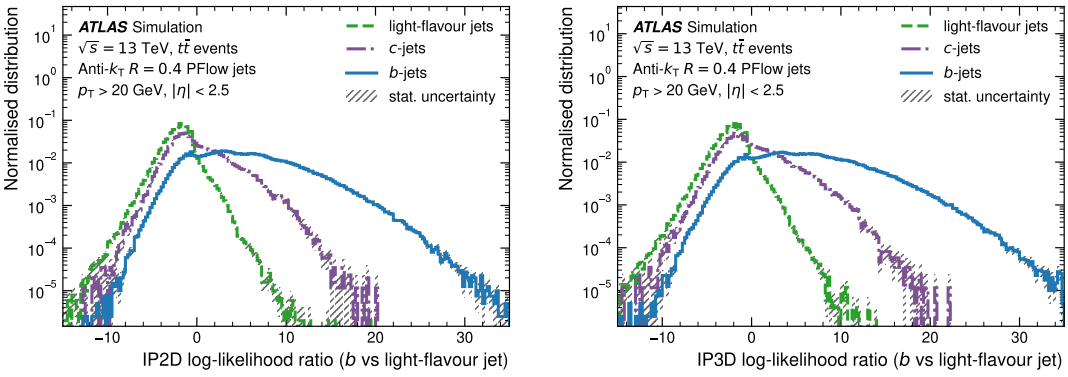

Figure 4.15. The LLR for the IP2D (left) and IP3D (right) b-tagging algorithm for b (solid green), c (dashed blue), and light-flavor (dotted red) jets in $t\bar{t}$ events. Figure taken from [119]

- **Secondary Vertex Based Algorithms** These algorithms aim to reconstruct secondary vertices within a jet. ATLAS uses the SV1 algorithm seeded by a pair of tracks, which can be identified as a two-track vertex. A single vertex is formed from the remaining tracks, and outlier tracks are iteratively removed. Properties like invariant vertex mass, number of tracks associated, and distance from the primary vertex are calculated and used as input to high-level taggers [172]. Figure 4.15 (left) shows the SV1 numbers of two-track vertices for different flavors of jets.

- **Decay chain multi-Vertex Algorithms** These algorithms aim at reconstructing the full decay chains using the Kalman filter [139]. ATLAS uses the JETFitter algorithm to reconstruct the full $b-$ and $c-$hadron decay chains. The $b-$hadron decay chains are reconstructed, assuming that secondary and tertiary vertices lie on a single line and are associated with a single track. Figure 4.15 (right) shows

the JetFitter numbers of two-track vertices for different flavors of jets. The reconstructed vertices' topological variables similar to those from SV1 are calculated and used as inputs to the high-level taggers [185].

- **RNNIP** A recursive neural network-based algorithm takes the signed impact parameter significance of each track, angular distances of each track from the jet axis, and the fraction of jet p_{T} [137].

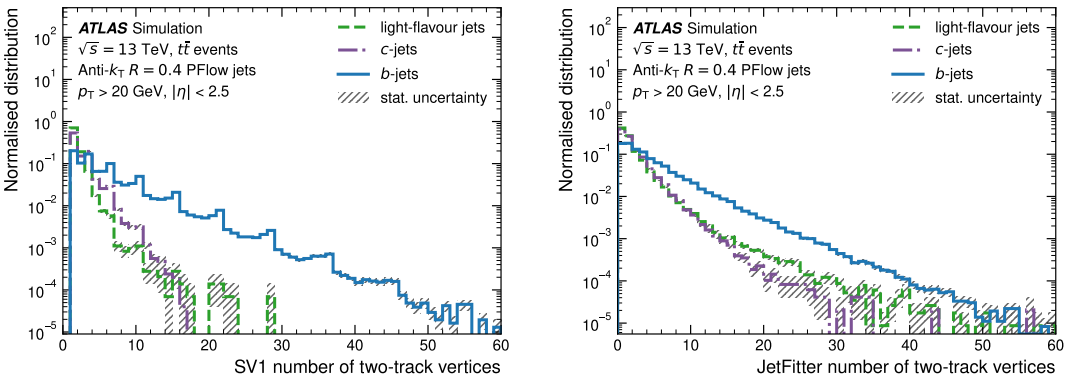

Figure 4.16. The number of two track vertices from the SV1 (left) and JETFITTER (right) b-tagging algorithm for b (solid green), c (dashed blue), and light-flavor (dotted red) jets in $t\bar{t}$ events. Figure taken from [119]

The output from the individual tagging algorithm is used as the input to the multivariate classifiers to form a final tagging discriminant.

High level taggers

- **MV2c10** The MV2C10 is a boosted decision tree (BDT) trained to discriminate between $b-$jets from a background of 7% $c-$jets and 93% light flavor jets from

simulated $t\bar{t}$ and Z' events. It uses the output of all the low-level taggers except the RNNIP score. Along with the tagger-related input variables, the p_{T} and $|\eta|$ of each jet are also used to exploit correlations with other input variables. To remove any bias from the kinematics of the jet flavors, the distributions of p_{T} and $|\eta|$ are reweighed for the b, c-jet to match with the light-flavor jets [78].

- **DL1** The DL1 tagger uses a deep-learning classifier with a feed-forward neural network architecture. The jet tagging is treated as a multi-class classification problem, and the outputs are the probabilities of the jet being a b (p_b), c (p_c), or light-jet (p_{light}). The output probabilities allow one to use it as a $b-$ or $c-$jet tagger [78]. The discriminant for b-tagging is constructed as

$$D_{\mathrm{DL1r}} = \ln\left(\frac{p_b}{f_c \cdot p_c + (1 - f_c) \cdot p_{\mathrm{light}}}\right) \tag{4.10}$$

The parameter f_c is set to 0.012 in ATLAS. Similarly Equation 4.10 the c-tagging discriminant constructed with $f_b = 0.2$ is given as

$$D^c_{\mathrm{DLlr}} = \ln\left(\frac{p_c}{f_b \cdot p_b + (1 - f_b) \cdot p_{\mathrm{light}}}\right). \tag{4.11}$$

For the high-level taggers, the efficiency of tagging a b-jet correctly is p_{T} dependent and given as

$$\epsilon_b(p_T) = \frac{N^{\text{b-jets}}_{\text{passing selection}}(p_T)}{N^{\text{b-jets}}_{\text{total}}(p_T)}, \tag{4.12}$$

where $N^{\text{b-jets}}_{\text{passing selection}}(p_T)$ is the number of b-tagged b-jets among $N^{\text{b-jets}}_{\text{total}}(p_T)$, the number of b-jets in the sample. Similar efficiency can be defined for misidentification and rejection of c- and light jets. WPs are defined by applying fixed cuts in the output score corresponding to $b-$jet efficiencies of 60%, 70%, 77%, and 85%. Additionally, analysis-specific pseudo-continuous b-tagging WPs are defined, e.g., for the VH ($H \to b\bar{b}$) analysis. Figure 4.17 compares the b-jet and c-jet tagging efficiency for the different jet tagging algorithms in the $t\bar{t}$ sample at 77% WP.

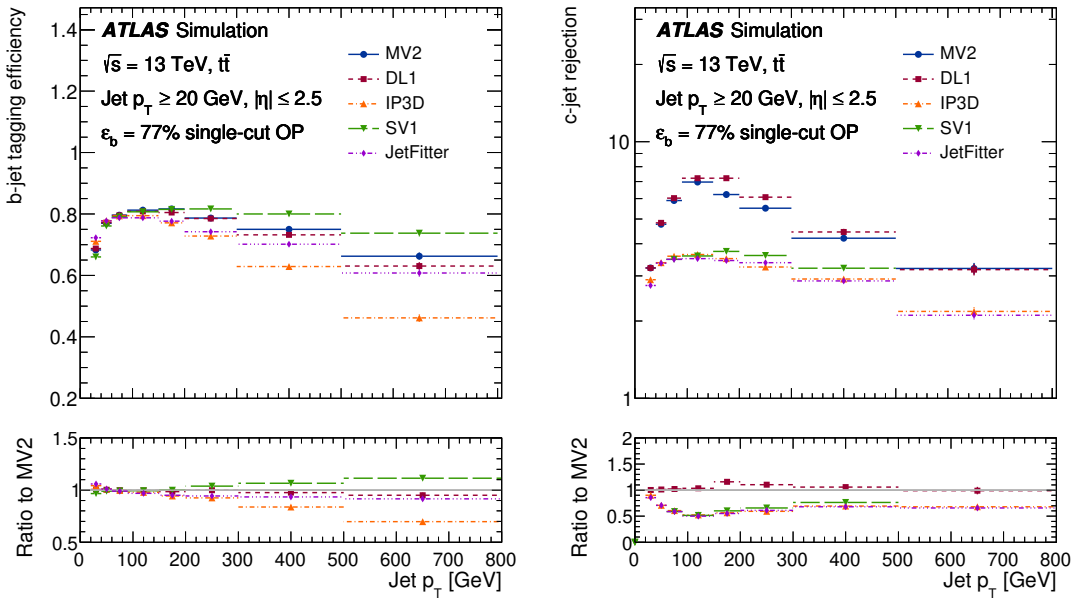

Figure 4.17. The b-jet tagging efficiency (left) and the c-jet rejection for different algorithms in the simulated $t\bar{t}$ events. Figure taken from [84]

4.4 Missing transverse energy

The only SM particles not detected with the ATLAS detector are the neutrinos since they interact very weakly, and interaction cross-sections with matter are extremely small. Information about neutrinos' presence can be inferred indirectly using energy/momentum conservation in the transverse plane. To a good approximation, the incoming partons do not carry any initial transverse momentum. Therefore, the vector sum of all particles should sum up to zero in the transverse plane. The missing transverse energy ($E_{\mathrm{T}}^{\mathrm{miss}}$) is a 2D vector defined in the transverse plane of the collisions that acts as a proxy for the non-interacting particles. The objects used in reconstructing the $E_{\mathrm{T}}^{\mathrm{miss}}$ can be divided into two categories: *hard term* and *soft term*. The hard term includes electrons, muons, photons, tau leptons, and jets. The soft term comprises the charged-particle tracks and momentum deposits in the calorimeters associated with the hard scatter but not assigned to any hard object. The different components used for the reconstruction of $E_{x(y)}^{\mathrm{miss}}$ are given in 4.13

$$E_{x(y)}^{\mathrm{miss}} = -\sum_{h\in\{\text{hard term}\}} p_{x(y),h} - \sum_{h\in\{\text{soft term}\}} p_{x(y),s} \tag{4.13}$$
$$\underbrace{\underbrace{\underbrace{-\sum_{electrons} p^{e}_{x(y)}}_{E^{\mathrm{miss},e}_{x(y)}} \underbrace{-\sum_{muons} p^{\mu}_{x(y)}}_{E^{\mathrm{miss},\mu}_{x(y)}} \underbrace{-\sum_{photons} p^{\gamma}_{x(y)}}_{E^{\mathrm{miss},\gamma}_{x(y)}} \underbrace{-\sum_{\tau\text{-leptons}} p^{\tau_{had}}_{x(y)}}_{E^{\mathrm{miss},\tau_{had}}_{x(y)}} \underbrace{-\sum_{jets} p^{jets}_{x(y)}}_{E^{\mathrm{miss},jet}_{x(y)}}}_{\text{hard term}} \underbrace{-\sum_{\text{unused tracks}} p^{\text{tracks}}_{x(y)}}_{E^{\mathrm{miss,\ soft}}_{x(y)}}}_{\text{soft term}}$$

The x and y components of the E^{miss} can be used to calculate the $E_{x(y)}^{\mathrm{miss}}$ as

$$E_{\mathrm{T}}^{\mathrm{miss}} = \sqrt{(E_x^{\mathrm{miss}})^2 + (E_y^{\mathrm{miss}})^2}. \tag{4.14}$$

Since $E_{\mathrm{T}}^{\mathrm{miss}}$ reconstruction involves information about the entire event, it is quite an imprecise object. A dedicated overlap removal is applied to avoid double-counting the signatures that can be counted in multiple object types. To account for uncertainties related to the track-based soft term, processes where no $E_{\mathrm{T}}^{\mathrm{miss}}$ is expected, such as $Z \to \mu\mu$ with no jets in the event, are used for such estimation. The $E_{\mathrm{T}}^{\mathrm{miss}}$ soft term's scale is calculated in topologies where $E_{\mathrm{T}}^{\mathrm{miss}}$ recoils against the reconstructed Z-boson in the transverse plane. The resolution of $E_{x(y)}^{\mathrm{miss}}$ varies depending on the pile-up, e.g., for $\mu \sim 5$, the resolution is about 10 GeV whereas for $\mu \sim 40$ the resolution is about 20 GeV.

$E_{\mathrm{T}}^{\mathrm{miss}}$ is a powerful signature for BSM searches where the new particle has an extremely weak interaction cross-section with the detector material, e.g., dark matter searches or supersymmetric particles.

CHAPTER 5

SEARCH FOR $A \to ZH \to \ell\ell t\bar{t}/\nu\bar{\nu}b\bar{b}$ DECAY

In 2012, the ATLAS and CMS collaborations discovered a Higgs boson (mass=125 GeV), which was confirmed to be consistent with the Standard Model (SM) predictions [30, 72]. However, there are still unanswered questions about whether the Higgs boson is part of an extended scalar sector as proposed by many theories beyond the SM that could provide a solution to the shortcomings of the SM explained in Section 2.1.3. These questions have motivated experimental searches at the LHC, leading to the exploration of extended scalar sectors [108] like the two-Higgs-doublet model (Section 2.1.4). Adding the second Higgs doublet in the scalar sector adds four new degrees of freedom (DOF), leading to eight DOF (four from each doublet). After the electroweak symmetry breaking, we end up with the three massive gauge bosons ($W^{\pm}, Z$) and five Higgs boson-like particles. The phenomenology of the 2HDM depends on many parameters, including the masses, mixing angles, and the parameters of the Higgs potential. This model and some of its extensions have received much attention in several new physics scenarios due to its rich phenomenology with possible outcomes such as supersymmetry [101], dark matter [5, 47], axions [144], electroweak baryogenesis (EWB) [75], and neutrino masses [145]. The analysis presented in the thesis explores the parameter space of the 2HDM model with its physics motivations, as detailed in the following section.

5.1 Motivation for $A \to ZH$

The ATLAS and CMS experiments have extensively searched for extended Higgs sectors like the 2HDM in various final states [108]. These searches typically assume a degeneracy between the masses of the heavy CP-even (H) and CP-odd (A) Higgs bosons, a condition motivated by the precision electroweak measurements [183][1]. However, lifting this mass degeneracy opens up new avenues for exploration. This approach is also supported by EWB models, such as for the $A \to Zh$ process [35, 73], where $m_A = m_H$ is assumed for simplicity when interpreting the results. The scenario $m_A \neq m_H$ is particularly compelling from electroweak baryogenesis models [46, 102, 104, 118, 186]; with $m_A > m_H$ being favored for a strong first-order phase transition in the early universe [102]. The A boson mass is also constrained to be not far above 1 TeV, while the h boson is required to have properties similar to those of the SM Higgs boson, making it compatible with the Higgs boson observed at the LHC [102].

5.2 Analysis Overview

The signal model for the analysis is based on the 2HDM model whose potential in its most general form contains 14 free parameters; however, by assuming CP-conservation and adding a softly broken $\mathcal{Z}_2$ symmetry [54], the number of free parameters is reduced to 7: m_A, m_H, $m_{H^\pm}$, $\tan\beta$, $\cos(\beta-\alpha)$, λ_3 (parameter of the scalar potential) and v (the vaccum expectation value). The details of 2HDM phenomenology have been discussed in

[1] In the context of this chapter, H represents the CP-even 2HDM Higgs boson and h represent the SM Higgs boson.

Section 2.1.4.

In the limit $\cos(\beta - \alpha) \to 0$, known as the weak decoupling limit, the h boson couplings equal those of the SM Higgs boson, and the H boson becomes gauge-phobic. The weak decoupling limit and the assumption of a mass degeneracy between the charged and the heavy CP-odd Higgs $m_{H^\pm} = m_A$ forms the basis for the EW baryogenesis models motivating the search for $A \to ZH$ process. For this search the signal signature at the LHC energy levels is an A boson produced either via gluon-gluon fusion (ggF, Figure 5.2a) or in association with b-quarks (bbA, Figure 5.2b) with a subsequent decay into ZH which is dominant when $m_A - m_H \gtrsim 250$, Fig 5.1a. The $A \to ZH$ signature has been sought at the LHC in final states where the Z boson decays leptonically ($Z \to \ell^+\ell^-$) and the H boson decays to $b\bar{b}$, WW and $\tau\tau$ [34, 74, 141]. Although very sensitive, these final states cannot probe the parameter space where m_H greater than 350 GeV, where the $H \to t\bar{t}$ decay becomes dominant (Figure 5.1b) [103, 181].

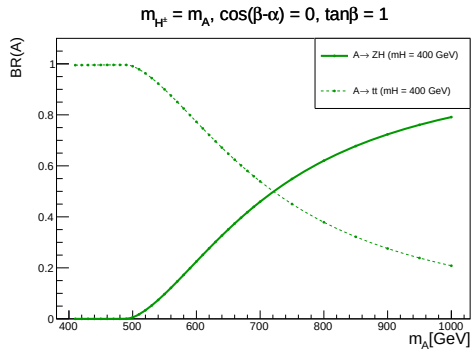

(a) Branching ratio of A for fixed m_H in type-II 2HDM, with $m_{H^\pm} = m_A$, $\cos(\beta - \alpha) = 0$ and $\tan\beta = 1$

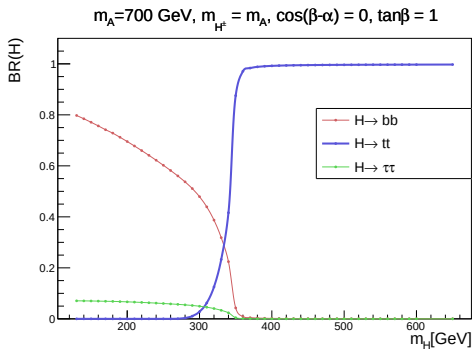

(b) Branching Ratio of H for fixed m_A in type-II 2HDM, with $m_{H^\pm} = m_A$, $\cos(\beta - \alpha) = 0$ and $\tan\beta = 1$

Figure 5.1. The branching ratios for the A boson (left) and the H boson (right).

The final state resulting from the $A \to Z(\to \ell^+\ell^-)H(\to t\bar{t})$ signal process (Figure 5.2a), where one top-quark decays semileptonically and the other decays hadronically, is expected to contain three high-p_{T} leptons, two of which should have an invariant mass close to the Z boson mass, m_Z, and a resonant $t\bar{t}$ pair. The main backgrounds expected in the $\ell\ell t\bar{t}$ channel consist of $t\bar{t}Z$ events, which have a non-resonant $m(t\bar{t})$ spectrum, and events with a jet misidentified as a lepton which mostly arises from the $t\bar{t}$ process with both top quarks decaying semileptonically.

The $A \to Z(\to \nu\bar{\nu})H(\to b\bar{b})$ signal process (Figure 5.2b) not explored till now, leads to a final state with large $E_{\mathrm{T}}^{\mathrm{miss}}$, no visible leptons, at least two b-jets and a resonant $m(b\bar{b})$ spectrum. The main backgrounds in the $\nu\bar{\nu}b\bar{b}$ channel are from $Z+$heavy-flavour (denoted by Zhf)[2] and $t\bar{t}$ processes. Differences between the signal and background processes in lepton multiplicity, flavor, charge, and kinematics are exploited to define background-enriched control regions that can constrain the main backgrounds, as described in the following sections.

Both ggF and bbA production modes are considered in the $\ell\ell t\bar{t}$, and $\nu\bar{\nu}b\bar{b}$ analyses, but the bbA production mode in the $\ell\ell t\bar{t}$ analysis is considered only in the 2 b-tagged region, since in the 3+ b-tagged (more than 3 b-tagged jets) region it leads to a very complicated final state and therefore is difficult to have any clear separation of signal events from the backgrounds with high confidence.

[2]Jets in simulated events are labeled as b/c-jets if a b/c-hadron with $p_{\mathrm{T}} > 5$ GeV is found within a cone of size $\Delta R = 0.3$ around the jet axis, or as light jets (l-jets) otherwise. In the $\nu\bar{\nu}b\bar{b}$ channel, the W/Z+jets events are divided according to the true flavor of the jets which constitute the Higgs boson candidate into heavy flavor, consisting of bb, bc, bl and cc, and light flavor, consisting of cl and ll. These components are denoted by Vhf and Vlf, respectively.

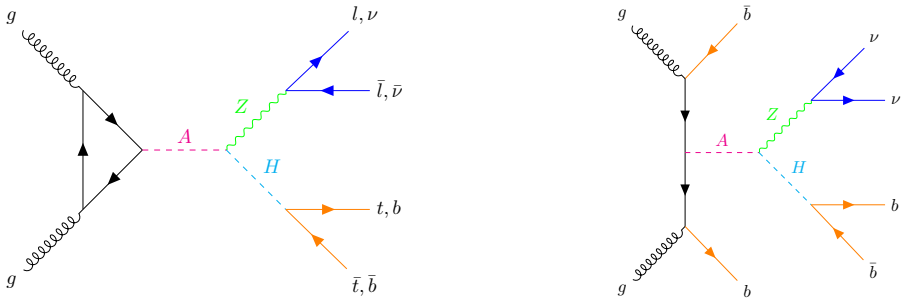

(a) gluon-gluon fusion (ggF) (b) b-associated (bbA)

Figure 5.2. Feynman diagrams for the ggF (a) and bbA (b) production modes. The searches presented in this paper target final states in which the H boson decays into $t\bar{t}$ or $b\bar{b}$ and the Z boson decays into $\ell^+\ell^-$ or $\nu\bar{\nu}$.

5.3 Data and Simulated Samples

5.3.1 Data

The analysis uses data recorded by the ATLAS detector from Run 2 of the LHC corresponding to a total integrated luminosity of 140 fb^{-1} of proton-proton collision data at a center-of-mass energy ($\sqrt{s}$) of 13 TeV. All events were required to pass basic data-quality requirements, ensuring all detector components functioned correctly [20].

Events for the $\ell\ell t\bar{t}$ final state were selected, which were triggered using a logical OR of single-electron triggers with transverse momentum (p_{T}) thresholds varying from 24 to 26 GeV or single-muon triggers with p_{T} thresholds varying from 20 to 26 GeV and a combination of lepton quality and isolation requirements. Leptons were required to be geometrically matched to the corresponding trigger object a p_{T} threshold of 1–2 GeV above the high-level trigger threshold to operate in the region where the trigger reaches its maximum efficiency. Events for the $\nu\bar{\nu}b\bar{b}$ final state were recorded by the missing

transverse momentum ($E_{\mathrm{T}}^{\mathrm{miss}}$) triggers with thresholds varying between 70 and 110 GeV, which become fully efficient for an offline $E_{\mathrm{T}}^{\mathrm{miss}}$ value of approximately 200 GeV. The trigger efficiencies in the simulation are corrected to match those observed in the data. This is done for the $E_{\mathrm{T}}^{\mathrm{miss}}$ triggers following the procedure in Ref. [2]. Events with one or two leptons define background-enriched control regions (CR) in the $\nu\bar{\nu}b\bar{b}$ channel and are selected with the same single-lepton triggers as in the $\ell\ell t\bar{t}$ channel.

5.3.2 Simulated Samples

5.3.2.1 Signal

Simulated signal events were generated with MadGraph5_aMC@NLO 2.3.3 [11], requiring an s-channel A boson that decays into a Z boson and H boson, and using the UFO model provided in Ref. [47] to calculate the loop-induced ggF process with a finite m_{top} value. Both the ggF and bbA production modes (Figure 5.2) were generated at leading order (LO) in QCD for various combinations of (m_A, m_H) using the NNPDF3.0nlo set of parton distribution functions (PDF) [42], with the former process including contributions from top-quark loop-induced processes but neglecting contributions from bottom-loop induced processes, which have a negligible impact on the kinematic distributions. The ggF samples were generated at $\tan\beta = 1$ and the bbA production samples were generated at $\tan\beta = 5$. Simulated events with different values of $\tan\beta$ were obtained via matrix-element (ME) reweighting [14]. MadGraph5_aMC (MG5aMC) [11] calculated the decay widths of the A and H bosons at LO, and finite-width effects were included in the simulations. The decays of the Z and H bosons were simulated using MadSpin [13, 114]. Pythia 8.244 [176] was used to model the parton shower (PS) and

hadronization. Non-resonant diagrams, in which the ZH final state is produced through a top-quark box, were found to have a negligible impact and thus were not included in the simulations. The interference between the resonant diagram shown in 5.2 and the non-resonant box diagrams, and also the SM $t\bar{t}Z$ process, were studied using the UFO model provided in Ref. [123] and found to be negligible. The generation of events in the $\nu\bar{\nu}b\bar{b}$ final state required $E_{\mathrm{T}}^{\mathrm{miss}} > 100$ GeV, which increased the efficiency of the simulation by improving the acceptance. Simulated events in the $\ell\ell t\bar{t}$ final state were filtered to select at least one top-quark decaying semileptonically, with no kinematic requirements on the generator-level leptons.

5.3.2.2 $t\bar{t}$ Background

The $t\bar{t}$ process is one of the main backgrounds for both $\ell\ell t\bar{t}$ and $\nu\bar{\nu}b\bar{b}$ channels. The tree-level diagrams contributing to the $t\bar{t}$ production are shown in Figure 5.3. Each of the two top quarks can decay hadronically and/or leptonically, giving three possibilities of decay as shown in figure 5.4. Nominal MC samples for $t\bar{t}$ events were modeled using the Powheg Box v2 [9, 116, 117, 156] ME generator interfaced with Pythia 8.230 [176] to model the PS and hadronization. Alternative variations are also considered to account for the uncertainties in the choice of ME and PS generators.

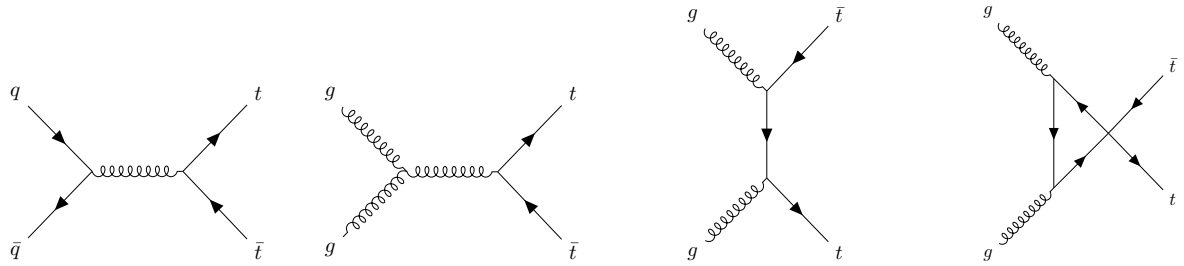

Figure 5.3. Feynman diagrams for the $t\bar{t}$ production.

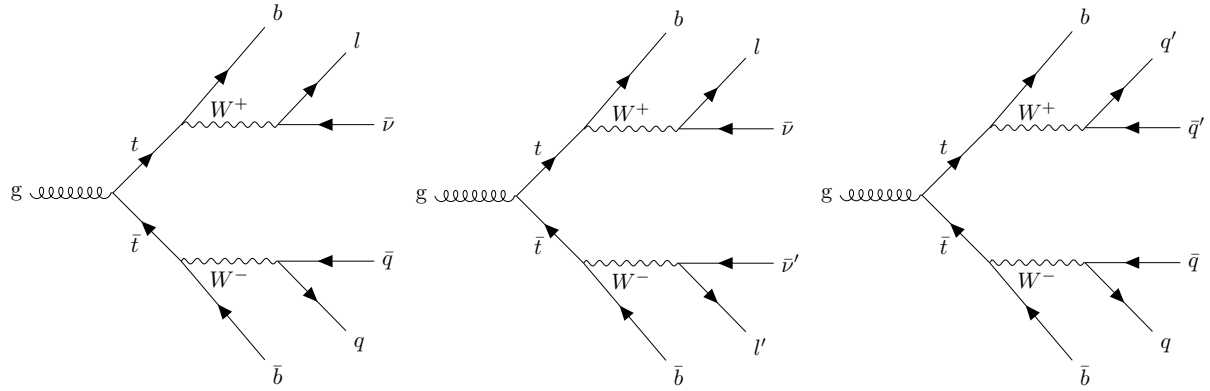

(a) Semi-leptonic (b) Fully-leptonic (c) Fully-hadronic

Figure 5.4. Feynman diagrams for the $t\bar{t}$ decays.

5.3.2.3 $t\bar{t}V$ Background

The $t\bar{t}Z$ process, shown in figure 5.5, has the same signature as the $\ell\ell t\bar{t}$ signal with two top quarks and two leptons. When the mass difference between A and H is in the proximity of the Z boson mass, it becomes extremely difficult to distinguish between the $\ell\ell t\bar{t}$ signal and the $t\bar{t}Z$ background. The $t\bar{t}V$ ($V = W/Z$) events were modeled using the MadGraph5_aMC@NLO 2.3.3 [11] generator interfaced with Pythia 8.210 [176].

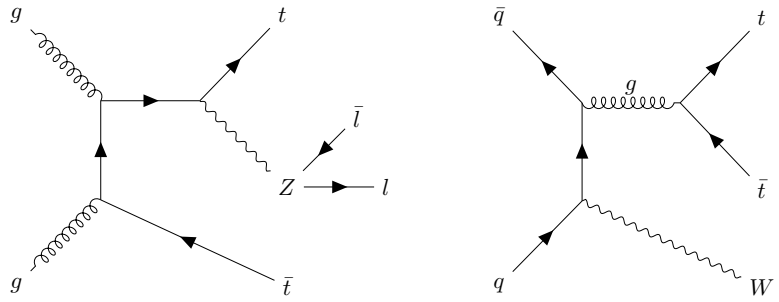

Figure 5.5. Feynman diagrams for the $t\bar{t}Z$ and $t\bar{t}W$.

5.3.2.4 V+Jets Background

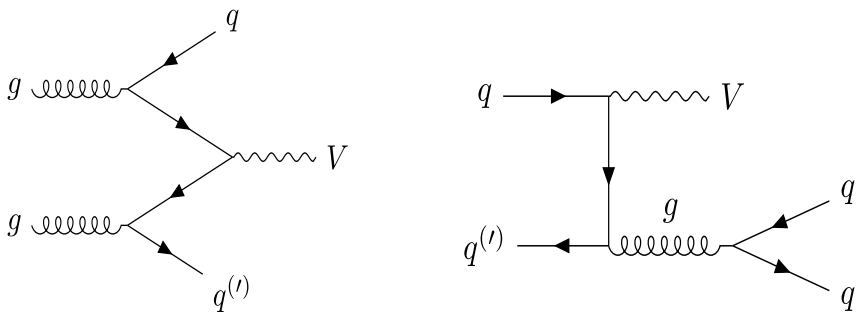

Figure 5.6. Feynman diagrams for the Z+jets and W+jets.

The vector boson V associated with jets (Figure 5.6) is a major background for the $\nu\bar{\nu}b\bar{b}$ channel. The production of V+jets was simulated with the SHERPA 2.2.1 [53] generator using next-to-leading-order (NLO) ME matched with SHERPA parton showers [171] using the MEPS@NLO prescription [70, 133, 134, 135].

5.3.2.5 Other Major Backgrounds

Other major backgrounds include the tW (Figure 5.7, left), tZq (Figure 5.7, right), tWZ (Figure 5.8) and single-top 5.9. The production methods of these backgrounds have been summarized in the Table 5.1

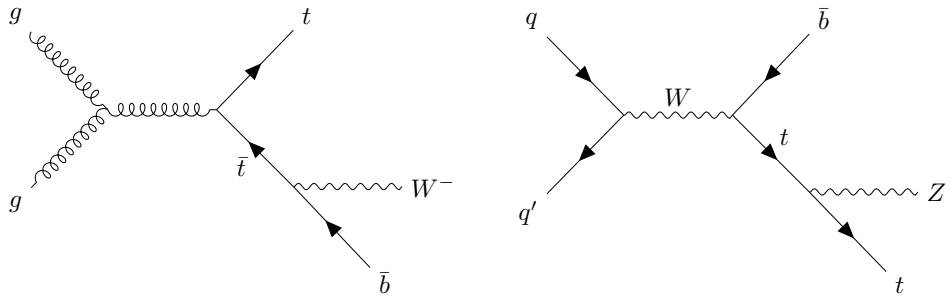

Figure 5.7. Feynman diagrams for the tW and tZq.

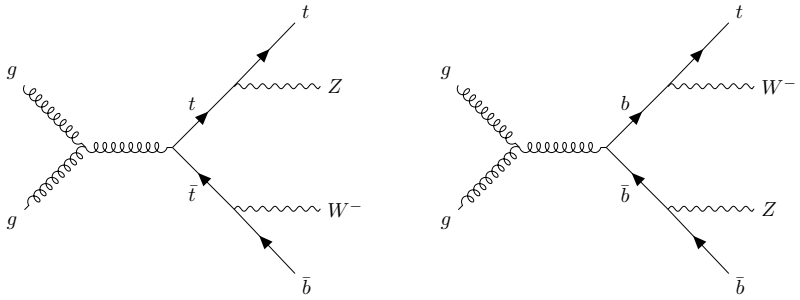

Figure 5.8. Feynman diagrams for the tWZ.

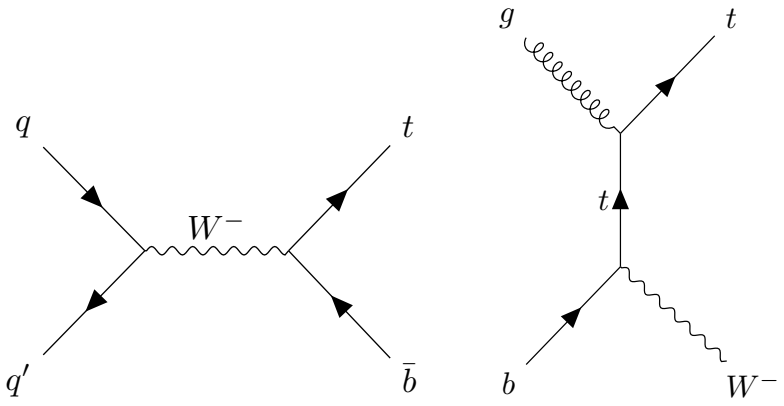

Figure 5.9. Feynman diagrams for the single top.

5.4 Object Selection and Event Categorization

This section aims to describe the selection criteria used to reconstruct the physics objects, the signal and control regions for both $\ell\ell t\bar{t}$ and $\nu\bar{\nu}b\bar{b}$ channels.

5.4.1 Primary vertices

Tracks measured in the ID are used to reconstruct interaction vertices [38]. The one with the highest Σp_{T}^2 of associated tracks is selected as the primary vertex, with its position the proton-proton collision point in the reconstruction.

5.4.2 Electrons

Electrons are reconstructed from a track matched to a cluster built from energy deposits in the calorimeter [23]. They are identified using a multivariate likelihood technique [24], using the 'loose' WP for the $\nu\bar{\nu}b\bar{b}$ channel and the 'medium' WP for the $\ell\ell t\bar{t}$ channel, and they are required to fulfill loose calorimeter isolation criteria. Electrons must

Table 5.1. List of generators used for the simulation of different processes. (N)(N)LO referring to (next-to-)(next-to-)leading order or or (N)NLL referring to (next-to-)next-to-leading-logarithm accuracy in the perturbative expansion of the cross-sections, while EW refers to the inclusion of electroweak corrections at the order indicated. For all samples using the A14 or AZNLO tune, the NNPDF2.3LO [43] or CTEQ6L1 [165] PDF set was used, respectively. The diagram removal (DR) and diagram subtraction (DS) schemes [115] were used to remove the overlap between the $t\bar{t}Z/tWZ$ and $t\bar{t}/tW$ processes, respectively. V denotes a W or a Z boson.

Process	Matrix element	QCD order	PDF	Parton shower	Tune	Cross-section	Special settings
$t\bar{t}$	POWHEG v2 [9, 116, 117, 156]	NLO	NNPDF3.0NLO [42]	PYTHIA 8.230 [176]	A14 [22]	NNLO+NNLL QCD [45, 48, 63, 94, 95, 96, 97]	$h_{\text{damp}} = 1.5m_{\text{top}}$
tW	POWHEG v2 [9, 116, 156, 167]	NLO	NNPDF3.0NLO [42]	PYTHIA 8.230 [176]	A14 [22]	NLO+NNLL QCD [142, 143]	DS scheme [115]
Single top t-channel	POWHEG v2 [9, 113, 116, 156]	NLO	NNPDF3.0NLO [42]	PYTHIA 8.230 [176]	A14 [22]	NLO QCD [8, 140]	4-flavour scheme
Single top s-channel	POWHEG v2 [9, 113, 116, 156]	NLO	NNPDF3.0NLO [42]	PYTHIA 8.230 [176]	A14 [22]	NLO QCD [8, 140]	5-flavour scheme
V+jets	SHERPA 2.2.1 [53]	0,1 jets @ NLO 2,3,4 jets @ LO	NNPDF3.0NNLO [42]	SHERPA [171]	default	NNLO [12]	MEPS@NLO [70, 133, 134, 135]
Diboson $q\bar{q} \to VV$	SHERPA 2.2.1 [53]	0,1 jets @ NLO 2,3 jets @ LO	NNPDF3.0NNLO [42]	SHERPA [171]	default	NLO QCD	MEPS@NLO [70, 133, 134, 135]
Diboson $gg \to VV$	SHERPA 2.2.2 [53]	0,1 jets @ LO	NNPDF3.0NNLO [42]	SHERPA [171]	default	NLO QCD	MEPS@NLO [70, 133, 134, 135]
$q\bar{q} \to Vh$	POWHEG v2 [9]	NLO	NNPDF3.0NLO [42]	PYTHIA 8.212 [176]	AZNLO [1]	NNLO QCD + NLO EW [55, 56, 67, 71, 109, 110, 111]	MINLO [124, 148]
$gg \to Zh$	POWHEG v2 [9]	NLO	NNPDF3.0NLO [42]	PYTHIA 8.212 [176]	AZNLO [1]	NLO+NLL QCD [10, 57, 129]	-
$t\bar{t}V$	MG5AMC 2.3.3 [11]	NLO	NNPDF3.0NLO [42]	PYTHIA 8.210 [176]	A14 [22]	NLO QCD + NLO EW [112]	$t\bar{t}\ell\ell$ scaled by $\mathcal{O}(\alpha_s^3\alpha)$ off-shell correction
$t\bar{t}H$	POWHEG v2 [9, 116, 117, 131, 156]	NLO	NNPDF3.0NLO [42]	PYTHIA 8.230 [176]	A14 [22]	NLO QCD + NLO EW [112]	-
tZq	MG5AMC 2.3.3 [11]	NLO	NNPDF3.0NLO [42]	PYTHIA 8.230 [176]	A14 [22]	NLO QCD	4-flavour scheme, off-shell effects, top decays in MADSPIN [13, 114]
$t\bar{t}t\bar{t}$ $t\bar{t}\,WW$	MG5AMC 2.3.2 [11]	LO	NNPDF3.1LO [42]	PYTHIA 8.186 [175]	A14 [22]	LO QCD	top decays in MADSPIN [13, 114]
tWZ	MG5AMC 2.6.2 [11]	LO	NNPDF3.1LO [42]	PYTHIA 8.235 [176]	A14 [22]	LO QCD	top decays in MADSPIN [13, 114], DR scheme [115]
VVV	SHERPA 2.2.2 [53]	0 jets @ NLO 1,2 jets @ LO	NNPDF3.0NNLO [42]	SHERPA [171]	default	NLO QCD	-

have $p_{\mathrm{T}} > 7$ GeV and $|\eta| < 2.47$. To ensure that they are compatible with the primary vertex, the track associated with the electron candidate is required to have $\sigma(d_0) < 5$ and $|z_0 \sin\theta| < 0.5$ mm, where $\sigma(d_0)$ is the significance of the transverse impact parameter, z_0 is the longitudinal impact parameter and θ is the polar angle of the track.

5.4.3 Muons

Muons are reconstructed by matching track segments in the muon spectrometer (MS) to a track in the ID [28]. They are identified by using selections in the quality of the tracks and the compatibility between the ID and MS measurements; they are required to satisfy the 'loose' identification WP and loose isolation criteria combining calorimeter and track information [28]. Muons are required to have $p_{\mathrm{T}} > 7$ GeV, $|\eta| < 2.5$, $\sigma(d_0) < 3$ and $|z_0 \sin\theta| < 0.5$ mm.

5.4.4 τ-leptons

Hadronically decaying τ-leptons are reconstructed from calorimeter-cell energy clusters [33] formed by the anti-k_t algorithm [65, 66] with a radius parameter of $R = 0.4$ (explained in previous chapter). Either one or three charged tracks must lie within a cone of $\Delta R = 0.2$ around the direction of the hadronically decaying τ candidate, which is identified using a recurrent neural network [26] and a 'loose' WP. The τ-lepton candidates must have $p_{\mathrm{T}} > 15$ GeV and lie within $|\eta| < 2.5$, excluding the calorimeter barrel/endcap transition region ($1.37 \leq |\eta| \leq 1.52$).

5.4.5 Jets

Jets are reconstructed from particle-flow objects [138] formed from ID tracks and calorimeter energy clusters by using the anti-k_t algorithm with a radius parameter of $R = 0.4$. Jets with $|\eta| < 2.5$ ($2.5 < |\eta| < 4.5$) are classified as central (forward) jets and are required to have $p_{\mathrm{T}} > 20$ (30) GeV. Central jets with 20 GeV $< p_{\mathrm{T}} <$ 60 GeV and $|\eta| < 2.4$ are required to pass the 'tight' jet vertex tagger (JVT) [32] WP to suppress jets originating from pile-up interactions.

Jets containing b-hadrons referred to as b-jets, are identified using the DL1r tagger [17]. A WP corresponding to a 77% efficiency in simulated inclusive $t\bar{t}$ events is used for the $\ell\ell t\bar{t}$ channel, while a WP corresponding to a 70% efficiency is used for the $\nu\bar{\nu}b\bar{b}$ channel. The decays of the b-hadrons can produce muons, which are vetoed when building particle-flow objects and, therefore, are not included in the energy of the reconstructed jets. To correct for this effect, the four-momentum of the closest non-isolated muon that satisfies $\Delta R(b\text{-jet}, \mu) < \min(0.4, 0.04 + 10/p_{\mathrm{T}}(\mu)[\text{ GeV}])$ is added to the four-momentum of the b-jet. The corrected four-momentum is used when defining the event selection criteria described in the following section.

5.4.6 Missing transverse momentum

The event's missing transverse momentum, $\vec{E}_{\mathrm{T}}^{\mathrm{miss}}$ (or $E_{\mathrm{T}}^{\mathrm{miss}}$ for its modulus), is defined as the negative vector sum of the transverse momenta of all the observable electron, muon and jet objects described above, plus a soft term comprising ID tracks that are matched to the primary vertex but not to any of the already included objects [15]. An

$E_{\mathrm{T}}^{\mathrm{miss}}$ significance variable ($\mathcal{S}_{\mathrm{MET}}$), sensitive to fake-$E_{\mathrm{T}}^{\mathrm{miss}}$ effects, is defined using the expected resolutions of all objects used in the $E_{\mathrm{T}}^{\mathrm{miss}}$ reconstruction and the correlations amongst them [29]. An overlap removal procedure is applied to avoid double-counting between the reconstructed leptons, including the hadronically decaying τ-leptons and jets.

A common preselection is applied to the $\ell\ell t\bar{t}$ and $\nu\bar{\nu}b\bar{b}$ channels to reject events without a reconstructed primary vertex or events containing jets with properties consistent with beam-induced background processes, cosmic-ray showers, or noisy calorimeter cells [36]. The subsequent channel-specific selections are described in the following sections.

5.4.7 $AZH \to \ell\ell t\bar{t}$ Event Selection

In the $\ell\ell t\bar{t}$ channel, the dominant background consists of $t\bar{t}Z$ events, which produce a non-resonant $m(t\bar{t})$ spectrum, unlike signal events. Another major background consists of $t\bar{t}$ events with two prompt leptons from the top-quark decays and an extra lepton, which is expected to originate from b-hadron decays in 60% of cases or a jet misidentified as a lepton in the remaining 40% of cases. Other backgrounds arise from multi-boson events and events with a single top quark produced in association with vector bosons; these backgrounds generally have lower lepton p_{T}, a non-resonant $m(t\bar{t})$ spectrum, and can be accompanied by Z bosons. Events are therefore separated into signal (SR), control (CR) and validation (VR) regions using a combination of requirements in the following three kinematic quantities: the p_{T} of the third-highest-p_{T} lepton ($p_{\mathrm{T}}(\ell_3)$), the mass of the

Z boson candidate (m_Z^{cand}) and the invariant mass of the H boson candidate (m_H^{cand}), as described below.

Events in all regions must have exactly three leptons (electrons or muons), leading to four flavor combinations eee, $ee\mu$, $\mu\mu e$, and $\mu\mu\mu$. The leptons must have $p_{\text{T}} > 7$ GeV, with the highest-p_{T} lepton having $p_{\text{T}} > 27$ GeV. Furthermore, only events with at least four jets and exactly two b-tagged jets are retained.[3] The events that do not contain any pairs of leptons with opposite-sign charges and the same flavor (OSSF), namely the $e^{\pm}e^{\pm}\mu^{\mp}$ and $\mu^{\pm}\mu^{\pm}e^{\mp}$ combinations, are selected for the same-sign (`ss`) region, and serves as the $t\bar{t}$ CR. Events with at least one OSSF lepton pair are considered further when selecting the SR, other CRs, and VRs.

Requirements on $p_{\text{T}}(\ell_3)$ define the following kinematic regions: the region with $p_{\text{T}}(\ell_3) > 13$ GeV (denoted by `L3hi`) is enriched in signal events, the region with 7 GeV $< p_{\text{T}}(\ell_3) < 13$ GeV (denoted by `L3lo`) is enriched in background events.

The Z candidate is defined as the OSSF lepton pair whose invariant mass is closest to m_Z [182] and only events with $|m_Z^{\text{cand}} - m_Z| < 20$ GeV. Events satisfying $|m_Z^{\text{cand}} - m_Z| < 10$ GeV define the `Zin` region, where most signal events are expected, and the remaining events define the `Zout` region. In the `ss` region, the Z candidate is reconstructed from the pair of leptons with the same flavor same-sign charges, and events with $|m_Z^{\text{cand}} - m_Z| < 20$ GeV are selected.

Combining the $p_{\text{T}}(\ell_3)$ and m_Z^{cand} requirements allows the definition of several re-

[3]For the bbA production mode, the majority of events with three or more b-jets ($\gtrsim 60\%$) are reconstructed in the 2-b-tag region since the additional b-jets are soft and forward.

gions enriched in either signal or background events. The signal events generally populate the `L3hi_Zin` region. Two signal-depleted regions are also defined: `L3lo_Zin`, with approximately equal contributions from Zhf, $t\bar{t}$ and $t\bar{t}Z$ background processes, and `L3hi_Zout`, with relatively large contributions from $t\bar{t}$ and $t\bar{t}Z$ background processes. These signal-depleted regions cannot be used as CRs to simultaneously constrain the normalization of the Zhf, $t\bar{t}$, and $t\bar{t}Z$ backgrounds because they receive fairly similar background contributions and have a limited number of events. They are, therefore, only used as VRs to verify that the fit model (described in Section 5.6) can describe the data in regions that are kinematically close to the SR. Figure 5.10 shows a sketch of the SR, CR, and VR for the $\ell\ell t\bar{t}$ channel with the distribution of Δm in Figure 5.11.

The semileptonically decaying top-quark candidate (t_{lep}) is reconstructed from the lepton not used in the reconstruction of the Z candidate with the b-jet closest in ΔR to this lepton, and $\vec{E}_{\text{T}}^{\text{miss}}$. To improve the resolution in $m_{t_{\text{lep}}}$, the longitudinal-momentum component of the neutrino from the t_{lep} decay is calculated by constraining the mass of the lepton–neutrino system to be equal to the W boson mass, m_W.[4] The hadronically decaying top-quark candidate (t_{had}) is reconstructed from the light-jet pair with mass m_{jj} closest to m_W and the b-jet that is not used in the t_{lep} reconstruction. To improve the resolution in $m_{t_{\text{had}}}$, the four-momenta of the light-jet pair, which constitutes the hadronic W candidate, is rescaled by m_W/m_{jj}.

[4] In the resulting quadratic equation, the neutrino p_z is taken from the real component in case of complex solutions or the smaller component of the two solutions if both solutions are real.

The H candidate is defined as the sum of the four-momenta of t_{lep} and t_{had}, while the A candidate is reconstructed as the sum of the four-momenta of the H candidate and the Z candidate. The fact that the decay of a resonance produces the H and Z candidates for signal events constrains the kinematic properties of these candidates, which depends on the m_A and m_H values of the signal hypothesis. In particular, the H candidate is expected to be produced more centrally than the background events. Thus, requiring the pseudorapidity of the H candidate in the rest frame of the A candidate ($ZH - r.fr$) to satisfy $\left|\eta^{\text{ZH-r.fr.}}_{H-\text{cand}}\right| < 2.2 + 0.0004 \cdot m(t\bar{t})$ [GeV] $- 0.0011 \cdot m(\ell\ell t\bar{t})$ [GeV] provides the optimal sensitivity across the whole (m_A, m_H) plane. The parameters of the linear function defining this requirement are determined by a fit to the values of the $\left|\eta^{\text{ZH-r.fr.}}_{H-\text{cand}}\right|$ selection cut to maximize the expected significance for each (m_A, m_H) hypothesis.

The presence of a signal would manifest itself as a resonance in the $m(t\bar{t})$ and $m(\ell\ell t\bar{t})$ distributions, as well as in the distribution of the mass difference $\Delta m = m(\ell\ell t\bar{t}) - m(t\bar{t})$ [123]. The region expected to contain most of the signal events for a given mass hypothesis m_H^{hypo} is constructed using a sliding window defined by the condition $|m(t\bar{t}) - m_H^{\text{hypo}}| < N \cdot \sigma$, where $\sigma \approx 0.16 \cdot m_H^{\text{hypo}}$ is the resolution in $m(t\bar{t})$ and $N = 2$ (1.5) for $m_H^{\text{hypo}} < (\geq) 500$ GeV; this region is referred as the `Hin` SR. The sideband regions with a lower or higher $m(t\bar{t})$ value define the `Hlo` and `Hhi` CRs, which are used to constrain the normalization of the simulated $t\bar{t}Z$ sample. The N factor, which defines the width of the signal region, is optimized to achieve the highest signal significance.

The four-momentum vector of the H candidate is rescaled by $m_H^{\text{hypo}}/m(t\bar{t})$ to improve the resolution in $m(\ell\ell t\bar{t})$. The rescaling is performed only in the SR, where the

resonance is expected, and is applied to both simulated and data events. After this rescaling, the resolution in $m(\ell\ell t\bar{t})$ improves by as much as a factor of three, particularly for signal hypotheses with small $m_A^{\text{hypo}} - m_H^{\text{hypo}}$ values, and ranges from 3% to 20% for small and large $m_A^{\text{hypo}} - m_H^{\text{hypo}}$ values, respectively.

The fraction of signal events passing the full event selection varies from 2% to 3.5%, depending on the mass hypothesis, and the fraction increases slightly with increasing m_H.

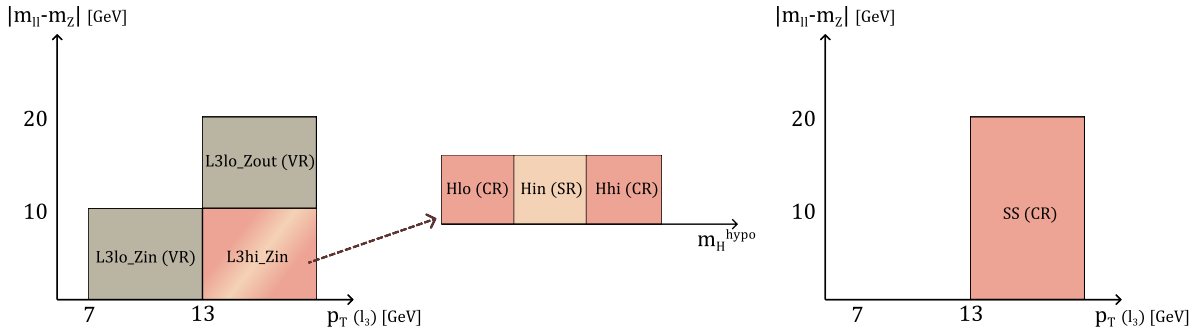

Figure 5.10. A sketch showing the different regions for classifying events in the $\ell\ell t\bar{t}$ channel.

A summary of the selection criteria defining the different regions considered in the statistical analysis is given in Table 5.2. The fit variable distributions in the regions `L3hi_Zin`, `L3hi_Zout`, `L3lo_Zin` and `ss` are shown in Fig. 5.11.

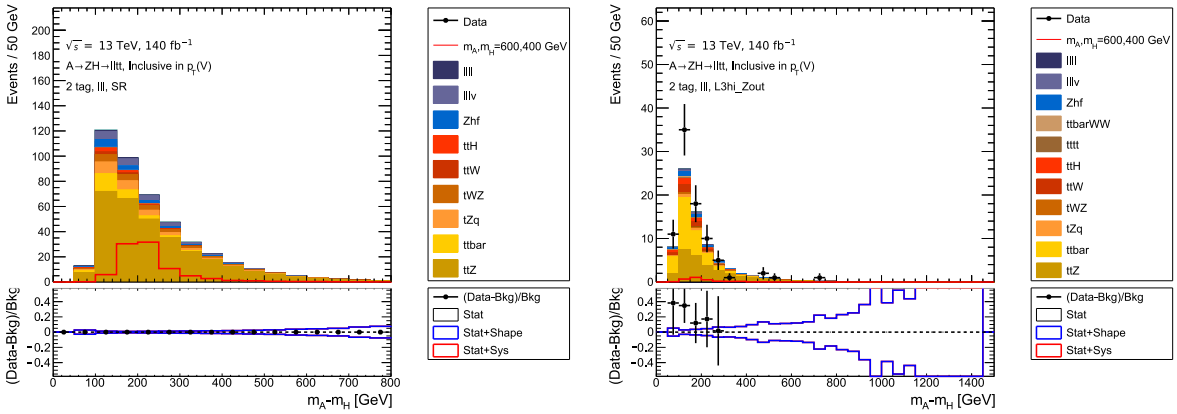

(a) `L3hi_Zin`

(b) `L3hi_Zout`

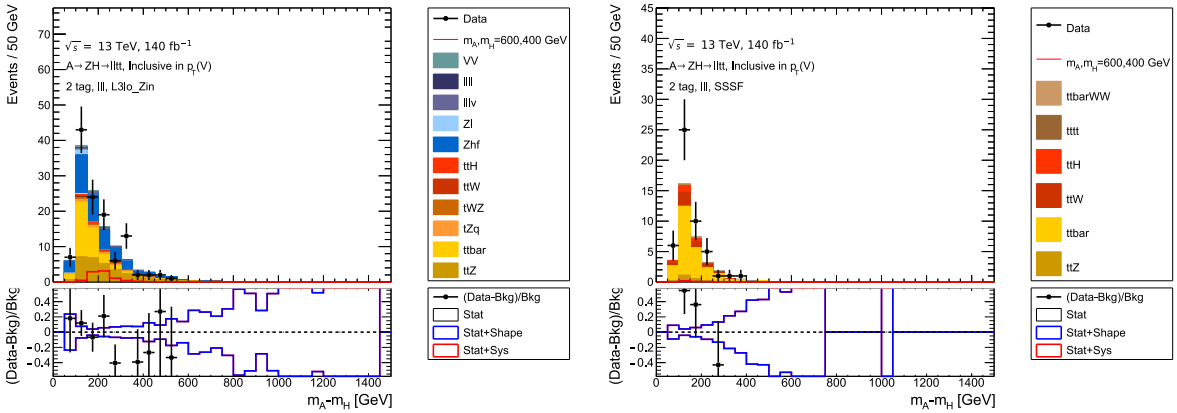

(c) `L3lo_Zin`

(d) SS

Figure 5.11. Pre-fit distribution of Δm in the `L3hi_Zin`, `L3hi_Zout`, `L3lo_Zin` and `ss` regions.

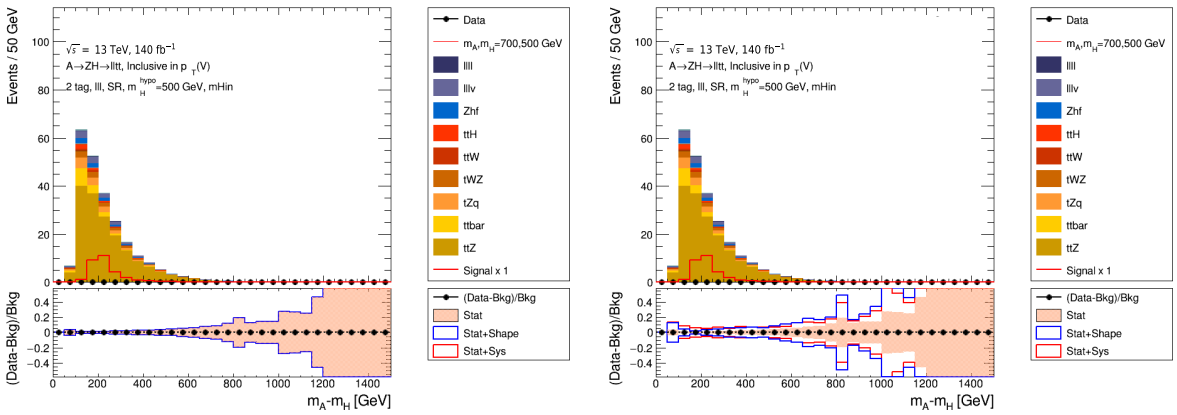

Figure 5.12. The Δm distribution in the signal region `L3hi_Zin_Hin500` without the systematic detector uncertainties (left) and with the systematic uncertainties (right).

Table 5.2. Event selection for the $\ell\ell t\bar{t}$ channel. The SR, CR, and VR symbols next to the region name indicate that this region is used as a signal, control, or validation region in the fit.

Requirement	**Regions**				
	`ss` **(CR)**	`L3hi_Zout` **(VR)**	`L3hi_Zin`		`L3lo_Zin` **(VR)**
			`Hlo` / `Hhi` **(CR)**	`Hin` **(SR)**	
Number of leptons	3				
$p_{\mathrm{T}}(\ell_1)$	> 27 GeV				
Number of jets	≥ 4				
Number of b-jets	2				
$\left\lvert\eta^{\mathrm{ZH-r.fr.}}_{H-\mathrm{cand}}\right\rvert$	$< 2.2 + 0.0004 \cdot m(t\bar{t})[GeV] - 0.0011 \cdot m(\ell\ell t\bar{t})[GeV]$				
$p_{\mathrm{T}}(\ell_3)$	> 13 GeV				> 7 GeV & < 13 GeV
Lepton flavour	$ee\mu/\mu\mu e$	$eee/ee\mu/\mu\mu e/\mu\mu\mu$			
OSSF lepton pairs	0	≥ 1			
$\lvert m_Z^{\mathrm{cand}} - m_Z\rvert$	< 20 GeV	> 10 GeV & < 20 GeV	< 10 GeV		
$\lvert m(t\bar{t}) - m_H^{\mathrm{hypo}}\rvert$ m_H^{hypo} ¡ 500 GeV	-		$> 0.32 \cdot m_H^{\mathrm{hypo}}$	$< 0.32 \cdot m_H^{\mathrm{hypo}}$	-
$m_H^{\mathrm{hypo}} \geq 500 GeV$			$> 0.24 \cdot m_H^{\mathrm{hypo}}$	$< 0.24 \cdot m_H^{\mathrm{hypo}}$	

5.4.8 $AZH \to \nu\bar{\nu}b\bar{b}$ Event Selection

In the $\nu\bar{\nu}b\bar{b}$ channel, the events are split into regions with different lepton multiplicities. The signal is expected to manifest in the region with no leptons. A region consisting of exactly two leptons of the same flavor (`2L`),[5] enriched in Zhf events, and a region with one electron and one muon (`e`μ), enriched in $t\bar{t}$ events, are used to constrain the corresponding background normalizations. Finally, a region with exactly one lepton (`1L`) is used as a VR. The SR, CR, and VR regions are divided into regions with exactly two and at least three b jets, which target the ggF and bbA production modes.

All events must contain at least two b-jets. In events with at least one lepton, the highest-p_{T} lepton must have $p_{\mathrm{T}}(\ell_1) > 27$ GeV. Events in all regions are required to have

[5] In principle, the `2L` region could also contain signal from the $A \to ZH \to \ell^+\ell^- b\bar{b}$ process. Based on the constraints on the cross-section for this process derived in Ref. [34] and given that the `2L` region is included in the statistical analysis as a single bin (see Section 5.6) it has been estimated that the impact of such signal contamination in the `2L` control region would be smaller than 3%, with a negligible impact in the analysis, and is therefore neglected.

$p_T(V) > 150$ GeV (V denotes a Z or W boson), where $p_T(V) = E_{\mathrm{T}}^{\mathrm{miss}}$ in the region with no leptons, $p_T(V) = |\vec{p_{\mathrm{T}}}(\ell) + \vec{E}_{\mathrm{T}}^{\mathrm{miss}}|$ in the 1L region and $p_T(V) = |\vec{p_{\mathrm{T}}}(\ell_1) + \vec{p_{\mathrm{T}}}(\ell_2)|$ in the 2L and eμ regions. A veto of events with more than five jets or events containing any hadronically decaying τ-lepton (τ^{had}) candidates is applied to suppress the $t\bar{t}$ background.

To suppress background from the multi-jet events, only those where the smallest azimuthal angle between $\vec{E}_{\mathrm{T}}^{\mathrm{miss}}$ and any jet, $\min_i \Delta\phi(E_{\mathrm{T}}^{\mathrm{miss}}, \vec{p}_i^{\mathrm{jet}})$, is larger than $\pi/10$ are selected. This background is further suppressed by selecting events with $\mathcal{S}_{\mathrm{MET}} > 3$ ($\mathcal{S}_{\mathrm{MET}} > 10$) in the region with one (zero) lepton(s). These selection criteria are found to reduce the multi-jet contamination to a negligible level. In contrast, a selection $\mathcal{S}_{\mathrm{MET}} < 5$ is applied in the 2L region to reduce the contamination from the $t\bar{t}$ background and maximize the purity in the Zhf background in this CR. The purity of the Zhf background in the 2L region is further increased by retaining only events that satisfy $|m_Z^{\mathrm{cand}} - m_Z| < 10$ GeV.

The H candidate is reconstructed from the two highest-p_{T} b-jets, and events with $m(b\bar{b}) > 50$ GeV are retained. The ΔR between the b-jets forming the H candidate must be smaller than 3.3 (3.5) for events with exactly two (at least three) b-jets.

To further suppress the $t\bar{t}$ background in events with no leptons, two top-quark-mass proxy variables are defined as [4]:

$$m_{\mathrm{top}}^{\mathrm{near/far}} = \sqrt{2 p_{\mathrm{T},b_{\mathrm{near/far}}} E_{\mathrm{T}}^{\mathrm{miss}} \left[1 - \cos\Delta\phi\left(\vec{p}_{\mathrm{T},b_{\mathrm{near/far}}}, \vec{E}_{\mathrm{T}}^{\mathrm{miss}}\right)\right]},$$

where near (far) refers to the H candidate's b-jet that is nearer to (farther from) the $\vec{E}_{\mathrm{T}}^{\mathrm{miss}}$ in azimuthal angle. The b-jet closer to $\vec{E}_{\mathrm{T}}^{\mathrm{miss}}$ in azimuthal angle is used for the calculation

of $m_{\text{top}}^{\text{near}}$, whereas the b-jet farther from $\vec{E}_{\text{T}}^{\text{miss}}$ is used for $m_{\text{top}}^{\text{far}}$. Events are retained only if $m_{\text{top}}^{\text{near}} > 180$ GeV and $m_{\text{top}}^{\text{far}} > 200$ GeV.

The presence of a signal would manifest as a broad resonance in the distribution of the A candidate transverse mass, $m_{\text{T}}(VH)$, in the final state with no leptons. The region expected to contain most of the signal events for a given mass hypothesis m_H^{hypo} is constructed using a sliding window defined by the condition $|m(b\bar{b}) - m_H^{\text{hypo}}| < 2 \cdot \sigma$, where $\sigma = 0.1 \cdot m_H^{\text{hypo}}$ is the resolution in $m(b\bar{b})$. The adjacent regions with a lower or higher $m(b\bar{b})$ define the `Hlo` and `Hhi` regions, used as CRs in the statistical analysis. The `Hlo` and `Hhi` regions contain events from a mix of background processes, so they constrain all the background processes present rather than a specific one.

Table 5.3. Event selection for the $\nu\bar{\nu}b\bar{b}$ channel. The SR, CR, and VR symbols next to the region name indicate that this region is used as a signal, control, or validation region in the fit.

Requirement	**Regions**				
	`2L` **(CR)**	`e`μ **(CR)**	`1L` **(VR)**	`0L`	
				`Hlo` / `Hhi` **(CR)**	`Hin` **(SR)**
Number of jets	2–5				
Number of b-jets	≥ 2				
$m(b\bar{b})$	> 50 GeV				
Number of τ^{had}	0				
$p_{\text{T}}(V)$	> 150 GeV				
$\min_i \Delta\phi(E_{\text{T}}^{\text{miss}}, \vec{p}_i^{\text{jet}})$	$> \pi/10$				
$\Delta R(b_1, b_2)$	< 3.3 (2 b-jets) < 3.5 (≥ 3 b-jets)				
Number of leptons	2		1	0	
Lepton flavour	$ee/\mu\mu$	$e\mu$	e/μ	-	
$p_{\text{T}}(\ell_1)$	> 27 GeV			-	
$\lvert m_Z^{\text{cand}} - m_Z \rvert$	< 10 GeV	-			
$\mathcal{S}_{\text{MET}}$	< 5	-	> 3	> 10	
$m_{\text{top}}^{\text{near}}$	-			> 180 GeV	
$m_{\text{top}}^{\text{far}}$	-			> 200 GeV	
$\lvert m(b\bar{b}) - m_H^{\text{hypo}} \rvert$	-			$> 0.2 \cdot m_H^{\text{hypo}}$	$< 0.2 \cdot m_H^{\text{hypo}}$

The four-momentum vector of the H candidate is rescaled by $m_H^{\text{hypo}}/m(b\bar{b})$ to improve the resolution in $m_{\text{T}}(VH)$. The rescaling is performed only in the SR, where the resonance is expected, and is applied to both simulated and data events. The resolution in $m_{\text{T}}(VH)$ after this rescaling ranges from 8% for signal hypotheses with high m_H and low $m_A - m_H$ values to 27% for signal hypotheses with low m_H and high $m_A - m_H$ values.

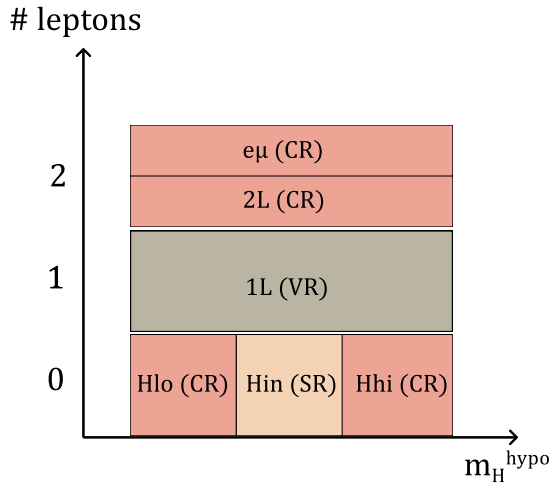

Figure 5.13. A sketch showing the different regions for classifying events in the $\nu\bar{\nu}b\bar{b}$ channel.

The fraction of signal events passing the full event selection varies from less than 1% for signal events with low $m_A - m_H$, which also have low $E_{\text{T}}^{\text{miss}}$, to about 21% for signal events with high $m_A - m_H$. Figure 5.13 shows a sketch of the different regions of the $\nu\bar{\nu}b\bar{b}$ analysis channel. The selection requirements applied in the SR, VRs and CRs are summarized in Table 5.3, and the pre-fit $m_T(VH)$ distribution in the 2-b-tag region (for $m_A = 700$ GeV and $m_H = 500$ GeV) and 3+-b-tag region (for $m_A = 500$ GeV and

$m_H = 200$ GeV) are shown in Figures 5.14 and 5.15 respectively.

5.4.9 Background Composition

The background composition of the regions in the $\ell\ell t\bar{t}$ channel is shown in Figure 5.16. The dominant background in the L3hi_Zin (SR) is $t\bar{t}Z$, and in the same-sign region (CR) is $t\bar{t}$. The background composition of the regions in the $\nu\bar{\nu}b\bar{b}$ channel (for the 2-b-tag and 3-b-tag) are shown in Figure 5.17. The major backgrounds for $\nu\bar{\nu}b\bar{b}$ are Zhf and $t\bar{t}$.

5.5 Systematic uncertainties

The variable of choice for statistical analysis may vary in its normalization and shape due to systematic uncertainties, categorized into two groups based on their source. These uncertainties are separate from the measurement's statistical uncertainties and are known as *experimental uncertainties* and *theoretical uncertainties*. Experimental uncertainties are linked to the performance of the ATLAS detector, particularly in the identification, reconstruction, and calibration of physics objects. Modeling uncertainties, on the other hand, arise from assumptions made in MC simulations of signal, background processes, and cross-section calculations. These uncertainties are called systematic uncertainties and are addressed by the prescription provided by the ATLAS combined performance groups. Systematics uncertainties play a vital role in the statistical analysis where they are incorporated as nuisance parameters (NP) in the Likelihood model.

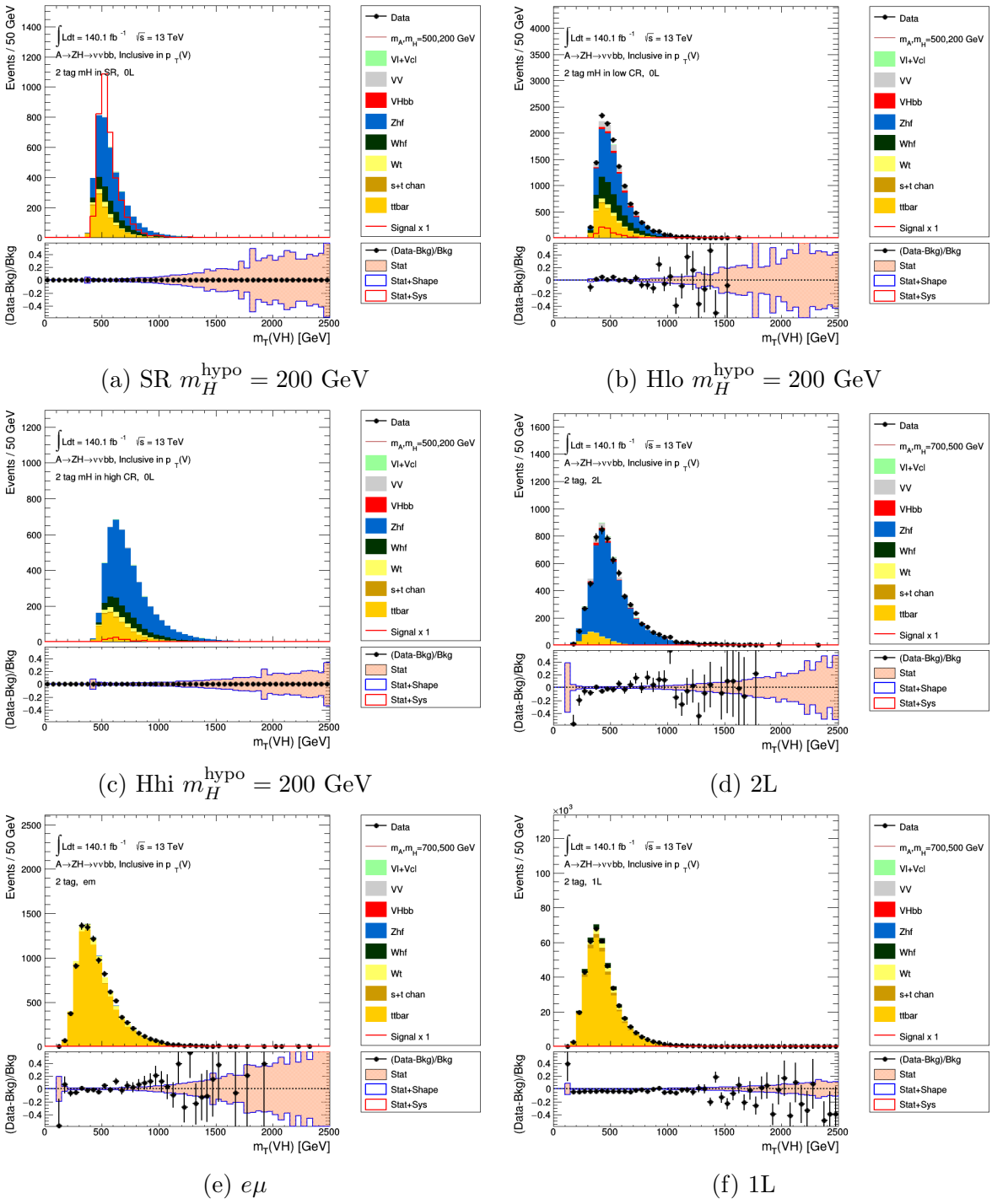

(a) SR $m_H^{\text{hypo}} = 200$ GeV

(b) Hlo $m_H^{\text{hypo}} = 200$ GeV

(c) Hhi $m_H^{\text{hypo}} = 200$ GeV

(d) 2L

(e) $e\mu$

(f) 1L

Figure 5.14. The $m_T(VH)$ distribution in the 2-b-tag region, for the `0L` region (`SR` and m_H side-bands) (top) and the `2L`, `e`μ and `1L` regions (bottom).

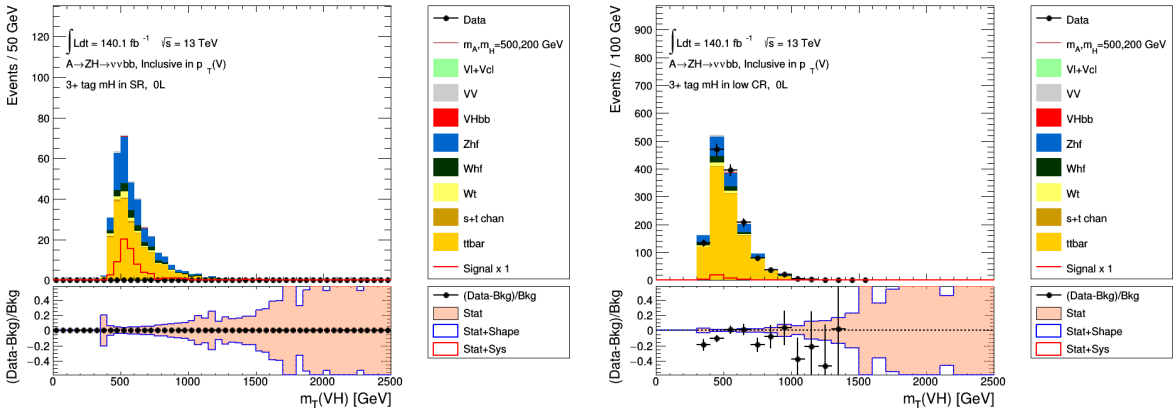

(a) SR $m_H^{\text{hypo}} = 200$ GeV

(b) Hlo $m_H^{\text{hypo}} = 200$ GeV

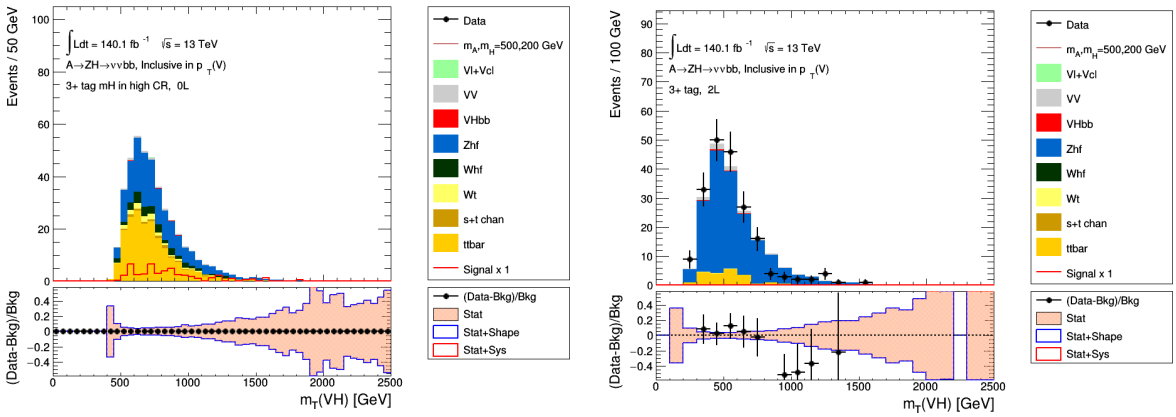

(c) Hhi $m_H^{\text{hypo}} = 200$ GeV

(d) 2L

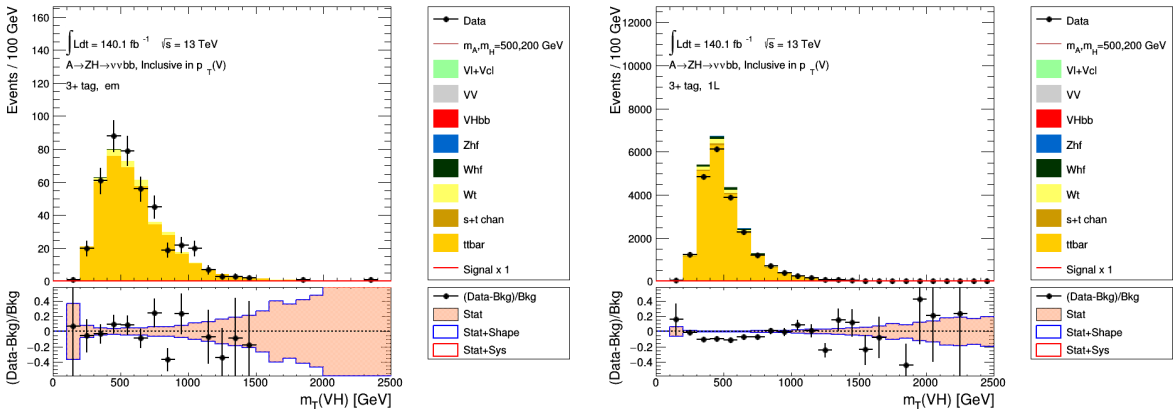

(e) $e\mu$

(f) $1L$

Figure 5.15. The $m_T(VH)$ distribution in the 3+-b-tag region, for the `0L` region (`SR` and m_H side-bands) (top) and the `2L`, `e`μ and `1L` regions(bottom).

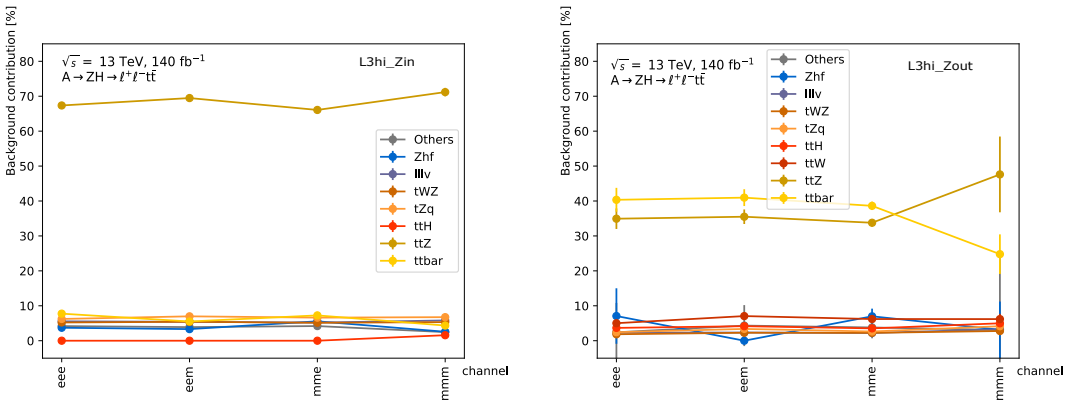

(a) L3hi_Zin

(b) L3hi_Zout

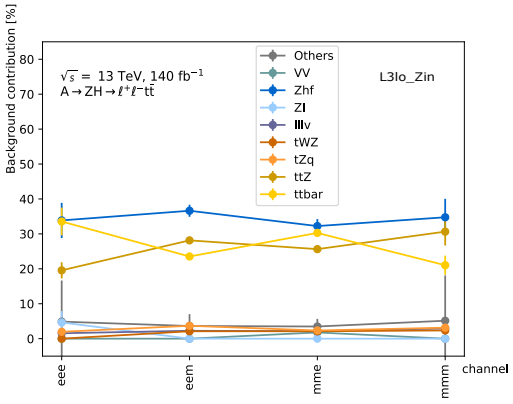

(c) L3lo_Zin

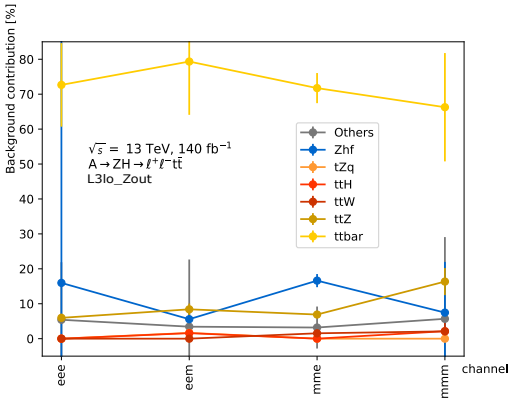

(d) L3hi_Zout

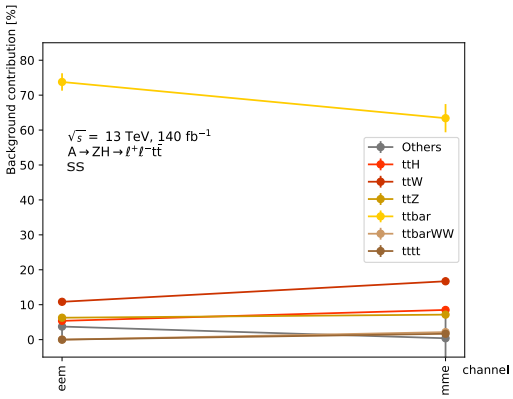

(e) same–sign

Figure 5.16. Background composition as a function of m_H^{cand} in the $\ell\ell t\bar{t}$, for the L3hi_Zin, L3hi_Zout, L3lo_Zin, L3hi_Zout and the same sign region.

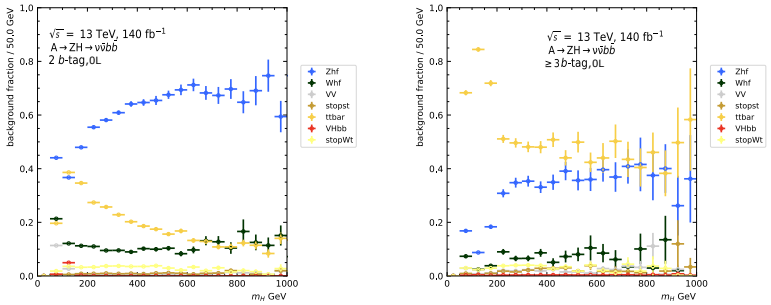

(a) 0L 2tag (b) 0L 3+tag

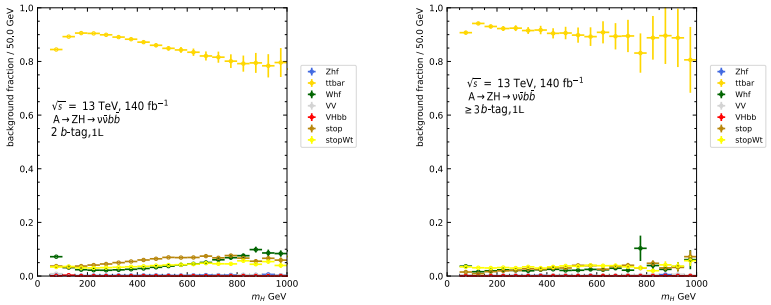

(c) 1L 2tag (d) 1L 3+tag

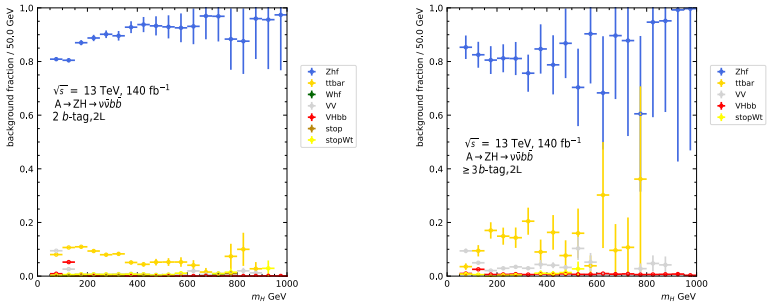

(e) 2L 2tag (f) 2L 3+tag

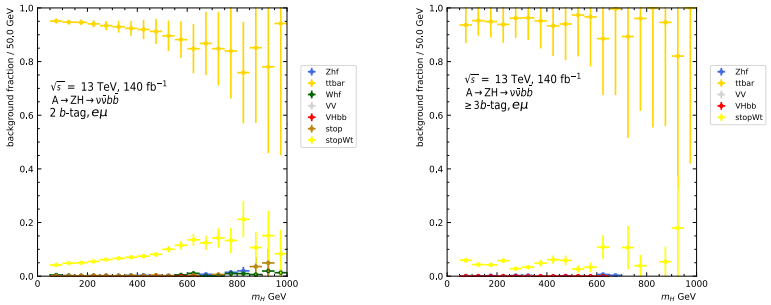

(g) $e\mu$ 2tag (h) $e\mu$ 3+tag

Figure 5.17. Background composition as a function of m_H^{cand} in the 2-b-tag (first column) and 3+-b-tag (second column) region, for the 2L, eμ and 1L channels.

5.5.1 Experimental uncertainties

The impact of experimental systematic uncertainties on the observable distributions used in the analysis is assessed by varying the simulation settings to $\pm 1\sigma$ bounds obtained from dedicated performance measurements. A qualitative summary of the experimental systematics considered in the analysis is shown in Table 5.4

5.5.1.1 Luminosity and Pileup

The luminosity scale for the data recorded by the ATLAS experiment during Run 2 is calibrated by van der Meer (vdM) scans each year and is extrapolated to the physics analysis. The total uncertainty for each year during Run 2 varied from $0.9 - 1.1\%$ [27]. The uncertainty in the total integrated luminosity is 0.83%, obtained using the LUCID-2 detector [40] for the primary luminosity measurements. The largest source of uncertainty is the calibration extrapolation from low-luminosity vdM scans to high-luminosity physics data-taking. The number of pile-up collisions in simulation is reweighed to match the data, and a 4% variation of this reweighing factor is assigned as an uncertainty.

5.5.1.2 Leptons

Systematic uncertainties in the trigger efficiencies, reconstruction, identification, and isolation are considered. For electrons, additional uncertainty on the electron energy scale and electron resolution are considered [23]. For muons, uncertainties on the muon momentum scale, track-to-vertex association, and momentum resolution are considered [28]. For τ-leptons, additional uncertainties on the overlap removal and in-situ energy scale correction are considered, as listed in Table 5.4.

5.5.1.3 $E_{\mathrm{T}}^{\mathrm{miss}}$ uncertainities

Uncertainties on the $E_{\mathrm{T}}^{\mathrm{miss}}$ come from the measurements of objects considered in the reconstruction of $E_{\mathrm{T}}^{\mathrm{miss}}$, including trigger and reconstruction terms. A 1σ statistical uncertainty on the trigger scale factor and the trigger efficiency are considered, along with the uncertainties on the track-based soft terms. Uncertainties in the reconstruction of $E_{\mathrm{T}}^{\mathrm{miss}}$ are applied as described in Ref. [31].

5.5.1.4 Jet

Uncertainties in the jet energy scale (JES) calibration and jet energy resolution (JER) measurements naturally play a role in the final object measurement. Only small R jet uncertainties are used, including 29 nuisance parameters for JES and 8 for JER.

5.5.1.5 Flavor Tagging

Thirteen nuisance parameters related to the flavor-tagging of jets are considered. Two additional NPs account for the extrapolation of the tagging SF from the calibrated regions to the high p_{T} jets, and from c-quarks to τ-lepton originated jets.

5.5.2 Signal and Background Modelling Uncertainties

Theory systematics originate from the Monte-Carlo modeling of signal and background processes. Missing higher orders from the matrix elements, PDF selection, choosing the Parton shower/hadronization algorithm, and re-summation scales fall in this category. These uncertainties can impact the shape and normalization in the MC, as shown in equation 2.39 and are described below.

- **Missing higher orders in calculating the inclusive matrix elements**: for

all processes, the cross-section calculation relies on a perturbative expansion of the scattering matrix, truncated at a certain order. The effect of the missing higher orders is estimated by varying the renormalization and factorization scales (μ_R and μ_F) independently by a factor of 2, excluding the $(\mu_R, \mu_F) = (\frac{1}{2}, 2), (2, \frac{1}{2}) \times \mu_{\text{central}}$ variations, which may lead to effects with large logarithms.

Group	Systematic uncertainty	Short description
Event	Luminosity	uncertainty on the total integrated luminosity
Electrons	EL_EFF_Trigger_TOTAL_1NPCOR_PLUS_UNCOR	trigger efficiency uncertainty
	EL_EFF_Reco_TOTAL_1NPCOR_PLUS_UNCOR	reconstruction efficiency uncertainty
	EL_EFF_ID_TOTAL_1NPCOR_PLUS_UNCOR	ID efficiency uncertainty
	EL_EFF_Iso_TOTAL_1NPCOR_PLUS_UNCOR	isolation efficiency uncertainty
	EG_SCALE_ALL	energy scale uncertainty
	EG_RESOLUTION_ALL	energy resolution uncertainty
Muons	MUON_EFF_TrigStatUncertainty	trigger efficiency uncertainties
	MUON_EFF_TrigSystUncertainty	
	MUON_EFF_RECO_STAT	reconstruction uncertainty for $p_{\text{T}} > 15$ GeV
	MUON_EFF_RECO_SYS	
	MUON_EFF_RECO_STAT_LOWPT	reconstruction and ID efficiency uncertainty for $p_{\text{T}} < 15$ GeV
	MUON_EFF_RECO_SYS _LOWPT	
	MUON_ISO_STAT	isolation efficiency uncertainty
	MUON_ISO_SYS	
	MUON_TTVA_STAT	track-to-vertex association efficiency uncertainty
	MUON_TTVA_SYS	
	MUON_SCALE	momentum scale uncertainty
	MUON_SAGITTA_RESBIAS	variations in the scale of the momentum (charge dependent)
	MUON_SAGITTA_DATASTAT	
	MUON_CB	momentum resolution uncertainty
τ-leptons	TAUS_TRUEHADTAU_EFF_RECO_TOTAL	Tau reconstruction efficiency uncertainty
	TAUS_TRUEHADTAU_EFF_RNNID_1PRONG...	Tau Identification efficiency uncertainties, Parametrised vs tau p_{T}
	TAUS_TRUEHADTAU_EFF_RNNID_3PRONG...	
	TAUS_TRUEHADTAU_EFF_RNNID_SYST	
	TAUS_TRUEHADTAU_EFF_RNNID_HIGHPT	
	TAUS_TRUEHADTAU_SME_TES_PHYSICSLIST	In-Situ Tau Energy Scale correction uncertainties
	TAUS_TRUEHADTAU_SME_TES_DETECTOR	
	TAUS_TRUEHADTAU_SME_TES_INSITUEXP	
	TAUS_TRUEHADTAU_SME_TES_INSITUFIT	
	TAUS_TRUEHADTAU_SME_TES_MODEL_CLOSURE	
	TAUS_TRUEHADTAU_EFF_ELEOLR_TOTAL	Uncertainty for tau electron overlap removal of true hadronic tau decays
	TAUS_TRUEELECTRON_EFF_ELEBDT_STAT	Uncertainties for tau electron overlap removal of true electrons faking hadronic taus
	TAUS_TRUEELECTRON_EFF_ELEBDT_SYST	
$E_{\text{T}}^{\text{miss}}$-**Trigger** and $E_{\text{T}}^{\text{miss}}$-**Terms**	METTrigStat	1σ statistical uncertainty of the trigger scale factor fit
	METTrigSumpt	trigger efficiency uncertainties
	METTrigTop/Z	
	MET_SoftTrk_ResoPerp	track-based soft term related to transversal resolution uncertainty
	MET_SoftTrk_ResoPara	track-based soft term related to longitudinal resolution uncertainty
	MET_SoftTrk_Scale	track-based soft term related to longitudinal scale uncertainty
	PRW_DATASF	uncertainty on data SF used for the computation of pileup reweighting
Small-R Jets	JET_EtaIntercalibration_Modelling	η-intercalibration: MC generator modelling uncertainty
	JET_EtaIntercalibration_TotalStat	η-intercalibration: statistical uncertainty
	JET_EtaIntercalibration_NonClosure_highE	η-intercalibration: non-closure uncertainty of jet response, high energy component
	JET_EtaIntercalibration_NonClosure_negEta	η-intercalibration: non-closure uncertainty of jet response, negative η component
	JET_EtaIntercalibration_NonClosure_posEta	η-intercalibration: non-closure uncertainty of jet response, positive η component
	JET_Pileup_OffsetMu	Pileup: Offset, term for number of interactions per crossing μ
	JET_Pileup_OffsetNPV	Pileup: Offset, term for number of primary vertices
	JET_Pileup_PtTerm	Pileup: Offset, p_{T} term
	JET_Pileup_RhoTopology	Pileup: Offset, ρ topology uncertainty on jet areas
	JET_Flavor_Composition	Flavor composition uncertainty

	JET_Flavor_Response	Flavor response uncertainty (dominated by gluon response)
	JET_PunchThrough_MC16	Punch-through correction uncertainty
	JET_EffectiveNP_Statistical	Statistical components of effective jet energy scale uncertainties; split into 6 components
	JET_EffectiveNP_Modelling	Modelling components of effective jet energy scale uncertainties; split into 4 components
	JET_EffectiveNP_Detector	Detector components of effective jet energy scale uncertainties; split into 2 components
	JET_EffectiveNP_Mixed	Effective jet energy scale uncertainties coming from various sources; split into 3 components
	JET_SingleParticle_HighPt	Uncertainty related to high p_{T} jets
	JET_BJES_Response	Jet energy scale uncertainty for b-jets
	JET_JER_DataVsMC_MC16	Nuisance parameter covering when jet energy resolution in data smaller than resolution in MC
	JET_JER_EffectiveNP	Effective jet energy resolution uncertainty; split into 6 components
	JET_JvtEfficiency	Jet Vertex Tagger efficiency uncertainty
b-tagging	FT_EFF_EIGEN_B FT_EFF_EIGEN_C FT_EFF_EIGEN_L	b-tagging efficiency uncertainties: *medium* eigenvector reduction scheme
	FT_EFF_EIGEN_extrapolation	b-tagging efficiency uncertainty on the extrapolation on high p_{T}-jets
	FT_EFF_EIGEN_extrapolation_from_charm	b-tagging efficiency uncertainty on τ-jets

Table 5.4. Qualitative summary of the experimental systematic uncertainties in the $A \to ZH$ analyses.

- **Uncertainties from the choice of PDFs and α_s**: These arise from uncertainties in the experimental measurements in determining the PDF sets used in each calculation, uncertainties from the choice of the functional form used in the PDF fits, and uncertainties associated to the experimental determination of α_s. These are estimated using the PDF4LHC prescription [62]

- **Merging-scale uncertainties**: for samples generated by merging matrix elements (ME) corresponding to different multiplicities, e.g. V+1,2,...jets, uncertainty related to the choice of the merging scale, i.e. the scale that separates soft from hard jets, is evaluated by varying the merging scale by a factor of 2 up and down.

- **Resummation scale uncertainties**: for SHERPA samples, an additional uncertainty related to the energy cut-off for the integration of MC counterterms in the parton shower (PS) is added [136].

- **Matching uncertainties**: for samples generated using a NLO matrix element

and matched to a parton shower, a comparison between samples generated with a POWHEG and a MG5aMC sample probe uncertainties related to the ME/PS matching procedure.

- **Parton shower/hadronization uncertainties**: uncertainties related to algorithmic or parametric differences in the modeling of the PS and hadronization can be assessed by comparing samples generated with different showering/hadronization (SHG) generators, typically between PYTHIA 8 and HERWIG 7.

- **Eigentune uncertainties**: are related to uncertainties in choosing the free parameters for the masses and couplings, renormalization and factorization scales, and cutoffs used in the parton shower and/or matching scheme (mainly the showering/hadronization programs). These uncertainties so as to encompass the data used in the ATLAS tuning program [22].

5.5.3 Derivation of Signal and Background Uncertainties

- **Normalization uncertainties** are implemented as Gaussian priors that affect the normalization of a given sample in all regions and are only applied to the samples whose normalization is not free to float in the fit. Normalization uncertainty for a sample is calculated as follows:

$$\sigma_{\text{norm}} = \sqrt{\sum_i \left(1 - \frac{N^{\text{alt},i}}{N^{\text{nom}}}\right)^2}, \tag{5.1}$$

where i runs over all alternative MC generators considered for a given process, and N corresponds to the total expected background yield for the sample in all regions

considered in the fit.

- **Shape uncertainties** are implemented on the shape of the fitted discriminant ($m_T(VH)$ or Δm) and are estimated by comparing the shape of the fit discriminant for the nominal and alternative MC samples.

- **Acceptance uncertainties** affect the relative normalization of backgrounds between analysis regions (signal and a control region) and refer to the uncertainties associated with the differences in the acceptance and efficiency of the detector and selections between the signal and the control region. These uncertainties are applied in the fit as Gaussian priors, and they also consider the shape changes of the observables in different regions. The acceptance uncertainties are calculated as follows

$$\sigma_{\text{accept}} = \sqrt{\sum_i \left(1 - \frac{N_{\text{SR}}^{\text{alt},i}}{N_{\text{CR}}^{\text{alt},i}} \Big/ \frac{N_{\text{SR}}^{\text{nom}}}{N_{\text{CR}}^{\text{nom}}}\right)^2}, \tag{5.2}$$

where i runs over all alternative MC generators in a given process.

5.6 Statistical Analysis

A profile likelihood function-based fit using all the Monte-Carlo templates for all the backgrounds to data is used, as discussed in section 2.3.1.4.

$$\mathcal{L}(\mu, \vec{\theta}, \vec{\gamma}) = \mathcal{L}_{\text{Pois}}(\mu, \vec{\theta}, \vec{\gamma}) \times \mathcal{L}_{\text{NP}}(\vec{\theta}) \times \mathcal{L}_{\text{Stat}}(\vec{\gamma}) \tag{5.3}$$

Systematic uncertainties described in section 5.5 are incorporated in the likelihood as NP, parameterized by flat, Gaussian, or log-normal priors. The nominal fit results for

μ and σ_μ are obtained by maximizing the likelihood function for all parameters. The test statistic q_μ is then constructed as described in Section 2.3 to measure the compatibility of the background-only model with the observed data and to derive exclusion intervals derived with the CL_s method [93]. The fit model used for the $\ell\ell t\bar{t}$ and the $\nu\bar{\nu}b\bar{b}$ analyses have been shown in Table 5.5 and the fractional squared uncertainty obtained from the fit in μ from the different sources of uncertainty for different (m_A, m_H) values in the $\ell\ell t\bar{t}$ and $\nu\bar{\nu}b\bar{b}$ channels are tabulated in Table 5.6.

5.7 Result and Interpretation

The likelihood fits show no significant deviation from the background-only hypothesis. The largest excess observed over the SM background prediction is $2.85\,\sigma$ in the $\ell\ell t\bar{t}$ channel for a signal hypothesis corresponding to $(m_A, m_H) = (650, 450)$ GeV. The global significance for the $\ell\ell t\bar{t}$ channel is estimated following Refs. [122, 187] to be $2.35\,\sigma$.

The yields and the post-fit distributions obtained from the background only fit to the data in SR and CRs are shown in Figures 5.18 and Tables 5.7, 5.8 and 5.9. Representative distributions of the fit discriminant and the mass of the H candidate in the SR are shown in Figures 5.19 and 5.20. Constraints obtained from the fits are applied to the VRs to gauge the fit's compatibility with data in regions kinematically close to the SR and CRs.

The normalization factors in the $\ell\ell t\bar{t}$ channel are close to one for the $t\bar{t}Z$ background. However, for the $t\bar{t}$ background, they vary from 1.5 to 1.8 for different m_H^{hypo} hypotheses, with an uncertainty of 0.5. The $t\bar{t}$ scaling factor is above one as it describes

Analysis	$\ell\ell t\bar{t}$	$\nu\bar{\nu}b\bar{b}$
Signal regions	`L3hi_Zin_Hin`	`0L_Hin`
Control regions	`ss` m_H side-bands: `L3hi_Zin_Hlo`, `L3hi_Zin_Hhi`	`2L`,`e`μ m_H side-bands: `0L_Hlo`, `0L_Hhi`
Validation regions	`L3lo_Zin`, `L3hi_Zout` (inclusive in m_H)	`1L`
Fit discriminant	$\Delta m = m_A - m_H$	$m_{\mathrm{T}}(VH)$
CR binning	1 bin	`e`μ: [0, 900, 2500] `2L` 2−tag: [0, 300, 500, 700, 900, 1100, 1300, 1500, 2500] all other CRs: 1 bin
SR binning	$m_H = 350$: [0, 100, 123, 150, 25 GeV bins, 275, 310, 350, 400, 480, 2000] $m_H = 700$: [0, 115, 150, 25 GeV bins, 275, 305, 340, 385, 450, 535, 2000] $m_H = 800$: [0, 115, 150, 25 GeV bins, 275, 305, 340, 385, 450, 550, 2000] other m_H: [0, 100, 125, 25 GeV bins, 350, 390, 430, 480, 565, 2000]	2-b-tag [0, 350, 50 GeV bins, 1300, 1400, 2500], $m_H = 130/150$ [0, 400, 50 GeV bins, 1300, 1400, 2500], $m_H = 200$ [0, 450, 50 GeV bins, 1250, 1350, 2500], $m_H = 250$ [0, 500, 50 GeV bins, 1300, 1400, 2500], $m_H = 300$ [0, 550, 50 GeV bins, 1300, 1400, 2500], $m_H = 350$ [0, 600, 50 GeV bins, 1300, 1400, 1500, 2500], $m_H = 400$ [0, 650, 50 GeV bins, 1300, 1400, 2500], $m_H = 450$ [0, 700, 50 GeV bins, 1350, 1450, 1600, 2500], $m_H = 500$ [0, 850, 50 GeV bins, 1350, 1450, 1600, 2500], $m_H = 600$ [0, 950, 50 GeV bins, 1400, 1500, 1650, 2500], $m_H = 700$ [0, 1050, 50 GeV bins, 1400, 1500, 1650, 2500], $m_H = 800$ 3+-b-tag [0, 400, 50 GeV bins, 1000, 2500], $m_H = 130/150$ [0, 450, 50 GeV bins, 900, 1000, 1100, 2500], $m_H = 200$ [0, 500, 50 GeV bins, 850, 950, 2500], $m_H = 250$ [0, 550, 50 GeV bins, 900, 1000, 2500], $m_H = 300$ [0, 600, 50 GeV bins, 900, 1000, 2500], $m_H = 350$ [0, 650, 50 GeV bins, 950, 1050, 2500], $m_H = 400$ [0, 700, 50 GeV bins, 950, 1050, 2500], $m_H = 450$ [0, 750, 50 GeV bins, 1000, 1100, 2500], $m_H = 500$ [0, 850, 50 GeV bins, 1050, 1150, 2500], $m_H = 600$ [0, 980, 1080, 1230, 2500], $m_H = 700$ [0, 1120, 1270, 2500], $m_H = 800$
Merged templates	$t\bar{t}X = t\bar{t}W,\ t\bar{t}H,\ t\bar{t}WW,\ t\bar{t}t\bar{t}$ $Z = Zbb,\ Zbc,\ Zbl,\ Zcc,\ Zcl,\ Zl$ multi$V = VV\ (llll),\ VVV$	stopst $= s, t$-channel single-top $VV = WW, WZ, ZZ$ (quark and gluon-induced) Zhf $= Zbb, Zbc, Zbl, Zcc$ Whf $= Wbb, Wbc, Wbl, Wcc$

Table 5.5. Fit model for $\ell\ell t\bar{t}$ and $\nu\bar{\nu}b\bar{b}$ analysis. The binning choices for the different

Source of uncertainty	Fractional squared uncertainty in μ				
	$\ell\ell t\bar{t}$ signals (m_A, m_H) [GeV]		$\nu\bar{\nu}b\bar{b}$ signals (m_A, m_H) [GeV]		
	(700, 500)	(1200, 800)	(400, 130)	(700, 300)	(1200, 800)
Total statistical uncertainty	0.91	0.90	0.19	0.27	0.48
Total systematic uncertainty	0.09	0.10	0.81	0.73	0.52
Statistical uncertainties					
Data statistics	0.40	0.72	0.16	0.24	0.48
$t\bar{t}Z$ normalisation	0.36	0.14		neglected	
Zhf normalisation	not free to float, included in 'Other'		0.01	0.05	0.12
$t\bar{t}$ normalisation	0.01	0.02	0.06	0.01	0.01
Systematic uncertainties					
Jets	0.02	0.01	0.15	0.10	0.10
b-tagging	< 0.01	< 0.01	0.02	< 0.01	0.05
$E_{\mathrm{T}}^{\mathrm{miss}}$ soft-term and pile-up	< 0.01	< 0.01	0.01	0.01	< 0.01
Luminosity	< 0.01	< 0.01	< 0.01	< 0.01	< 0.01
Other experimental sources	< 0.01	< 0.01	< 0.01	< 0.01	< 0.01
$t\bar{t}Z$ modelling	0.03	0.05		not applied	
$t\bar{t}$ modelling	0.01	0.02	0.05	0.01	0.01
Zhf modelling	included in 'Other'		0.21	0.47	0.30
Whf modelling	neglected		0.14	0.04	0.10
tW modelling	neglected		0.02	0.03	< 0.01
Other modelling sources	0.01	0.02	0.08	0.01	< 0.01
Signal modelling	< 0.01	< 0.01	< 0.01	< 0.01	< 0.01
MC sample size	0.01	0.01	0.05	0.05	0.05

Table 5.6. Fractional squared uncertainty in μ from the different sources of uncertainty for different (m_A, m_H) values in the $\ell\ell t\bar{t}$ and $\nu\bar{\nu}b\bar{b}$ channels. Because of the correlations between the different systematics components, we do not expect the sum of squares of the individual systematic uncertainties being equal to the square of the total systematics uncertainty

the mismodelling of fake leptons (misidentified jet or a non-prompt lepton) rate in the simulated samples.

In the $\nu\bar{\nu}b\bar{b}$ channel, the normalization factors for the $t\bar{t}$ background are close to one, while for the Zhf background, they range from 1.2 to 1.3 with an uncertainty of 0.1 in the 2-b-tag region and from 1.4 to 1.7 with an uncertainty of 0.2 in the $\geq$ 3-b-tag regions. The Zhf normalization factors are higher than one due to the mismodeling of the Zhf process in SHERPA [2, 4, 35]. In the $\ell\ell t\bar{t}$ channel, the $t\bar{t}$ template represents $t\bar{t}$ events with two prompt leptons and one non-prompt or misidentified lepton. On the other hand,

	L3hi_Zin				(VR)	(VR)
	Hlo450 (CR)	Hin450 (SR)	Hhi450 (CR)	ss (CR)	L3hi_Zout	L3lo_Zin
$t\bar{t}Z$	5.1 ± 0.9	200 ± 22	113 ± 13	2.3 ± 0.6	29.0 ± 3.2	30.8 ± 3.4
$t\bar{t}$	1.2 ± 0.8	29 ± 9	16 ± 6	40 ± 7	46 ± 14	54 ± 17
tWZ	0.40 ± 0.14	12 ± 4	10 ± 4	0.13 ± 0.04	1.6 ± 0.5	2.2 ± 0.7
tZq	0.6 ± 0.4	13 ± 8	10 ± 6	0.046 ± 0.032	1.8 ± 1.2	2.4 ± 1.6
VV+VVV	1.5 ± 0.5	15 ± 4	11.1 ± 3.5	0.034 ± 0.013	2.3 ± 0.6	3.1 ± 0.9
Z	1.5 ± 1.1	11 ± 4	3.9 ± 1.6	0.025 ± 0.010	3.7 ± 1.4	39 ± 15
$t\bar{t}W$+$t\bar{t}H$+$t\bar{t}WW$+$t\bar{t}t\bar{t}$	0.16 ± 0.05	6.8 ± 0.9	4.9 ± 0.9	7.4 ± 1.8	8.4 ± 1.8	1.63 ± 0.27
Total background	10.5 ± 1.5	285 ± 15	169 ± 10	50 ± 7	93 ± 13	133 ± 21
Data	7	303	153	49	84	119

Table 5.7. Yields in the $\ell\ell t\bar{t}$ channel obtained from the background-only fit to data using Hin450 as the signal region. The indicated uncertainties include statistical and systematic components. The value next to the region name refers to the m_H^{hypo} hypothesis.

in the $\nu\bar{\nu}b\bar{b}$ channel, it represents $t\bar{t}$ events with two prompt leptons. Therefore, the two normalization factors obtained above are not comparable.

5.7.1 Upper limits on the production cross-sections

Upper limits on the production cross-section for the A boson multiplied by the decay branching ratios, $B(A \to ZH) \times B(H \to t\bar{t})$ in the $\ell\ell t\bar{t}$ channel and $B(A \to ZH) \times B(H \to b\bar{b})$ in the $\nu\bar{\nu}b\bar{b}$ channel, are obtained for the ggF and bbA production modes. These limits are illustrated in Figures 5.21 and 5.22.

The limits for this search depend on the natural width of the A and H bosons. However, in the parameter space relevant to this search, only the width of the A boson is significant, as the width of the H boson is always very small compared to the experimental resolution. The width of the A boson increases as $m_A - m_H$ increases and is roughly independent of $\tan\beta$ for $\tan\beta \gtrsim 5$, but becomes larger for smaller values of $\tan\beta$ (i.e., $\tan\beta \lesssim 5$). Consequently, the limits provided for $\tan\beta = 10$ are generally applicable for

	0L					
	Hlo300 (CR)	Hin300 (SR)	Hhi300 (CR)	2L (CR)	eμ (CR)	1L (VR)
$t\bar{t}$	3800 ± 400	600 ± 80	290 ± 40	370 ± 60	8700 ± 500	336000 ± 28000
Single-top (s-, t-chan)	93 ± 18	26 ± 4	16.7 ± 3.1	0.70 ± 0.15	12.4 ± 0.7	16700 ± 1100
Single-top tW	600 ± 400	160 ± 90	90 ± 60	43 ± 23	800 ± 500	23000 ± 12000
Whf	2800 ± 900	330 ± 100	230 ± 70	2.8 ± 1.0	29 ± 9	21000 ± 7000
Zhf	8500 ± 900	2200 ± 120	1620 ± 90	5370 ± 120	18.1 ± 1.3	1070 ± 90
Vlf	44 ± 8	10.8 ± 1.7	12.3 ± 2.3	23 ± 5	0.35 ± 0.08	330 ± 60
$VHbb$	210 ± 130	0.8 ± 0.5	0.48 ± 0.31	60 ± 40	0.37 ± 0.23	350 ± 220
VV	770 ± 150	15.4 ± 1.7	12.3 ± 1.6	207 ± 24	1.63 ± 0.20	1260 ± 140
Total background	16960 ± 170	3350 ± 50	2270 ± 50	6080 ± 90	9620 ± 110	400000 ± 26000
Data	16961	3389	2266	6037	9618	415808

Table 5.8. Yields in the 2-b-tag regions of the $\nu\bar{\nu}b\bar{b}$ channel obtained from the background-only fit to data using Hin300 as the signal region. The indicated uncertainties include statistical and systematic components. The value next to the region name refers to the m_H^{hypo} hypothesis.

	0L					
	Hlo300 (CR)	Hin300 (SR)	Hhi300 (CR)	2L (CR)	eμ (CR)	1L (VR)
$t\bar{t}$	1200 ± 70	101 ± 8	80 ± 9	16.9 ± 3.1	385 ± 26	19300 ± 1400
Single-top (s-, t-chan)	11.0 ± 1.2	3.9 ± 0.5	4.0 ± 0.4	–	0.28 ± 0.10	310 ± 27
Single-top tW	70 ± 50	13 ± 8	8 ± 7	1.2 ± 0.8	27 ± 19	1000 ± 700
Whf	82 ± 28	18 ± 6	14 ± 5	0.13 ± 0.04	1.2 ± 0.4	530 ± 170
Zhf	340 ± 50	106 ± 10	91 ± 10	173 ± 13	0.60 ± 0.16	43 ± 5
Vlf	0.73 ± 0.33	0.14 ± 0.05	0.17 ± 0.04	0.0040 ± 0.0020	–	6.9 ± 2.8
$VHbb$	3.7 ± 2.4	0.48 ± 0.31	0.42 ± 0.27	1.1 ± 0.7	0.010 ± 0.007	5.3 ± 3.4
VV	21 ± 4	3.7 ± 0.5	3.3 ± 0.4	6.6 ± 0.9	0.037 ± 0.018	35 ± 4
Total background	1720 ± 40	245 ± 9	201 ± 8	199 ± 12	415 ± 19	21200 ± 1300
Data	1702	251	203	198	428	21356

Table 5.9. Yields in the $\geq$ 3-b-tag regions of the $\nu\bar{\nu}b\bar{b}$ channel obtained from the background-only fit to data using Hin300 as the signal region. The indicated uncertainties include statistical and systematic components. The value next to the region name refers to the m_H hypothesis.

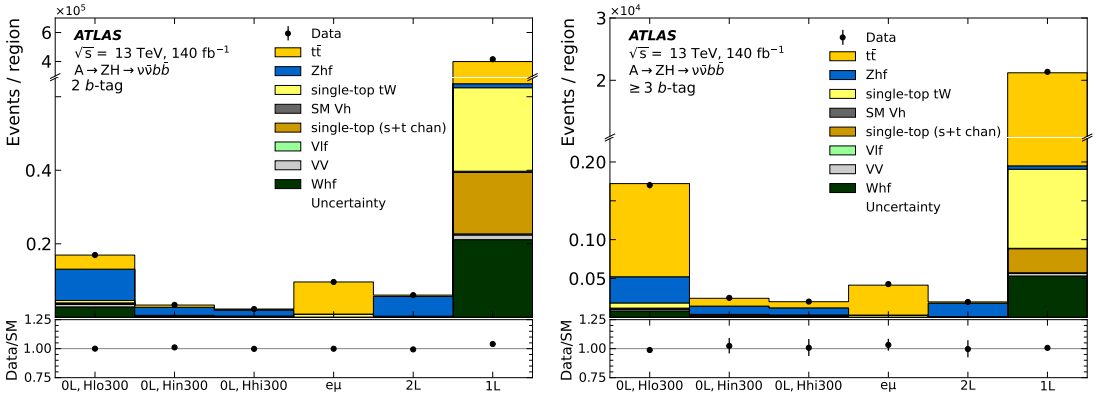

(a) $\nu\bar{\nu}b\bar{b}$ yield in 2-b-tag regions

(b) $\nu\bar{\nu}b\bar{b}$ yield in $\geq$ 3-b-tag regions

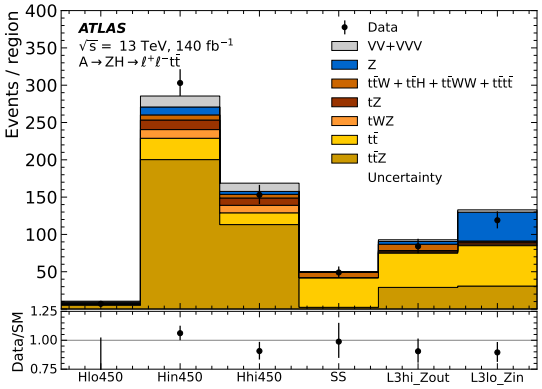

(c) $\ell\ell t\bar{t}$ yield

Figure 5.18. Yields in the SR, CRs, and VRs used in the in (a) 2-b-tag and (b) $\geq$ 3-b-tag regions of the $\nu\bar{\nu}b\bar{b}$ channel and (c) $\ell\ell t\bar{t}$ channel. The yields are obtained from a background-only fit to data. The value next to the region name in the x-axis labels refers to the m_H^{hypo} hypothesis. The data are black points, and the associated error bars represent the statistical uncertainty. The hatched band indicates the combined statistical and systematic uncertainty in the sum of the backgrounds.

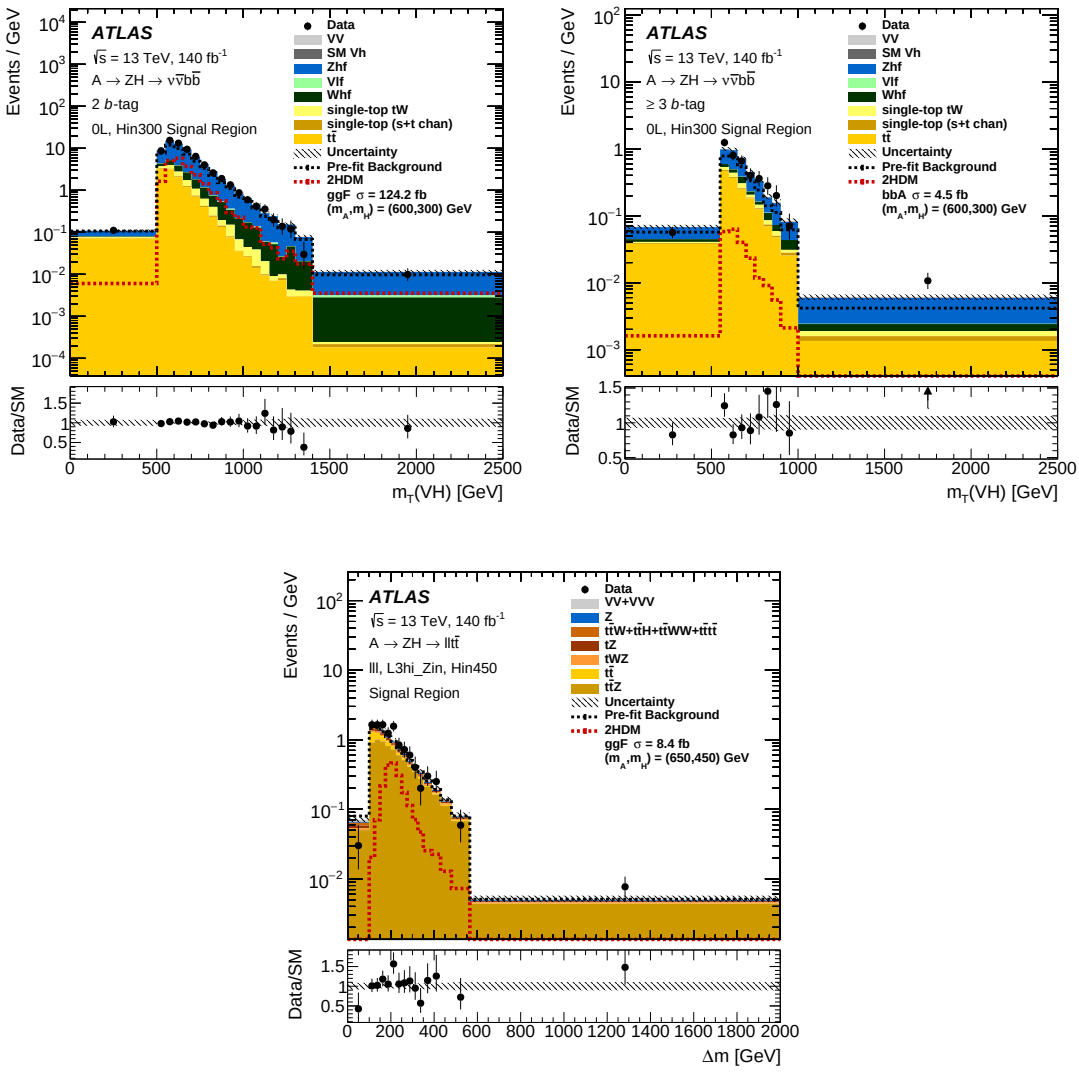

Figure 5.19. The distribution of the fit discriminant $\Delta m = m(\ell\ell t\bar{t}) - m(t\bar{t})$ in the SR of the $\ell\ell t\bar{t}$ channel for the $m_H^{\text{hypo}} = 450$ GeV hypothesis (a). The distribution of the fit discriminant $m_{\text{T}}(VH)$ in the SR of the $\nu\bar{\nu}b\bar{b}$ channel in the 2-b-tag (b) and $\geq$ 3-b-tag (c) region, for the $m_H^{\text{hypo}} = 300$ GeV hypothesis. The background yields are obtained from a background-only fit to data. Signal distributions corresponding to ggF or bbA production normalized to the theory cross-section are compared. The data are black points, and the associated error bars represent the statistical uncertainty. The hatched band indicates the combined statistical and systematic uncertainty for the sum of backgrounds. The quantity on the vertical axis is the number of events divided by the bin width in GeV.

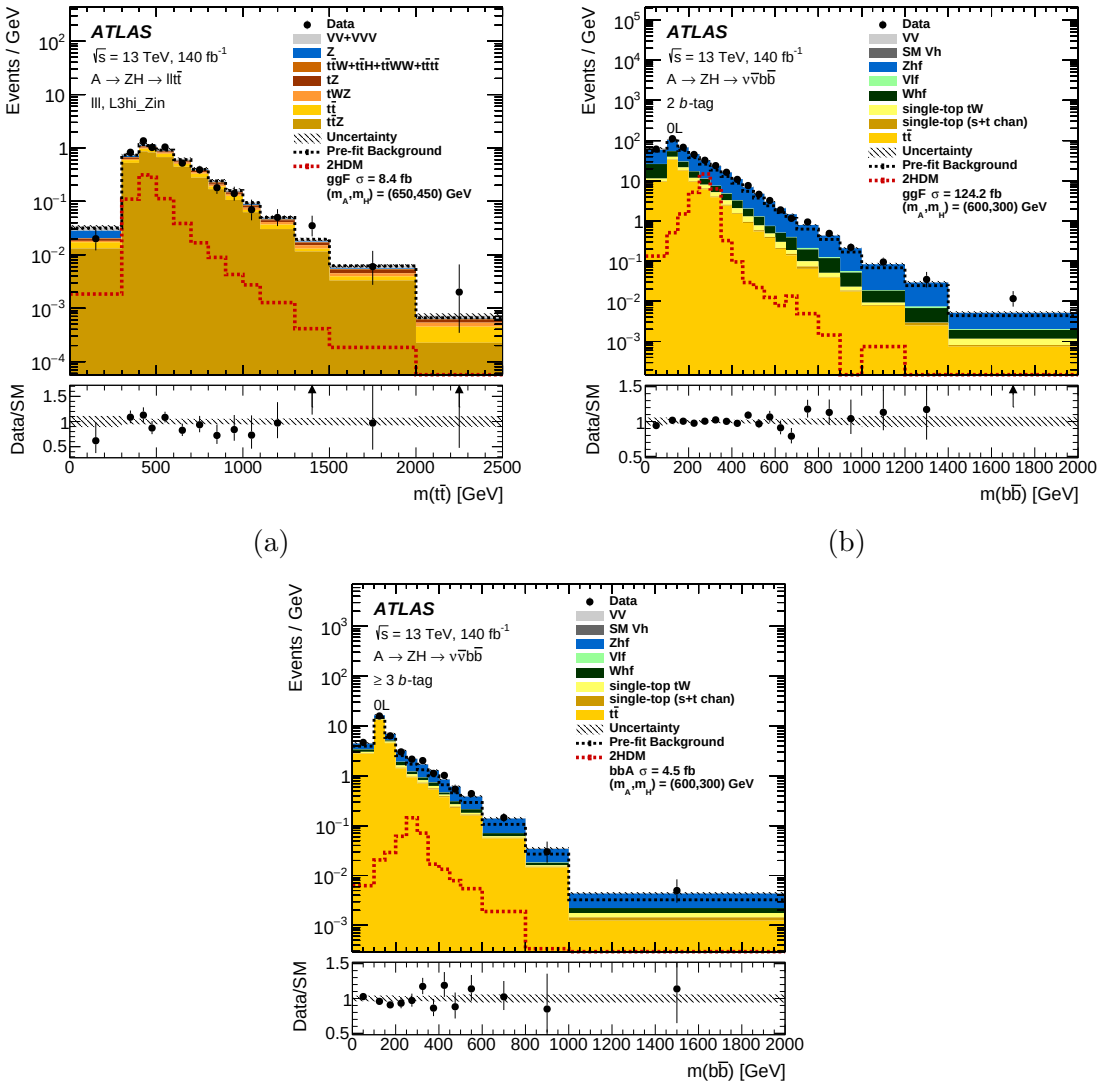

Figure 5.20. The $m(t\bar{t})$ distribution in the `L3hi_Zin` region of the $\ell\ell t\bar{t}$ channel (a) and the $m(b\bar{b})$ distribution in the $\nu\bar{\nu}b\bar{b}$ channel in the 2-b-tag (b) and $\geq$ 3-b-tag (c) `0L` region. The background yields are obtained from a background-only fit to data. Signal distributions corresponding to ggF or bbA production normalized to the theory cross-section are compared. The data are black points, and the associated error bars represent the statistical uncertainty. The hatched band indicates the combined statistical and systematic uncertainty for the sum of backgrounds. The quantity on the vertical axis is the number of events divided by the bin width in GeV.

$\tan\beta \gtrsim 5$, while the limits provided for $\tan\beta = 1$ are only suitable for that specific $\tan\beta$ value. For intermediate $\tan\beta$ values, limits can be obtained by interpolating between the limits for the given $\tan\beta$ values.

To obtain more realistic limits, instead of using only narrow-width A bosons, the signals are generated with a natural width that corresponds to the prediction of the 2HDM for $\tan\beta = 1$ in ggF production and $\tan\beta = 10$ in bbA production. For the 2HDM benchmarks considered and the parameter space that is relevant for this search (see Section 5.7.2), the $\tan\beta$ and Higgs boson mass values are enough to define the A boson width. The choice $\tan\beta = 10$ is made for bbA production because, at this value, this production mechanism is dominant in the benchmark models discussed in Section 5.7.2 (Type-II and flipped 2HDM). In the 2HDM benchmarks considered here, the width of the A boson relative to its mass is a few percent for low m_A values and increases at high m_A. For example, for the m_A range shown in Figures 5.21 for the $\ell\ell t\bar{t}$ channel, the A boson width ranges from 4.3% to 37% of its mass. The observed upper limit in the $\ell\ell t\bar{t}$ channel in the ggF production process varies from 75.0 fb for $(m_A, m_H) = (1200, 600)$ GeV to 992 fb for $(m_A, m_H) = (550, 450)$ GeV; this will be compared with the respective expected limits of 90.8 fb and 582 fb. The observed upper limit in the $\ell\ell t\bar{t}$ channel in the bbA production process varies from 79.4 fb for $(m_A, m_H) = (800, 400)$ GeV to 636 fb for $(m_A, m_H) = (650, 450)$ GeV; this is to be compared with the respective expected limits of 162 fb and 257 fb. Similarly, for the $\nu\bar{\nu}b\bar{b}$ channel, the observed upper limit for ggF production varies from 6.2 fb for $(m_A, m_H) = (1200, 300)$ GeV to 3700 fb for $(m_A, m_H) = (350, 150)$ GeV; to be compared with the respective expected limits of 10.6 fb and 3520 fb.

Finally, for the $\nu\bar{\nu}b\bar{b}$ channel, the observed upper limit for bbA production varies from 3.62 fb for $(m_A, m_H) = (1200, 200)$ GeV to 1750 fb for $(m_A, m_H) = (350, 150)$ GeV; to be compared with the respective expected limits of 9.92 fb and 1910 fb.

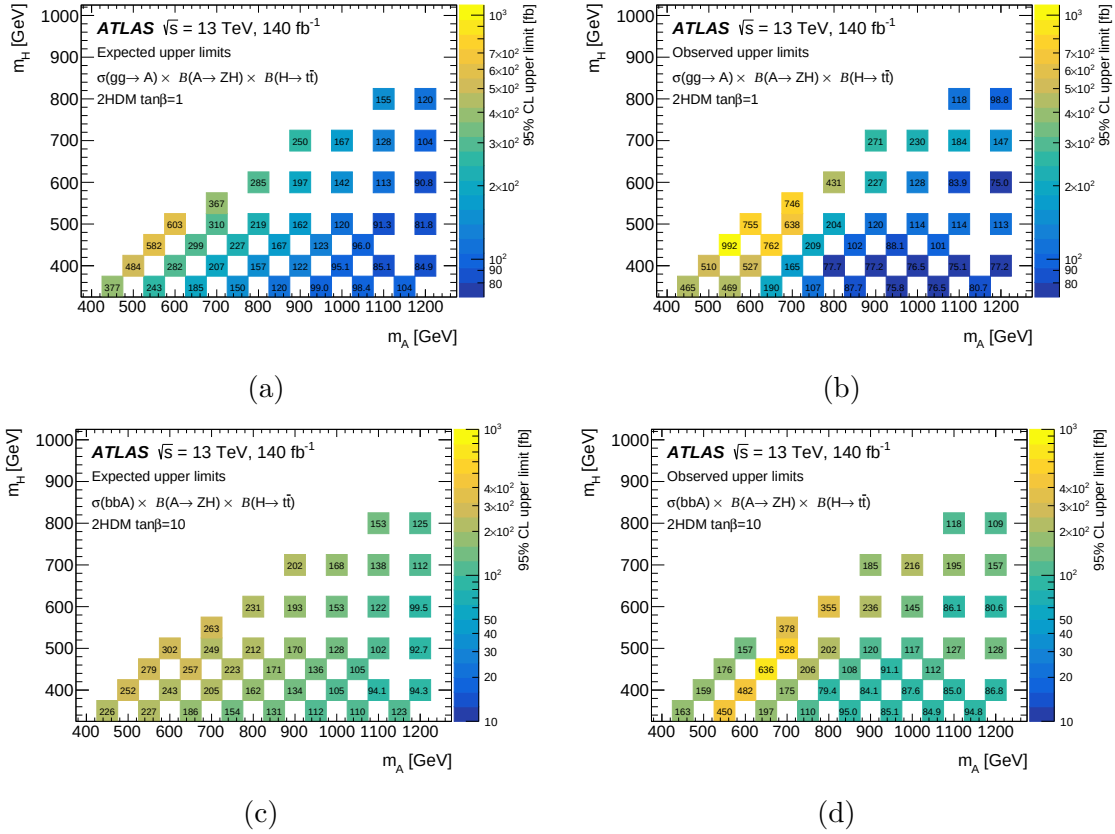

Figure 5.21. Expected (a,c) and observed (b,d) upper limits at 95% CL on $\sigma(gg \to A) \times B(A \to ZH) \times B(H \to t\bar{t})$ (a,b) and $\sigma(b\bar{b}A) \times B(A \to ZH) \times B(H \to t\bar{t})$ (c,d) in the (m_A, m_H) plane. The limits are shown for $\tan\beta = 1$ or $\tan\beta = 10$ in ggF or bbA production, respectively. The $\tan\beta$ value is relevant only for the A boson width choice.

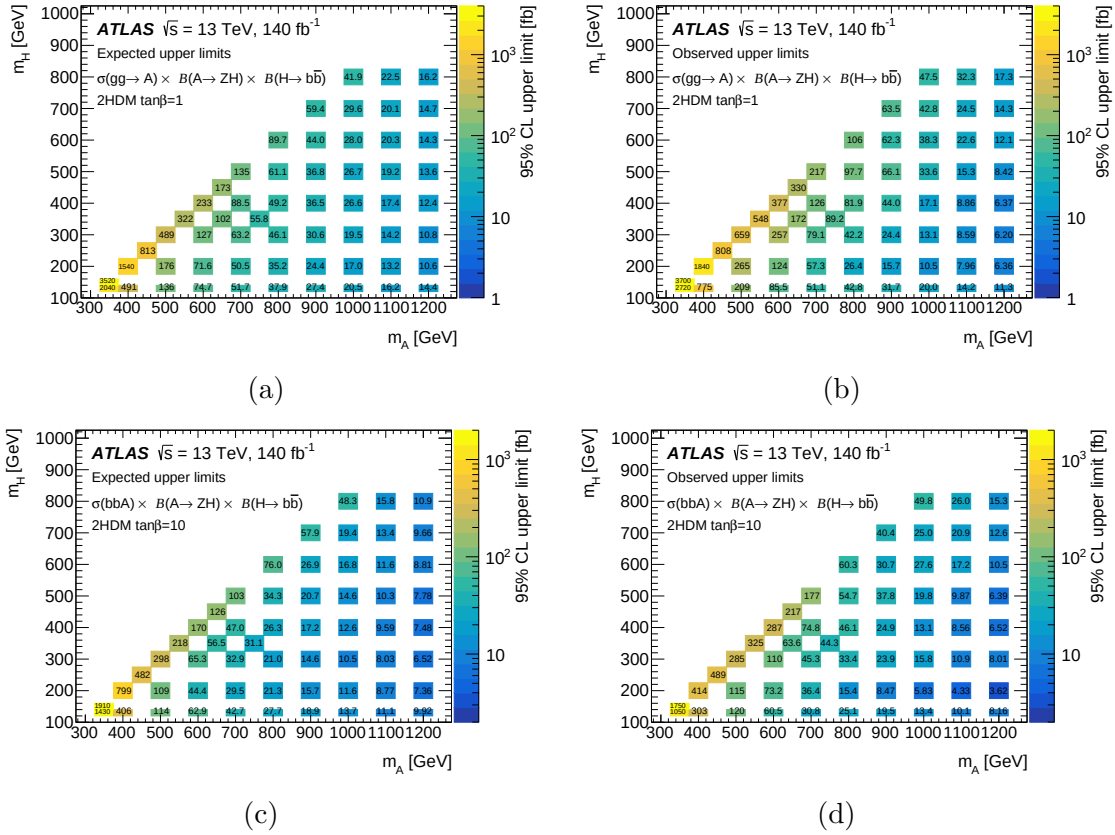

Figure 5.22. Expected (a,c) and observed (b,d) upper limits at 95% CL on $\sigma(gg \to A) \times B(A \to ZH) \times B(H \to b\bar{b})$ (a,b) and $\sigma(b\bar{b}A) \times B(A \to ZH) \times B(H \to b\bar{b})$ (c,d) in the (m_A, m_H) plane. The limits are shown for $\tan\beta = 1$ or $\tan\beta = 10$ in ggF or bbA production, respectively. The $\tan\beta$ value is relevant only for the A boson width choice.

5.7.2 Interpretation in the context of 2HDM

The upper limits described in Section 5.7.1 are interpreted within the framework of the CP-conserving 2HDM simplified with several assumptions to constrain the number of free parameters. In this interpretation, the $H^{\pm}$ bosons are assumed to have the same mass as the A boson, and it is assumed that $m_H < m_A$ for the masses of the A and H bosons. Additionally, the 2HDM parameter m_{12}^2 is set to a fixed value of $m_A^2 \tan\beta/(1 + \tan^2\beta)$. "Alignment limit" is assumed in which the h boson has a mass of 125 GeV, and its couplings to fermions and vector bosons are set to be the same as those of the SM Higgs boson at the lowest order. The widths of the A and H bosons are taken from the predictions of the 2HDM [54]. These assumptions leave three free parameters: m_A, m_H, and $\tan\beta$. In addition, the Yukawa couplings have four possible arrangements: type-I, type-II, lepton-specific, and flipped 2HDM (Section 2.1.4). For the parameter space relevant in this search, the widths of the A and H bosons differ very little across the 2HDM types compared with the experimental mass resolution. In the same parameter space, the A boson width is larger than the H boson width, so the quoted limits from this search cannot be interpreted as limits for the $H \to ZA$ process. The cross-sections for A boson production in the 2HDM are calculated with corrections up to NNLO in QCD for ggF and bbA production in the five-flavor scheme as implemented in SusHi [126, 127, 128, 130]. For bbA production, a cross-section in the four-flavor scheme is also calculated as described in Refs. [98, 100]; the results are combined with the five-flavor scheme calculation following Ref. [125]. The Higgs boson branching ratios are calculated using 2HDMC [106]. The

procedure from Ref. [112] is followed to calculate the cross-sections and branching ratios and to select 2HDM parameter values.

The upper limits are interpreted as constraints in the (m_A, m_H) plane for several $\tan\beta$ values. The widths of the A and H bosons change as a function of $\tan\beta$, and these variations are considered when calculating the constraints. The results are quoted only for cases in which the width of the A boson is no more than 25% of m_A. Figures 5.23(a) and 5.23(b) show the constraints from the $\ell\ell t\bar{t}$ channel for the type-I and type-II 2HDM, respectively. Constraints from this channel for the lepton-specific 2HDM are very similar to type-I. Constraints from the $\nu\bar{\nu}b\bar{b}$ channel are shown in Figure 5.23(c) for the type-I 2HDM, and in Figures 5.23(d) and 5.23(e) for the type-II 2HDM. The result from the analysis extends the reach of the $A \to ZH \to \ell\ell b\bar{b}$ search reported in Ref. [34], especially in parts of the parameter space with $m_H > 350$ GeV and $m_A > 800$.

The search explored parameter space of 2HDM that had not been looked previously in the ATLAS collaboration and upper limits on the production cross-section times the branching ratios for $B(A \to ZH) \times B(H \to t\bar{t})$ in the $\ell\ell t\bar{t}$ channel and $B(A \to ZH) \times B(H \to t\bar{t})$ were derived for the ggF and bbA production modes. The search has already been well-received by the theorists, as in Ref [49], the results from the $\ell\ell t\bar{t}$ and the $\nu\bar{\nu}b\bar{b}$ channel have been used to provide combined exclusions for the EWB and a strong first-order phase transition. The $2.85\,\sigma$ in the $\ell\ell t\bar{t}$ channel for a signal hypothesis corresponding to $(m_A, m_H) = (650, 450)$ GeV is in the region sensitive to the strong first-order phase transitions that could also be tested with gravitational wave experiments.

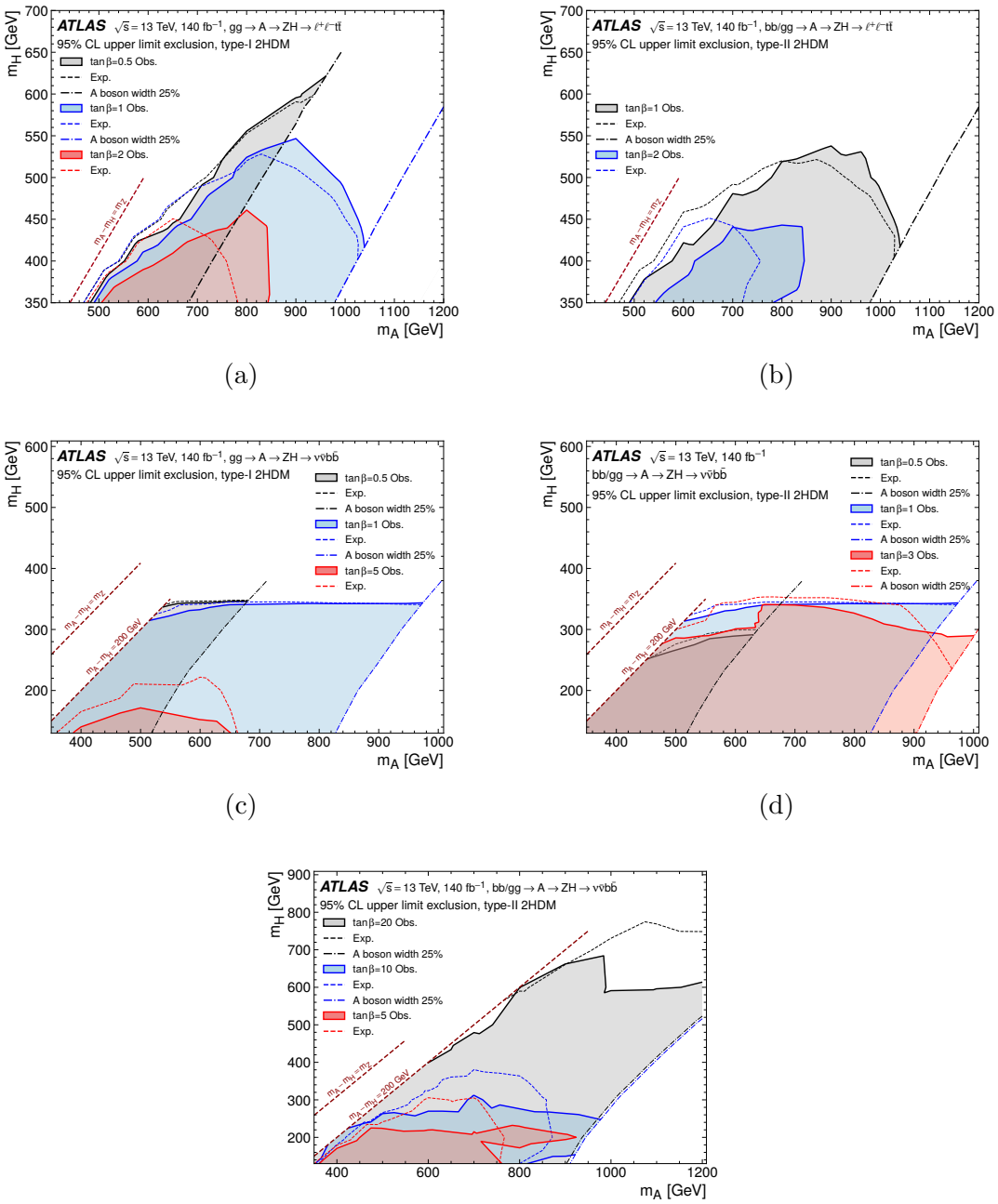

Figure 5.23. Observed and expected 95% CL exclusion regions in the (m_A, m_H) plane for various $\tan\beta$ values for the $\ell\ell t\bar{t}$ channel, type-I (a) and type-II (b) 2HDM, and $\nu\bar{\nu}b\bar{b}$ channel, type-I (c) and type-II (d,e) 2HDM. The line at $m_A - m_H = 200$ GeV shown in (c–e) corresponds to the edge of the analysis sensitivity due to the $E_{\mathrm{T}}^{\mathrm{miss}}$ requirement.

5.7.3 Model-Independent limits

The upper limits mentioned in Section 5.7.1 are based on the assumption that the final state's Z and H candidates are produced resonantly, leading to a significant model dependence. In addition to the 2HDM interpretation, we can obtain limits with less model dependence by slightly modifying the fit model. Assuming a resonance X decays into a $t\bar{t}$ or $b\bar{b}$ pair produced in association with a Z boson, the number of signal events recorded by the detector in a specific bin of the reconstructed $m(t\bar{t})$ or $m(b\bar{b})$ distribution will be equal to the integrated luminosity multiplied by the 'visible cross-section' $\sigma_{\text{vis}}(Z(\ell\ell)X(t\bar{t}))$ or $\sigma_{\text{vis}}(Z(\nu\bar{\nu})X(b\bar{b}))$.

Upper limits are determined at a 95% CL for the visible cross sections of $Z(\ell\ell)X(t\bar{t})$ and $Z(\nu\bar{\nu})X(b\bar{b})$ using the fitting model detailed in Section 5.6, with the exception that the distributions of $m(t\bar{t})$ or $m(b\bar{b})$ for events passing the SR selection are fitted using three bins. The signal template is created by adding a single signal event in the central bin of the $m(t\bar{t})$ or $m(b\bar{b})$ distribution, with the adjacent bins serving as control regions (CRs). The same-sign region and the $\mathtt{e}\mu$ and 2L regions are also utilized as CRs in this fit without any adjustments. Utilizing the $m(t\bar{t})$ or $m(b\bar{b})$ distributions instead of the Δm or $m_{\text{T}}(VH)$ distributions in the fit guarantees that the resulting limit is independent of how the Z and H candidates are produced. Furthermore, utilizing a large bin containing all of the signal events ensures that the limit is not heavily reliant on the lineshape of the $t\bar{t}$ or $b\bar{b}$ resonance.[6]

[6]For signals predicting a $t\bar{t}$ or $b\bar{b}$ resonance with a mass falling between the bin edges in Figure 5.24, the limits from all contributing bins need to be combined, accounting for their

The upper limits on the visible cross-section are determined as functions of $m(t\bar{t})$ and $m(b\bar{b})$ by performing multiple independent fits using different signal regions (SRs) defined by the bin edges shown in Figure 5.24. These limits can be used to assess sensitivities for theories involving high-mass $t\bar{t}$ or $b\bar{b}$ resonances by comparing the upper limits shown in Figure 5.24 with the visible cross-section predicted by a specific theory, given by

$$\sigma_{\text{vis}}^{\text{theory}} = \sigma_{\text{theory}} \times B \times (\mathcal{A} \cdot \epsilon)_{m(t\bar{t})/m(b\bar{b})}, \tag{5.4}$$

where σ_{theory} is the inclusive signal cross-section, B is the product of the branching ratios for the decay chain, and $(\mathcal{A}\cdot\epsilon)_{m(t\bar{t})/m(b\bar{b})}$ is the acceptance times efficiency for reconstructing a signal-model event in a given bin of the $m(b\bar{b})$ or $m(t\bar{t})$ distribution.

Utilizing the limits shown in Figure 5.24 requires obtaining the value of $(\mathcal{A} \cdot \epsilon)_{m(t\bar{t})/m(b\bar{b})}$ for a given signal model from a Monte Carlo 'truth'-level analysis that replicates the event selection described in Section 5.4, incorporating the detector effects. This can be achieved, for example, through fast simulation packages such as DELPHES [99] or smearing routines like the ones provided in the RIVET framework [50, 60].

---

respective acceptances.

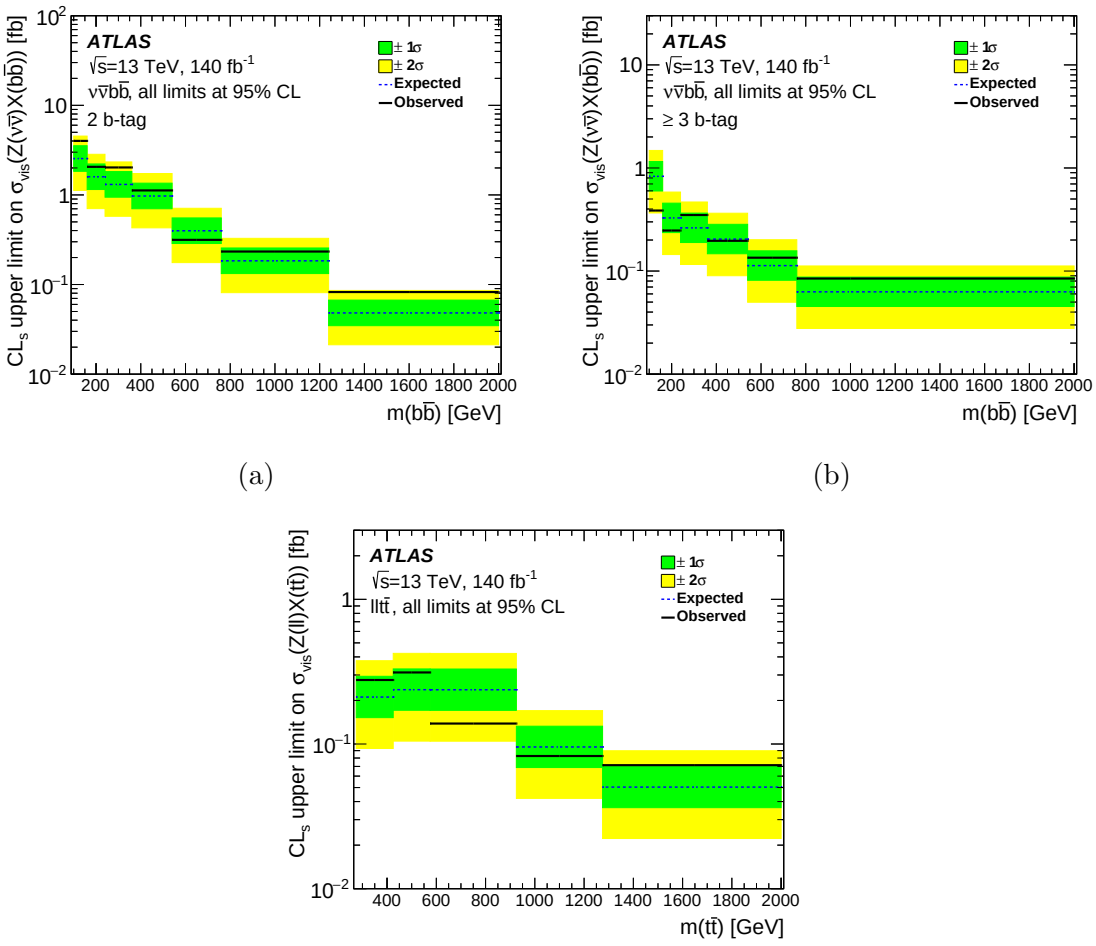

Figure 5.24. Observed and expected 95% CL exclusion regions in the (m_A, m_H) plane for various $\tan\beta$ values for the $\ell\ell t\bar{t}$ channel, type-I (a) and type-II (b) 2HDM, and $\nu\bar{\nu}b\bar{b}$ channel, type-I (c) and type-II (d,e) 2HDM. The line at $m_A - m_H = 200$ GeV shown in (c–e) corresponds to the edge of the analysis sensitivity due to the $E_{\mathrm{T}}^{\mathrm{miss}}$ requirement.

CHAPTER 6

SILICON STRIP DETECTOR

Silicon has revolutionized semiconductor detectors and electronic chips for commercial purposes. Sophisticated detectors are common because of Silicon's versatile properties, such as variable band gap, radiation hardness, and economic benefits over other semiconductor materials. This chapter looks at the basics of the particle matter interaction in Section 6.1.

6.1 The Particle - Matter interactions

Detecting particles involves observing their interactions with matter. As a charged particle travels through an absorbing medium, it interacts with the atomic electrons, mainly governed by the electromagnetic process. The particle's energy and proximity of each particle-electron interaction can cause the electron to move to a higher energy level within the atom (excitation), be released entirely from the atom (ionization), or create free electrons in the conduction band and holes in the valence bands of the material. The incoming particle loses a small amount of its initial energy during each interaction, and the average energy loss of the particle is determined using the *Bethe Bloch formula* (6.1).

$$-\frac{1}{\rho}\left\langle\frac{dE}{dx}\right\rangle = 2\pi N_A r_e^2 m_e c^2 \frac{Z}{A}\frac{z^2}{\beta^2}\left\{\ln\left(\frac{2m_e c^2\beta^2\gamma^2 W_{\max}}{I^2}\right) - 2\beta^2 - \delta - 2\frac{C}{Z}\right\} \tag{6.1}$$

Here ρ is the density of the absorbing material, z is the charge of the incident particle in the units of e, Z is the atomic number of the absorbing material, A is the atomic

weight of the absorbing material, N_a is the Avogadro's number ($6.022 \times 10^{23}\text{mol}^{-1}$), m_e is the electron mass, r_e is the classical electron radius, $\beta = v/c$ of the incident particle, $\gamma = 1/\sqrt{1-\beta^2}$, δ is the density correction, C is the shell correction, I is the mean excitation potential and W_{max} corresponds to the maximum kinetic energy that can be imparted to a free electron in a single head-on collision. The first two terms in (6.1) come from calculating energy loss due to ionization, the third term δ describes the density correction to the energy loss that becomes relevant at high energies, and the last term C/Z describes shell corrections due to atomic binding energy that is important at low energies [182].

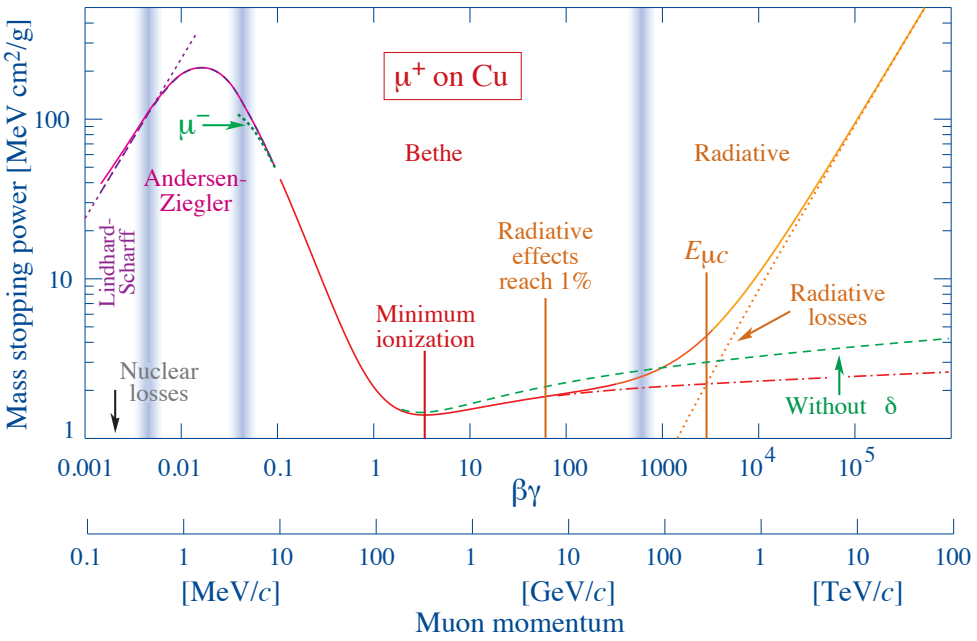

Figure 6.1. Average energy loss for a μ^+ in Copper medium [182].

Figure 6.1 shows the energy loss (mass stopping power) as a function $\beta\gamma$. At lower

$\beta\gamma$ values, we see a high energy loss, which comes from the velocity of the incoming particle being comparable to the speed of the orbital electrons. With the increase in $\beta\gamma$, the energy loss decreases $\propto 1/\beta^2$ for $\beta\gamma < 3$ with a minimum at $\beta\gamma \approx 3$. For regions beyond $\beta\gamma \approx 3.5$, increasing the particle's energy does not increase the energy loss due to the logarithmic term becoming effective, and simultaneously, radiative effects as the Cherenkov radiation and Bremsstrahlung start to become relevant. As $\beta\gamma$ increases, density corrections δ due to the polarization of the atoms close to the trajectory of the incident particles become more effective.

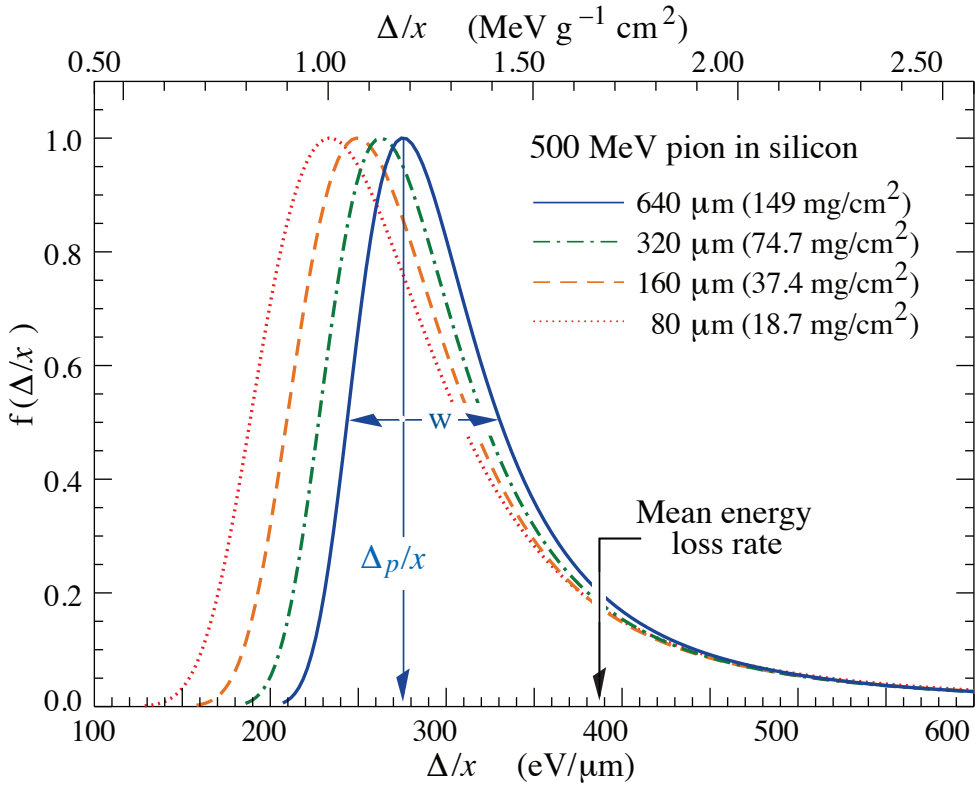

Figure 6.2. Normalized Landau distribution of 500 MeV pion interacting with different thicknesses of silicon. [182].

A relativistic particle suffering the minimum energy loss while traversing a material, called a Minimum Ionizing Particle (MIP), is used as a reference for detector designs, e.g. muons produced at the LHC. However, the energy deposited by the MIP in thin silicon absorbers is probabilistic and can be described by a Landau distribution as seen in figure 6.2. We also see the distribution of energy loss for an MIP for different thicknesses of silicon in figure 6.2. Electrons produced at LHC have a larger $\beta\gamma$ with processes like Bremsstrahlung dominating the energy loss.

Neutral particles like photons do not interact with coulomb force, but their passage through the material causes ionizations that can be detected. The main interaction for the high energy photons produced at the LHC is pair production, explained in the following section. If the photon energy is significantly larger than twice the electron's rest mass, the photon can convert into an electron-positron pair. The electrons lose energy mainly through Bremsstrahlung, and the amount lost is proportional to the particle's energy.

$$-\left(\frac{dE}{dx}\right)_{rad} = \frac{1}{X_0}E \tag{6.2}$$

Where X_0 is a characteristic property of the material called the radiation length, it represents the distance at which the particle's energy is reduced to $1/e$ of its original value. Similarly, λ represents the distance after which the 1/e of photons have undergone pair production and is related with X_0 as $\lambda = \frac{7}{9}X_0$. We try to minimize the radiation lengths for trackers to reduce the particles' unwanted interactions until they reach the calorimeter.

6.2 The Photon - Matter interactions

The interactions of matter and photons differ from those of massive particles. A photon interacts mainly via the photoelectric effect, Compton scattering, and pair production, depending on the material and the photon's energy. Figure 6.3 shows the absorption coefficient of silicon against the photon energy.

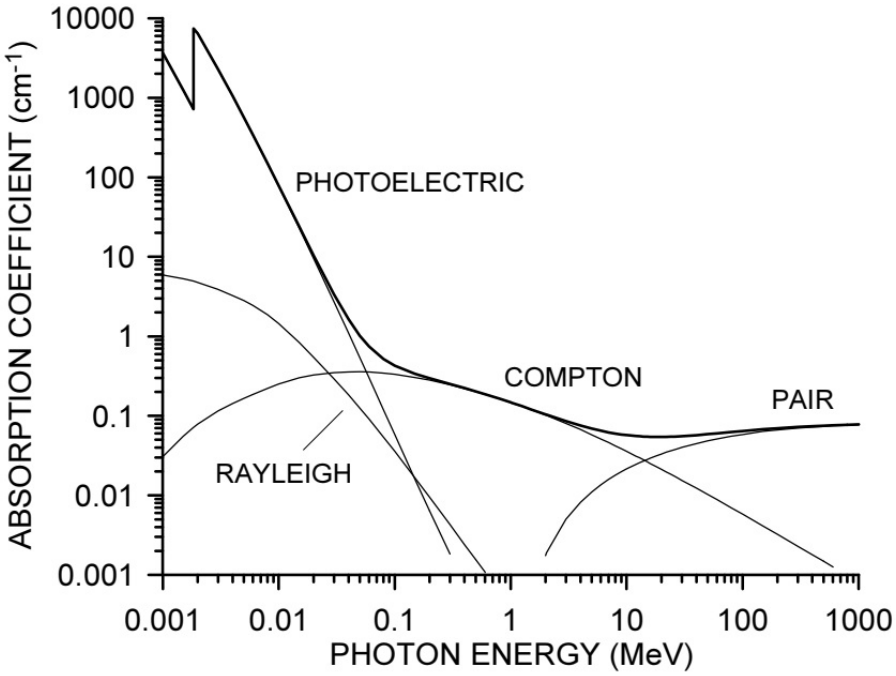

Figure 6.3. The photon absorption coefficient μ vs. energy in silicon. At low energies, photoelectric absorption dominates. Above 100 keV, Compton scattering takes over, and at high energies, pair production dominates. [177].

Photoelectric effect

The Photoelectric effect, discovered by the physicist Heinrich Rudolf Hertz, is the electron emission phenomenon when light with a specific frequency shines on a material. In his Nobel prize-winning paper, Einstein used Max Planck's quanta of energy concept to theorize that the energy of each quantum of light is Planck's constant times the frequency of the light $E_\gamma = h\nu$ and that the energy of the incident photon is wholly absorbed in the atom. This absorbed energy is transferred to electrons bound to the nucleus with binding energy E_{BE}. When the energy of the incoming photon exceeds the atom's binding energy, the excess energy gets converted into kinetic energy T of the emitted photoelectron $T = E_\gamma - E_{BE}$. This emission of electrons from the valance shell creates a hole, and an electron from the higher energy orbit fills the inner shell by emitting a photon of energy $E_\gamma = E_f - E_i$ that can be observed as the current in the detectors' readout.

Compton scattering

Arthur Holly Compton discovered Compton scattering during his work on X-rays. Compton scattering is the inelastic scattering between the high-energy incoming photons and the electrons in the atom's outer shells. These loosely bound outer shell electrons get ejected "Compton recoil electrons" after taking a fraction of the energy from the photons. The scattered outgoing photon of a lower energy can also be observed.

Pair Production

When a high-energy photon interacts with the coulomb field of a heavy atom's nucleus, it can produce an electron-positron pair. This process is kinematically constrained

by the mass of the electron and positron, which is why it becomes dominant only when the energy of the incoming photon exceeds 1.02 MeV $\approx$ twice the electron's rest mass.

6.3 Semiconductors and p-n Junction diodes

In Isolated atoms, electrons occupy discrete energy levels known as orbitals. When Isolated atoms are brought together to form a crystal lattice, their wave functions overlap, and due to Pauli's exclusion principle, their energy levels are split to form bands. These bands represent a continuum of energy states the electrons can occupy. A **valance band** is formed from the atomic orbitals of the atoms' outermost electrons responsible for chemical properties from the valance band. At absolute zero temperature, the valance band is filled with electrons. **Conduction bands** are formed from the empty higher-energy atomic orbitals in the atom's ground state. Electrons in conduction bands are free to move in the material, enabling electricity to be conducted. The bandgap is the energy difference between the valance band's top and the conduction band's bottom energy levels. If the band gap is small, electrons from the valance band can easily jump into the conduction band, thus enabling conduction. The bandgap in energy is used to classify materials into conductors, insulation, and semiconductors. At any arbitrary temperature, Insulators will have a very large bandgap (greater than 4 eV); conductors have a very small to negligible band gap, and semiconductors have a band gap that can be crossed under a change of physical conditions (approx 1 eV), for example, temperature.

The Fermi-Dirac distribution gives the probability of an electron occupying an energy state E as:

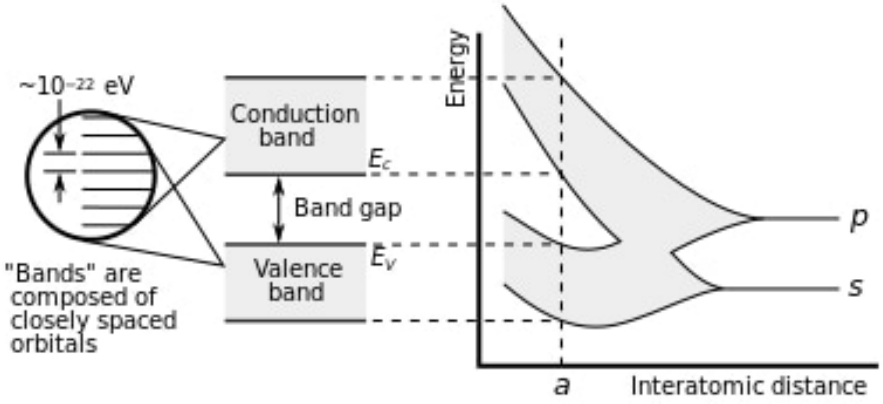

Figure 6.4. Formation of bands in carbon atoms when forming a diamond crystal of size "a". [44]

$$f_e(E,T) = \frac{1}{1+\exp\frac{E-E_f}{kT}} \tag{6.3}$$

where T is the temperature, E_f is the Fermi energy and k is the Boltzmann constant. The probability of holes (absence of electrons) occupying an energy state is given by

$$f_h(E,T) = 1 - f_e(E,T) \tag{6.4}$$

When the concentration of the electrons and holes is equal, the Fermi level lies in the middle of the valance band and the conduction band.

Intrinsic Semiconductors

Intrinsic semiconductors are materials that do not contain any impurities. The concentration of electrons and holes in these materials are equal, which means the Fermi level is between the valance and conduction bands. The number of charge carriers

$$n_i \propto T^{\frac{3}{2}} \exp -\frac{\Delta E}{2kT} \tag{6.5}$$

At room temperature for intrinsic silicon, $n_i \approx 10^{10}$ cm^{-3} .

Extrinsic Semiconductors

Adding impurities in a controlled manner, called "Doping," can alter the characteristics of intrinsic semiconductors. In Doping, we replace the atoms from the intrinsic semiconductor's lattice with an electron donor (n-type) or acceptor (p-type); see Figure 6.5. In *n-type*, the silicon lattice is doped with a material with more than 4 electrons in the valance shell, e.g., Phosphorus. The free electrons raise the Fermi level close to the conduction band, which makes it easier for electrons to jump to the conduction band. In *p-type*, the silicon lattice is doped with a material with less than 4 electrons in the valance shell, e.g., Aluminum. This lowers the Fermi level close to the valance band, which makes it easier to conduct holes. The concentration of doping is usually between 10^{12} to 10^{21} cm^{-3}. Although the number of charge carriers is large, the noise due to the charge carriers is also very high. This is solved by joining the p-type and n-type doped semiconductors to form a junction diode.

p-n Junction Diode

A p-n junction diode is a semiconductor device with a p-type and a n-type semiconductor forming a junction. Due to concentration gradient, i.e., a high number of electrons on the n-type side and holes on the p-type side, the majority charge carriers tend to diffuse to the other sides, creating uncompensated dopant atoms and a region that

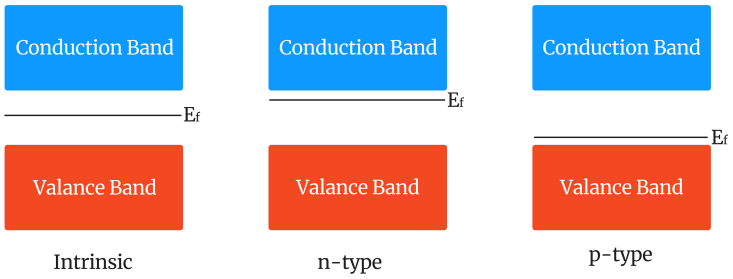

Figure 6.5. A visualization of the band diagrams and the Fermi energy level E_f for the Intrinsic, p-type, and n-type semiconductors.

lacks free charge carriers, known as the depletion region. As the charge carriers diffuse, there is a buildup of an Electric field from the uncompensated dopants that oppose the movement of the charge carriers across the junction. At equilibrium, the depletion layer no longer grows, and the built-in electric field balances the diffusion of majority charge carriers. The electric field E and potential ϕ in the depletion region can be calculated using Poisson's equation $\nabla^2 = -\frac{\rho}{\epsilon}$ where the ρ is the spatial charge distribution, and ϵ is the absolute permittivity [149]. It is possible to calculate the built-in voltage (ΔV) using the Doping concentrations and the number of free carriers of the acceptor (N_A, n_a) and the donor (N_D, n_d), respectively.

$$\Delta V = \frac{kT}{q} \log \frac{N_A N_D}{n_a n_d} \tag{6.6}$$

The Width of the depletion region is calculated using the built-in voltage and doping concentrations as

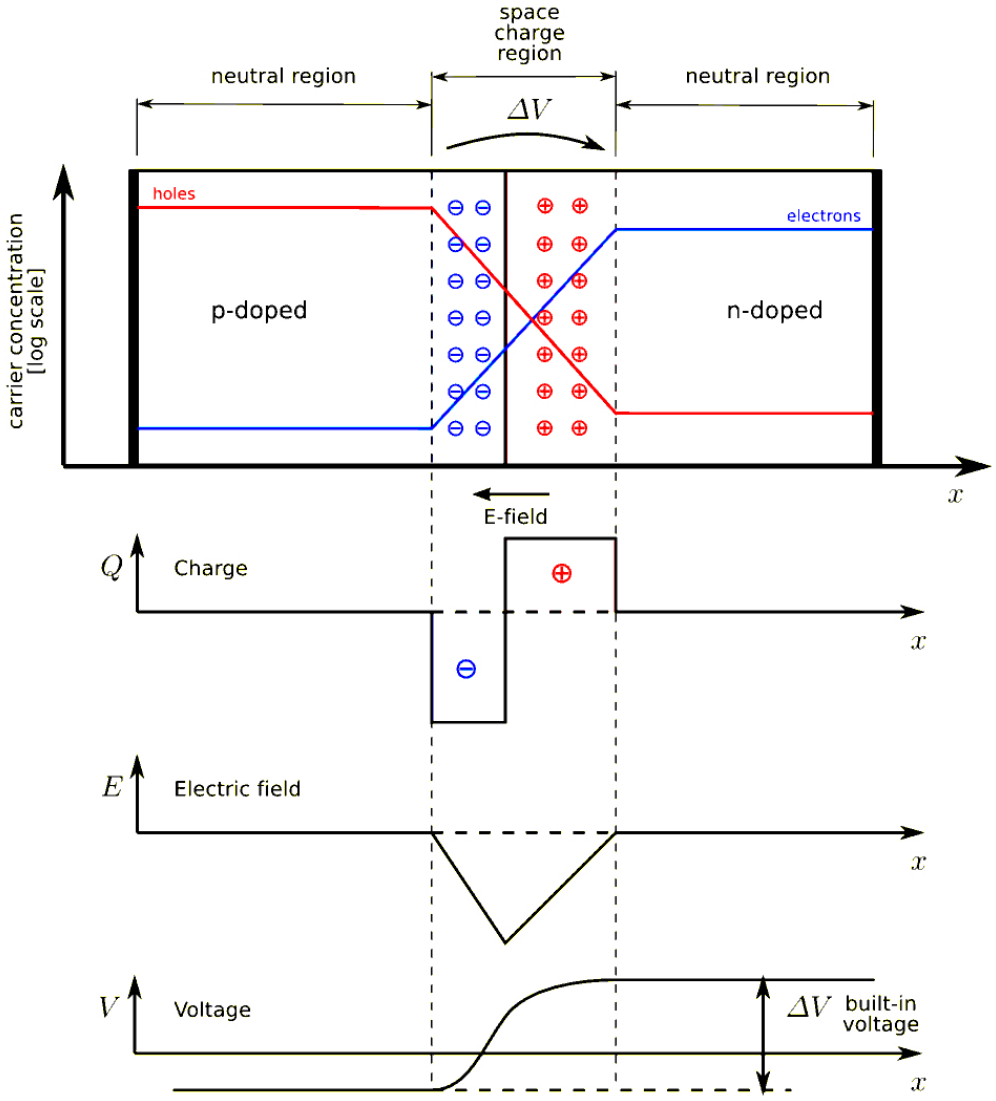

Figure 6.6. An Illustration of the p-n junction diode. The top image shows the carrier concentration with holes in red and electrons in blue. The second graph shows the charge across the junction. The third graph shows the electric field and the lowest graph shows the voltage across the junction. Figure adapted from [157]

$$W = \sqrt{\frac{2\epsilon\epsilon_0 \left(N_\mathrm{A} + N_\mathrm{D}\right)}{qN_\mathrm{A}N_\mathrm{D}}\Delta V} \tag{6.7}$$

The p-n junction diode is connected to an external voltage source during operation.

The depletion region increases if the external bias voltage V_{bias} is applied to the junction in the same direction as the built-in voltage. In this state of operation, the diode is called *reverse biased*. When the external voltage applied is opposite to the built-in voltage, the depletion region shrinks, and the diode is said to be *forward bias*. In equation (6.8), the sign of the V_{bias} increases or decreases the width of the depletion region.

$$W = \sqrt{\frac{2\epsilon\epsilon_0 \left(N_{\mathrm{A}} + N_{\mathrm{D}}\right)}{qN_{\mathrm{A}}N_{\mathrm{D}}}(\Delta V + V_{bias})} \tag{6.8}$$

The depletion layer also acts as a capacitor; its capacitance per unit area depends on the width of the depletion layer W, absolute permittivity ϵ, and vacuum permittivity ϵ_0, given in the (6.9).

$$C = \frac{\epsilon\epsilon_0}{W} \tag{6.9}$$

For a silicon diode of thickness 100 μm, the capacitance is approximately 1 pf/ mm^2. When the bias voltage is much larger than the built-in voltage, the capacitance can be approximated to

$$C \propto \frac{1}{\sqrt{V_{bias}}} \tag{6.10}$$

The general configuration used to increase the width of the depletion layer is to sandwich a lightly doped region between two highly doped regions, as shown in figure 6.7. This configuration leads to an asymmetric junction that depletes into the bulk by applying a minimum bias voltage.

A MIP traversing 300 μm intrinsic silicon semiconductor creates approximately 2×10^4 electrons, but the number of free charge carriers is $\approx 10^9$. Giving a signal-

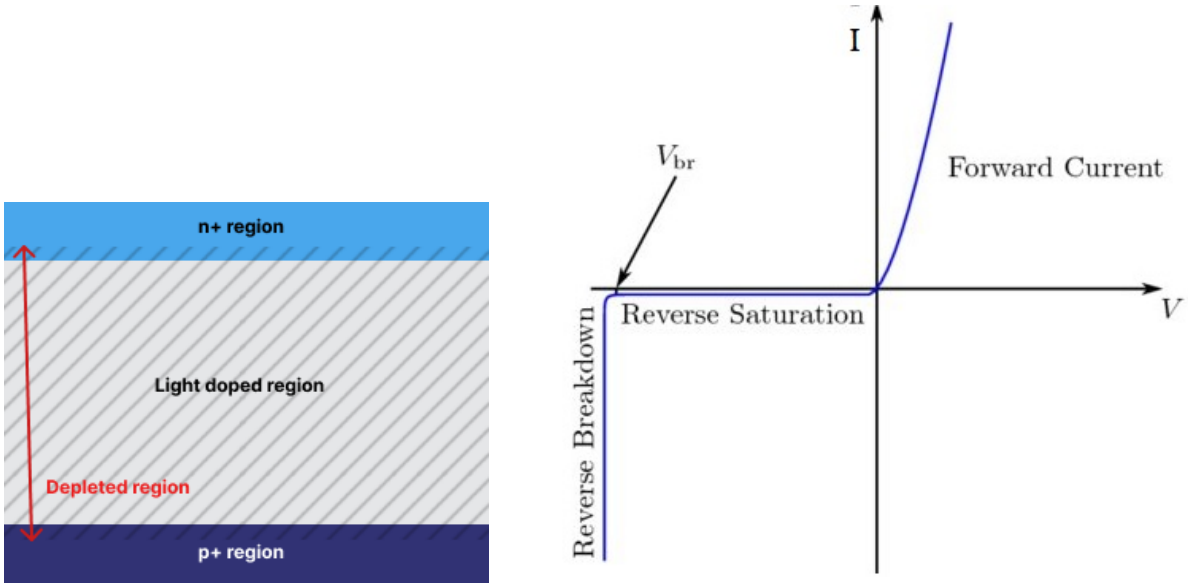

Figure 6.7. The left figure shows a visualization of a typical configuration used in silicon sensors where a lightly doped region is sandwiched between two heavily doped regions. The figure on the right shows typical IV characteristics of a p-n Junction diode in the forward-biased and reversed mode. V_{br} is the breakdown voltage.

to-noise ratio of 10^{-5}. To improve the signal-to-noise ratio, the detector is operated in reverse-biased mode, with the depletion region covering the entire silicon, thereby reducing the number of free charge carriers. However, this reverse biasing also results in a leakage current due to thermally generated electrons in the circuit despite removing mobile carriers from the depleted region. The leakage current is mainly temperature-dependent and is expressed as $I_{leakage} \propto T^2 \exp -\frac{kT}{E_g}$ where E_g is the band gap energy and k is the Boltzmann's constant. To reduce the effect of the leakage current in signal detection, the detectors are typically run at cold temperatures $\approx -35°$C.

6.3.1 Strip Sensor

The silicon strip sensors are diodes in which one electrode is segmented in one of the directions to improve position resolution in that direction. The image in Figure 6.8 illustrates an n+ in p sensor, which comprises strips of n+ doped silicon placed into a p bulk. When the bulk is fully depleted with a full bias voltage V_{FD}, an electric field is produced inside the sensor. A particle passing through the sensor creates electron and hole pairs, which move toward the appropriate electrodes under the influence of the electric fields. In Figure 6.8, a thin layer of SiO_2 is used to AC couple the signal to the readout electronics via the aluminum lines placed on top of the implants.

The segmentation pitch determines the spatial resolution in one direction as

$$\sigma = \frac{d}{\sqrt{12}} \tag{6.11}$$

where σ is the error in position measurement, and d is the strip pitch. It can be demonstrated by assuming uniform particle occupancy and a binary readout.

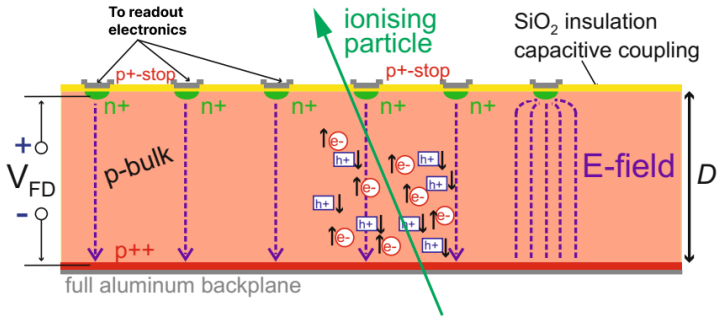

Figure 6.8. A visualization of n+ in p sensor with bulk thickness D that is fully depleted under the application of V_{FD}. Figure adapted from [132]

Figure 6.9 shows a closer look at the different components of a strip sensor. An *isolation layer* is added to ensure proper isolation between the strips. In the case of n+ in p-type sensors, the inter-strip isolation is attained by adding a p-type region called "p-stop" between the n-type implants, see Figure 6.8. The *bias ring* and the backplane are the primary contacts to apply bias voltage. The bias ring surrounds the whole active area of the sensor to ensure a homogeneous potential for all strips. Strips connect to the bias ring in parallel; this helps ensure a common ground for all strips. To minimize edge effects, the *guard ring* shapes the electric field within the sensitive area to ensure uniform potential for all strips, including the ones at the edge. *AC pads* serve as electrical contacts for readout electronics and measure coupling and inter-strip capacitance. *DC pads* are connected to n+ implants for measuring inter-strip, bias, and coupling resistance. A thin layer of SiO_2 protects the active semiconductor surface called *Passivation*.

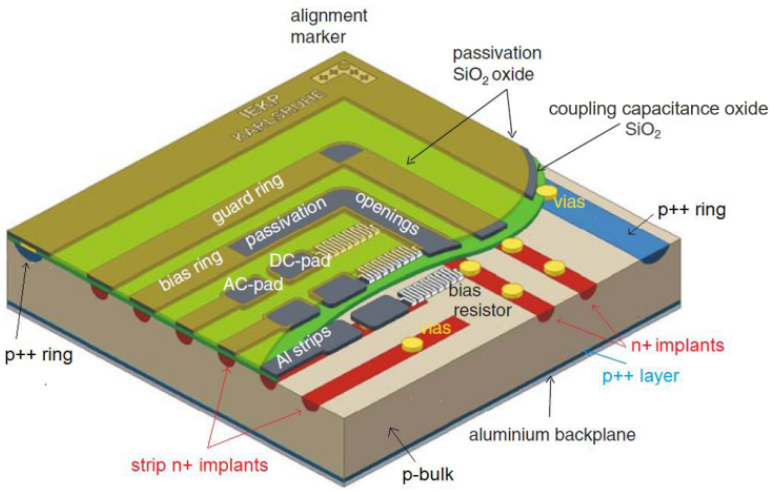

Figure 6.9. A realistic visualization of n+ in p sensor. Figure adapted from [132]

6.3.2 Radiation Damage

Detectors in High-energy physics operate in high-radiation environments. Prototypes of detectors like the ATLAS Inner Tracker are often irradiated with radioactive sources to study their expected behavior in actual operation. Understanding their behavior and the radiation damage before we put them in caverns is paramount. There are two types of radiation damage: bulk damage and surface damage.

6.3.2.1 Bulk Damage

Bulk damage in silicon refers to the structural and electrical modifications that occur within the main volume of silicon material due to external factors. The primary cause of bulk damage is Non-Ionizing Energy Loss (NIEL), which occurs when a particle passes through the bulk material, causing changes in the crystal's structure. When high-energy particles such as neutrons, protons, or heavy ions collide with silicon atoms, these atoms are displaced from their original positions in the lattice structure. As a result, *vacancies* and *interstitials* are created, forming complex defects that can trap charge carriers and, consequently, degrade the semiconductor properties of the material. These damages can significantly affect the properties and performance of the detector, manifesting in an increasing leakage current, changing depletion voltage, and decreasing charge collection efficiency, see Figure 6.10 (left).

One of the phenomena observed in n-type semiconductors is "Type inversion". In Figure 6.10(right), one observes effective doping concentration decreases with an increase in particle fluence and reaching a minimum of around 10^{12} n_{eq} cm^{-2}. The effective doping

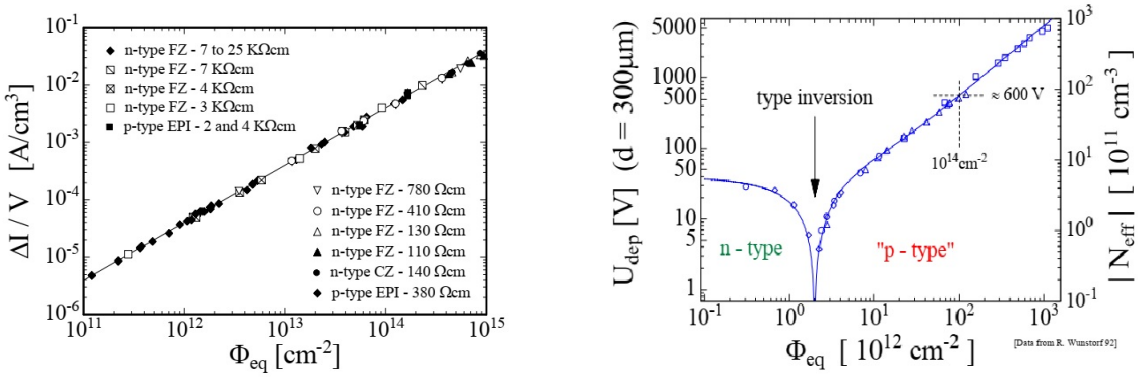

Figure 6.10. The left figure shows the damage-induced leakage current change $\Delta I/V$ as a function of the particle fluence Φ_{eq}. The figure on the right shows the effective doping concentration change in standard silicon, as measured immediately after neutron irradiation. [154]

concentration flips at this point, hence the name type inversion. Figure 6.11 shows type-inversion, and Figure 6.12 shows increased leakage current observed during the Run-2 of the ATLAS SCT.

6.3.2.2 Surface Damage

Silicon sensors are also susceptible to surface damage, mainly caused by ionizations that create electron-hole pairs in the SiO_2 surface. Although electrons can escape the insulating layer before recombination, the holes get trapped. These trapped holes attract electrons from the sensor, causing a buildup at the interface, which shorts the strips. To mitigate these effects in the strip sensors, a p-layer is used around the implant to ensure inter-strip isolation. In ASICs, we notice a similar surface phenomenon where holes get stuck in deep trapping centers in the SiO_2 material, creating an electrical field around the transistors' edges, indirectly increasing leakage current. However, at a high Total Ionizing

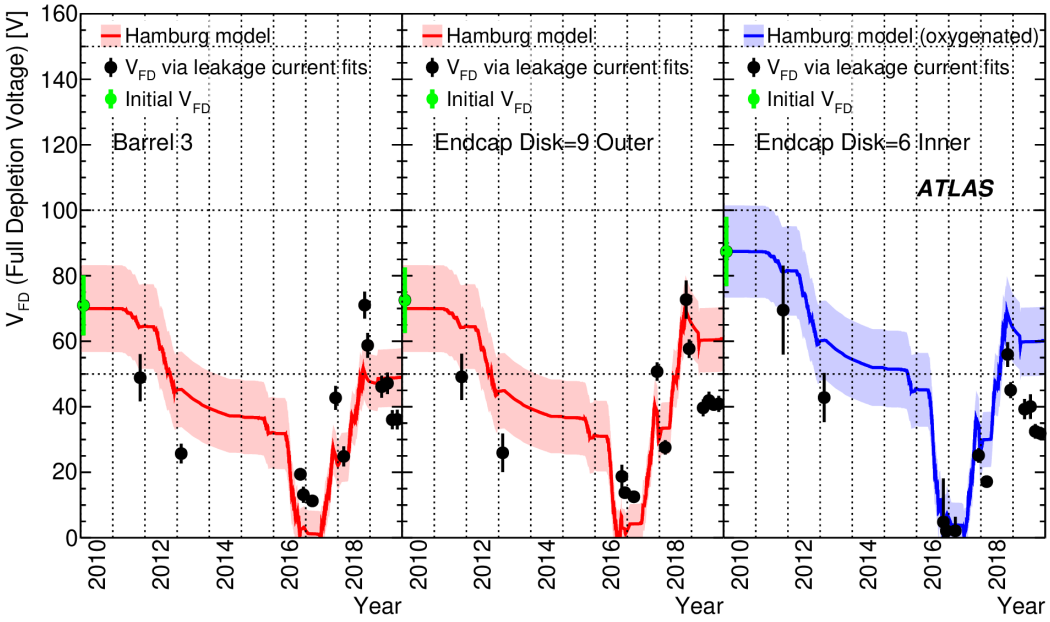

Figure 6.11. Evolution of V_{FD} over the years as estimated from the I–V curves. [3]

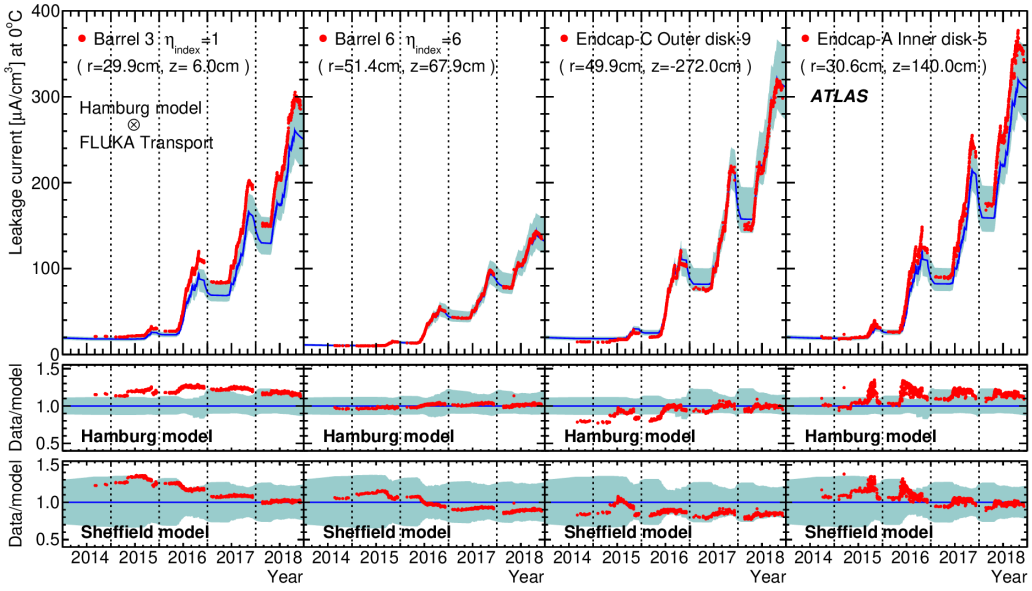

Figure 6.12. The main plot shows the evolution of normalized leakage currents for four groups of modules of the SCT. [3]

Dose (TID), ionizing radiation activates the trapping center at the Si-SiO_2 interface. In the NMOS transistor, these centers trap electrons in the p-type silicon, compensating for a part of the positive charge trapped in the oxide. The leakage current in ITk strips front-end ASICs increases to 0.6 Mrad and then decreases; see Figure 6.13.

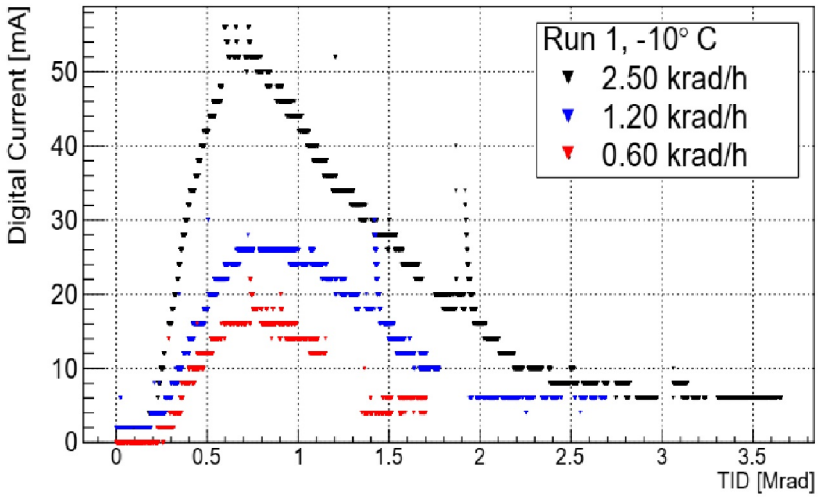

Figure 6.13. Current change in ABC130 chips as a function of TID for non pre-irradiated chips [180]

6.3.2.3 Damage in Readout electronics

Radiation can also affect digital electronics. High linear energy transfer (LET) from charged heavy particles can cause faults in the digital readout logic. When heavy ion particles strike the depleted region of a transistor, they deposit a large amount of energy and alter the state of memory cells. This phenomenon is called Single Event Upset (SEU), which can cause errors in the chip's performance or permanent damage.

An SEU can cause a memory cell's bit to flip, leading to incorrect information being recorded by the chip. One of the ways to mitigate this is by Triplication, which consists of replicating memory cells combined with majority vote logic to provide more robustness to the digital logic.

After being exposed to radiation, the properties of silicon tend to change over time; this process is known as annealing [149]. During this process, a vacancy can combine with an interstitial, or the defect can transform into a different defect with new properties. The impact of radiation damage reduces within a few weeks at room temperature due to beneficial annealing. However, after some time, reverse annealing is observed where the space charge increases, adversely affecting the detector's performance. Annealing is expected to happen faster at higher temperatures, facilitating higher atomic mobility and bond breaking. Keeping the radiated samples at low temperatures would reduce the mobility and the frequency of bond breaking; thus, radiation samples are recommended to be kept at low temperatures to prevent changes in detector properties due to annealing.

6.3.3 Readout of Sensors

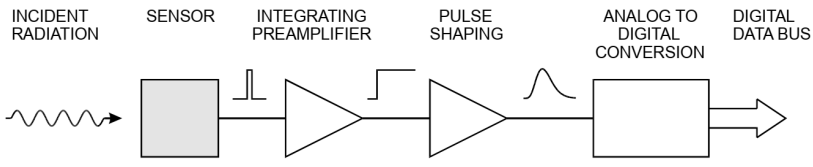

Figure 6.14. Basic detector functions: Radiation is absorbed in the sensor and converted into an electrical signal. The low-level signal is integrated into the preamplifier, fed to a pulse shaper, and digitized for storage and analysis. Figure adapted from [177]

Readout electronics are an important part of any detector. The signals from the sensors undergo amplification, shaping, and digitization and are then stored for further analysis; Figure 6.14 shows a sketch of the first steps of the readout chain. The following section provides a brief overview of the readout electronics.

Sensor

The function of the sensor is to transform the energy transferred by a particle into an electrical signal. In the case of silicon sensors, the ionization caused by a particle passing generates holes and electrons. These holes and electrons move toward the electrodes in the electric field. The number of electron-hole pairs depends on the energy absorbed; therefore, the signal charge is obtained by integrating the signal current.

Preamplifier

Silicon sensors have minimal signal charges that depend on the thickness of the sensor (typically 4 fC in a high-energy tracker); therefore, they need amplification. The magnitude of the sensor signal is also subject to noise; hence, the preamplifiers are designed carefully to minimize electronic noise.

Shaper

Shapers are commonly used in detector systems to enhance the signal-to-noise ratio. It functions by analyzing the frequency spectrum of the preamplifier's output. One can customize the output in the frequency domain to benefit the signal by utilizing a combination of high-pass and low-pass filters. Since modifying the preamplifier's output in the frequency domain impacts it in the time domain, it is also referred to as a shaper.

Digitizer

The shaper's output is precisely tuned to the signal frequencies. The ADCs then translate these continuous analogue signals into a unique bit pattern output or a binary output of 0 or 1, depending on pre-set thresholds.

6.3.3.1 Calibration circuit

Along with the basic architecture described above, some additional auxiliary electronics are useful in the detector's operation. A calibration charge injection circuit is placed in parallel to the sensor to help calibrate the thresholds and timings of the front-end electronics.

6.3.4 Sources of Noise in Semiconductor Detectors

Signals picked up by detectors are often affected by unwanted fluctuations or variations from the sensor or the front-end electronics, commonly called "noise." These fluctuations can worsen the signal quality, making it challenging to draw accurate conclusions and further processing. Distinguishing between signals and noise is a fundamental concept in signal processing. It is particularly critical in semiconductor detectors, where the noise variance is much higher than the signal variance. Most detectors measure the charge delivered by an ionization event. The equivalent noise charge (ENC) is the most commonly used parameter to characterize the noise. ENC is the input charge producing an output signal amplitude at the shaper equal to the root-mean-square (RMS) noise. The ENC represents the minimum detectable charge by the system that makes the signal-to-noise ratio equal to 1.

In a closed system, the current flowing between two electrodes, a distance s apart, is:

$$i = \frac{nev}{s} \tag{6.12}$$

where n is the number of electrons, e is the electric charge, and v is the velocity of the electrons. The total differential can give the fluctuations in this current.

$$\langle di \rangle^2 = \left(\frac{ne}{s}\langle dv \rangle\right)^2 + \left(\frac{ev}{s}\langle dn \rangle\right)^2 \tag{6.13}$$

The two statistically uncorrelated terms in (6.13) give us an idea of the noise contributions to the total noise, called the velocity fluctuations of the number fluctuations. The three primary sources of noise for the context of the thesis work are *Thermal noise*, *Shot noise*, and $1/f$ *noise*. Noise analysis is generally done in the spectral space. For our case, we look at the voltage spectrum or current spectrums, defined as $dv_n/df \equiv e_n$ and $di_n/df \equiv i_n$ for the following analysis.

Thermal Noise

Thermal noise, also known as Johnson-Nyquist Noise, is caused by the random movement of electrons in conductors due to thermal energy. This noise adds to the velocity fluctuations in (6.13). It is described by Planck's black body spectrum at long wavelengths, where the spectral density is constant, hence classified as "white" noise. The power in a resistor is $i^2R = v^2/R$ with R the resistance, k is the Boltzmann constant, and T is the absolute temperature. For thermal noise the spectral voltage noise density

is given as

$$\frac{dv_n^2}{df} = 4kTR, \tag{6.14}$$

and the spectral current noise density is given as

$$\frac{di_n^2}{df} = \frac{4kT}{R}. \tag{6.15}$$

Equation 6.14 and 6.15 are useful in noise simulations where a resistor can be modeled as a voltage source with a resistor in series or a current source in parallel with the resistor. It is impossible to eliminate this type of noise at non-zero absolute temperatures.

Shot Noise

Shot noise is Poisson-distributed fluctuations in the number of charge carriers in a device. One example of this type of noise is the thermionic emissions or current flow in a semiconductor diode where the probability of crossing the potential barrier is uncorrelated among the charge carriers. It is a part of the number fluctuations in (6.13). The spectral density of these fluctuations is constant. Hence, they are also a part of the "white noise".

The current spectral noise density of shot noise is given as

$$\frac{di_n^2}{df} = 2Ie \tag{6.16}$$

where I is the average current and e is the electronic charge. In the case of ohmic devices, the Shot noise is zero as the random fluctuations between the positive and the negative charge carriers cancel out.

1/f Noise

The fluctuations in the charge carriers getting trapped in the imperfections of a crystal lattice and then released with a characteristic time constant also contribute to the

number fluctuations in (6.13). It is also called "flicker noise", and unlike the Shot and Thermal noise, it has a frequency-dependent power spectrum $\equiv 1/f^{\alpha}$ where α typically ranges between $0.5 - 2$

6.3.5 Noise calculation for Strip Semiconductor Detectors

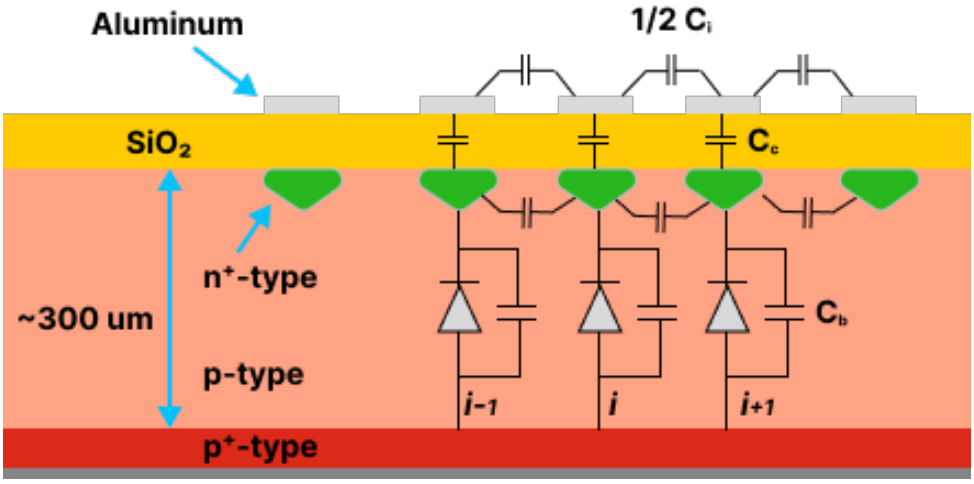

Figure 6.15. Visualization of a silicon strip detector as a corresponding electrical model.

This section reviews the noise in strip detectors via its electrical model. Each strip of the ITk strip sensor is modeled as a diode in reverse bias, as shown in Figure 6.15. C_b is the strip's capacitance to the sensor's backplane parallel to the diode, C_c is the coupling capacitance between the aluminium and the n+ implants, and C_i is the inter-strip capacitance. Another noise source considered is the first input transistor of a bipolar transistor in the preamplifier, exhibiting shot noise.

In figure 6.16, we can see a simplistic electrical and noise model for the strips where

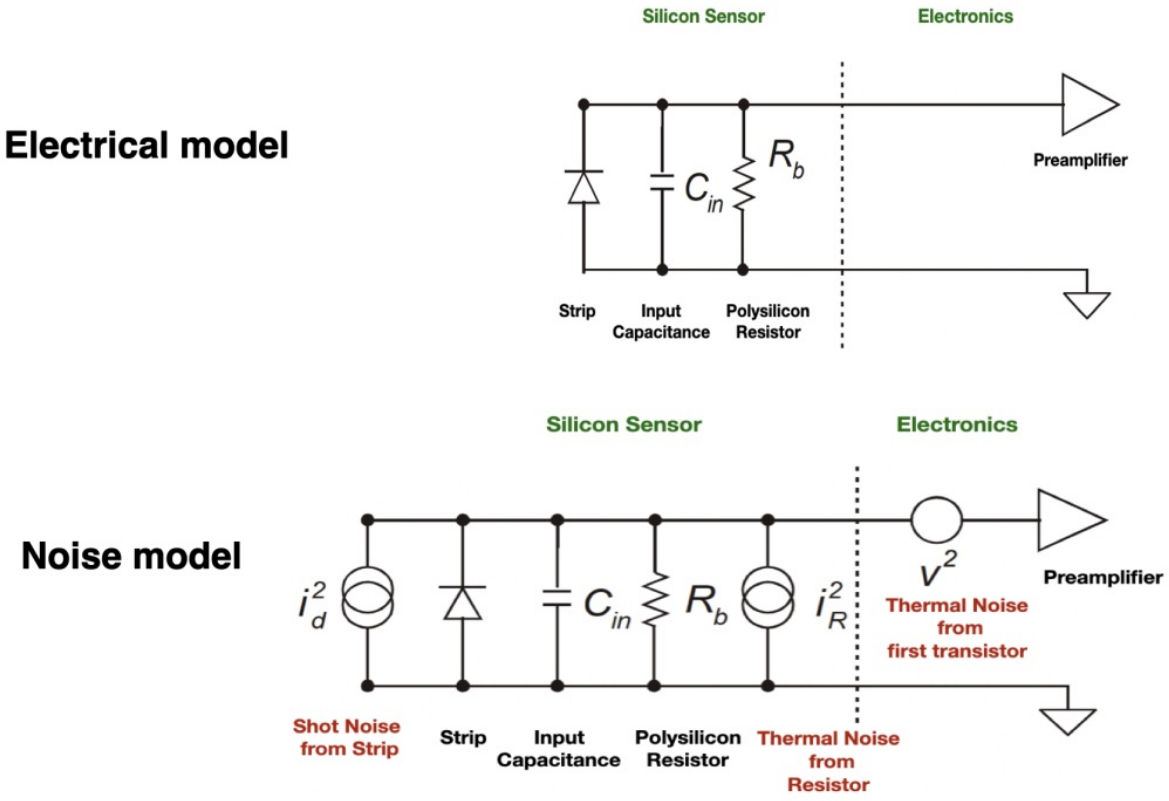

Figure 6.16. Electrical(top) and noise (bottom) models for one channel of silicon strip detector and front-end electronics. Figure adapted from [68]

the C_{in} is the input capacitance corresponding to $C_{in} = C_b + 2C_i$. The noise model in 6.16 considers the contributions from the thermal and shot noise from the possible sources in the circuit, disregarding the flicker noise for simplicity. We see a time-dependent response $V(t)$ at the preamplifier's output for a particle passing through the detector; however, for the following discussion, we use $h(t)$, which is a normalized version of $V(t)$. Noise sources in strips like the leakage current, bias resistors, and the preamplifier input transistor have been modelled as thermal and shot noises. Noise studies are generally conducted by examining the preamplifier's output. This gives us a basis for classifying noise sources

as parallel or series noise based on whether the source is parallel to the detector or in series with the preamplifier. The noise sources in our cases can be classified as parallel to the signal current source (like the shot noise from stips or thermal noise from polysilicon resistors) or series voltage noise from the first transistor. The analytic form of these noises is given as [166]:

$$\text{Parallel Noise: } \text{ENC}^2 = \frac{1}{2} W_0 \int_0^\infty h^2(t) dt, \tag{6.17}$$

and

$$\text{Series Noise: } \text{ENC}^2 = \frac{1}{2} 4kTR_b C_{in}^2 \int_0^\infty h'^2(t) dt, \tag{6.18}$$

with spectral density $W_0 = 4kT/R$ for thermal noise and $W_0 = 2Ie$ for shot noise. The exact analytic form of the response function is generally not easily available, but the peaking time t_p is known, so in most cases, the analysis is done using a triangular response with t_p as the peaking time, as shown in figure 6.17.

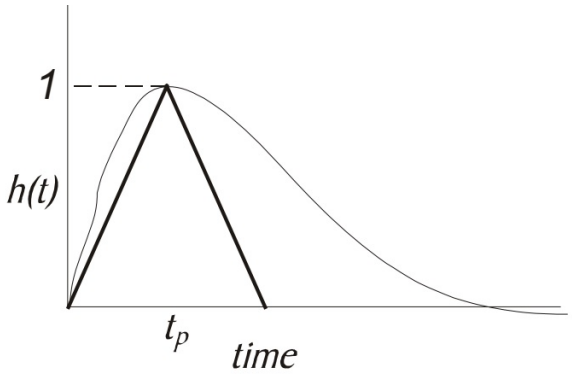

Figure 6.17. Typical impulse response and a triangular response approximation.

Approximating the triangular function $h(t)$ as

$$h(t) = \begin{cases} t/t_p, & \text{if } 0 < t < t_p \\ 2 - t/t_p, & \text{if } t > t_p \end{cases} \tag{6.19}$$

we get the series and parallel noise contributions as

$$\text{Parallel Noise: ENC}^2 = \begin{cases} \frac{4kTt_p}{3R_b}, & \text{thermal noise} \\ \frac{2Iet_p}{3}, & \text{shot noise} \end{cases} \tag{6.20}$$

and

$$\text{Series Noise: ENC}^2 = \frac{4kTR_bC_{in}^2}{t_p}, \tag{6.21}$$

From equation 6.20 and 6.21, we can identify the main factors contributing to the noise in strip detectors, i.e., the input capacitance C_{in}, the bias resistors R_b and the leakage current I. The series noise is linearly proportional to C_{in}; hence, lower input capacitance is favourable, as seen from figure 6.18. A lower bias resistance is preferred when placed in series with the preamplifier, while a larger value is preferred when placed in parallel. Additionally, a large leakage current leads to a large parallel noise. An optimal choice of shaping time is made when designing the front-end electronics of a detector; as we can see from equation 6.20 and 6.21, a large shaping time would increase the parallel noise but reduce the series noise.

The total noise is $\text{ENC}_{total} = \sqrt{\sum \text{ENC}^2}$. For a chip with 10 pF input capacitance, 1 nA leakage current, and 2 MΩ resistors for each chip, a peaking time of 25 ns, and a collector current of 200 nA, the total noise is approximately 570 e. Figure 6.18 shows the change in noise with the input capacitance in different prototype chips and sensors tested for the ATLAS ITk strip detector.

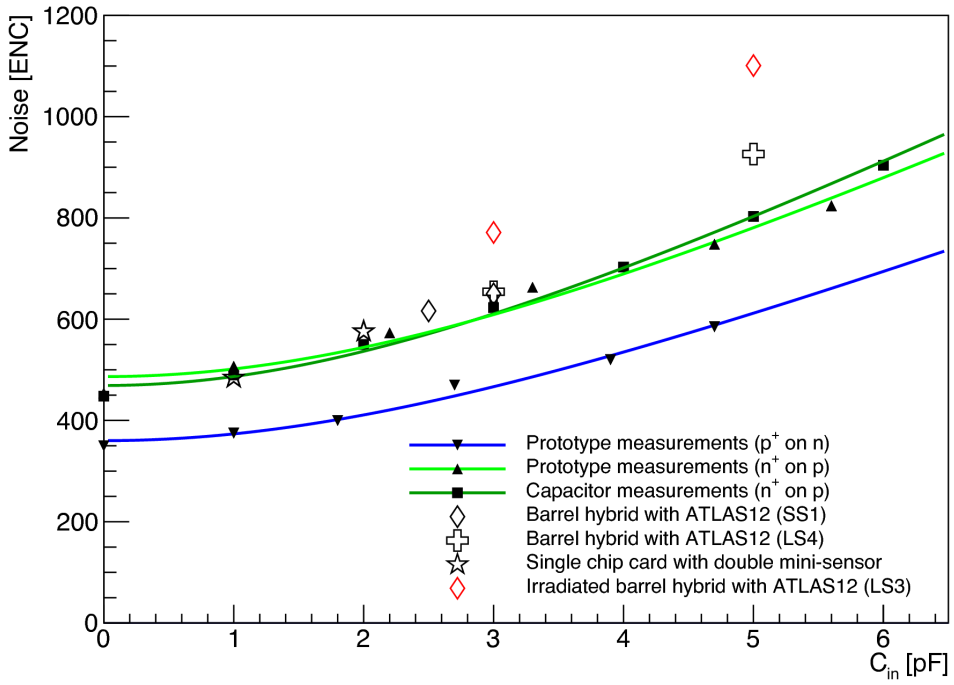

Figure 6.18. Measured noise as a function of input capacitance for a range of prototype devices. [21]

6.4 ITk strips

A planned LHC upgrade starting in 2029 will increase the luminosity of the machine up to instantaneous luminosity of 7×10^{34} s^{-1} cm^{-2}, corresponding to a maximum pile-up of 200 inelastic proton-proton collisions per beam crossing and the hadron fluence of approximately 2×10^{16} n_{eq} cm^{-2} [21]. To withstand this high radiation environment of accumulated luminosity 3000 fb^{-1}, detector upgrades for the High Luminosity-LHC (HL-LHC) have already started.

The current ATLAS Inner Detector (ID) was designed to operate at a constant instantaneous luminosity of 1×10^{34} s^{-1} cm^{-2} with 14 TeV centre-of-mass energy, 25

ns between bunch crossings, and an average pile-up (the average number of particle interactions per bunch-crossing) of 23 proton-proton interactions per crossing. In 2016, the LHC exceeded the design parameters when the peak instantaneous luminosity was 1.37×10^{34} s^{-1} cm^{-2} with a peak pileup of 40 and an average pile-up of 24.2. Even with a higher pile-up, the performance of the Inner Detector was adequate for the physics program. Despite its success, the current ID was not designed to withstand the conditions of HL-LHC and meet the requirements of the physics program; hence, it will be replaced, citing several compelling reasons, such as radiation damage, bandwidth saturation, occupancy limitations, trigger requirements, and better coverage to achieve the physics goals.

6.4.1 ITk Layout

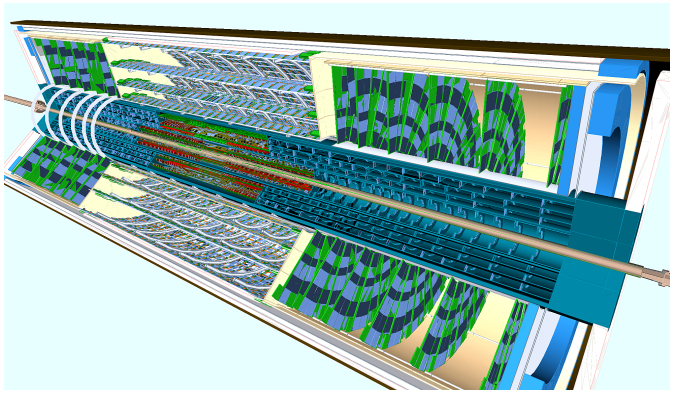

Figure 6.19. A visualization of the ITk implemented in the simulation framework [21].

The ITk will be entirely composed of silicon and cover a much larger area and solid

angle. The pixel detector will be the innermost part of the ITk. A silicon strip detector will surround it with four-barrel layers and six-layer end cap regions on each side, covering the pseudorapidity range of $|\eta| < 2.7$. The dimensions and the pseudorapidity coverage of the detector can be seen in figure 6.20

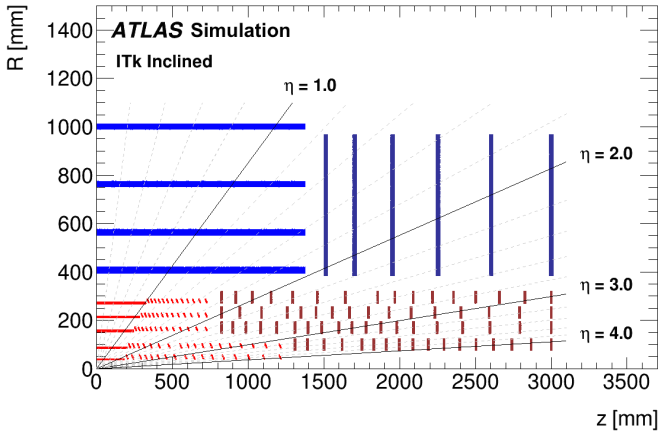

Figure 6.20. Schematic layout of the ITk for the HL-LHC phase of ATLAS showing only one quadrant and only active detector elements. The horizontal axis is along the beam pipe with $z = 0$ representing the interaction point, and the vertical axis is the radius measured from $z = 0$. [21]

Barrel Staves

The ITk strip barrel consists of staves that serve as a support structure for electrical, optical, and cooling services. These staves are constructed using a low-mass composite carbon fiber support structure. The staves consist of a honeycomb structure sandwiched between carbon fiber face sheets and a U-shaped titanium pipe embedded for cooling (C_6F_{14} or evaporative CO_2) of the electronics and sensor. Bus tapes made of copper-

polyimide are co-cured on both sides of the stave to connect the data, clock, and power lines from all the modules on one side to the End-of-Substructure (EoS) card; see Figure 6.21.

The EoS card consists of one(two) Low-Power GigaBit Transceiver (lpGBT) radiation-tolerant ASICs used to implement multipurpose high-speed bidirectional optical links commonly used in high-energy physics experiments. The critical task of an lpGBT is serializing and deserializing data. The data from the modules is serialized so that it can be sent to the Data Acquisition (DAQ) systems (uplink) using the electro-optical conversion circuit and the Versatile Transceiver (VTRX). For the downlink, data coming from the DAQ is deserialized and sent to the module on the stave. A stave consists of 28 barrel modules with 14 modules per side. Figure 6.21 shows one side of a barrel stave with 14 module.

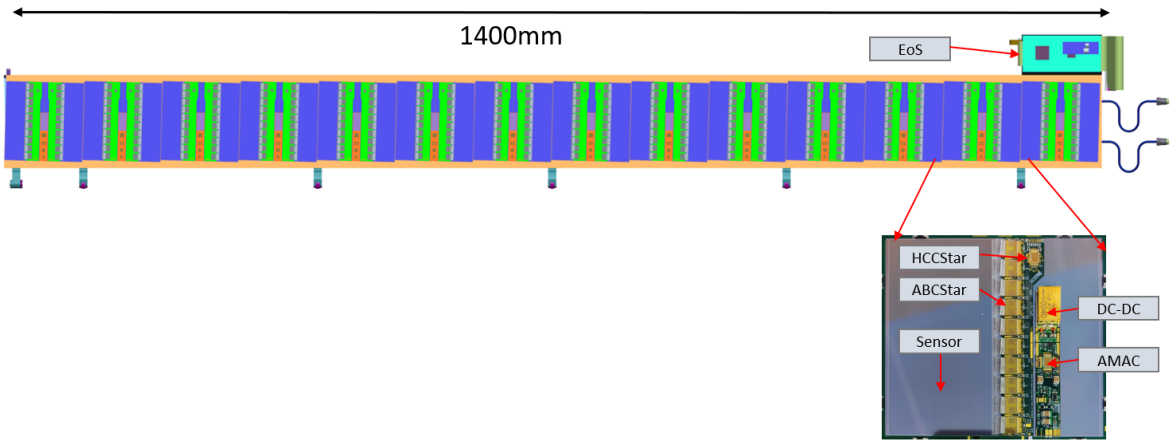

Figure 6.21. ATLAS ITk barrel stave with the different components [21].

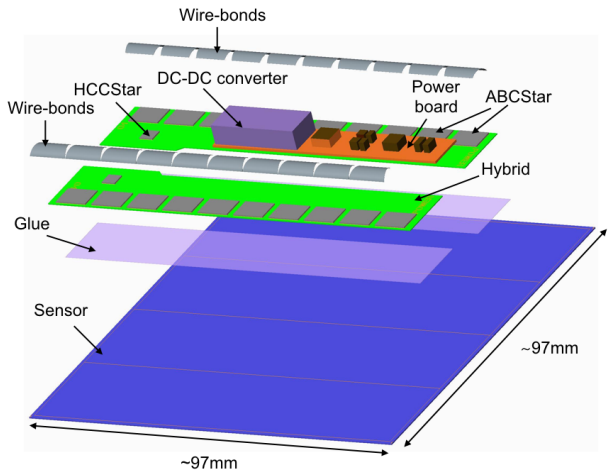

Figure 6.22. An exploded view of a barrel module with all relevant components [21].

ITk Strips Modules

The module is the smallest functional unit of the ITk strip detector. There are two types of barrel modules as well as end-cap modules. This section will mainly focus on the barrel modules (Figure 6.22).

A barrel module is made of sub-components mentioned below:

- **Sensor** The ITk strip sensor is n+-in-p with n+ implants in the p-type float zone. It differs from the p in n currently used in the SCT. Studies showing an increase in charge by a factor of two motivated the change. The collected particle is an electron, which makes the charge collection faster. It was also shown that the improved design shows no radiation-induced type inversions. The barrel strip sensor has an active area of 97×97 mm^2 and comes in two flavors: Long Strip (LS) with two rows of strip length of 48.3 mm to be used in the outer cylinders. Short Strip (SS) with

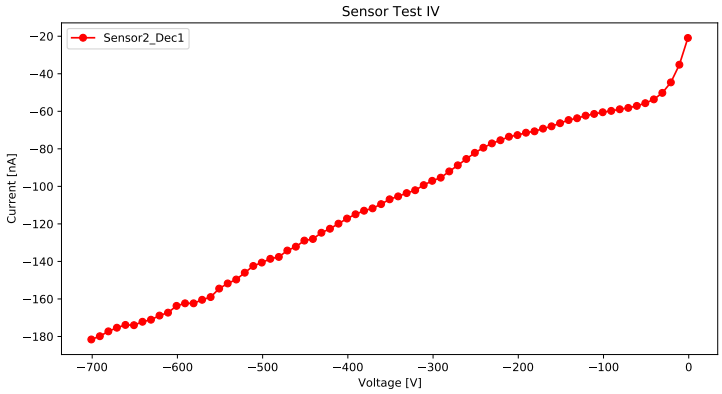

Figure 6.23. Characteristic IV curve of a Long-Strip sensor for one of the sensors tested at Brookhaven National Lab.

four rows of strip length of 24.1 mm to be used in the inner two cylinders. Figure 6.23 shows a typical IV curve for an LS sensor.

- **Powerboard** The powerboard is a custom-made PCB that holds electronics for controlling and monitoring the running conditions of the Data Acquisition system and the sensor. It hosts the programmable Autonomous Monitoring and Control (AMAC) chip that monitors temperatures (hybrid NTCs, powerboard NTCs, etc.), sensor bias return current, and reference voltages for the front-end ASICs. A Wilkinson-ADC is used to convert the analog outputs from comparator circuits to digital values, which, after calibration, are converted into human-readable form. The powerboard hosts the radiation hard buck DC-DC converter (FEAST), which converts an 11 V input to 1.5 V required by the front-end ASICS. It also has the Gallium Nitride FET (GaNFET), which is used as a switch to control the bias voltage applied to the sensor.

- **Hybrid** A hybrid is a custom-made low-mass PCB that hosts the readout front-end electronics, namely the HCC star and the ABC star ASICS where "star" represents the star-like topology between one HCC star and ten ABC stars (Figure 6.24).

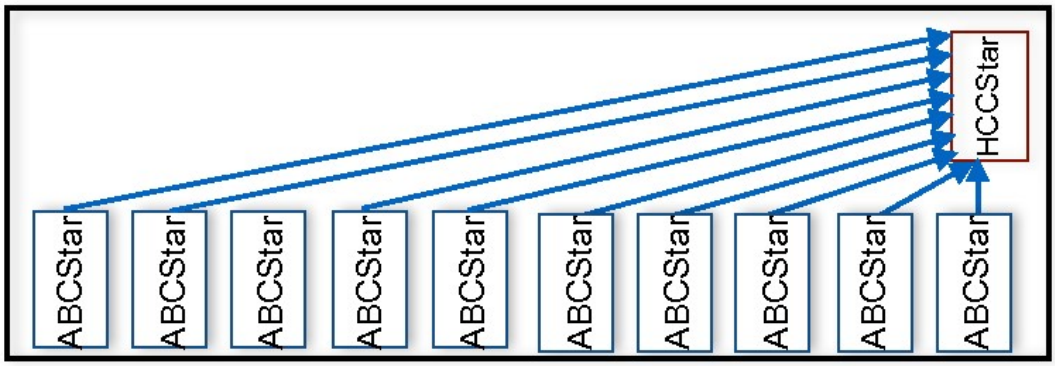

Figure 6.24. A diagram representing the star topology connection between the ABC stars and the HCC star

  - **ATLAS Binary Chip (ABC)** It is a binary readout chip built with 130 nm CMOS technology. The chip processes signals from 256 channels (Si strips) and gives a binary output of "0" or "1" for each signal, depending on the discriminator threshold. Most front-end electronics have five main stages: detection, pre-amplification, shaping, analog to digital conversion, and data acquisition/processing. The ABCStar has a pre-amplifier, shaper, and differential discriminator in the analog block and a derandomizer buffer, command decoder, readout buffer, and data compression logic circuits in the digital block.

A calibration circuit is used at the pre-amp's input to simulate the conditions of a hit (particle passing through the sensor detected by a channel). The pre-amplifier and shaper circuit (characteristic peaking time of 21 ns and approximate gain of ∼80 mV/fC) shapes and amplifies the input signal. The discriminator (mainly a comparator circuit) defines a threshold marking the signal to be counted as a "0" or "1". This hit information is stored in the (L0Buffer) for a programmable amount of time. This information is transferred to another buffer (EvtBuffer) with a specific tag (L0ID). If a readout request corresponds to an L0ID, the data with the tag is passed on to the HCCStar.

– **Hybrid Controller Chip (HCC)** The HCC interfaces the lpGBT with the ABC chips. The chip receives a 160 MHz clock and 160 Mbps control data called "CCR signals" from the EoS. The clock generation circuit generates a 40MHz (bunch crossing clock) and relays the clock and control data to the ABC.

6.5 Calibration Scans

The front-end electronics must be calibrated and characterized before they are used for any physics operation. The charge collection circuit and the comparator threshold characterize the per-channel threshold, latencies, the observed gain at the discriminator, and the observed noise. The performance of a module is evaluated by analyzing the data from the parameter scan. The "threshold scan" is the most commonly used parameter

scan, which forms the basis of all the characterization scans. In the threshold scan, as shown in figure 6.25, one scans over the comparator threshold "BVT" (x-axis) while measuring the number of hits (occupancy, fraction of input signal pulses exceeding the threshold, y-axis) at each step. In an ideal case, one would get a step-function starting with 100% occupancy and falling to 0% when the threshold value is greater than or equal to the signal's amplitude. In the presence of noise, in reality, the step function takes the shape of an "s-curve" shape.

The s-curve is fitted to an error function whose characteristic shape looks like an "S",

$$f(x) = p_3 + 0.5 \times \text{erfc}\left(\frac{x - p_0}{\sqrt{2}p_1}\right) \times p_2 \tag{6.22}$$

where x is BVT. Here, the parameter p_0, or the "mean," is called "vt50," or the midpoint of the s-curve. It represents the threshold at which the occupancy is 50%; p_1 is the width of the distribution and represents the noise amplitude at the discriminator output, also called the "output noise". p_2 and p_3 control the amplitude and offset of the s-curve, respectively.

6.5.1 Trim Scan

The ABC has 256 input channels, and all the channels have readout circuits, which differ slightly due to process variations. A trim scan aims to fine-tune the channel-to-channel variations of the threshold to get a uniform response across the chips and the modules. This is done by setting a TrimDAC (5-bit trim DAC) and trim range (BTRange) values for each channel such that one finds an optimal target voltage of the vt50 (from

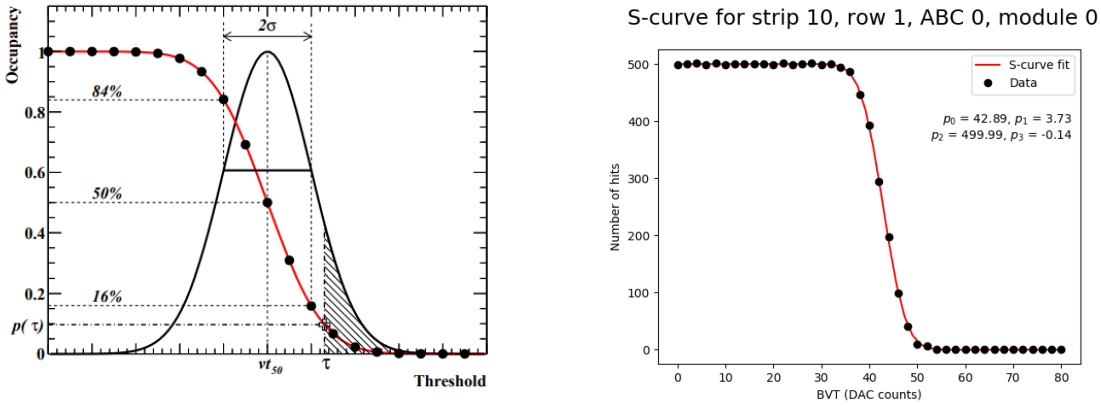

Figure 6.25. Illustration of a threshold scan. Left: An s-curve overlayed with the Gaussian error function. Here τ represents the threshold. Right: s-curve output from YARR(Readout software)

threshold scans) that the maximum number of channels can achieve.

A trim scan can be done with or without injected charge; the usual choice is to do a trim scan without injected charge (called a Pedastal trim scan).

An example shown in figure 6.26 gives an overview of how trimming works.

6.5.2 Strobe Delay

A Strobe delay scan aims to optimize the delay time between the calibration signal (injected charge) and the clock phase so that sampling is done at the signal's maximum. In this test, a calibration charge is injected with varied strobe delay settings. One then looks at the occupancy as a function of strobe delay settings per channel, which would look like a square pulse. The left and right edges of the square pulse are obtained by fitting with two s-curve functions. The midpoint of the two s-curve fits that satisfy the criteria of occupancy being greater than a fixed value (e.g., 90%) is used to find the maximum

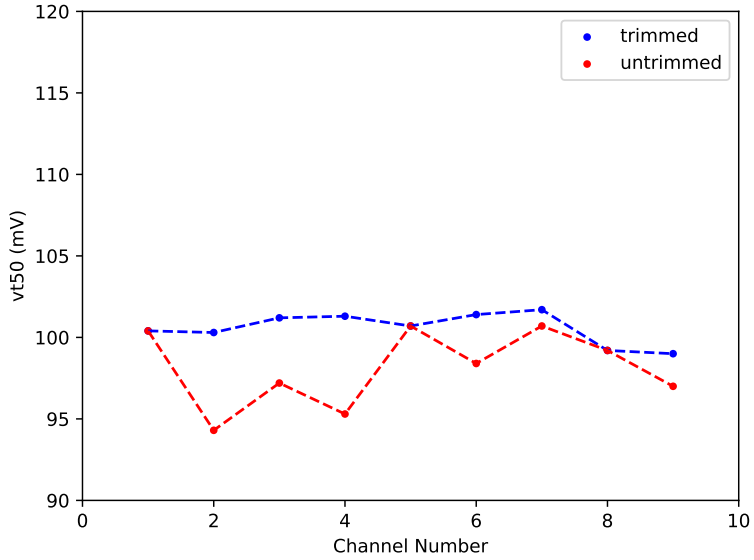

Figure 6.26. An example plot showing the vt50 before and after trimming.

left edge and minimum right edge over all channels in an ABC chip. The optimal strobe delay is set per chip as the 57% point between the maximum left edge and the minimum right edge [162].

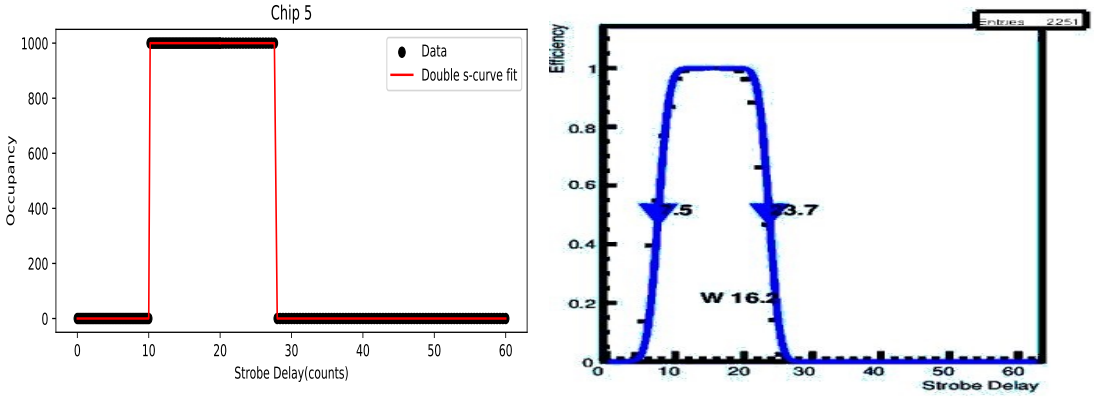

Figure 6.27. Left: An example plot of the strobe delay scan for one of the chips, with the double s-curve fit. Right: An actual Strobe delay plot for one ABC chip.

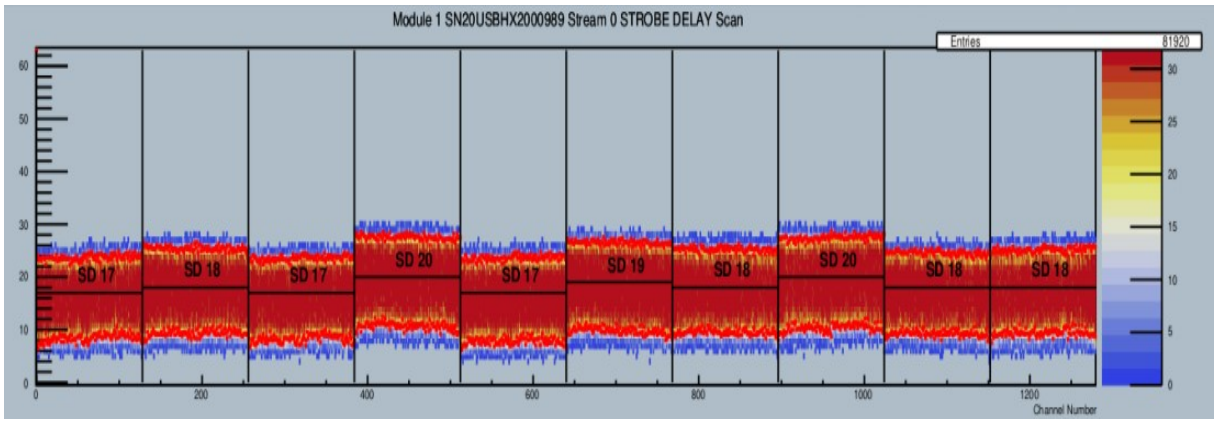

Figure 6.28. Strobe delay scan on all the channels of an ABC chip.

A Strobe-delay scan must be done after trimming as this scan uses injected charges.

6.5.3 N-Point Gain

The goal of an N-Point gain scan is to characterize the response (gain) at the discriminator's input by providing a calibration between the threshold (mV or DAC counts) and charges (fC). Given the information from the scans mentioned previously, a heuristic approach is to first do a pedestal-trim scan to have a uniform response across all channels. This gives us a reference value for the threshold or vt50. Second, a strobe delay scan is done to optimize the delay between the clock phases and the calibration signal. This helps us sample the signal at (or around) the maximum. Finally, threshold scans with different injected charges and a fit on the observed vt50 and the injected charge. For a linear fit, the slope of vt50 (mV) and injected charge (fC) gives the front-end response to the injected charge. The ABC chip's response for charges below 5 fC can be approximated to be linear, but beyond that point, it becomes non-linear and can be fitted to a quadratic

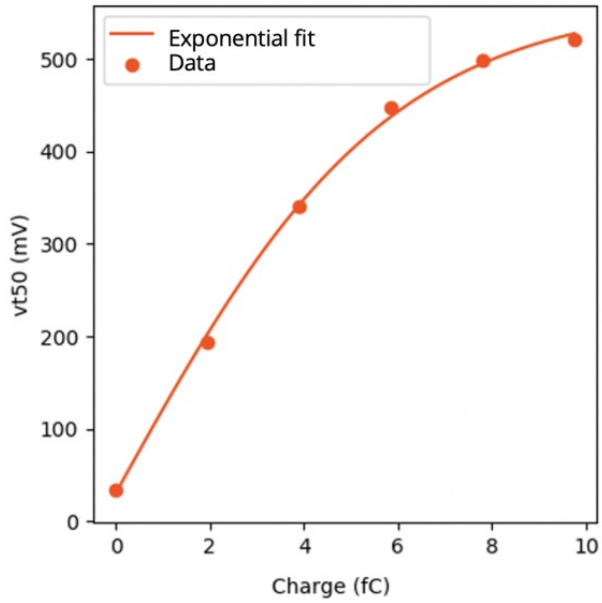

Figure 6.29. An example response curve from 6-point gain scan for one ABCStar.

or exponential function. Figure 6.29 shows a visualization of the gain for the ABC chips. The exponential fit would have a form

$$f(x) = p_2 + \frac{p_0}{1 + \exp\left(\frac{-x}{p_1}\right)} \tag{6.23}$$

The work in the thesis focuses on testing the performance of the sensors and front-end electronics and validating the performance of readout chains for the ITk strips. Two readout chains are commonly used in the ITk strips community for these purposes. The first one is ITk Strips Data Acquisition (ITSDAQ), mainly used to test the ITk strip modules and support structures (staves and petals). It uses commercial Field Programmable Gate Arrays (FPGA) with custom electronic boards to read the front-end electronics. The second one is the Yet Another Rapid Readout (YARR), which is under development and will be used by ITk strips and pixels. It uses a custom-made board called Front-End

Link Exchange (FELIX) and is scalable to handle many front-ends.

6.6 Results from Modules testing

During the entire operational period of the upgraded ATLAS detector, which is expected to last about ten years, the Inner Tracker (ITk) will experience several temperature changes as it is cooled for operations and warmed for maintenance. This includes at least one yearly warm-up due to the end-of-the-year shutdowns. It is crucial that these temperature changes do not critically damage the detector components and that all assembled modules are mechanically robust enough to continue taking high-quality data throughout the lifetime of the ITk. The silicon strip modules undergo QA/QC before being mounted on the stave core. This involves doing a visual inspection followed up by a "Thermal Cycle" (TC) inside the "Coldbox" (A Faraday cage with temperature, relative humidity, and Interlock), shown in Figure 6.30. A TC involves testing the modules at room temperature (+20°C) and doing ten cycles between -35°C and +40°C. DAQ scans "Trim Scan," "Strobe Delay," and "3 Point Gain" are done at every temperature change, with a High Voltage stability test at the end. Results from a three-point gain scan done on an LS module at different temperatures are shown in Figure 6.32. The results show that output noise does not change with temperature changes. The gain increases, and the input noise decreases with a decrease in temperature.

Results from the three-point gain of 18 modules tested at room temperature are shown in Figure 6.33.

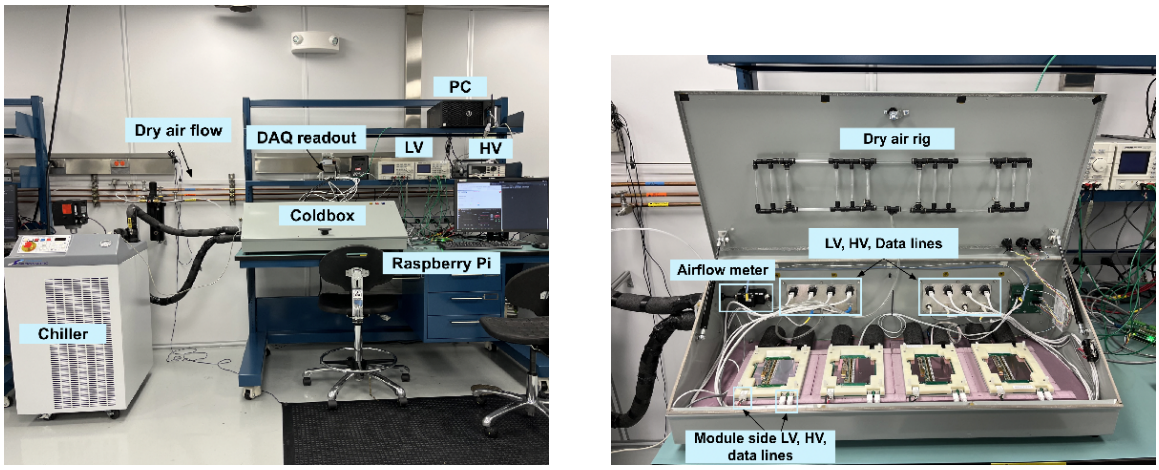

Figure 6.30. Left: Test bench with the coldbox for doing the strip module thermal cycling at BNL. Right: Barrel modules coldbox with four modules at BNL.

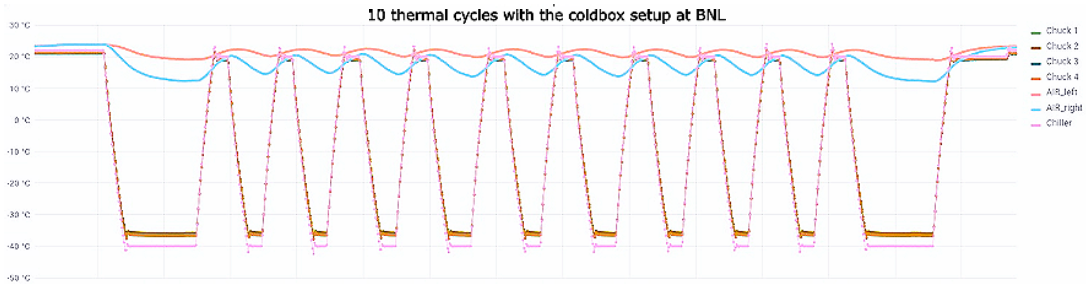

Figure 6.31. 4 modules thermal cycled between -35°C and +20°C

6.7 Results from Stave testing

After the stave is built at the production site (Brookhaven National Laboratory (BNL) in the US and Rutherford Appleton Laboratory (RAL) in the UK), it is tested and shipped to CERN for further development, testing, and integration. It is critical to test the stave at different stages of integration to check for damages or breakdowns that may occur after it is shipped. We also wanted to test the development of the new software

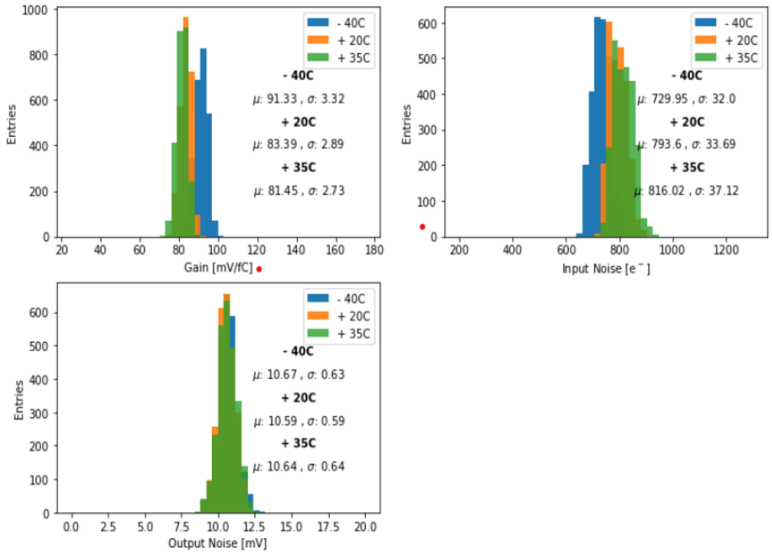

Figure 6.32. Single LS module tested at three different temperatures showing the change in gain, which results in a change in output noise.

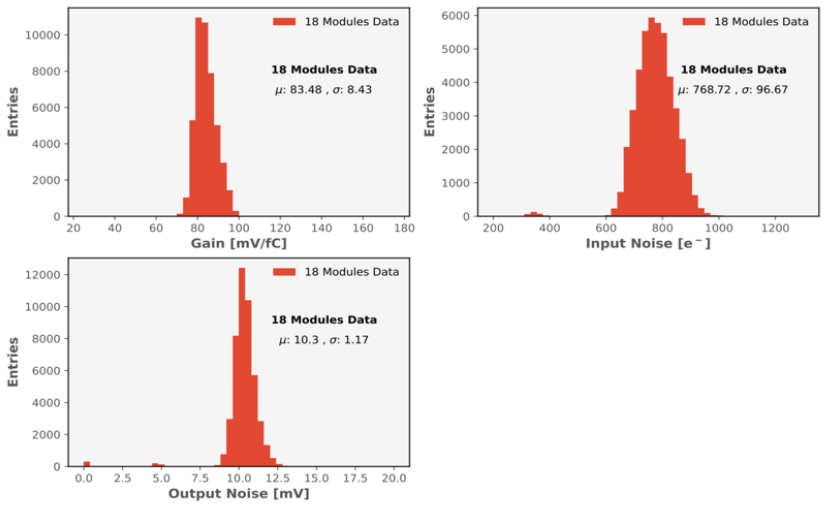

Figure 6.33. 18 LS modules tested at +20°C

YARR, which is planned to be used as the calibration software for the ITk stips and pixels.

Figures 6.34, 6.35 and 6.36 show the noise performance of the staves when it was tested

at the production site (BNL or RAL) versus when it was tested at CERN. No significant changes in the noise performance were observed, meaning that the staves were shipped and integrated without any damage. Figure 6.37 shows histograms for comparing the output of calibration scans from the two software, YARR, and ITSDAQ. This validated YARR to be used to test multiple staves in parallel and as a potential online software for ITk strips.

While at BNL, I was one of the main developers of the QA/QC software, developing the thermal cycling routines, stave shipment protocols, and storage protocols. During my time at CERN, I worked on the front-end calibration scans with ITSDAQ and YARR with the staves that arrived from RAL and BNL. I was a part of a team working toward the development and validation of YARR as a candidate for the ITk software.

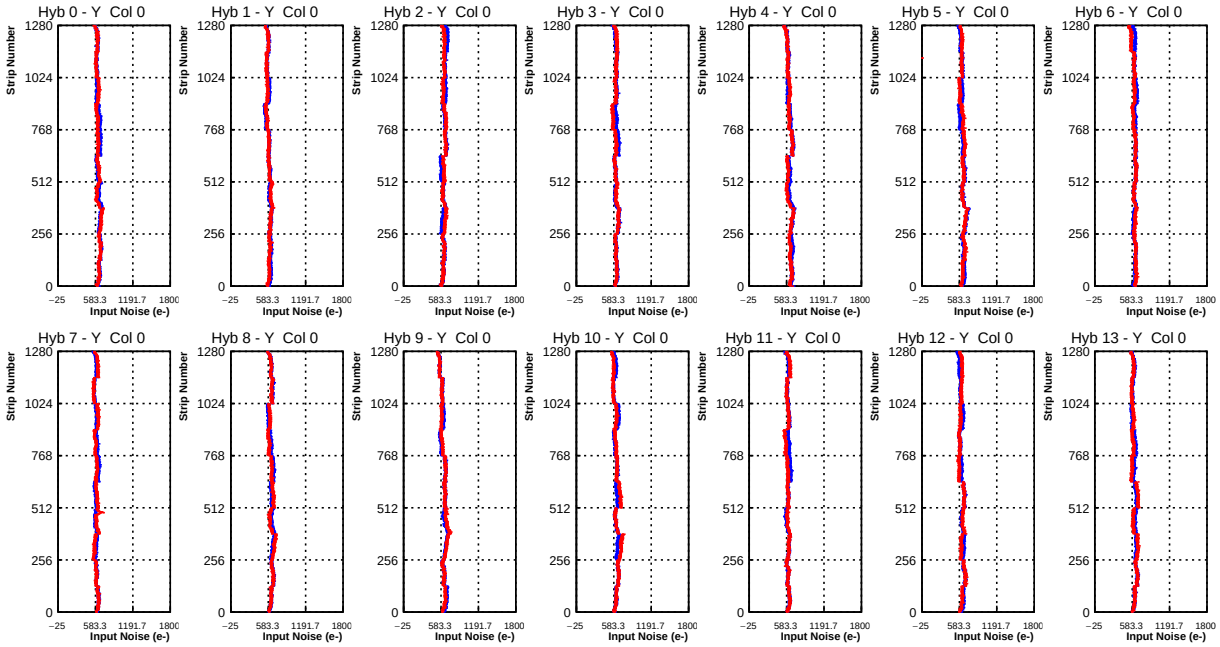

Figure 6.34. Input noise from one column of strips from the hybrids of an SS stave with 14 modules on one side.

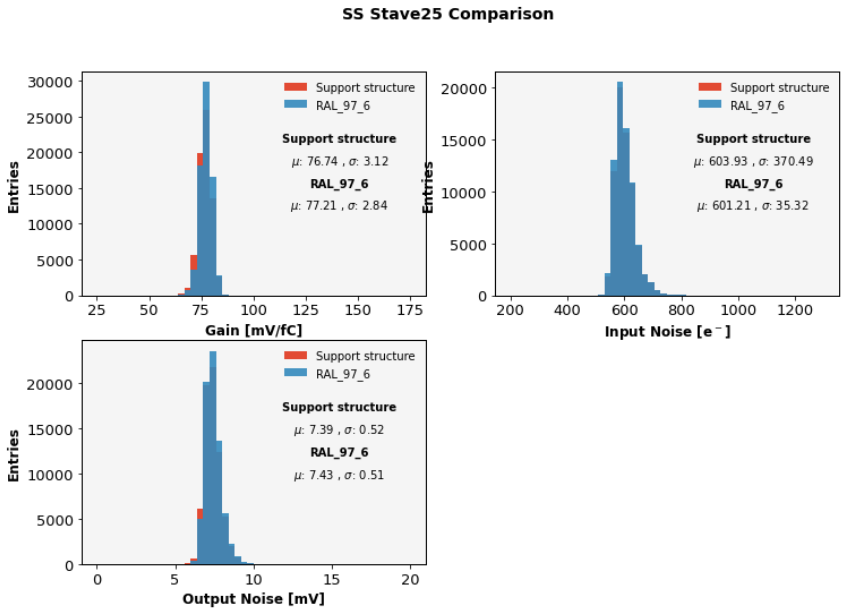

Figure 6.35. A SS stave tested at Rutherford Appleton Laboratory (RAL) and CERN (RadLab, SR1).

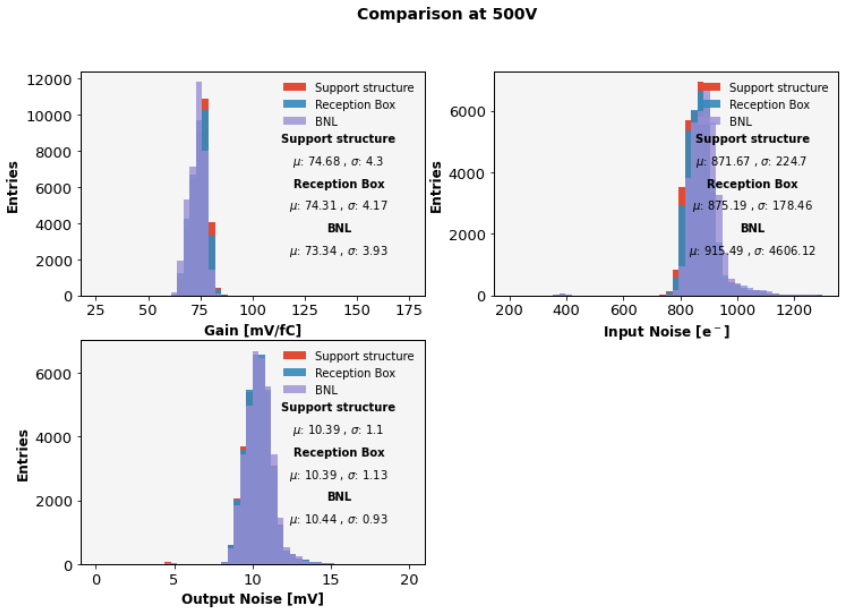

Figure 6.36. A LS stave tested at Brookhaven National Laboratory (BNL) and CERN (RadLab, SR1)

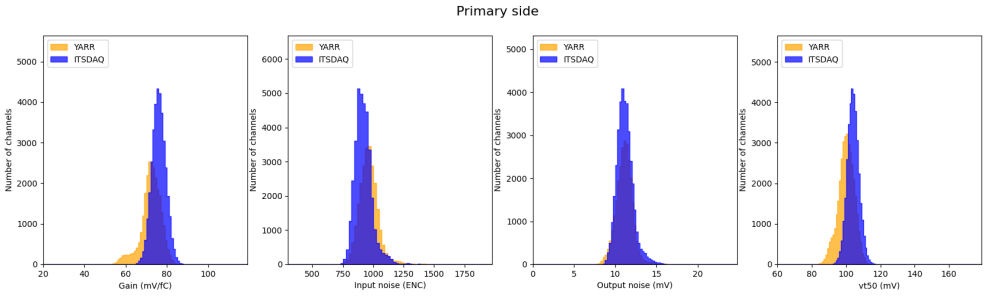

Figure 6.37. Stave test comparison between YARR and ITSDAQ

CHAPTER 7

CONCLUSION AND OUTLOOK

A search motivated by the EWB models looking for a the CP-odd Higgs boson decaying into a heavy CP-even Higgs boson and a Z boson in the final stages of $\ell\ell t\bar{t}$ and $\nu\bar{\nu}b\bar{b}$ is done using the complete Run-2 dataset of pp collisions at $\sqrt{s} = 13$ TeV corresponding to an integrated luminosity of 140.1 fb^{-1} as recorded by the ATLAS experiment has been presented in the thesis. No significant deviation from the background-only hypothesis is observed in the likelihood fits. The largest excess over the SM background prediction, amounting to a local significance of $2.85\,\sigma$, is observed in the $\ell\ell t\bar{t}$ channel, for the signal hypothesis corresponding to $(m_A, m_H) = (650, 450)$ GeV. The global significance for the $\ell\ell t\bar{t}$ channel is estimated to be $2.35\,\sigma$. The search explored parameter space of 2HDM that had not been looked previously in the ATLAS collaboration and upper limits on the production cross-section times the branching ratios for $B(A \to ZH) \times B(H \to t\bar{t})$ in the $\ell\ell t\bar{t}$ channel and $B(A \to ZH) \times B(H \to t\bar{t})$ were derived for the ggF and bbA production modes. The upper limits were interpreted in the context of the 2HDM model, and 95% CL upper limit exclusion curves were generated for $\ell\ell t\bar{t}$ and $\nu\bar{\nu}b\bar{b}$ channels in the m_A and m_H phase space. The search has already been well-received within the theorists for the EWB models, as in Ref [49] suggesting future searches with Run 3, HL-LHC data and new channels like $H^{\pm} \to W^{\pm}H \to l^{\pm}\nu t\bar{t}$.

The second part of the thesis presents the upgrade of the ATLAS Inner Tracker for the HL-LHC. The ATLAS ITk is an all-silicon detector made of silicon pixel and strip

layers, giving better coverage of the interaction point in a higher radiation environment. The components of the ITk tip sensors and the associated front-end electronics need to be characterized at different stages of the production process. The outcome of the ITk stip sensor characterization scans at different stages of the production process has been presented in the thesis.

APPENDIX A

MEASUREMENT OF VH($b\bar{b}/c\bar{c}$) PROCESS

A.1 Introduction

Since the Higgs boson (m_H = 125GeV) was discovered, extensive searches and measurements of its production and decay modes have been conducted.

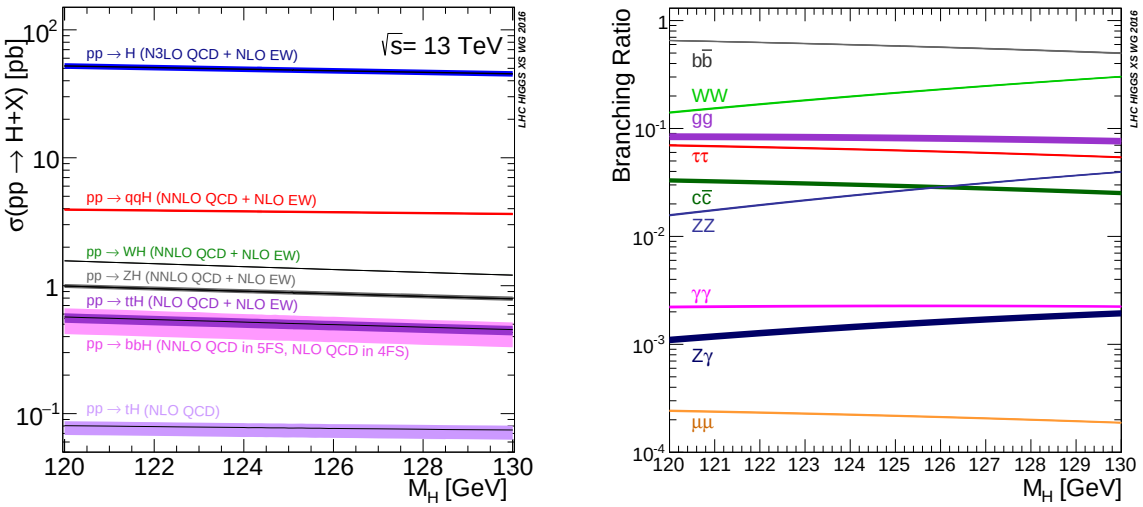

Figure A.1. Left: Production cross-section of Higgs boson through different channels at $\sqrt{13}$ TeV as a function of Higgs boson mass. Right: Higgs boson decay branching ratios as a function of Higgs boson mass. Figure adapted from [164]

The decay $H \to b\bar{b}$ is the most probable decay for SM Higgs boson as the branching ratio for the process is 58.2% [152] for $m_H = 125$ GeV (Figure A.1(right)). The efficiency of identification of jets originating from $b-$quarks is critical in distinguishing this channel from the overwhelming background of the QCD multijet processes. To suppress the

backgrounds, measurements can be conducted in the VH production mode (one with a reasonable production cross-section, Figure A.1(Left)), where vector boson V (W or Z) leptonic decays could be tagged with using the lepton triggers. Interaction of the Higgs boson with the third-generation fermions has been observed by both ATLAS [80, 82, 83] and CMS [88, 89, 90] experiments. Higgs coupling to fermions' first and second generation is still to be firmly established. Higgs boson decay into a pair of charm quarks has a branching ratio of 2.89% and is one of the promising decays that has not been observed though, upper limits on the cross-section times branching fractions of $H \to c\bar{c}$ have been set via the direct searches [81]. The similarity in the signatures of the $VH(\to b\bar{b}, c\bar{c})$ decays has made combining studies of both channels possible. This chapter provides a brief overview of $VH(\to b\bar{b}, c\bar{c})$ analysis, focusing on the signal modelling and measurement techniques used for the $VH(b\bar{b})$ channel.

A.1.1 Analysis overview

The $VH(\to b\bar{b}, c\bar{c})$ analysis is categorized in the regions based on the number of leptons in the vector boson decay, $ZH \to \nu\nu b\bar{b}$ and $ZH \to \nu\nu c\bar{c}$ are referred to as "0-lepton channel" (0L), $WH \to l\nu b\bar{b}$ and $WH \to l\nu c\bar{c}$ as "1-lepton channel" (1L) and $ZH \to llb\bar{b}$ and $ZH \to llc\bar{c}$ as "2-lepton channel" (2L). Jets originating from the beauty quark (b) and charm quark (c) are tagged using DL1R algorithms. A baseline categorization is used in terms of $p_T(V)$ regions including $75 < p_T(V) < 150$ GeV (1 and 2-lepton channels), $150 < p_T(V) < 250$ GeV, $250 < p_T(V) < 400$ GeV, and jet multiplicity (2, 3 and 4+-jets) called as resolved regions. Regions with $p_T(V) > 400$ GeV are considered boosted

with an additional split at 600 GeV ($400 < p_T(V) < 600$ GeV, $p_T(V) > 600$ GeV). Signal regions are optimized to maximize the sensitivity of the $VH(\rightarrow b\bar{b}, c\bar{c})$ process with CR defined to estimate the background processes using data events. The major background in this analysis comes from the Z+jets, W+jets, and $t\bar{t}$ events, for which CRs based on a topological cut ΔR and c, b-jet tagging-based categorizations are used. Figure A.2 shows all the regions used in the analysis.

A.2 Differential measurements

The ATLAS experiment has gathered substantial data, enabling unprecedented precision measurements of the Higgs boson properties. The increasingly large dataset has enabled differential measurements of the Higgs boson, where we split the phase spaces into regions that could be measured independently of theoretical assumptions without compromising the experimental sensitivity. One such framework is the Simplified Template for cross-section measurement(STXS)[112] in which Higgs boson measurements are carried out in exclusive regions of phase space that have been agreed upon across experiments. This section provides an overview of the STXS measurements for the $VHbb$ channel while briefly introducing the full fiducial measurements.

A.2.1 Signal Strength Measurement

Measurements are generally done in signal strengths called μ, for example, the signal strenth for a process $pp \rightarrow H(+X) \rightarrow$ FS, where FS is any final state can be calculated as

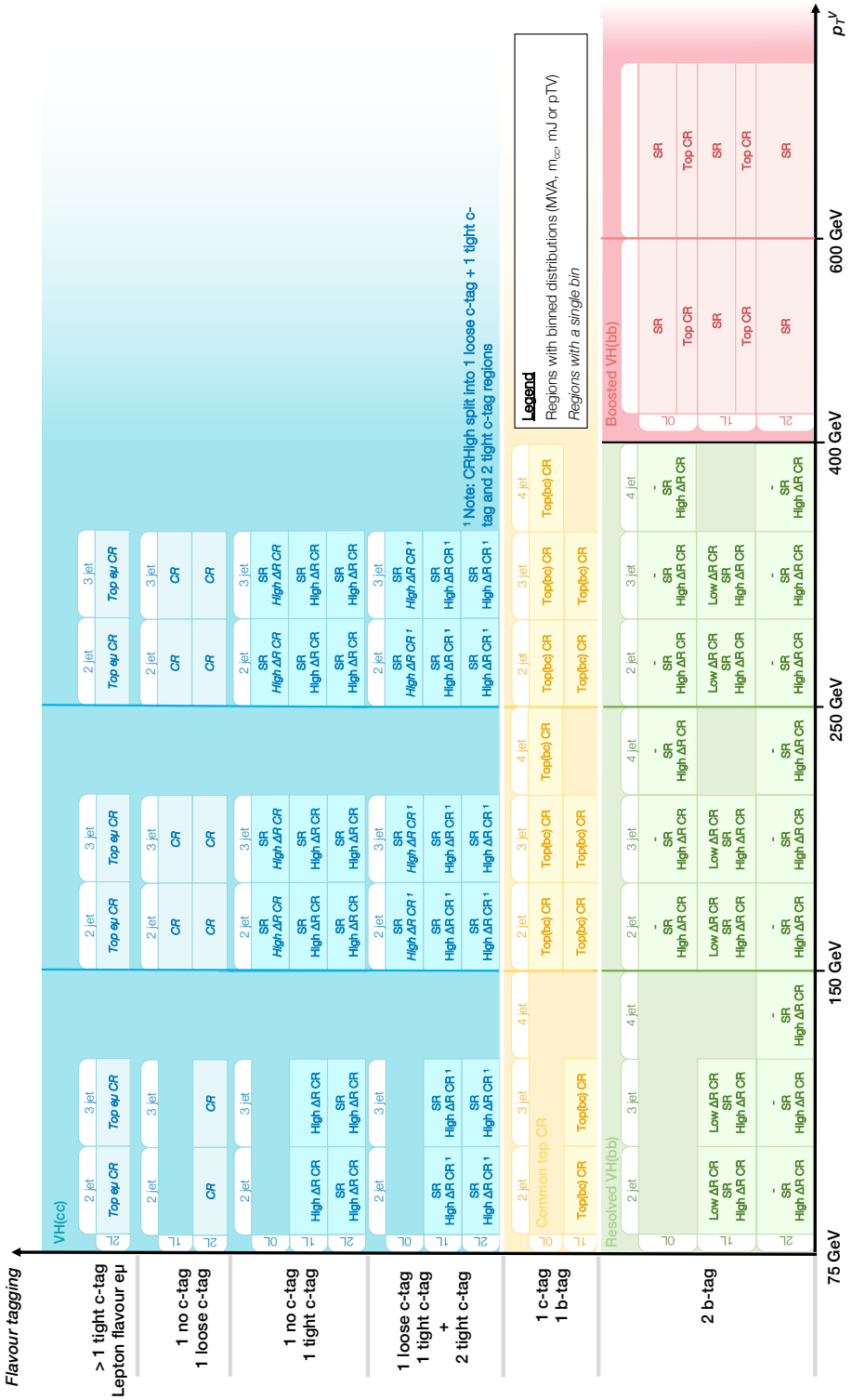

Figure A.2. A schematic view of all the regions used in the $VH(\to b\bar{b}, c\bar{c})$ analysis.

$$\mu(pp \to H(+X) \to \text{FS}) = \frac{[\sigma(pp \to H + (X)) \times \text{BR}(H \to \text{FS})]_{\text{measured}}}{[\sigma(pp \to H + (X)) \times \text{BR}(H \to \text{FS})]_{\text{predicted}}} \tag{A.1}$$

where the total signal yield is compared to the SM prediction. The μ measurements are fully dependent on the underlying theory. This dependence comes from the kinematics of the Higgs boson used to predict the number of events in a region of phase space. Along with this, the uncertainty of the measurement is fully dependent on the theoretical uncertainty associated with the signal simulation. Due to these two dependencies, measurements are redone if there is any non-trivial change in the underlying theory.

A.2.2 Fully fiducial cross-section measurements

The fully fiducial measurements are only moderately theory-dependent, as the fiducial region of the measured phase space has to be as close as possible to the experimental selection, disqualifying the use of complex MVA in the definition of selections. The definition of the fiducial volume needs to be as neutral as possible in terms of production mode to ensure that the measurement is not biased by the SM prediction of the production mode mixture. This approach minimizes reliance on underlying theoretical assumptions and extrapolations, with most remaining assumptions associated with correcting for detector effects.

A.2.2.1 Fiducial and differential cross-section measurement of VH production mode

For the $H \to b\bar{b}$, the complexity of the final state has limited the measurement's granularity and sensitivity with the differential measurement [79] and [150]. Additional difficulties like the bad resolution on $E_{\text{T}}^{\text{miss}}$, jet, and large background modeling

uncertainties make the VHbb fiducial measurements even more difficult. The latest measurement of the fiducial and differential cross-section of WH/ZH production for the b-jets + $E_{\mathrm{T}}^{\mathrm{miss}}$ (0-Lepton) final state in pp collisions had been carried out in two $E_{\mathrm{T}}^{\mathrm{miss}}$ bins of 150 GeV $\leq E_{\mathrm{T}}^{\mathrm{miss}}$ 250 GeV and $E_{\mathrm{T}}^{\mathrm{miss}} \geq 250$ GeV (Figure A.3) [150].

The measurement involves the construction of a yield matrix for events that pass the particle level selection called "in fiducial" (T_i), events that fail to pass the particle level selection called "out-of-fiducial" (O^{T_i}), and events that fall in the region that are not considered for the analysis "off-fiducial" (O^{Off}) events in the $E_{\mathrm{T}}^{\mathrm{miss}}$ bins of 150 GeV $\leq E_{\mathrm{T}}^{\mathrm{miss}} < 250$ GeV or $E_{\mathrm{T}}^{\mathrm{miss}} \geq 250$ GeV (i=2) split into the number of jets, see Figure A.4. The expected signal yields are then parameterized using the different $E_{\mathrm{T}}^{\mathrm{miss}}$ and jet multiplicity regions for a profiled likelihood unfolding method[1].

To cross-check the primary $VH(\rightarrow b\bar{b}, c\bar{c})$ analysis with truth level studies, preliminary tests were conducted to measure the $VH(b\bar{b})$ fiducially and differentially in the zero-lepton A.5 and one-lepton A.6 channels with updated selections and regions according the VH(bb/cc) analysis. The event selection used for the 0L channel was the same as used in [150] whereas the event selection used for the 1L channel was taken from Ref. [92]. Further studies on the full fiducial differential measurement in the 0L, 1L, and 2L channels have been planned in the near future that would include the boosted $E_{\mathrm{T}}^{\mathrm{miss}}$ regions.

[1]The measured spectrum of a physical observable is often distorted by detector effects like finite resolution and limited acceptance. To compare this measured spectrum with theoretical predictions, we need to remove these effects and obtain the true, underlying physical spectrum. Unfolding is a method that corrects the measured distributions for the detector effects.

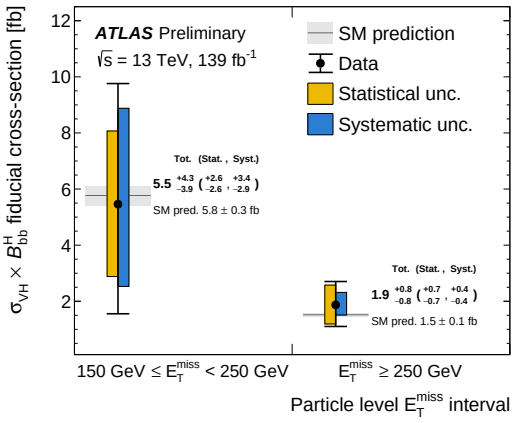

Figure A.3. Measured values of the fiducial cross-section (σ_{VH}) times the branching ratio of $H \to b\bar{b}$ (BR(Hbb)) in the two particle-level-$E_{\mathrm{T}}^{\mathrm{miss}}$ intervals, along with a breakdown of the statistical and systematic uncertainty components. The shaded area around the SM prediction indicates the size of the total uncertainty for this value. [150]

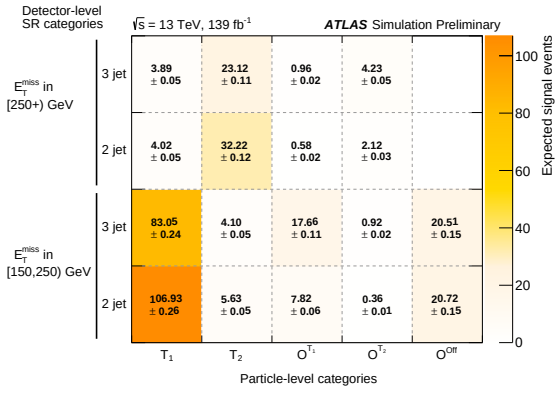

Figure A.4. Expected signal event yields for each detector-level category as a function of their particle-level category. The MC statistical uncertainty is also shown. The category T_i corresponds to reconstructed events that pass the particle-level selection and have a particle-level $E_{\mathrm{T}}^{\mathrm{miss}}$ satisfying either 150 GeV $\leq E_{\mathrm{T}}^{\mathrm{miss}} <$ 250 GeV (i=1) or $E_{\mathrm{T}}^{\mathrm{miss}} \geq$ 250 GeV (i=2), respectively. The category O^{T_i} represents reconstructed events that belong to that particle-level $E_{\mathrm{T}}^{\mathrm{miss}}$ bin but fail the other particle-level selection criteria. In contrast, events with particle-level $E_{\mathrm{T}}^{\mathrm{miss}} <$ 150 GeV contribute to O^{Off}. [150]

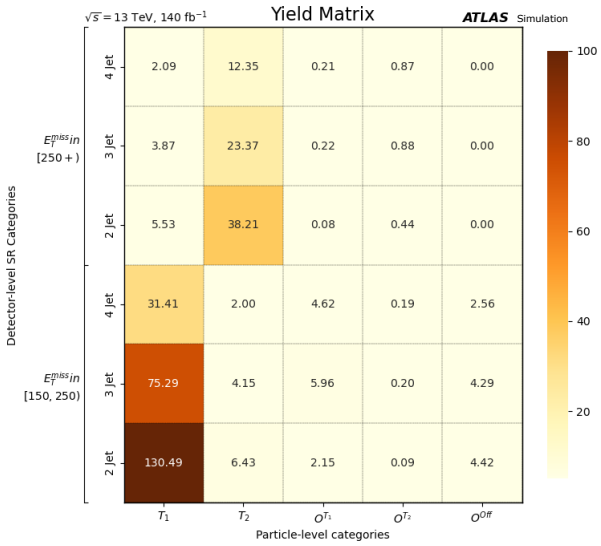

Figure A.5. Expected signal event yields for each detector-level category as a function of their particle-level category for the 1L channel.

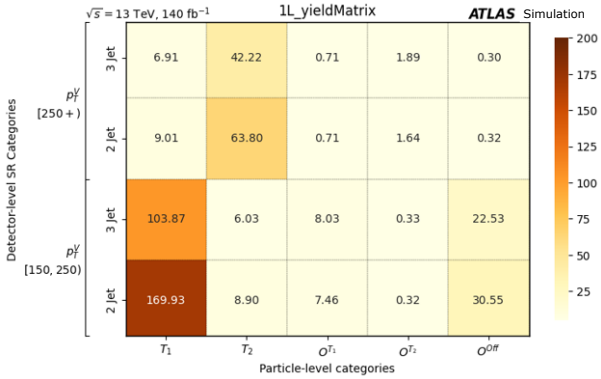

Figure A.6. Expected signal event yields for each detector-level category as a function of their particle-level category for 1L channel.

A.2.3 STXS Measurement

In Run 2 and further, the STXS framework is used with the collected data to make differential measurements that balance experimental precision with theoretical independence. This framework splits the phase space into separate regions where theory uncertainties may evolve while identifying parts of the production phase space where physics beyond the SM (BSM) predicts significant deviations from SM expectations.

Unlike full fiducial measurements, STXS is less theory-independent, but it allows for the use of complex multivariate analysis (MVA) techniques, performed in $H \to b\bar{b}$ and $H \to \tau\bar{\tau}$. Figure A.7 illustrates the STXS framework, where the Higgs boson signal is split by production mode into ggF, VBF, $t\bar{t}H$, $b\bar{b}H$, tH, $V(\to \text{quark})H$ and $V(\to \text{leptons})H$. To enable the combination of STXS measurements across analyses, the splitting in Higgs boson decay channels is not performed. Only Higgs bosons with a rapidity of $y_H < 2.5$ are considered for excellent detector acceptance. The different production modes are further split into exclusive regions of phase spaces called STXS 'bins.' These bins aim to minimize theory dependence by solely relying on the kinematic predictions of the SM within each bin. The bin widths are also chosen to ensure flat experimental acceptance within each bin, where feasible. This split allows us to isolate regions sensitive to potential BSM physics, for example, the high $p_T(V)$ bin in the $V(\to \text{leptons})H$ channel that could serve as input to constrain Wilson coefficients of a SMEFT or BSM model. The definition of the STXS bins evolves depending on the precision of the measurements; for more precise measurements, finer binning could be used.

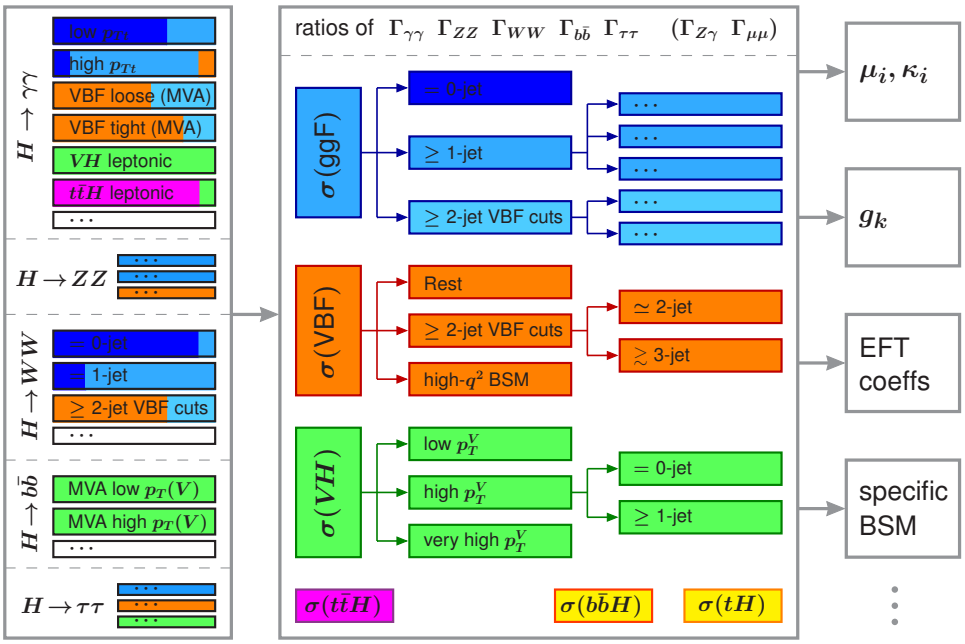

Figure A.7. An illustration of the Higgs STXS framework. Figure adapted from [112]

The phase space would be split into the production modes for the $V(\to \text{leptons})H$ production mode, $gg \to ZH$, $qq \to ZH$, and $qq \to WH$. Further splitting is introduced as a function of $p_T(V)$ with bin boundaries at 75, 150, 250, 400, and 600 GeV and the number of additional jets in the event. The current experimental sensitivity is not good enough to measure all the production modes separately; hence, the $gg \to ZH$ and $qq \to ZH$ have been merged to define a reduced STXS stage, shown in Figure A.8.

A.3 Signal modelling

For the $VH(\to b\bar{b}, c\bar{c})$, several sources of uncertainties were considered; this includes uncertainty in the assumed $H \to b\bar{b}$ branching ratio, uncertainties in the $p_T(V)$ dependent NLO electroweak (EW) correction factors, on the parton shower, variation of

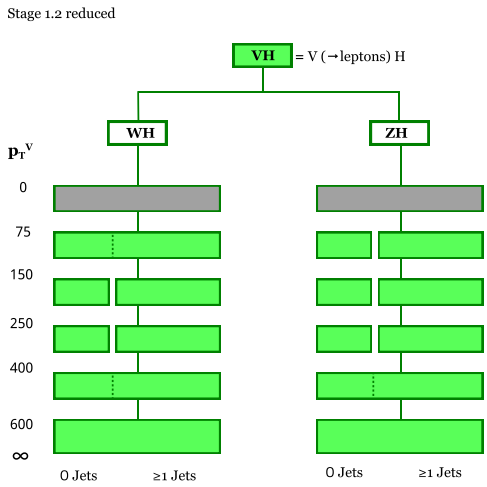

Figure A.8. Stage 1.2 reduced STXS splitting for VH production mode split in the number of jets (nJets) and the p_{T}^{V}.

the renormalization μ_R and factorization scale μ_F, in the choice of PDF and the strong coupling constant α_s.

Branching ratio

Theoretical uncertainty on the calculation of the $H \to b\bar{b}$ branching ratio is 1.6% [112] with the largest contributions coming from the limited knowledge of m_b, α_s and the missing higher order corrections.

NLO EW correction

To account for the missing higher orders in the EW corrections, a $p_T(V)$ dependent systematic uncertainty Δ_{EW} is added to the qq initiated VH channels in addition to the NLO EW correction factors κ_{EW}^{NLO} following the prescription in Ref [112].

Parton shower

To consider the uncertainties arising from the choice of the parton shower (PS) model, the nominal sample POWHEG + PYTHIA 8 [176] is compared with the POWHEG + MiNLO+ HERWIG 7 alternative sample. Both shape and acceptance uncertainties are derived for the signal regions. Figure A.9 shows the acceptance uncertainties from PS in the three production modes maximally split in the STXS bins.

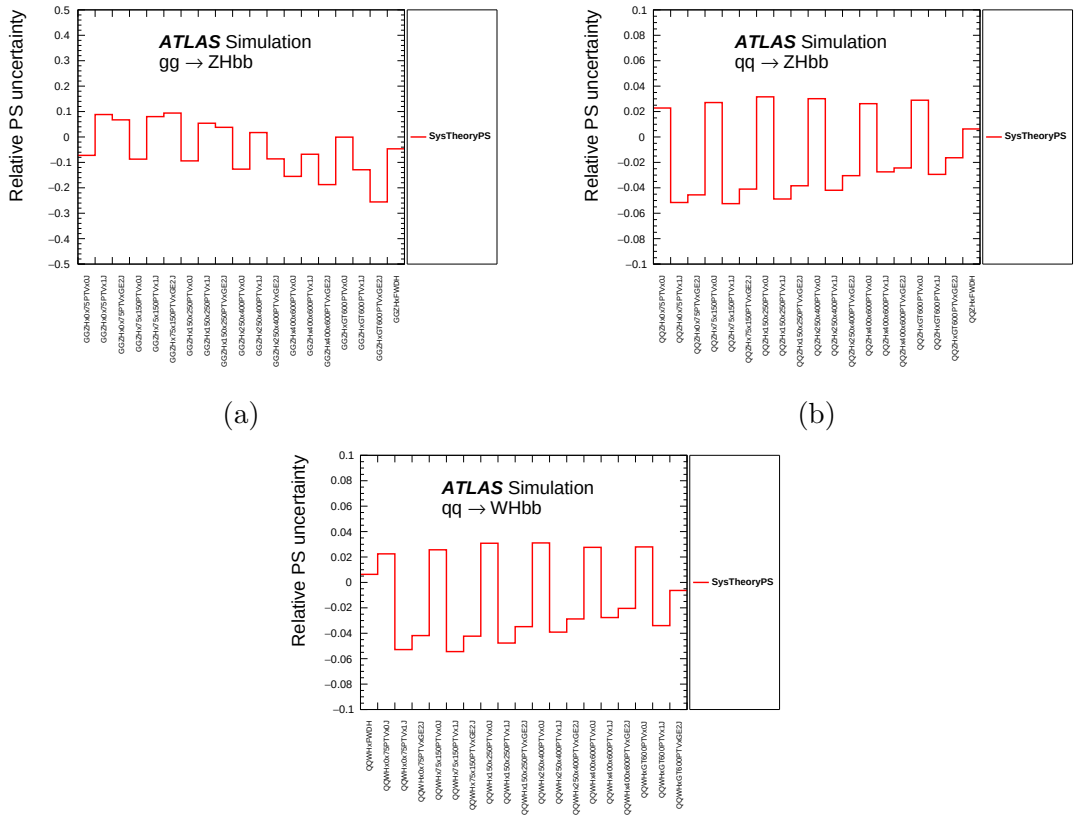

Figure A.9. Parton shower acceptance uncertainty for the three production channels in the different STXS bins.

PDF and α_s

To account for the systematic uncertainty from the PDF and the precision of the α_s, the PDF4LHC15_30 set of PDFs are compared with the nominal. It includes 30 PDF variations and two variations for the α_s, one with a higher value of α_s and one with a lower value of α_s whose average is used to calculate the acceptances in the maximally split STXS bins. Figure A.10 shows the acceptance uncertainties from PDF and α_s in the three production modes in the maximally split STXS bins for the $VH(b\bar{b})$ channel.

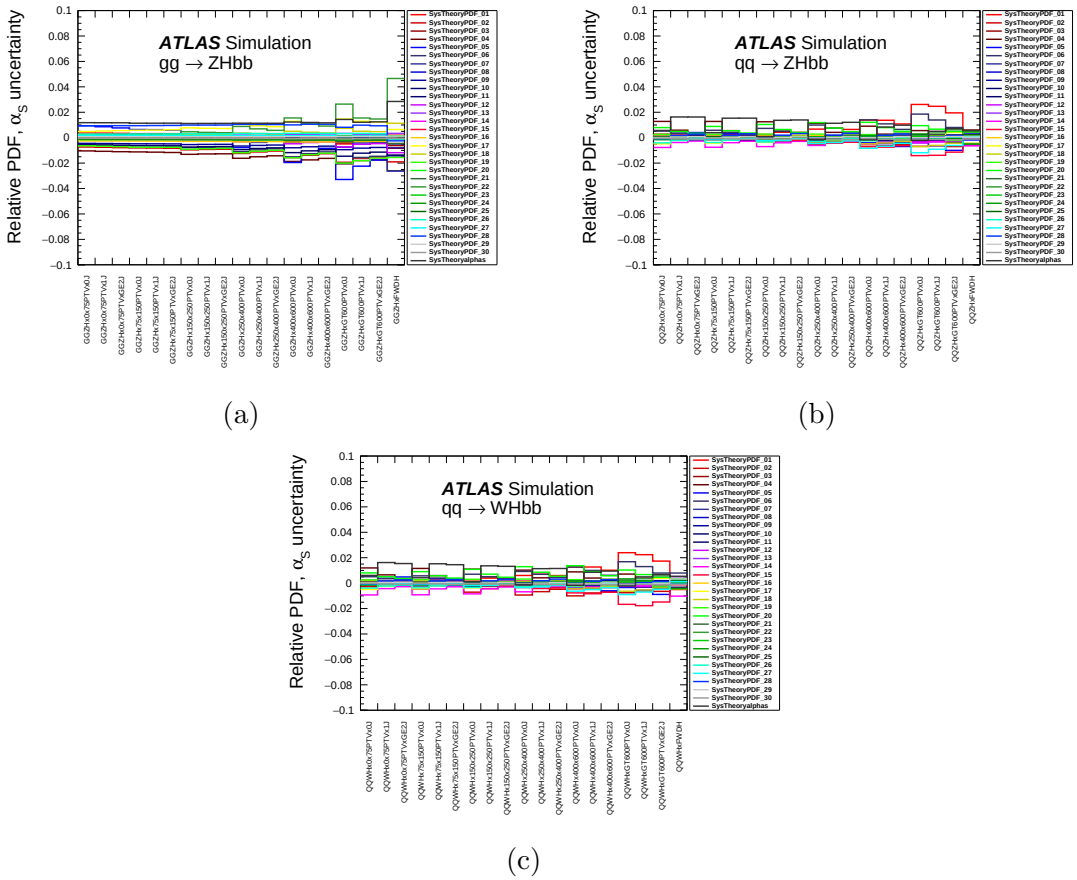

Figure A.10. PDF and α_s uncertainty for the three production channels.

QCD Scale

To account for the uncertainty on the choice of the μ_R and μ_F, variations of the two parameters are considered correlated (both up or both down) and uncorrelated (one up and other down). These variations can cause changes in the overall normalizations and the relative signal acceptance between the different STXS bins (nJets and $p_T(V)$). To account for the STXS bin migrations, the Stuart-Tackmann procedure is used [107], giving us a set of uncertainties referred to as Δs:

- Δ_Y: impact on the overall cross-section. It represents the QCD scale uncertainty on the total production cross-section calculation and is taken directly from the CERN Yellow report. [112]

- Δ_{75}, Δ_{150}, Δ_{250}, Δ_{400} and Δ_{600} represent the migration acceptance between the different STXS $p_T(V)$ bins. These uncertainties are generally evaluated inclusive of nJets bins.

- Δ_1 and Δ_2 represent the migration acceptance between the nJets bins and are calculated inclusive of $p_T(V)$.

Figures A.11 show the QCD scale variations for the $p_T(V)$ and overall cross-section. The gg production channel has higher uncertainty as these samples are only LO in QCD, and the dependence of the result on μ_R and μ_F decreases with higher perturbative orders, like the qq production channel samples.

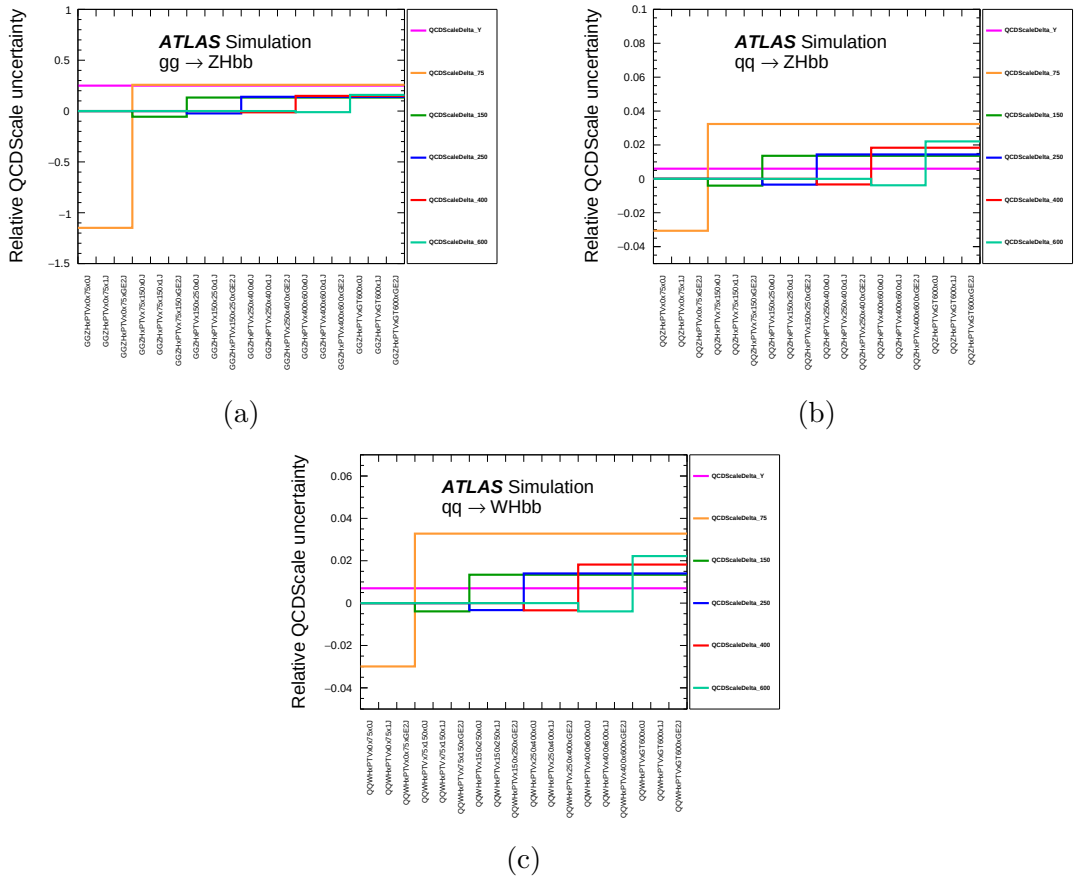

Figure A.11. QCD scale uncertainty for the three production channels.

A.4 Expected results and Improvements

The previous run of the $VH(b\bar{b})$ combined analysis measured the production cross-section times branching fractions in seven STXS bins (3 WH and 4 VH), as shown in Figure A.12. At the time of writing the thesis, the current analysis plans to measure the production cross-section times the branching fractions normalized to the SM in 13 STXS bins, with additional bins coming from the nJets split of the $p_T(V)$ bins in the ZH channel and the addition of $p_T(V)$ split at 600 GeV. The latest results on the pro-

duction cross-section times and the branching fractions relative to the SM in 13 STXS bins measurements can be seen in Figure A.13. The 13 STXS bin measurement is the finest in the VH channel, which agrees with the SM. Along with the measurements of μ for the $VH(b\bar{b})$ channel, 95% CL upper limits on the measurements of $\mu_{VH(\to c\bar{c})}$ are calculated, shown in Figure A.14, where the observed combined limit is better than any current public measurement.

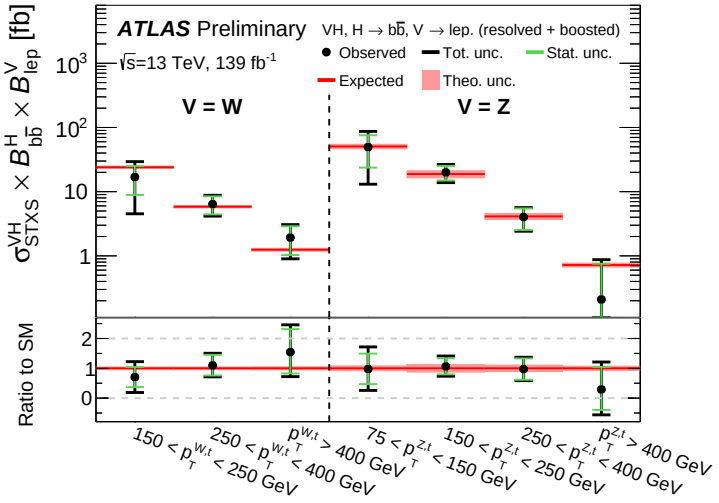

Figure A.12. Result from the previous analysis run with three WH STXS bins and four ZH STXS bins [92].

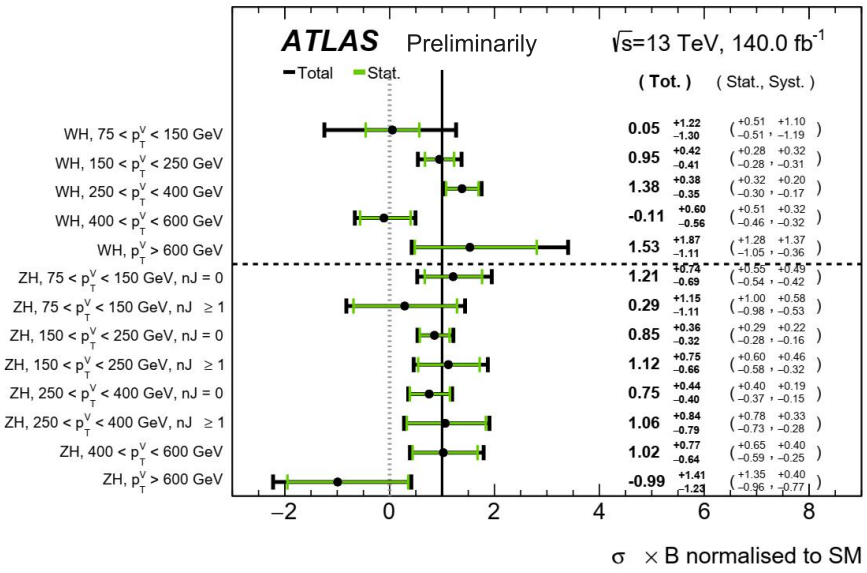

Figure A.13. Preliminary results from the current analysis run with five WH STXS bins and eight VH STXS bins.

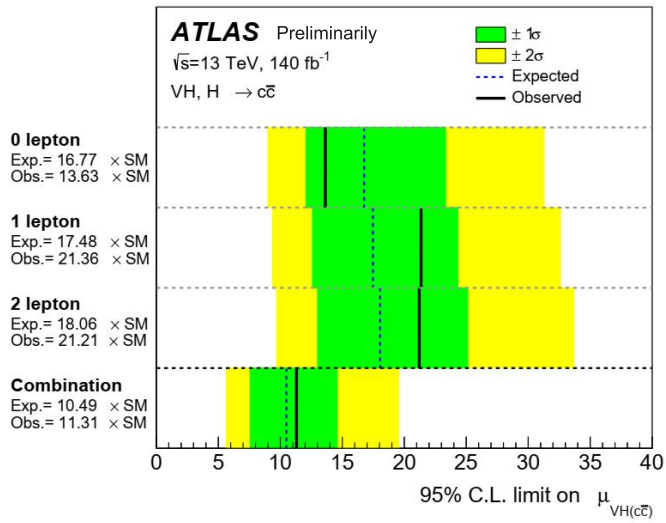

Figure A.14. Preliminary limits on the $\mu_{VH(\to c\bar{c})}$ split in different lepton channels and overall combined.

List of Symbols and Abbreviations

2HDM	Two Higgs Doublet Model
ABCstar	ATLAS Binary Chip with Star Topology
AMAC	Autonomous Monitoring and Control Chip
ASICs	Application Specific Integrated Circuit
BSM	Beyond Standard Model
DAQ	Data Acquisition
ECAL	Electromagnetic Calorimeter
ENC	Equivalent Noise Charge
EoS	End of Substructure
EWB	Electroweak Baryogenesis
FSR	Final state radiation
HCAL	Hadronic Calorimeter
HCCstar	Hybrid Controller Chip with Star Topology
HL-LHC	High-Luminosity Large Hadron Collider
ID	Inner Detector
ISR	Initial state radiation
ITk	Inner Tracker
JER	Jet Energy Resolution
JES	Jet Energy Scale
LAr	Liquid Argon
LHC	Large Hadron Collider
lpGBT	low power Gigabit Transceivers
MDT	Muon Drift Tubes
MIP	Minimum Ionizing particle
MS	Muon Spectrometer

PDF	Parton Distribution Function
PS	Parton Shower
QA/QC	Quality Assurance and Quality Control
SCT	Semiconductor Tracker
SM	Standard Model
TC	Thermal Cycling
TRT	Transition Radiation Tracker
UE	Underlying Events
VTRX	Versatile Transceivers
YARR	Yet Another Rapid Readout

γ	Photon
μ	Muon
μ_F	Factorization Scale
μ_R	Renormalization Scale
ν	Neutrinos
τ	Tau lepton
A	2HDM CP-Odd heavy Higgs boson
b	Beauty Quark
c	Charm Quark
d	Down Quark
e^+	Positron
e^-	Electron
g	Gluon
H	2HDM CP-Even heavy Higgs boson
H	SM Higgs boson
$SU(n)$	Special Unitary group of degree n

t	Top Quark
u	Up Quark
W	W Boson
Z	Z Boson

BIBLIOGRAPHY

[1] Georges Aad et al. "Measurement of the Z/γ^* boson transverse momentum distribution in pp collisions at $\sqrt{s} = 7$ TeV with the ATLAS detector." In: *JHEP* 09 (2014), p. 145. DOI: 10.1007/JHEP09(2014)145. arXiv: 1406.3660 [hep-ex].

[2] Georges Aad et al. "Measurements of WH and ZH production in the $H \to b\bar{b}$ decay channel in pp collisions at 13 TeV with the ATLAS detector." In: *Eur. Phys. J. C* 81.2 (2021), p. 178. DOI: 10.1140/epjc/s10052-020-08677-2. arXiv: 2007.02873 [hep-ex].

[3] Georges Aad et al. "Operation and performance of the ATLAS semiconductor tracker in LHC Run 2." In: *JINST* 17.01 (2022), P01013. DOI: 10.1088/1748-0221/17/01/P01013. arXiv: 2109.02591 [physics.ins-det].

[4] Georges Aad et al. "Search for dark matter produced in association with a Standard Model Higgs boson decaying into b-quarks using the full Run 2 dataset from the ATLAS detector." In: *JHEP* 11 (2021), p. 209. DOI: 10.1007/JHEP11(2021)209. arXiv: 2108.13391 [hep-ex].

[5] Jalal Abdallah et al. "Simplified models for dark matter searches at the LHC." In: *Physics of the Dark Universe* 9-10 (2015), pp. 8–23. DOI: 10.1016/j.dark.2015.08.001. arXiv: 1506.03116 [hep-ph].

[6] S. Agostinelli, J. Allison, K. Amako, et al. "Geant4—a simulation toolkit." In: *Nuclear Instruments and Methods in Physics Research Section A: Accelerators, Spectrometers, Detectors and Associated Equipment* 506.3 (2003), pp. 250–303. ISSN: 0168-9002. DOI: https://doi.org/10.1016/S0168-9002(03)01368-8. URL: https://www.sciencedirect.com/science/article/pii/S0168900203013688.

[7] M. Aguilar, L. Ali Cavasonza, B. Alpat, et al. "Antiproton Flux, Antiproton-to-Proton Flux Ratio, and Properties of Elementary Particle Fluxes in Primary Cosmic Rays Measured with the Alpha Magnetic Spectrometer on the International Space Station." In: *Phys. Rev. Lett.* 117 (9 Aug. 2016), p. 091103. DOI: 10.1103/PhysRevLett.117.091103. URL: https://link.aps.org/doi/10.1103/PhysRevLett.117.091103.

[8] M. Aliev, H. Lacker, U. Langenfeld, et al. "HATHOR – HAdronic Top and Heavy quarks crOss section calculatoR." In: *Comput. Phys. Commun.* 182 (2011), pp. 1034–1046. DOI: 10.1016/j.cpc.2010.12.040. arXiv: 1007.1327 [hep-ph].

[9] Simone Alioli, Paolo Nason, Carlo Oleari, and Emanuele Re. "A general framework for implementing NLO calculations in shower Monte Carlo programs: the POWHEG BOX." In: *JHEP* 06 (2010), p. 043. DOI: 10.1007/JHEP06(2010)043. arXiv: 1002.2581 [hep-ph].

[10] Lukas Altenkamp, Stefan Dittmaier, Robert V. Harlander, et al. "Gluon-induced Higgs-strahlung at next-to-leading order QCD." In: *JHEP* 02 (2013), p. 078. DOI: 10.1007/JHEP02(2013)078. arXiv: 1211.5015 [hep-ph].

[11] J. Alwall, R. Frederix, S. Frixione, et al. "The automated computation of tree-level and next-to-leading order differential cross sections, and their matching to parton shower simulations." In: *JHEP* 07 (2014), p. 079. DOI: 10.1007/JHEP07(2014)079. arXiv: 1405.0301 [hep-ph].

[12] Charalampos Anastasiou, Lance J. Dixon, Kirill Melnikov, and Frank Petriello. "High precision QCD at hadron colliders: Electroweak gauge boson rapidity distributions at next-to-next-to leading order." In: *Phys. Rev. D* 69 (2004), p. 094008. DOI: 10.1103/PhysRevD.69.094008. arXiv: hep-ph/0312266.

[13] Pierre Artoisenet, Rikkert Frederix, Olivier Mattelaer, and Robbert Rietkerk. "Automatic spin-entangled decays of heavy resonances in Monte Carlo simulations." In: *JHEP* 03 (2013), p. 015. DOI: 10.1007/JHEP03(2013)015. arXiv: 1212.3460 [hep-ph].

[14] Pierre Artoisenet, Vincent Lemaitre, Fabio Maltoni, and Olivier Mattelaer. "Automation of the matrix element reweighting method." In: *JHEP* 12 (2010), p. 068. DOI: 10.1007/JHEP12(2010)068. arXiv: 1007.3300 [hep-ph].

[15] ATLAS Collaboration. *E_T^{miss} performance in the ATLAS detector using 2015–2016 LHC pp collisions*. ATLAS-CONF-2018-023. 2018. URL: https://cds.cern.ch/record/2625233.

[16] ATLAS Collaboration. *ApprovedPlotsDAQ*. February 8. 2024. URL: https://twiki.cern.ch/twiki/bin/view/AtlasPublic/ApprovedPlotsDAQ.

[17] ATLAS Collaboration. "ATLAS b-jet identification performance and efficiency measurement with $t\bar{t}$ events in pp collisions at $sqrts = 13$ TeV." In: *Eur. Phys. J. C* 79 (2019), p. 970. DOI: 10.1140/epjc/s10052-019-7450-8. arXiv: 1907.05120 [hep-ex].

[18] ATLAS Collaboration. *ATLAS Computing: Technical Design Report*. ATLAS-TDR-17; CERN-LHCC-2005-022. 2005. URL: https://cds.cern.ch/record/837738.

[19] ATLAS Collaboration. "ATLAS data quality operations and performance for 2015 to 2018 data-taking." In: *Journal of Instrumentation* 15.04 (Apr. 2020), P04003. DOI: 10.1088/1748-0221/15/04/P04003. URL: https://dx.doi.org/10.1088/1748-0221/15/04/P04003.

[20] ATLAS Collaboration. "ATLAS data quality operations and performance for 2015–2018 data-taking." In: *JINST* 15 (2020), P04003. DOI: 10.1088/1748-0221/15/04/P04003. arXiv: 1911.04632.

[21] ATLAS Collaboration. *ATLAS Inner Tracker Strip Detector: Technical Design Report*. ATLAS-TDR-025; CERN-LHCC-2017-005. 2017. URL: https://cds.cern.ch/record/2257755.

[22] ATLAS Collaboration. *ATLAS Pythia 8 tunes to 7 TeV data*. ATL-PHYS-PUB-2014-021. 2014. URL: https://cds.cern.ch/record/1966419.

[23] ATLAS Collaboration. "Electron and photon performance measurements with the ATLAS detector using the 2015–2017 LHC proton–proton collision data." In: *JINST* 14 (2019), P12006. DOI: 10.1088/1748-0221/14/12/P12006. arXiv: 1908.00005 [hep-ex].

[24] ATLAS Collaboration. "Electron reconstruction and identification in the ATLAS experiment using the 2015 and 2016 LHC proton–proton collision data at $\sqrt{s} = 13\,\text{TeV}$." In: *Eur. Phys. J. C* 79 (2019), p. 639. DOI: 10.1140/epjc/s10052-019-7140-6. arXiv: 1902.04655 [hep-ex].

[25] ATLAS Collaboration. *Expected performance of the ATLAS b-tagging algorithms in Run-2*. ATL-PHYS-PUB-2015-022. 2015. URL: https://cds.cern.ch/record/2037697.

[26] ATLAS Collaboration. *Identification of hadronic tau lepton decays using neural networks in the ATLAS experiment*. ATL-PHYS-PUB-2019-033. 2019. URL: https://cds.cern.ch/record/2688062.

[27] ATLAS Collaboration. "Luminosity determination in pp collisions at $\sqrt{s} = 13\,\text{TeV}$ using the ATLAS detector at the LHC." In: (2022). arXiv: 2212.09379 [hep-ex].

[28] ATLAS Collaboration. "Muon reconstruction and identification efficiency in ATLAS using the full Run 2 pp collision data set at $\sqrt{s} = 13\,\text{TeV}$." In: *Eur. Phys. J. C* 81 (2021), p. 578. DOI: 10.1140/epjc/s10052-021-09233-2. arXiv: 2012.00578 [hep-ex].

[29] ATLAS Collaboration. *Object-based missing transverse momentum significance in the ATLAS Detector*. ATLAS-CONF-2018-038. 2018. URL: https://cds.cern.ch/record/2630948.

[30] ATLAS Collaboration. "Observation of a new particle in the search for the Standard Model Higgs boson with the ATLAS detector at the LHC." In: *Phys. Lett. B* 716 (2012), p. 1. DOI: 10.1016/j.physletb.2012.08.020. arXiv: 1207.7214 [hep-ex].

[31] ATLAS Collaboration. "Performance of missing transverse momentum reconstruction with the ATLAS detector using proton-proton collisions at $\sqrt{s} = 13$ TeV." In: *Eur. Phys. J. C* 78.11 (2018), p. 903. DOI: 10.1140/epjc/s10052-018-6288-9. arXiv: 1802.08168 [hep-ex].

[32] ATLAS Collaboration. "Performance of pile-up mitigation techniques for jets in pp collisions at $\sqrt{s} = 8\,\text{TeV}$ using the ATLAS detector." In: *Eur. Phys. J. C* 76 (2016), p. 581. DOI: 10.1140/epjc/s10052-016-4395-z. arXiv: 1510.03823 [hep-ex].

[33] ATLAS Collaboration. *Reconstruction, Energy Calibration, and Identification of Hadronically Decaying Tau Leptons in the ATLAS Experiment for Run-2 of the LHC*. ATL-PHYS-PUB-2015-045. 2015. URL: https://cds.cern.ch/record/2064383.

[34] ATLAS Collaboration. "Search for a heavy Higgs boson decaying into a Z boson and another heavy Higgs boson in the $\ell\ell bb$ and $\ell\ell WW$ final states in pp collisions at $\sqrt{s} = 13\,\text{TeV}$ with the ATLAS detector." In: *Eur. Phys. J. C* 81 (2020), p. 396. DOI: 10.1140/epjc/s10052-021-09117-5. arXiv: 2011.05639 [hep-ex].

[35] ATLAS Collaboration. "Search for heavy resonances decaying into a Z or W boson and a Higgs boson in final states with leptons and b-jets in 139 fb^{-1} of pp collisions at $\sqrt{s} = 13$ TeV with the ATLAS detector." In: *JHEP* 06 (2023), p. 016. DOI: 10.1007/JHEP06(2023)016. arXiv: 2207.00230 [hep-ex].

[36] ATLAS Collaboration. *Selection of jets produced in 13 TeV proton–proton collisions with the ATLAS detector*. ATLAS-CONF-2015-029. 2015. URL: https://cds.cern.ch/record/2037702.

[37] ATLAS Collaboration. "The ATLAS Experiment at the CERN Large Hadron Collider." In: *JINST* 3 (2008), S08003. DOI: 10.1088/1748-0221/3/08/S08003.

[38] ATLAS Collaboration. *Vertex Reconstruction Performance of the ATLAS Detector at $\sqrt{s} = 13$ TeV*. ATL-PHYS-PUB-2015-026. 2015. URL: https://cds.cern.ch/record/2037717.

[39] *ATLAS Track Reconstruction – General Overview — atlassoftwaredocs.web.cern.ch*. https://atlassoftwaredocs.web.cern.ch/trackingTutorial/idoverview/. [Accessed 27-03-2024].

[40] G. Avoni et al. "The new LUCID-2 detector for luminosity measurement and monitoring in ATLAS." In: *JINST* 13.07 (2018), P07017. DOI: 10.1088/1748-0221/13/07/P07017.

[41] M. Bähr et al. "Herwig++ physics and manual." In: *Eur. Phys. J. C* 58 (2008), p. 639. DOI: 10.1140/epjc/s10052-008-0798-9. arXiv: 0803.0883 [hep-ph].

[42] Richard D. Ball et al. "Parton distributions for the LHC run II." In: *JHEP* 04 (2015), p. 040. DOI: 10.1007/JHEP04(2015)040. arXiv: 1410.8849 [hep-ph].

[43] Richard D. Ball et al. "Parton distributions with LHC data." In: *Nucl. Phys. B* 867 (2013), p. 244. DOI: 10.1016/j.nuclphysb.2012.10.003. arXiv: 1207.1303 [hep-ph].

[44] *Band gap - Wikipedia — en.wikipedia.org*. https://en.wikipedia.org/wiki/Band_gap. [Accessed 20-03-2024].

[45] Peter Bärnreuther, Michal Czakon, and Alexander Mitov. "Percent-Level-Precision Physics at the Tevatron: Next-to-Next-to-Leading Order QCD Corrections to $q\bar{q} \to t\bar{t} + X$." In: *Phys. Rev. Lett.* 109 (2012), p. 132001. DOI: 10.1103/PhysRevLett.109.132001. arXiv: 1204.5201 [hep-ph].

[46] P. Basler, M. Krause, M. Mühlleitner, et al. "Strong first order electroweak phase transition in the CP-conserving 2HDM revisited." In: *JHEP* 02 (2017), p. 121. DOI: 10.1007/JHEP02(2017)121. arXiv: 1612.04086 [hep-ph].

[47] Martin Bauer, Ulrich Haisch, and Felix Kahlhoefer. "Simplified dark matter models with two Higgs doublets: I. Pseudoscalar mediators." In: *JHEP* 05 (2017), p. 138. DOI: 10.1007/JHEP05(2017)138. arXiv: 1701.07427 [hep-ph].

[48] M. Beneke, P. Falgari, S. Klein, and C. Schwinn. "Hadronic top-quark pair production with NNLL threshold resummation." In: *Nucl. Phys. B* 855 (2012), pp. 695–741. DOI: 10.1016/j.nuclphysb.2011.10.021. arXiv: 1109.1536 [hep-ph].

[49] Thomas Biekötter, Sven Heinemeyer, Jose Miguel No, et al. "First shot of the smoking gun: probing the electroweak phase transition in the 2HDM with novel searches for A → ZH in $\ell^+\ell^- t\bar{t}$ and $\nu\nu b\bar{b}$ final states." In: *Journal of High Energy Physics* 2024.1 (Jan. 2024). ISSN: 1029-8479. DOI: 10.1007/jhep01(2024)107. URL: http://dx.doi.org/10.1007/JHEP01(2024)107.

[50] Christian Bierlich et al. "Robust Independent Validation of Experiment and Theory: Rivet version 3." In: *SciPost Phys.* 8 (2020), p. 026. DOI: 10.21468/SciPostPhys.8.2.026. arXiv: 1912.05451 [hep-ph].

[51] Christian Bierlich, Smita Chakraborty, Nishita Desai, et al. *A comprehensive guide to the physics and usage of PYTHIA 8.3*. 2022. arXiv: 2203.11601 [hep-ph].

[52] M. Boezio, V. Bonvicini, P. Schiavon, et al. "The Cosmic-Ray Antiproton Flux between 3 and 49 GeV." In: *The Astrophysical Journal* 561.2 (Nov. 2001), p. 787. DOI: 10.1086/323366. URL: https://dx.doi.org/10.1086/323366.

[53] Enrico Bothmann et al. "Event generation with Sherpa 2.2." In: *SciPost Phys.* 7.3 (2019), p. 034. DOI: 10.21468/SciPostPhys.7.3.034. arXiv: 1905.09127 [hep-ph].

[54] G. C. Branco, P. M. Ferreira, L. Lavoura, et al. "Theory and phenomenology of two-Higgs-doublet models." In: *Phys. Rept.* 516 (2012), pp. 1–102. DOI: 10.1016/j.physrep.2012.02.002. arXiv: 1106.0034 [hep-ph].

[55] Oliver Brein, Abdelhak Djouadi, and Robert Harlander. "NNLO QCD corrections to the Higgs-strahlung processes at hadron colliders." In: *Phys. Lett. B* 579 (2004), pp. 149–156. DOI: 10.1016/j.physletb.2003.10.112. arXiv: hep-ph/0307206.

[56] Oliver Brein, Robert Harlander, Marius Wiesemann, and Tom Zirke. "Top-quark mediated effects in hadronic Higgs-Strahlung." In: *Eur. Phys. J. C* 72 (2012), p. 1868. DOI: 10.1140/epjc/s10052-012-1868-6. arXiv: 1111.0761 [hep-ph].

[57] Oliver Brein, Robert V. Harlander, and Tom J. E. Zirke. "vh@nnlo – Higgs Strahlung at hadron colliders." In: *Comput. Phys. Commun.* 184 (2013), pp. 998–1003. DOI: 10.1016/j.cpc.2012.11.002. arXiv: 1210.5347 [hep-ph].

[58] Oliver Sim Brüning, Paul Collier, P Lebrun, et al. *LHC Design Report*. CERN Yellow Reports: Monographs. Geneva: CERN, 2004. DOI: 10.5170/CERN-2004-003-V-1. URL: https://cds.cern.ch/record/782076.

[59] Andy Buckley, Jonathan Butterworth, Stefan Gieseke, et al. "General-purpose event generators for LHC physics." In: *Physics Reports* 504.5 (July 2011), pp. 145–233. ISSN: 0370-1573. DOI: 10.1016/j.physrep.2011.03.005. URL: http://dx.doi.org/10.1016/j.physrep.2011.03.005.

[60] Andy Buckley, Deepak Kar, and Karl Nordström. "Fast simulation of detector effects in Rivet." In: *SciPost Phys.* 8 (2020), p. 025. DOI: 10.21468/SciPostPhys.8.2.025. arXiv: 1910.01637 [hep-ph].

[61] C. Burgard. *Standard Model Infographics*. Accessed on Date of access. 2024. URL: https://texample.net/tikz/examples/model-physics/.

[62] Jon Butterworth et al. "PDF4LHC recommendations for LHC Run II." In: *J. Phys. G* 43 (2016), p. 023001. DOI: 10.1088/0954-3899/43/2/023001. arXiv: 1510.03865 [hep-ph].

[63] Matteo Cacciari, Michal Czakon, Michelangelo Mangano, et al. "Top-pair production at hadron colliders with next-to-next-to-leading logarithmic soft-gluon resummation." In: *Phys. Lett. B* 710 (2012), pp. 612–622. DOI: 10.1016/j.physletb.2012.03.013. arXiv: 1111.5869 [hep-ph].

[64] Matteo Cacciari and Gavin P. Salam. "Pileup subtraction using jet areas." In: *Physics Letters B* 659.1 (2008), pp. 119–126. ISSN: 0370-2693. DOI: https://doi.org/10.1016/j.physletb.2007.09.077. URL: https://www.sciencedirect.com/science/article/pii/S0370269307011094.

[65] Matteo Cacciari, Gavin P. Salam, and Gregory Soyez. "FastJet user manual." In: *Eur. Phys. J. C* 72 (2012), p. 1896. DOI: 10.1140/epjc/s10052-012-1896-2. arXiv: 1111.6097 [hep-ph].

[66] Matteo Cacciari, Gavin P. Salam, and Gregory Soyez. "The anti-k_t jet clustering algorithm." In: *JHEP* 04 (2008), p. 063. DOI: 10.1088/1126-6708/2008/04/063. arXiv: 0802.1189 [hep-ph].

[67] John M. Campbell, R. Keith Ellis, and Ciaran Williams. "Associated production of a Higgs boson at NNLO." In: *JHEP* 06 (2016), p. 179. DOI: 10.1007/JHEP06(2016)179. arXiv: 1601.00658 [hep-ph].

[68] Francesca Capocasa. "Building the ATLAS ITk Strip detector: a journey from sensors to multi-module staves." PhD thesis. 2023. DOI: 10.48617/etd.1040.

[69] Tancredi Carli, Klaus Rabbertz, and Steffen Schumann. "Studies of Quantum Chromodynamics at the LHC." In: *The Large Hadron Collider*. Springer International Publishing, 2015, pp. 139–194. ISBN: 9783319150017. DOI: 10.1007/978-3-319-15001-7_5. URL: http://dx.doi.org/10.1007/978-3-319-15001-7_5.

[70] S. Catani, F. Krauss, B. R. Webber, and R. Kuhn. "QCD Matrix Elements + Parton Showers." In: *JHEP* 11 (2001), p. 063. DOI: 10.1088/1126-6708/2001/11/063. arXiv: hep-ph/0109231.

[71] M. L. Ciccolini, S. Dittmaier, and M. Krämer. "Electroweak radiative corrections to associated WH and ZH production at hadron colliders." In: *Phys. Rev. D* 68 (2003), p. 073003. DOI: 10.1103/PhysRevD.68.073003. arXiv: hep-ph/0306234 [hep-ph].

[72] CMS Collaboration. "Observation of a new boson at a mass of 125 GeV with the CMS experiment at the LHC." In: *Phys. Lett. B* 716 (2012), p. 30. DOI: 10.1016/j.physletb.2012.08.021. arXiv: 1207.7235 [hep-ex].

[73] CMS Collaboration. "Search for heavy resonances decaying into a vector boson and a Higgs boson in final states with charged leptons, neutrinos, and b quarks." In: *Phys. Lett. B* 768 (2017), p. 137. DOI: 10.1016/j.physletb.2017.02.040. arXiv: 1610.08066 [hep-ex].

[74] CMS Collaboration. "Search for new neutral Higgs bosons through the $H \to ZA \to \ell^+\ell^- b\bar{b}$ process in pp collisions at $\sqrt{s} = 13\,\text{TeV}$." In: *JHEP* 03 (2020), p. 055. DOI: 10.1007/JHEP03(2020)055. arXiv: 1911.03781 [hep-ex].

[75] Andrew G. Cohen, D. B. Kaplan, and A. E. Nelson. "Progress in Electroweak Baryogenesis." In: *Ann. Rev. Nucl. Part. Sci.* 43 (1993), pp. 27–70. DOI: 10.1146/annurev.ns.43.120193.000331. arXiv: hep-ph/9302210 [hep-ph].

[76] ATLAS Collaboration. *Electron and photon efficiencies in LHC Run 2 with the ATLAS experiment*. 2023. arXiv: 2308.13362 [hep-ex].

[77] ATLAS Collaboration. "Muon reconstruction and identification efficiency in ATLAS using the full Run 2 pp collision data set at $\sqrt{s} = 13$ TeV." In: *The European Physical Journal C* 81.7 (July 2021). ISSN: 1434-6052. DOI: 10.1140/epjc/s10052-021-09233-2. URL: http://dx.doi.org/10.1140/epjc/s10052-021-09233-2.

[78] The ATLAS Collaboration. "ATLAS b-jet identification performance and efficiency measurement with $t\bar{t}$ events in pp collisions at $\sqrt{s} = 13$ TeV." In: *The European Physical Journal C* 79.11 (Nov. 2019). ISSN: 1434-6052. DOI: 10.1140/epjc/s10052-019-7450-8. URL: http://dx.doi.org/10.1140/epjc/s10052-019-7450-8.

[79] The ATLAS Collaboration. "Constraints on Higgs boson production with large transverse momentum using $H \to b\bar{b}$ decays in the ATLAS detector." In: *Phys. Rev. D* 105 (9 May 2022), p. 092003. DOI: 10.1103/PhysRevD.105.092003. URL: https://link.aps.org/doi/10.1103/PhysRevD.105.092003.

[80] The ATLAS Collaboration. "Cross-section measurements of the Higgs boson decaying into a pair of τ-leptons in proton-proton collisions at $\sqrt{s} = 13$ TeV with the ATLAS detector." In: *Phys. Rev. D* 99 (7 Apr. 2019), p. 072001. DOI: 10.1103/PhysRevD.99.072001. URL: https://link.aps.org/doi/10.1103/PhysRevD.99.072001.

[81] The ATLAS Collaboration. "Direct constraint on the Higgs–charm coupling from a search for Higgs boson decays into charm quarks with the ATLAS detector." In: *The European Physical Journal C* 82.8 (Aug. 2022). ISSN: 1434-6052. DOI: 10.1140/epjc/s10052-022-10588-3. URL: http://dx.doi.org/10.1140/epjc/s10052-022-10588-3.

[82] The ATLAS Collaboration. "Observation of $H \to b\bar{b}$ decays and VH production with the ATLAS detector." In: *Physics Letters B* 786 (2018), pp. 59–86. ISSN: 0370-2693. DOI: https://doi.org/10.1016/j.physletb.2018.09.013. URL: https://www.sciencedirect.com/science/article/pii/S0370269318307056.

[83] The ATLAS Collaboration. "Observation of Higgs boson production in association with a top quark pair at the LHC with the ATLAS detector." In: *Physics Letters B* 784 (2018), pp. 173–191. ISSN: 0370-2693. DOI: https://doi.org/10.1016/j.physletb.2018.07.035. URL: https://www.sciencedirect.com/science/article/pii/S0370269318305732.

[84] The ATLAS collaboration. "ATLAS b-jet identification performance and efficiency measurement with $t\bar{t}$ events in pp collisions at $\sqrt{s} = 13$ TeV." In: *The European Physical Journal C* 79.11 (Nov. 2019). ISSN: 1434-6052. DOI: 10.1140/epjc/s10052-019-7450-8. URL: http://dx.doi.org/10.1140/epjc/s10052-019-7450-8.

[85] The ATLAS collaboration. "Jet energy scale and resolution measured in proton–proton collisions at $\sqrt{s} = 13$ TeV with the ATLAS detector." In: *The European Physical Journal C* 81.8 (Aug. 2021). ISSN: 1434-6052. DOI: 10.1140/epjc/s10052-021-09402-3. URL: http://dx.doi.org/10.1140/epjc/s10052-021-09402-3.

[86] The ATLAS collaboration. "Operation of the ATLAS trigger system in Run 2." In: *Journal of Instrumentation* 15.10 (Oct. 2020), P10004. DOI: 10.1088/1748-0221/15/10/P10004. URL: https://dx.doi.org/10.1088/1748-0221/15/10/P10004.

[87] The ATLAS collaboration. "The ATLAS Simulation Infrastructure." In: *The European Physical Journal C* 70.3 (Sept. 2010), pp. 823–874. ISSN: 1434-6052. DOI: 10.1140/epjc/s10052-010-1429-9. URL: http://dx.doi.org/10.1140/epjc/s10052-010-1429-9.

[88] The CMS collaboration. "Observation of $t\bar{t}H$ Production." In: *Phys. Rev. Lett.* 120 (23 June 2018), p. 231801. DOI: 10.1103/PhysRevLett.120.231801. URL: https://link.aps.org/doi/10.1103/PhysRevLett.120.231801.

[89] The CMS collaboration. "Observation of Higgs Boson Decay to Bottom Quarks." In: *Phys. Rev. Lett.* 121 (12 Sept. 2018), p. 121801. DOI: 10.1103/PhysRevLett.121.121801. URL: https://link.aps.org/doi/10.1103/PhysRevLett.121.121801.

[90] The CMS collaboration. "Observation of the Higgs boson decay to a pair of τ leptons with the CMS detector." In: *Physics Letters B* 779 (2018), pp. 283–316. ISSN: 0370-2693. DOI: https://doi.org/10.1016/j.physletb.2018.02.004. URL: https://www.sciencedirect.com/science/article/pii/S0370269318301035.

[91] John C. Collins, Davison E. Soper, and George Sterman. "FACTORIZATION OF HARD PROCESSES IN QCD." In: *Perturbative QCD*, pp. 1–91. DOI: 10.1142/9789814503266_0001. eprint: https://www.worldscientific.com/doi/pdf/10.1142/9789814503266_0001. URL: https://www.worldscientific.com/doi/abs/10.1142/9789814503266_0001.

[92] *Combination of measurements of Higgs boson production in association with a W or Z boson in the $b\bar{b}$ decay channel with the ATLAS experiment at $\sqrt{s} = 13$ TeV.* Tech. rep. Geneva: CERN, 2021. URL: https://cds.cern.ch/record/2782535.

[93] Glen Cowan, Kyle Cranmer, Eilam Gross, and Ofer Vitells. "Asymptotic formulae for likelihood-based tests of new physics." In: *Eur. Phys. J. C* 71 (2011), p. 1554. DOI: 10.1140/epjc/s10052-011-1554-0. arXiv: 1007.1727 [physics.data-an]. Erratum: in: *Eur. Phys. J. C* 73 (2013), p. 2501. DOI: 10.1140/epjc/s10052-013-2501-z.

[94] Michal Czakon, Paul Fiedler, and Alexander Mitov. "Total Top-Quark Pair Production Cross Section at Hadron Colliders Through $O(\alpha_S^4)$." In: *Phys. Rev. Lett.* 110 (2013), p. 252004. DOI: 10.1103/PhysRevLett.110.252004. arXiv: 1303.6254 [hep-ph].

[95] Michal Czakon and Alexander Mitov. "NNLO corrections to top pair production at hadron colliders: the quark-gluon reaction." In: *JHEP* 01 (2013), p. 080. DOI: 10.1007/JHEP01(2013)080. arXiv: 1210.6832 [hep-ph].

[96] Michal Czakon and Alexander Mitov. "NNLO corrections to top-pair production at hadron colliders: the all-fermionic scattering channels." In: *JHEP* 12 (2012), p. 054. DOI: 10.1007/JHEP12(2012)054. arXiv: 1207.0236 [hep-ph].

[97] Michal Czakon and Alexander Mitov. "Top++: A program for the calculation of the top-pair cross-section at hadron colliders." In: *Comput. Phys. Commun.* 185 (2014), p. 2930. DOI: 10.1016/j.cpc.2014.06.021. arXiv: 1112.5675 [hep-ph].

[98] S. Dawson, C. B. Jackson, L. Reina, and D. Wackeroth. "Exclusive Higgs boson production with bottom quarks at hadron colliders." In: *Phys. Rev. D* 69 (2004), p. 074027. DOI: 10.1103/PhysRevD.69.074027. arXiv: hep-ph/0311067.

[99] DELPHES 3 Collaboration. "DELPHES 3: A modular framework for fast simulation of a generic collider experiment." In: *JHEP* 02 (2014), p. 057. DOI: 10.1007/JHEP02(2014)057. arXiv: 1307.6346 [hep-ex].

[100] Stefan Dittmaier, Michael Krämer, and Michael Spira. "Higgs radiation off bottom quarks at the Fermilab Tevatron and the CERN LHC." In: *Phys. Rev. D* 70 (2004), p. 074010. DOI: 10.1103/PhysRevD.70.074010. arXiv: hep-ph/0309204.

[101] Abdelhak Djouadi. "The anatomy of electroweak symmetry breaking Tome II: The Higgs bosons in the Minimal Supersymmetric Model." In: *Phys. Rept.* 459 (2008), pp. 1–241. DOI: 10.1016/j.physrep.2007.10.005. arXiv: hep-ph/0503173 [hep-ph].

[102] G. C. Dorsch, S. J. Huber, K. Mimasu, and J. M. No. "Echoes of the Electroweak Phase Transition: Discovering a second Higgs doublet through $A_0 \to ZH_0$." In: *Phys. Rev. Lett.* 113.21 (2014), p. 211802. DOI: 10.1103/PhysRevLett.113.211802. arXiv: 1405.5537 [hep-ph].

[103] G. C. Dorsch, S. J. Huber, K. Mimasu, and J. M. No. "The Higgs Vacuum Uplifted: Revisiting the Electroweak Phase Transition with a Second Higgs Doublet." In: *JHEP* 12 (2017), p. 086. DOI: 10.1007/JHEP12(2017)086. arXiv: 1705.09186 [hep-ph].

[104] G. C. Dorsch, S. J. Huber, and J. M. No. "A strong electroweak phase transition in the 2HDM after LHC8." In: *JHEP* 10 (2013), p. 029. DOI: 10.1007/JHEP10(2013)029. arXiv: 1305.6610 [hep-ph].

[105] "Electron reconstruction and identification in the ATLAS experiment using the 2015 and 2016 LHC proton–proton collision data at $\sqrt{s} = 13$ TeV." In: *The European Physical Journal C* 79.8 (Aug. 2019). ISSN: 1434-6052. DOI: 10.1140/epjc/s10052-019-7140-6. URL: http://dx.doi.org/10.1140/epjc/s10052-019-7140-6.

[106] David Eriksson, Johan Rathsman, and Oscar Stål. "2HDMC – two-Higgs-doublet model calculator." In: *Comput. Phys. Commun.* 181 (2010), pp. 189–205. DOI: 10.1016/j.cpc.2009.09.011. arXiv: 0902.0851 [hep-ph].

[107] *Evaluation of theoretical uncertainties for simplified template cross section measurements of V-associated production of the Higgs boson.* Tech. rep. Geneva: CERN, 2018. URL: https://cds.cern.ch/record/2649241.

[108] Arnaud Ferrari and Nikolaos Rompotis. "Exploration of Extended Higgs Sectors with Run-2 Proton–Proton Collision Data at the LHC." In: *Symmetry* 13.11 (2021). ISSN: 2073-8994. DOI: 10.3390/sym13112144. URL: https://www.mdpi.com/2073-8994/13/11/2144.

[109] Giancarlo Ferrera, Massimiliano Grazzini, and Francesco Tramontano. "Associated WH production at hadron colliders: a fully exclusive QCD calculation at NNLO." In: *Phys. Rev. Lett.* 107 (2011), p. 152003. DOI: 10.1103/PhysRevLett.107.152003. arXiv: 1107.1164 [hep-ph].

[110] Giancarlo Ferrera, Massimiliano Grazzini, and Francesco Tramontano. "Associated ZH production at hadron colliders: the fully differential NNLO QCD calculation." In: *Phys. Lett.* B740 (2015), pp. 51–55. DOI: 10.1016/j.physletb.2014.11.040. arXiv: 1407.4747 [hep-ph].

[111] Giancarlo Ferrera, Massimiliano Grazzini, and Francesco Tramontano. "Higher-order QCD effects for associated WH production and decay at the LHC." In: *JHEP* 04 (2014), p. 039. DOI: 10.1007/JHEP04(2014)039. arXiv: 1312.1669 [hep-ph].

[112] D. de Florian et al. "Handbook of LHC Higgs Cross Sections: 4. Deciphering the Nature of the Higgs Sector." In: (2016). DOI: 10.23731/CYRM-2017-002. arXiv: 1610.07922 [hep-ph].

[113] Rikkert Frederix, Emanuele Re, and Paolo Torrielli. "Single-top t-channel hadroproduction in the four-flavour scheme with POWHEG and aMC@NLO." In: *JHEP* 09 (2012), p. 130. DOI: 10.1007/JHEP09(2012)130. arXiv: 1207.5391 [hep-ph].

[114] Stefano Frixione, Eric Laenen, Patrick Motylinski, and Bryan R. Webber. "Angular correlations of lepton pairs from vector boson and top quark decays in Monte Carlo simulations." In: *JHEP* 04 (2007), p. 081. DOI: 10.1088/1126-6708/2007/04/081. arXiv: hep-ph/0702198.

[115] Stefano Frixione, Eric Laenen, Patrick Motylinski, et al. "Single-top hadroproduction in association with a W boson." In: *JHEP* 07 (2008), p. 029. DOI: 10.1088/1126-6708/2008/07/029. arXiv: 0805.3067 [hep-ph].

[116] Stefano Frixione, Paolo Nason, and Carlo Oleari. "Matching NLO QCD computations with parton shower simulations: the POWHEG method." In: *JHEP* 11 (2007), p. 070. DOI: 10.1088/1126-6708/2007/11/070. arXiv: 0709.2092 [hep-ph].

[117] Stefano Frixione, Giovanni Ridolfi, and Paolo Nason. "A positive-weight next-to-leading-order Monte Carlo for heavy flavour hadroproduction." In: *JHEP* 09 (2007), p. 126. DOI: 10.1088/1126-6708/2007/09/126. arXiv: 0707.3088 [hep-ph].

[118] Lars Fromme, Stephan J. Huber, and Michael Seniuch. "Baryogenesis in the two-Higgs doublet model." In: *JHEP* 11 (2006), p. 038. DOI: 10.1088/1126-6708/2006/11/038. arXiv: hep-ph/0605242 [hep-ph].

[119] Geoffrey Gilles, Manuel Guth, Philipp Gadow, et al. *ATLAS b-tagging algorithms for the LHC Run 2 dataset*. Tech. rep. Geneva: CERN, 2022. URL: https://cds.cern.ch/record/2806947.

[120] Sheldon L. Glashow and Steven Weinberg. "Natural conservation laws for neutral currents." In: *Phys. Rev. D* 15 (7 Apr. 1977), pp. 1958–1965. DOI: 10.1103/PhysRevD.15.1958. URL: https://link.aps.org/doi/10.1103/PhysRevD.15.1958.

[121] David J. Gross and Frank Wilczek. "Ultraviolet Behavior of Non-Abelian Gauge Theories." In: *Phys. Rev. Lett.* 30 (26 June 1973), pp. 1343–1346. DOI: 10.1103/PhysRevLett.30.1343. URL: https://link.aps.org/doi/10.1103/PhysRevLett.30.1343.

[122] Eilam Gross and Ofer Vitells. "Trial factors for the look elsewhere effect in high energy physics." In: *Eur. Phys. J. C* 70 (2010), pp. 525–530. DOI: 10.1140/epjc/s10052-010-1470-8. arXiv: 1005.1891 [physics.data-an].

[123] Ulrich Haisch and Giacomo Polesello. "Searching for heavy Higgs bosons in the $t\bar{t}Z$ and tbW final states." In: *JHEP* 09 (2018), p. 151. DOI: 10.1007/JHEP09(2018)151. arXiv: 1807.07734 [hep-ph].

[124] Keith Hamilton, Paolo Nason, and Giulia Zanderighi. "MINLO: multi-scale improved NLO." In: *JHEP* 10 (2012), p. 155. DOI: 10.1007/JHEP10(2012)155. arXiv: 1206.3572 [hep-ph].

[125] Robert Harlander, Michael Krämer, and Markus Schumacher. "Bottom-quark associated Higgs-boson production: reconciling the four- and five-flavour scheme approach." In: (2011). arXiv: 1112.3478 [hep-ph].

[126] Robert V. Harlander and Philipp Kant. "Higgs production and decay: analytic results at next-to-leading-order QCD." In: *JHEP* 12 (2005), p. 015. DOI: 10.1088/1126-6708/2005/12/015. arXiv: hep-ph/0509189.

[127] Robert V. Harlander and William B. Kilgore. "Higgs boson production in bottom quark fusion at next-to-next-to leading order." In: *Phys. Rev. D* 68 (2003), p. 013001. DOI: 10.1103/PhysRevD.68.013001. arXiv: hep-ph/0304035.

[128] Robert V. Harlander and William B. Kilgore. "Next-to-next-to-leading order Higgs production at hadron colliders." In: *Phys. Rev. Lett.* 88 (2002), p. 201801. DOI: 10.1103/PhysRevLett.88.201801. arXiv: hep-ph/0201206.

[129] Robert V. Harlander, Anna Kulesza, Vincent Theeuwes, and Tom Zirke. "Soft gluon resummation for gluon-induced Higgs Strahlung." In: *JHEP* 11 (2014), p. 082. DOI: 10.1007/JHEP11(2014)082. arXiv: 1410.0217 [hep-ph].

[130] Robert V. Harlander, Stefan Liebler, and Hendrik Mantler. "SusHi: A program for the calculation of Higgs production in gluon fusion and bottom-quark annihilation in the Standard Model and the MSSM." In: *Comput. Phys. Commun.* 184 (2013), pp. 1605–1617. DOI: 10.1016/j.cpc.2013.02.006. arXiv: 1212.3249 [hep-ph].

[131] Heribertus B. Hartanto, Barbara Jäger, Laura Reina, and Doreen Wackeroth. "Higgs boson production in association with top quarks in the POWHEG BOX." In: *Phys. Rev. D* 91.9 (2015), p. 094003. DOI: 10.1103/PhysRevD.91.094003. arXiv: 1501.04498 [hep-ph].

[132] Frank Hartmann. *Evolution of Silicon Sensor Technology in Particle Physics*. Vol. 275. Springer Tracts in Modern Physics. Springer, 2017. ISBN: 978-3-319-64434-9. DOI: 10.1007/978-3-319-64436-3.

[133] Stefan Höche, Frank Krauss, Marek Schönherr, and Frank Siegert. "A critical appraisal of NLO+PS matching methods." In: *JHEP* 09 (2012), p. 049. DOI: 10.1007/JHEP09(2012)049. arXiv: 1111.1220 [hep-ph].

[134] Stefan Höche, Frank Krauss, Marek Schönherr, and Frank Siegert. "QCD matrix elements + parton showers. The NLO case." In: *JHEP* 04 (2013), p. 027. DOI: 10.1007/JHEP04(2013)027. arXiv: 1207.5030 [hep-ph].

[135] Stefan Höche, Frank Krauss, Steffen Schumann, and Frank Siegert. "QCD matrix elements and truncated showers." In: *JHEP* 05 (2009), p. 053. DOI: 10.1088/1126-6708/2009/05/053. arXiv: 0903.1219 [hep-ph].

[136] Stefan Hoeche and Marek Schonherr. "Uncertainties in next-to-leading order plus parton shower matched simulations of inclusive jet and dijet production." In: *Phys. Rev.* D86 (2012), p. 094042. DOI: 10.1103/PhysRevD.86.094042. arXiv: 1208.2815 [hep-ph].

[137] *Identification of Jets Containing b-Hadrons with Recurrent Neural Networks at the ATLAS Experiment*. Tech. rep. All figures including auxiliary figures are available at https://atlas.web.cern.ch/Atlas/GROUPS/PHYSICS/PUBNOTES/ATL-PHYS-PUB-2017-003. Geneva: CERN, 2017. URL: https://cds.cern.ch/record/2255226.

[138] "Jet reconstruction and performance using particle flow with the ATLAS Detector." In: *The European Physical Journal C* 77.7 (July 2017). ISSN: 1434-6052. DOI: 10.1140/epjc/s10052-017-5031-2. URL: http://dx.doi.org/10.1140/epjc/s10052-017-5031-2.

[139] R. E. Kalman. "A New Approach to Linear Filtering and Prediction Problems." In: *Journal of Basic Engineering* 82.1 (Mar. 1960), pp. 35–45. ISSN: 0021-9223. DOI: 10.1115/1.3662552.

[140] P. Kant, O. M. Kind, T. Kintscher, et al. "HatHor for single top-quark production: Updated predictions and uncertainty estimates for single top-quark production in hadronic collisions." In: *Comput. Phys. Commun.* 191 (2015), pp. 74–89. DOI: 10.1016/j.cpc.2015.02.001. arXiv: 1406.4403 [hep-ph].

[141] Vardan Khachatryan et al. "Search for neutral resonances decaying into a Z boson and a pair of b jets or τ leptons." In: *Phys. Lett. B* 759 (2016), pp. 369–394. DOI: 10.1016/j.physletb.2016.05.087. arXiv: 1603.02991 [hep-ex].

[142] Nikolaos Kidonakis. "Top Quark Production." In: *Proceedings, Helmholtz International Summer School on Physics of Heavy Quarks and Hadrons (HQ 2013)* (JINR, Dubna, Russia, July 15–28, 2013), pp. 139–168. DOI: 10.3204/DESY-PROC-2013-03/Kidonakis. arXiv: 1311.0283 [hep-ph].

[143] Nikolaos Kidonakis. "Two-loop soft anomalous dimensions for single top quark associated production with a W^- or H^-." In: *Phys. Rev. D* 82 (2010), p. 054018. DOI: 10.1103/PhysRevD.82.054018. arXiv: 1005.4451 [hep-ph].

[144] Jihn E. Kim and Gianpaolo Carosi. "Axions and the strong CP problem." In: *Rev. Mod. Phys.* 82 (2010), pp. 557–602. DOI: 10.1103/RevModPhys.82.557. arXiv: 0807.3125 [hep-ph]. Erratum: Rev.Mod.Phys. **91** (2019) 049902.

[145] S. F. King. "Neutrino mass models." In: *Rept. Prog. Phys.* 67 (2003), pp. 107–158. DOI: 10.1088/0034-4885/67/2/R01. arXiv: hep-ph/0310204 [hep-ph].

[146] David Krohn, Jesse Thaler, and Lian-Tao Wang. "Jet trimming." In: *Journal of High Energy Physics* 2010.2 (Feb. 2010). ISSN: 1029-8479. DOI: 10.1007/jhep02(2010)084. URL: http://dx.doi.org/10.1007/JHEP02(2010)084.

[147] V.A. Kuzmin, V.A. Rubakov, and M.E. Shaposhnikov. "On anomalous electroweak baryon-number non-conservation in the early universe." In: *Physics Letters B* 155.1 (1985), pp. 36–42. ISSN: 0370-2693. DOI: https://doi.org/10.1016/0370-2693(85)91028-7. URL: https://www.sciencedirect.com/science/article/pii/0370269385910287.

[148] Gionata Luisoni, Paolo Nason, Carlo Oleari, and Francesco Tramontano. "$HW^{\pm}$/HZ + 0 and 1 jet at NLO with the POWHEG BOX interfaced to GoSam and their merging within MiNLO." In: *JHEP* 10 (2013), p. 083. DOI: 10.1007/JHEP10(2013)083. arXiv: 1306.2542 [hep-ph].

[149] Gerhard Lutz. "Basic Semiconductor Structures." In: *Semiconductor Radiation Detectors: Device Physics*. Berlin, Heidelberg: Springer Berlin Heidelberg, 2007. ISBN: 978-3-540-71679-2. DOI: 10.1007/978-3-540-71679-2_3. URL: https://doi.org/10.1007/978-3-540-71679-2_3.

[150] *Measurement of the fiducial and differential cross-section of WH/ZH production for the b-jets + E_T^{miss} final state in pp collisions at $\sqrt{s} = 13$ TeV with the ATLAS detector*. Tech. rep. All figures including auxiliary figures are available at https://atlas.web.cern.ch/Atlas/GROUPS/PHYSICS/CONFNOTES/ATLAS-CONF-2022-015. Geneva: CERN, 2022. URL: https://cds.cern.ch/record/2805712.

[151] S van der Meer. *Calibration of the effective beam height in the ISR*. Tech. rep. Geneva: CERN, 1968. URL: https://cds.cern.ch/record/296752.

[152] Bruce Mellado Garcia, Pasquale Musella, Massimiliano Grazzini, and Robert Harlander. "CERN Report 4: Part I Standard Model Predictions." In: (2016). URL: https://cds.cern.ch/record/2150771.

[153] Esma Mobs. "The CERN accelerator complex in 2019. Complexe des accélérateurs du CERN en 2019." In: (2019). General Photo. URL: https://cds.cern.ch/record/2684277.

[154] Michael Moll. "Radiation damage in silicon particle detectors: Microscopic defects and macroscopic properties." Ph.D. Thesis (Advisor: G. Lindstrom); Dissertation, Universität Hamburg, 1999. Dissertation. Universität Hamburg, 1999, p. 251. DOI: 10.3204/PUBDB-2016-02525. URL: https://bib-pubdb1.desy.de/record/300958.

[155] David E Morrissey and Michael J Ramsey-Musolf. "Electroweak baryogenesis." In: *New Journal of Physics* 14.12 (Dec. 2012), p. 125003. DOI: 10.1088/1367-2630/14/12/125003. URL: https://dx.doi.org/10.1088/1367-2630/14/12/125003.

[156] Paolo Nason. "A new method for combining NLO QCD with shower Monte Carlo algorithms." In: *JHEP* 11 (2004), p. 040. DOI: 10.1088/1126-6708/2004/11/040. arXiv: hep-ph/0409146.

[157] *p–n junction - Wikipedia — en.wikipedia.org*. https://en.wikipedia.org/wiki/P-n_junction. [Accessed 20-03-2024].

[158] R. D. Peccei and Helen R. Quinn. "CP Conservation in the Presence of Pseudoparticles." In: *Phys. Rev. Lett.* 38 (25 June 1977), pp. 1440–1443. DOI: 10.1103/PhysRevLett.38.1440. URL: https://link.aps.org/doi/10.1103/PhysRevLett.38.1440.

[159] Joao Pequenao. "Computer Generated image of the ATLAS calorimeter." 2008. URL: https://cds.cern.ch/record/1095927.

[160] Joao Pequenao. "Computer generated image of the ATLAS Liquid Argon." 2008. URL: https://cds.cern.ch/record/1095928.

[161] Joao Pequenao and Paul Schaffner. "How ATLAS detects particles: diagram of particle paths in the detector." 2013. URL: https://cds.cern.ch/record/1505342.

[162] PW Phillips. "Design, development, characterisation and operation of ATLAS ITk strip staves." PhD thesis. 2020. URL: https://ora.ox.ac.uk/objects/uuid:16ea0c42-8bae-482d-bfbc-e1d898124461.

[163] H. David Politzer. "Reliable Perturbative Results for Strong Interactions?" In: *Phys. Rev. Lett.* 30 (26 June 1973), pp. 1346–1349. DOI: 10.1103/PhysRevLett.30.1346. URL: https://link.aps.org/doi/10.1103/PhysRevLett.30.1346.

[164] C T Potter, H Mantler, S Lehti, et al. *Handbook of LHC Higgs Cross Sections: 3. Higgs Properties: Report of the LHC Higgs Cross Section Working Group*. en. 2013. DOI: 10.5170/CERN-2013-004. URL: http://cds.cern.ch/record/1559921.

[165] J. Pumplin et al. "New Generation of Parton Distributions with Uncertainties from Global QCD Analysis." In: *JHEP* 07 (2002), p. 012. DOI: 10.1088/1126-6708/2002/07/012. arXiv: hep-ph/0201195.

[166] Veljko Radeka. "Low-Noise Techniques In Detectors." In: *Annual Review of Nuclear and Particle Science* 38 (Nov. 2003), pp. 217–277. DOI: 10.1146/annurev.ns.38.120188.001245.

[167] Emanuele Re. "Single-top Wt-channel production matched with parton showers using the POWHEG method." In: *Eur. Phys. J. C* 71 (2011), p. 1547. DOI: 10.1140/epjc/s10052-011-1547-z. arXiv: 1009.2450 [hep-ph].

[168] A. D. Sakharov. "Violation of CP Invariance, C asymmetry, and baryon asymmetry of the universe." In: *Pisma Zh. Eksp. Teor. Fiz.* 5 (1967), pp. 32–35. DOI: 10.1070/PU1991v034n05ABEH002497.

[169] Gavin P Salam and Grégory Soyez. "A practical seedless infrared-safe cone jet algorithm." In: *Journal of High Energy Physics* 2007.05 (May 2007), pp. 086–086. ISSN: 1029-8479. DOI: 10.1088/1126-6708/2007/05/086. URL: http://dx.doi.org/10.1088/1126-6708/2007/05/086.

[170] Schramm, Steven. "ATLAS Jet Reconstruction, Calibration, and Tagging of Lorentz-boosted Objects." In: *EPJ Web Conf.* 182 (2018), p. 02113. DOI: 10.1051/epjconf/201818202113. URL: https://doi.org/10.1051/epjconf/201818202113.

[171] Steffen Schumann and Frank Krauss. "A parton shower algorithm based on Catani–Seymour dipole factorisation." In: *JHEP* 03 (2008), p. 038. DOI: 10.1088/1126-6708/2008/03/038. arXiv: 0709.1027 [hep-ph].

[172] *Secondary vertex finding for jet flavour identification with the ATLAS detector.* Tech. rep. Geneva: CERN, 2017. URL: https://cds.cern.ch/record/2270366.

[173] Oruganti U. Shanker. "Flavor Violation, Scalar Particles and Leptoquarks." In: *Nucl. Phys. B* 206 (1982), pp. 253–272. DOI: 10.1016/0550-3213(82)90534-X.

[174] J. L. Sievers, J. R. Bond, J. K. Cartwright, et al. "Cosmological Parameters from Cosmic Background Imager Observations and Comparisons with BOOMERANG, DASI, and MAXIMA." In: *The Astrophysical Journal* 591.2 (July 2003), pp. 599–622. DOI: 10.1086/375510. URL: https://doi.org/10.1086%2F375510.

[175] T. Sjöstrand, S. Mrenna, and P. Skands. "A brief introduction to PYTHIA 8.1." In: *Comput. Phys. Commun.* 178 (2008), pp. 852–867. DOI: 10.1016/j.cpc.2008.01.036. arXiv: 0710.3820 [hep-ph].

[176] Torbjörn Sjöstrand, Stefan Ask, Jesper R. Christiansen, et al. "An introduction to PYTHIA 8.2." In: *Comput. Phys. Commun.* 191 (2015), p. 159. DOI: 10.1016/j.cpc.2015.01.024. arXiv: 1410.3012 [hep-ph].

[177] Helmuth Spieler. "Detector Systems Overview." In: *Semiconductor Detector Systems.* Oxford University Press, Aug. 2005. ISBN: 9780198527848. DOI: 10.1093/acprof:oso/9780198527848.003.0001. URL: https://doi.org/10.1093/acprof:oso/9780198527848.003.0001.

[178] *Standard Model Summary Plots October 2023.* Tech. rep. Geneva: CERN, 2023. URL: https://cds.cern.ch/record/2882448.

[179] Giles Strong. "On the impact of selected modern deep-learning techniques to the performance and celerity of classification models in an experimental high-energy physics use case." In: *Machine Learning: Science and Technology* 1 (Sept. 2020). DOI: 10.1088/2632-2153/ab983a.

[180] Stefania Antonia Stucci, Russel Burns, Dave Lynn, et al. "Effect of Gamma Irradiation on Leakage Current in CMOS Read-out Chips for the ATLAS Upgrade Silicon Strip Tracker at the HL-LHC." In: *PoS* TWEPP-17 (2018), p. 094. DOI: 10.22323/1.313.0094.

[181] Wei Su, Anthony G. Williams, and Mengchao Zhang. "Strong first order electroweak phase transition in 2HDM confronting future Z & Higgs factories." In: *JHEP* 04 (2021), p. 219. DOI: 10.1007/JHEP04(2021)219. arXiv: 2011.04540 [hep-ph].

[182] M. Tanabashi, K. Hagiwara, K. Hikasa, et al. "Review of Particle Physics." In: *Phys. Rev. D* 98 (3 Aug. 2018), p. 030001. DOI: 10.1103/PhysRevD.98.030001. URL: https://link.aps.org/doi/10.1103/PhysRevD.98.030001.

[183] The Gfitter Group. "Update of the global electroweak fit and constraints on two-Higgs-doublet models." In: *Eur. Phys. J. C* 78.8 (2018), p. 675. DOI: 10.1140/epjc/s10052-018-6131-3. arXiv: 1803.01853 [hep-ph].

[184] Mark Thomson. *Modern Particle Physics*. Cambridge University Press, 2013.

[185] *Topological b-hadron decay reconstruction and identification of b-jets with the JetFitter package in the ATLAS experiment at the LHC*. Tech. rep. Geneva: CERN, 2018. URL: https://cds.cern.ch/record/2645405.

[186] Neil Turok and John Zadrozny. "Electroweak baryogenesis in the two-doublet model." In: *Nucl. Phys. B* 358 (1991), pp. 471–493. DOI: 10.1016/0550-3213(91)90356-3.

[187] Ofer Vitells and Eilam Gross. "Estimating the significance of a signal in a multi-dimensional search." In: *Astropart. Phys.* 35 (2011), pp. 230–234. DOI: 10.1016/j.astropartphys.2011.08.005. arXiv: 1105.4355 [astro-ph.IM].